La fissuration thermique dans les roches

Luke Griffiths

UNIVERSITÉ DE STRASBOURG

ÉCOLE DOCTORALE 413

L'Institut de Physique du Globe de Strasbourg

THÈSE présentée par :

Luke Griffiths

soutenue le : **23 février 2018**

pour obtenir le grade de : **Docteur de l'université de Strasbourg**

Discipline/ Spécialité : Géophysique

La fissuration thermique dans les roches

THÈSE dirigée par :

Baud Patrick	Professeur, Université de Strasbourg

RAPPORTEURS :

KOHL Thomas	Professeur, Karlsruher Institut für Technologie
WONG Teng-fong	Professeur, The Chinese University of Hong Kong

---

AUTRES MEMBRES DU JURY :

DAVID Christian	Professeur, Université de Cergy-Pontoise
VIOLAY Marie	Professeure Assistante, École Polytechnique Fédérale de Lausanne

For Mum, Dad, and Julia.

ABSTRACT

Rock may undergo thermal microcracking when heated, affecting its physical, mechanical, thermal, and transport properties. Thermal microcrack monitoring in the laboratory has mainly been performed during heating, and rarely during the cyclic heating and cooling relevant for volcanoes and geothermal reservoirs. For this, a new dedicated apparatus for the acoustic emission monitoring and wave velocity measurement at high temperatures was elaborated, building on previous designs. Microcrack damage was assessed with a new algorithm for quantitative microstructural analysis, and the influence of thermal microcracks on rock properties was measured and modelled. Depending on the rock type and initial microcrack content, microcracking occurred during either heating, cooling, or neither, and existing microcracks reversibly opened or closed with increasing temperature. In Earth's crust, the evolution of rock properties with temperature may be significant and is determined by the microstructure.

RÉSUMÉ

Lorsqu'elle est chauffée, la roche peut subir une microfissuration thermique, qui influence ses propriétés physiques, mécaniques, thermiques, et de transport. La surveillance de la microfissuration thermique en laboratoire a été principalement réalisée pendant le chauffage, et rarement lors du refroidissement ou du chauffage cyclique que la roche subit dans les volcans et les réservoirs géothermiques. Un nouvel appareil a été élaboré pour surveiller les émissions acoustiques et mesurer les vitesses des ondes élastiques à haute température. L'état de fissuration a été évalué grâce à un nouvel algorithme d'analyse microstructurale, et l'influence des microfissures sur les propriétés des roches a été mesurée et modélisée. Selon la microstructure, la microfissuration peut avoir lieu pendant le chauffage ou le refroidissement, et les microfissures existantes peuvent s'ouvrir et se fermer de façon réversible avec des changements de température, et influencer les propriétés de la roche.

ACKNOWLEDGMENTS

This PhD was funded in part by the Ministère de l'Education Nationale, de l'Enseignement supérieur et de la Recherche, and in part by the Laboratoire d'Excellence (LABEX) grant ANR-11-LABX-0050_G-EAU-THERMIE-PROFONDE managed by the Agence National de la Recherche (ANR) as part of the "Investissements d'avenir" program.

First and foremost, I would like to express my deepest gratitude to my advisor Patrick Baud for his guidance and support, for allowing me to lead this project in the direction I thought best, and for generously providing me with many occasions to present my work.

I am delighted to have been co-supervised by Michael J. Heap, who has schooled me in all aspects of research and has showed me patience and encouragement throughout, and Jean Schmittbuhl, whose suggestions and expert advice have benefited this work immeasurably.

I am very grateful to Olivier Lengliné for his aid in collecting and processing the wave velocity data; Thierry Reuschlé for many valuable discussions on all aspects of laboratory measurement; Bertrand Renaudié for preparing the samples used in this study; Laurent Rihouey and Alain Steyer for machining and building parts for the experimental apparatus; and Emmanuelle Calmès and Andrea Caciolo who were always happy to help with my paperwork.

I am indebted to Alexandra Kushnir and Jamie Farquharson for showing me how to measure permeability, and for countless insightful coffee breaks. I thank them, as well as my fellow PhD students Baptiste Gombert and Frédéric Dubois, for their humour and support.

Special thanks go to Christopher Griffiths (Dad) for his help in editing this thesis.

I gratefully acknowledge a Cai Yuanpei Partenariats Hubert Curien (PHC) grant (project number 36605ZB), implemented and funded by the Ministry of Foreign Affairs (MAEDI) and the Ministry of Higher Education and Research (MENESR) in France, and the Ministry of Education and the China Scholarship Council (CSC) in China, which allowed me to visit Northeastern Univeristy, Shenyang, China, to visit Prof. Tao Xu and Chong-feng Chen, who treated me royally during my trip, and with whom I was lucky to have worked with.

Alexandre Schubnel generously provided me with a block of Westerly Granite, and Lucas Pimienta undertook the laborious task of preparing it; I am very grateful to them both. I kindly thank Albert Genter for sharing his expert knowledge on the Soultz-sous-Forêts geothermal project, and for providing me with access to the Bunsandstein core.

CONTENTS

LIST OF FIGURES

LIST OF TABLES

LISTINGS

1 INTRODUCTION

1.1 THERMAL MICROCRACKS

Rocks commonly contain microscopic cracks (Kranz, 1983; Simmons and Richter, 1976). These microcracks have a length of typically 0.1 mm or less (Simmons and Richter, 1976) and an aspect ratio, i.e. the ratio of their aperture and their length, of less than 1×10^{-2}, generally in the range of 1×10^{-3}–1×10^{-5}. Microcracks may be mechanically, chemically, or thermally induced (Kranz, 1983). This thesis focuses on the latter: thermal microcracking.

Thermal microcracks are caused by changes in temperature in both time and space, which may occur in the many thermally dynamic environments of the Earth's crust. Although small, thermal microcracks can significantly affect the physical properties of rock. For example, David et al. (1999) measured a decrease in the acoustic wave velocity of a fine-grained granite by more than 30 % when heated to 450 °C and cooled, and saw its permeability (its ability to transmit fluids) to increase by 3 orders of magnitude. Kant et al. (2017) measured a 75 % decrease in the thermal conductivity of granite following heating to 500 °C, and Homand-Etienne and Houpert (1989) measured a 30–40 % decrease in the uniaxial strength of two granites once heated to 600 °C and cooled.

Fluctuations in temperature are naturally occurring. At tectonically active zones, the heat generated by frictional sliding may result in a large increase in temperature along faults (for example, Cardwell et al. (1978)). Within volcanoes, the rise of magma causes cyclic changes in temperature of the surrounding rock (Heap et al., 2017). At the Earth's surface, solar-induced thermal stress weathering can lead to rock breakdown and, ultimately, soil formation (Eppes et al., 2016).

In addition to natural causes, temperature changes may occur at geo-engineering sites, including geothermal reservoirs (Grant, 2013; Huenges et al., 2013; Kolditz et al., 2013) and underground disposal facilities for nuclear waste (Faletti and Ethridge, 1988; Hodgkinson et al., 1983; Ougier-Simonin et al., 2011; Paterson and Wong, 2005).

The thermal stressing of rock has important implications for deep geothermal reservoirs, which formed the original motivation for this thesis. For example, reservoir modelling has shown thermo-elastic effects to cause large tensile stresses, especially near the injection well (Kohl et al., 1995), where the thermal stresses due to the injection of cool water have been shown to contribute to well instability (Bérard and Cornet, 2003; De Simone et al., 2013). Thermal stresses may how-

ever be beneficial for geothermal energy production, for example, increasing permeability between the well and the reservoir through: the thermal cracking of rock around the injection well due to cooling (Grant, 2013; Jeanne et al., 2017; Kitao et al., 1995; Siratovich et al., 2011); and widening pre-existing fractures allowing mineral precipitation to be flushed out (Siratovich et al., 2011) (fracture sealing by mineral precipitation decreases permeability and can occur well within the lifetime of a geothermal site (Elders et al. (1979), Griffiths et al. (2016), McNamara et al. (2016a), and Xu et al. (2012); see Section C.1)).

To assess the potential effect of thermal microcracks in such environments, it is essential to understand the thermal conditions required for thermal microcracking, and the influence of thermal microcracks on rock properties, taking in to account the specificities of the rock type.

1.2 HOW THERMAL MICROCRACKS FORM

Thermal microcracks result from an incompatible mismatch in the thermal expansion of the crystals composing the rock, which may be due to (Kranz, 1983; Meredith et al., 2001):

A. A difference in the thermoelastic moduli between neighbouring crystals;

B. An anisotropy of the thermoelastic moduli of variably oriented neighbouring crystals;

C. Thermal gradients across crystals, or even within a single crystal.

Figure 1.1 illustrates the three causes of thermal stress within rock.

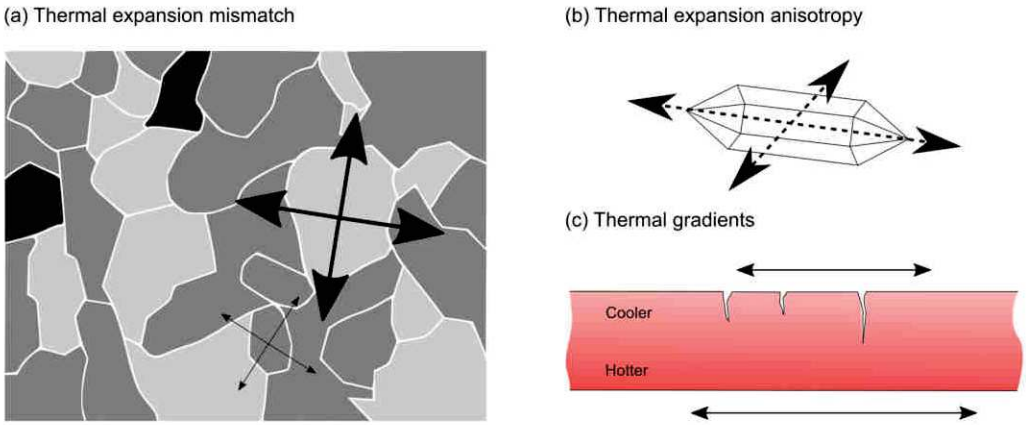

Figure 1.1: A thermal expansion mismatch within rock may be due to: (a) a difference in the thermoelastic moduli between neighbouring crystals; (b) an anisotropy of the thermoelastic moduli of variably oriented neighbouring crystals; and (c) thermal gradients.

Early work on thermal microcracking focused on ceramic materials, within which thermal stresses were due to the thermal expansion anisotropy of crystals (Clarke, 1980; Evans, 1978b; Hasselman, 1969; Kuszyk and Bradt, 1973). This knowledge was soon applied and expanded to the study of thermal microcracking in rock.

Fredrich and Wong (1986) applied micromechanical modelling methods used originally on ceramics to study the origin of thermal microcracking within rock. To model microcrack propagation and arresting within and around a rock crystal or grain, they considered a 2D square inclusion of anisotropic thermal expansion, embedded within a homogeneous elastic matrix. They then calculated the conditions for the propagation of both intra (within the grain) and inter-granular (at the grain boundary) cracks as a function of (amongst others parameters) the thermal expansion mismatch between the inclusion and the matrix, and the change in temperature.

Fredrich and Wong (1986) then heated a suite of samples of three crustal rocks (Westerly Granite, Frederick diabase, and Oak Hall limestone) to a range of temperatures, and through microscopic observation post-heating, they quantified the amount of induced thermal microcracking. They observed that thermal microcracking had occurred when samples were heated to temperatures within the range of 100–165 °C and above, and found a similar number of microcracks within grains as along grain boundaries. When the rocks were heated to 250 °C and beyond they saw that most of the grain boundaries were cracked, and all were cracked when heated to 500 °C.

The model of Fredrich and Wong (1986) best predicted the temperature conditions for microcracking within the Westerly Granite, where microcracks along grain boundaries between the quartz and microcline formed most easily, owing to their contrasting thermal ex-

pansion coefficients. Further, Fredrich and Wong (1986) found that microcracking at the corners of the square inclusion was favoured when the inclusion had an anisotropic thermal expansion coefficient (which is true for quartz grains). The square inclusion model was also compatible with observations of microcracking in the diabase, however, not for the limestone, which was suggested to be due to its plastic deformation, that was unaccounted for in the model.

Meredith et al. (2001) heated the isotropic and 99 % pure Basal Quartzite from Scotland, UK, from 30 to 270 °C in both intact and powdered form. Meredith et al. (2001) found that the average thermal expansion of the unconstrained quartz grains in the powder was greater than that of the rock sample; the strain deficit observed for the sample was explained to be due to the mechanical constraint imposed on grains by the surrounding rock matrix. They also found that, within the rock matrix, the calculated compressive thermal stresses on grains at the threshold temperature for thermal microcracking was close to the bulk tensile stress of the rock. Meredith et al. (2001) showed how a thermal strain deficit, resulting from a mismatch in thermal expansion between neighbouring crystals led to an accumulation of thermal stresses and, ultimately, microcracking.

1.3 OBSERVATION AND QUANTIFICATION OF THERMAL MICROCRACKING

Microstructural observation is commonly used to characterise and quantify the extent of microcracking in rock (Arena et al., 2014; Fredrich and Wong, 1986; Fredrich et al., 1989; Homand-Etienne and Houpert, 1989; Menéndez et al., 1999). An established method for quantifying microcrack density is the use of the stereological techniques of Underwood (1967) (Fredrich et al., 1989; Heap et al., 2009b, 2014a; Tapponnier and Brace, 1976; Wong, 1982; Wong, 1985; Wu et al., 2000). This method involves superposing an array of "test" lines over a microscope image and counting the number of intersections between microcracks and the lines, which can then be used to calculate the crack surface area density, assuming the rock is isotropic (Underwood, 1967).

With technological advances, digital images of microcracks could be generated automatically, using image segmentation techniques to create binary images of the microcracks. For example, Arena et al. (2014) and Delle Piane et al. (2015) used image processing software to segment backscattered Scanning Electron Microscopy (SEM) micrographs of Carrara Marble. Carrara Marble is a monomineralic calcite aggregate (Ramez and Murrell, 1964), making it an ideal choice for microstructural observation of microcracks and the processing of micrographs. For polymineralic rock such as granite, a tailored approach to image processing and segmentation is required to extract

images of the microcracks. For the subsequent analysis of fracture networks, dedicated tools now exist, for example FracPaq (Healy et al., 2017).

Measurements of microcrack characteristics can help understand and explain the behaviour of rock at the laboratory scale, for example, via the use of micromechanical models to predict rock strength (Ashby and Sammis, 1990) and stiffness (David et al., 1999; Walsh, 1965). In this vein, Chapter 3 looks to develop the association between measurements of microcrack density and length with the mechanical properties at the sample scale. Whilst numerical models have been used to simulate the deformation and failure of rock containing higher aspect ratio elliptical voids/pores (Griffiths et al. (2017b), see Section C.2), analytical micromechanical models were preferred here as it is possible to consider a large population of low aspect ratio microcracks and their interaction without encountering model resolution issues. To inform the models, the development of a new method for processing, segmentation, and analysis of 2D micrographs was required, to be optimised for use on optical micrographs (Griffiths et al., 2017a).

1.4 MONITORING THERMAL MICROCRACKING

When rock is stressed, transient elastic waves may be released from small defects, such as microcracks. These waves are known as Acoustic Emissions (AE), and AE monitoring has been a common technique for monitoring the cracking of brittle materials due to both mechanical and thermal stressing.

Glover et al. (1995) performed AE monitoring on a number of rock samples (granite, mylonite, amphibolite, hornblendite) during heating to 900 °C at a rate of 1 °C/min. Figure 1.2 shows the rate of detected AE with furnace temperature, during the heating of La Peyratte Granite (grain diameter of 0.5–1.5 mm). Glover et al. (1995) observed an onset of AE at around 70 °C due to thermal microcracking. Threshold temperatures for thermal microcracking in granite have commonly been observed between 70–80 °C (Bauer et al., 1979; Johnson et al., 1978; Todd, 1973; Yong and Wang, 1980).

The presence of quartz favours thermal microcrack development due to its abnormally high thermal expansion and thermal expansion anisotropy (Kranz, 1983). In the Glover et al. (1995) data (Figure 1.2), the peak in AE rate at 573 °C is due to the quartz α/β phase transition, across which quartz undergoes a sudden thermal expansion, amplifying thermal stresses within the rock, and resulting in increased thermal microcracking, and hence the increased AE.

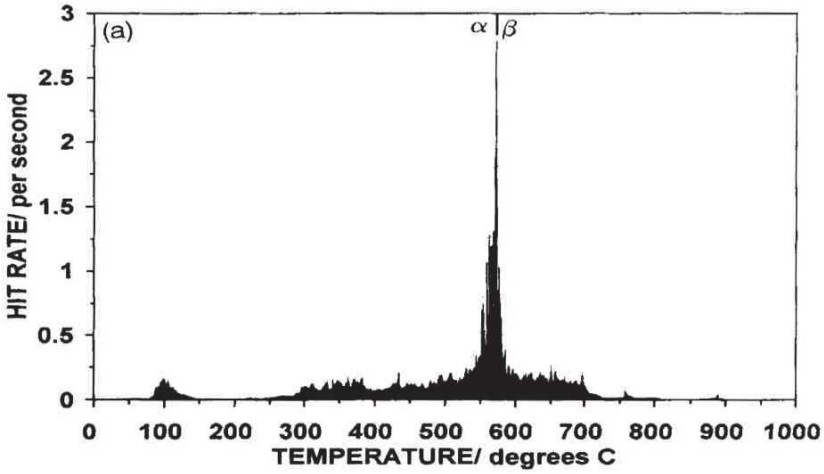

Figure 1.2: The rate of detected acoustic emissions (AE) during the heating of La Peyratte Granite to 900 °C at 1 °C/min. The onset of AE occurs at around 70 °C due to thermal microcracking, and a peak in AE rate is observed at 573 °C, the temperature of the α/β phase transition of quartz. (from Glover et al. (1995)).

Generally, AE monitoring of thermal microcracking has been performed during only the heating phase (for example, Fredrich and Wong (1986), Glover et al. (1995), Meredith et al. (2001), and Vinciguerra et al. (2005)), and very rarely during multiple heating and cooling cycles, which is not only relevant in a number of environments, including volcanoes and geothermal reservoirs, but also helps understand the process of thermal microcracking.

A small number of studies have considered AE during cooling. Todd (1973) monitored AE in granite during heating and cooling, although no AE was detected during cooling. In more recent studies, however, AE has been detected in volcanic rocks during cooling (Browning et al., 2016; Heap et al., 2014a). Browning et al. (2016) performed AE monitoring during the heating and cooling of a Nea Kameni Dacite (Santorini, Greece) and Seljadur Basalt (Iceland) to a peak temperature of 1100 °C, and observed significantly more AE during cooling than during heating (Figure 1.3), which the authors attributed to thermal microcracking. These contrasting results suggest that AE monitoring during cooling warrants further study to better understand how microcracks form during heating and cooling in different rock types.

For the effective comparison of AE data on different rocks, it is essential to provide consistency in AE monitoring during and across experiments. More specifically, a constant mechanical coupling between the rock sample and the AE transducer is required. For AE monitoring at high temperature, piezo-transducers are generally placed outside of the furnace, owing to their sensitivity to temperature, and a waveguide is required to detect AE emanating from the sample. The methods employed to ensure coupling between the waveguide and

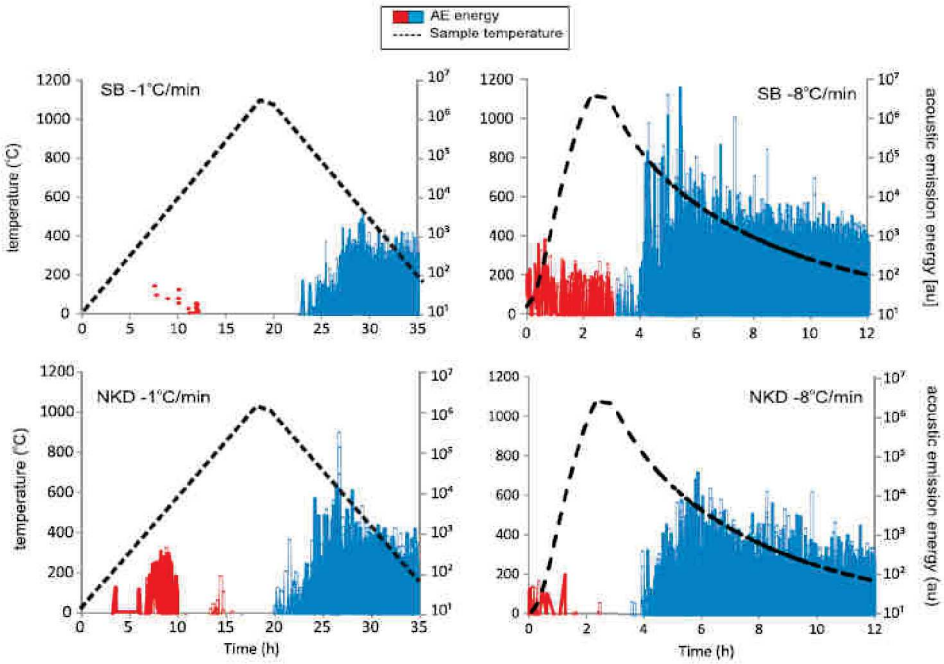

Figure 1.3: Acoustic emission energy and temperature with time during the heating of Seljadalur Basalt (SB; from Iceland) and Nea Kameni Dacite (NKD; from Greece) to 1100 °C and cooling, at two different heating and cooling rates of 1 °C/min and 8 °C/min (black dashed lines). Red indicates AE generated during the heating phase, and blue indicates AE generated during the cooling phase (from Browning et al. (2016)).

the sample include: clamping the waveguide to the sample (Glover et al., 1995), using a spring within the furnace acting on the waveguide (Browning et al., 2016), or cementing the two (Yong and Wang, 1980). These solutions are not ideal, as it is difficult to assess any changes in coupling with the sample, and ensure that the stress on the sample is constant.

To address these issues, Chapter 2 details the development and construction of a new experimental apparatus dedicated to the monitoring of thermal microcracking in rock at high temperatures and under cyclic heating and cooling. Using the new apparatus, AE monitoring was performed on samples of granite (Chapter 4) and volcanic rock (basalt and andesite; Chapter 5) during multiple heating cycles at temperatures of up to 450 °C, and at higher temperatures of up to 700 °C.

1.5 THE INFLUENCE OF THERMAL MICROCRACKS ON ROCK PROPERTIES

THERMAL MICROCRACKS IN GRANITE Many studies of the influence of microcracking on rock properties have used thermally-stressed granite samples, as granite is considered a major constituent of the Earth's crust (Wedepohl, 1995), and as varying amounts of crack damage may be induced within a granite sample through heating to different temperatures, whilst maintaining a constant mineralogy.

To compare the influence of both mechanically and thermally-induced microcracks on the physical properties of granite, David et al. (1999) made a series of measurements in the laboratory on both mechanically and thermally-stressed granite samples. The granite used was La Peyratte Granite (France), in which grains have a diameter of 0.5–1.5 mm. The mechanically-stressed samples were prepared by deforming La Peyratte Granite under 10 MPa confining pressure and under maximum deviatoric stresses of 312–360 MPa. Thermally-stressed samples were prepared by heating to 220 or 450 °C at 1 °C/min and cooled.

Measurements made by David et al. (1999) of the physical properties of the damaged granite samples included: the connected porosity, the P-wave velocity (v_P), the P-wave attenuation, the electrical conductivity, and the permeability. Figure 1.4 shows the porosity and v_P for both the intact and damaged samples. With increasing thermal stressing temperature, the porosity was seen to increase (Figure 1.4a), and v_P decrease (Figure 1.4b) due to the formation of thermal microcracks. Changes in porosity and velocity due to microcracking were of a similar magnitude to those observed for the mechanically-stressed samples.

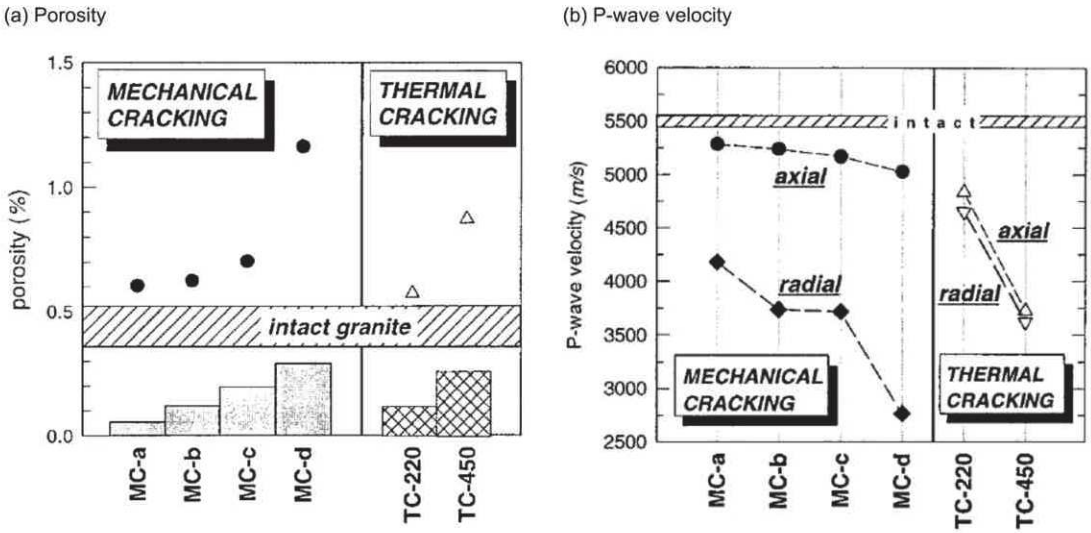

Figure 1.4: Measurements of the connected porosity and P-wave velocity of samples of La Peyratte granite, which have been either mechanically (MC) or thermally (TC) stressed. Mechanically-stressed samples were deformed under 10 MPa confining pressure and maximum deviatoric stresses of 312–360 MPa; "MC-a" is the least damaged, and "MC-d" the most. Thermally-stressed samples were heated to 220 or 450 °C at 1 °C/min and cooled (from David et al. (1999)).

Note that for the mechanically-stressed sample, David et al. (1999) found v_P to be greater in the axial direction than in the radial direction (Figure 1.4b). This is because microcracks extend along a preferential orientation, which is parallel to the direction of the maximum applied stress (axial, here), and the wave velocity is greater when the direction of propagation is parallel to the microcracks. In the thermal microcracks, however, there is no velocity anisotropy (Figure 1.4b), suggesting that the thermal microcracks have no preferential orientation within this granite. Thermal microcracking in granite is studied further in Chapter 3 and Chapter 4.

THERMAL MICROCRACKS IN BASALT Vinciguerra et al. (2005) heated the low porosity (~1 %) Seljadur Basalt to 900 °C, and measured a decrease in v_P by more than 40 % from its initial value of 5.4 km/s, attributed to the formation of thermal microcracks. Jones et al. (1997) observed an increase in the permeability of the Seljadur Basalt (from the same quarry) by a factor of 9 when heated to 700 °C, and Nara et al. (2011) measured an increase in the permeability of Seljadur Basalt by almost three orders of magnitude when heated to 800 °C.

However, when Vinciguerra et al. (2005) measured the wave velocity of a higher porosity basalt (~4 %) from Mt. Etna before and after heating to 900 °C, they found no significant change from the low

initial values (e.g. v_P ranged from 3.05–3.43 km/s prior to heating, significantly lower than the Seljadur Basalt). They attributed the lack of velocity change to the high initial crack density in the basalt and a Kaiser memory effect (Kaiser, 1953)—whereby stresses in the rock must surpass those previously experienced to induce further damage. The difference in behaviour between these two basalts highlights the potential variation of the microcrack damage with temperature in different rocks, and the importance of laboratory measurements performed at elevated temperatures to monitor microcrack occurrence. The aim of Chapter 5 is to better understand thermal microcracking in volcanic rock.

SEISMIC MONITORING Of the previous measurements made on thermally microcracked rock, the wave velocity is highly sensitive to microcracking (Guéguen and Schubnel, 2003). Understanding the influence of temperature on the seismic velocity of rock is essential for the seismic monitoring and modelling of geothermal reservoirs, volcanoes, and fault zones. Changes in the seismic velocity of rock over time may be due to a number of factors, including changes in temperature, porosity, crack density, confining pressure, pore fluid pressure, fluid saturation, and fluid viscosity (Sanders et al., 1995). As volcanic rock was studied here, the example is given of Patane et al. (2002), who used 2D earthquake tomography to observe changes in v_P, v_S, and their ratio (v_P/v_S) at Mt. Etna (Figure 1.5). Patane et al. (2002) observed a high v_P/v_S anomaly (the blue region in Figure 1.5b), which was attributed to a molten dyke intrusion prior to the 2001 eruption.

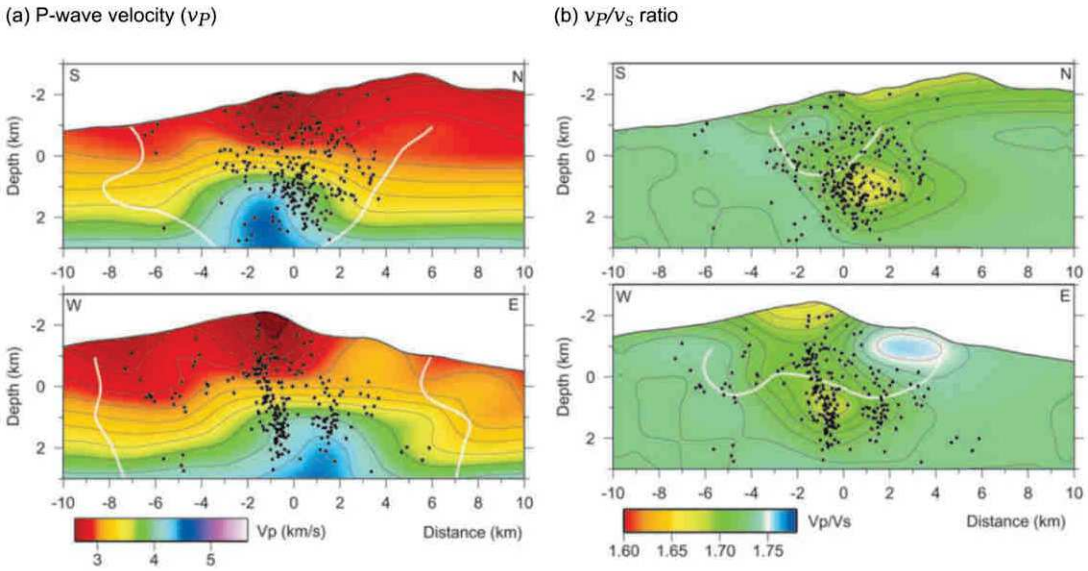

Figure 1.5: S-N and W-E vertical sections of (a) v_P and (b) v_P/v_S models of Mt Etna. White lines delimit the well-resolved regions of the model, and black dots show the earthquakes which occurred at ±1 km from the sections. The high v_P/v_S anomaly in the W–E section is interpreted as a molten dyke intrusion (from Patane et al. (2002)).

Another method to infer changes in the velocity and structure of volcanoes is Coda Wave Interferometry (CWI), which has been applied to the Mt. Erebus volcano, Antarctica (Grêt, 2005), the Merapi volcano, Indonesia (Sens-Schönfelder and Wegler, 2006), and Volcàn de Colima, Mexico (Lamb et al., 2017). More recently, this technique has also been used at geothermal reservoirs to link velocity changes to reservoir activities, including fluid circulation (Lehujeur et al., 2017; Obermann et al., 2015). These studies highlight the importance of measurements of the wave velocity of rock at elevated temperature.

CWI is a technique to infer minute changes in the wave velocity of a medium from assessments of the small relative time delays of multi-scattered waves using cross-correlations of waveforms (Snieder, 2002). Grêt (2004) demonstrated the use of CWI in the laboratory to observe microstructural changes of different rocks due to changes in fluid saturation, mechanical deformation, and temperature. For the temperature experiments, samples of granite were heated to 90 °C and cooled, whilst performing CWI. Grêt (2004) observed an irreversible apparent decrease in the wave velocity of the granite with heating due to thermal microcracking.

Measurements of the wave velocities of different rocks have previously been made at elevated temperatures (Ide, 1937; Kern, 1979, 1982; Wang et al., 1989), showing generally the velocity of all rock types to decrease with increasing temperature and, in most cases, velocity measurements have been made under confining pressure, required to

ensure coupling between the sample and the piezo-transducers (Kern, 1979, 1982; Wang et al., 1989).

To assess the extent of thermal microcracking, it is noted that, in general, studies compare measurements of velocity made at room temperature before and after heating. Previously observed changes in velocity with temperature highlight the need for measurements performed under in-situ temperature conditions.

Improvements in the operating temperature range of piezo-transducers has opened up new possibilities for acoustic measurements, whereby transducers may be placed within the furnace. Chapter 2 details the development of the new experimental apparatus, using temperature resistant acoustic transducers in direct contact with the rock sample to monitor microstructural changes using both measurements of v_P, and CWI, which are then used to study thermal microcracking in granites and volcanic rocks.

In this thesis, the focus was on the influence of temperature on microstructural changes within rock, monitored using P-wave velocity measurements, the highly sensitive CWI technique, and AE monitoring. Velocity measurements were performed on samples of granite (Chapter 4) and volcanic rocks (basalt and andesite; Chapter 5) during multiple heating cycles at temperatures of up to 450 °C. These data will be showed in conjuction with AE monitoring to temperatures of up to 700 °C to shed new light on thermal microcracking in rock.

1.6 THE INFLUENCE OF COMBINED MECHANICAL AND THERMAL STRESS

Wang et al. (1989) made several measurements of v_P during heating and cooling of Westerly Granite under confining pressures of 7, 28, and 55 MPa. Under 7 MPa confining pressure, they measured a decrease in v_P from around 4.7 km/s to 3.4 km/s at 300 °C. Upon cooling, Wang et al. (1989) found that v_P returned to the value prior to heating, which they interpreted as the closure of newly created microcracks by the confining pressure. Confining pressure had the effect of increasing the threshold temperature for thermal microcracking; around 90 °C at 7 MPa, 115 °C at 28 MPa, and 135 °C at 55 MPa.

Recently, Violay et al. (2017) performed high-temperature (up to 1000 °C), high-pressure (130 MPa) triaxial experiments on granite samples to emulate conditions within the ductile crust. Violay et al. (2017) found that when samples were heated to the target temperatures under a confining pressure, their permeability (at pressure and temperature) was higher when the temperature was higher, as a result of thermal microcracking. The results of Violay et al. (2017) showed that thermal microcracks in granite can open, and remain open, when heated under confining pressure.

The formation of thermal microcracks with heating has been studied under constant confining pressures, or at ambient pressure conditions, which is not the case in nature, where rock is under low differential stresses. In Chapter 6, samples of a basalt and a granite are heated under a constant uniaxial stress, to determine whether thermal microcracks have a preferential orientation when formed under differential stresses, as was the case for mechanically-induced cracks in the study by David et al. (1999).

1.7 STRUCTURE OF THE THESIS

The thesis is structured as follows:

- Chapter 2 describes the design and conception of a new apparatus for AE monitoring and in-situ velocity measurements (using both P-wave direct travel time and Coda Wave Interferometry (CWI) techniques) during the heating and cooling of rock samples. This is followed by a description of the methods used to measure the physical, transport, thermal, and mechanical properties of rock samples;

- Chapter 3 presents a numerical tool for the processing and analysis of optical micrographs of thin sections of rock, for the quantification of thermal microcrack damage. The method is illustrated on variably thermally-damaged samples of a fine-grained granite. The resulting microcrack characteristics were then used to constrain micromechanical models for rock strength and stiffness, and compared with laboratory measurements;

- Chapter 4 studies the influence of repeated thermal stressing cycles (up to 450 °C) on three granites of different grain sizes, beginning with a demonstration of the AE and velocity monitoring procedure on the well-studied Westerly Granite. The same procedure was then applied to the two other granites, followed by high temperature AE monitoring tests (up to 700 °C) on all three granites, and characterisation of the physical, transport, thermal and mechanical properties of thermally-stressed (shock and slow-cooled) granite samples;

- Chapter 5 examines the influence of repeated thermal stressing cycles (up to 450 °C) on two basalts of different initial porosities using AE monitoring and velocity measurements, to study the influence of rock type on thermal microcracking mechanisms, and the resulting changes in wave velocity. Two basalt samples were also heated to 700 °C whilst monitoring AE, to compare the thermal microcracking behaviour at higher temperatures. Additionally, a higher porosity andesite was subject to the same thermal stress cycling experiments up to 450 °C, to examine

the influence of pores on thermal microcracking and changes in wave velocity. Further measurements were also made, at room temperature, of the physical, transport, thermal, and mechanical properties of thermally-stressed (shock and slow-cooled) samples of one of the basalts (selected for its homogeneity and similar porosity to the granites), for comparison with the granites.

- Chapter 6 investigates the effect of superposed mechanical and thermal stresses on the formation of thermal microcracks, through the heating and cooling of granite and basalt samples under varying uniaxial loads, and subsequent measurement of their physical and transport properties.

2 EXPERIMENTAL METHODS

The experimental methods and measurement techniques used within the following chapters are described here:

Firstly, the design, conception, and operation of a new experimental apparatus which performs acoustic emission (AE) monitoring and velocity measurement on rock samples at elevated temperature;

Secondly, the methods used to measure the physical, thermal, transport, and mechanical properties of rock samples at room temperature.

Any variation on these procedures specific to a particular chapter are explained therein.

2.1 NEW APPARATUS FOR MONITORING THERMAL MICROCRACKING

The main aim of this PhD project was the development and construction of experimental apparatus for monitoring thermal microcracking in rock at high temperatures, under controlled cyclic heating and cooling, and under a servo-controlled uniaxial load. The initial phase focused on AE monitoring to study thermal microcracking in different rocks. Following the initial phase, the apparatus was then used to measure changes in ultrasonic velocities of rock with temperature.

2.1.1 *Design specifications*

The experimental apparatus was designed to fulfil the following criteria:

- Requirement—The maximum operating temperature must exceed 600 °C, to be comfortably above the temperature of the quartz α/β phase transition at 573 °C (Glover et al., 1995).

  Rationale—In quartz-bearing rock, this temperature is accompanied by significant thermal microcracking and AE, providing both an interesting target temperature for study, and a verification of the AE acquisition method.

- Requirement—The performance of AE sensors should not be affected by temperature.

  Rationale—Although many AE sensors are operational at temperatures in excess of 100 °C, the response of the piezo-ceramic within an AE sensor is sensitive to temperature, and their condition fatigues when heated beyond their operating range. This

could cause loss of sensitivity and reduce the detection threshold, leading to possible errors in interpretation. To address this, in the new apparatus, sensors were installed outside of the furnace and cooled.

- Requirement—The AE waveguide must be a continuous cylinder of 40 mm in diameter or less.

  Rationale—Dong and Zou (2017) provided guidelines for the dimensions of waveguides used for AE monitoring, resulting from a combined experimental and numerical study of AE propagation. They observed only a slight effect of the waveguide diameter and length on the detection threshold for AE events when using waveguides of diameters within the range of 5–40 mm and lengths within the range of 0.5–5 m.

- Requirement—The number of interfaces between the sample and the AE sensor must be kept to a minimum.

  Rationale—AE energy is attenuated and scattered when crossing interfaces.

- Requirement—The AE sensors must be embedded within the waveguide, facing towards the sample.

  Rationale—Often, AE transducers are placed in suboptimal positions, such as on the side of pistons. In the new apparatus, the AE sensor was embedded within the waveguide facing towards the sample to maximise AE energy arriving at the sensor.

- Requirement—Coupling between the transducer and the sample must be constant during an experiment and reproducible between experiments.

  Rationale—The detection threshold of the acquisition system is affected by changes in coupling with the sample. For AE monitoring at high temperature, coupling between the waveguide and the sample has been ensured by: clamping the two together (Glover et al., 1995); and using a spring acting on the waveguide (Browning et al., 2016). Firstly, the disadvantage of clamping is that the thermal expansion of the sample is not accommodated for, and the pressure against the waveguide may increase with temperature. Secondly, the force applied by a spring depends on its stiffness and elongation, which both vary as the spring is heated, and the waveguide and sample expand. In both of these cases, coupling with the sensor is unquantified and may vary significantly with temperature. In the new apparatus, mechanical coupling between the sensor and the rock sample is ensured by a servo-controlled uniaxial press, a method which has not yet been used within a device dedicated to high temperature AE monitoring.

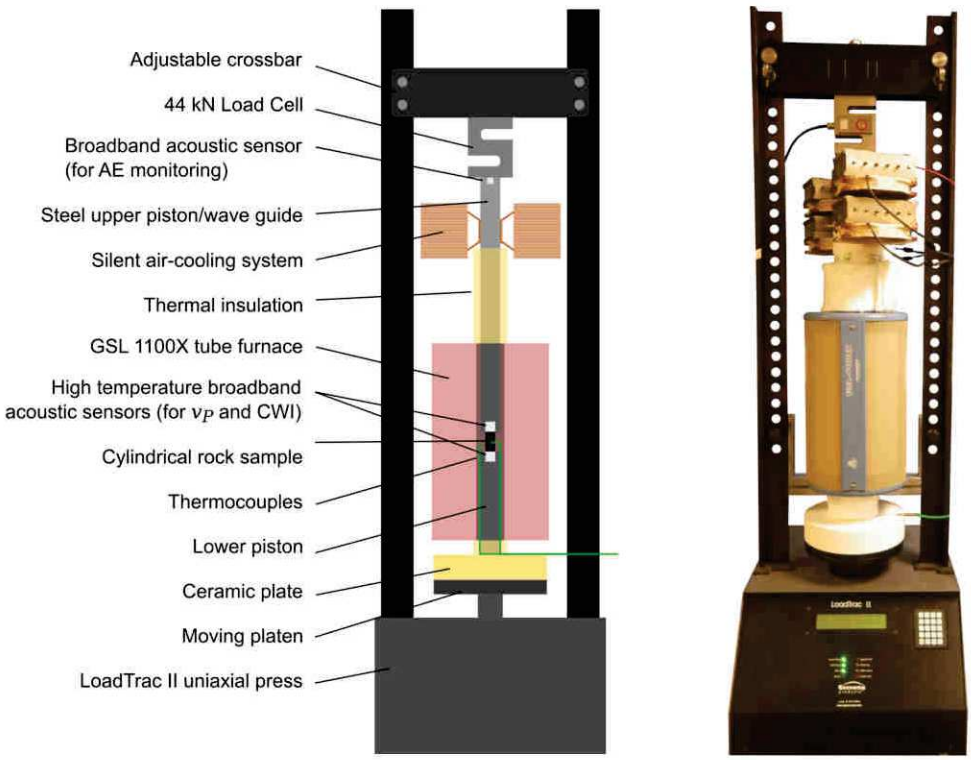

Figure 2.1: A schematic and a photograph of the experimental apparatus for acoustic emission monitoring and velocity measurements at elevated temperatures. The apparatus consists of a LoadTrac II uniaxial press and a GSL 1100X tube furnace. For AE monitoring, a single acoustic sensor is embedded within the top of the upper piston. For CWI and P-wave travel-time measurements, a pair of high temperature acoustic sensors are in direct contact with opposing ends of a rock sample.

2.1.2 *Components*

To these ends, the experimental apparatus for high temperature AE monitoring and velocity measurements, shown in Figure 2.1, is comprised of:

- A uniaxial press—The LoadTrac II uniaxial press from Geocomp is servo-controlled and has a maximum capacity of 45 kN (~140 MPa using 20 mm diameter cylindrical samples). The load cell is above the upper piston, attached to a movable crossbar (Figure 2.1), allowing flexibility in terms of piston length and sample size. The displacement transducer measures the movement of the lower platen and has a range of 76 mm and a high resolution of 0.0013 mm. For uniaxial compression tests, the displacement rate of the piston can be set within the range of 3×10^{-5} mm to 15 mm per minute (strain rates of 1.25×10^{-8}–6.25×10^{-3}).

- A tube furnace—The GSL 1100X tube furnace from MTI has a maximum temperature of 1100 °C (< 1 hour), a maximum working temperature of 1000 °C, and can heat at a maximum rate of 10°C per minute. It has a heating zone of 300 mm in length, and a constant temperature zone (uniform within 1 °C) of 80 mm in length. The temperature is controlled by PID automatic control and may be programmed to follow up to 30 heating and cooling segments. The furnace contains a k-type thermocouple, with an accuracy of 1 °C.

- Two heat-resistant pistons—Two vertical pistons made from grade 310 stainless steel, which resists oxidation up to temperatures of 1100 °C. Importantly, this steel may be used under cyclic temperature conditions. The 310 steel is easily machinable using standard tools, allowing flexibility in design, unlike ceramic pistons.

- An air-cooling system—Two NH-D15 D-type coolers manufactured by Noctua make up a silent air-cooling system. They are composed of an aluminium base plate (40 x 45 mm) which is linked to two radiators via heatpipes. The radiators are each cooled by two 140 mm low-noise fans. Two coolers were attached to opposite sides of the upper piston, at 300 mm above the furnace. At this location, the piston was flattened to maximise the contact area with the cooler base-plates, and a thin layer of thermal paste was applied between them, to maximise heat transfer. The maximum heat dissipation of the heat sinks has been estimated by the manufacturers to be around 100 W, which is sufficient for continuous use of the furnace at 700 °C. Assuming the piston is entirely insulated between the furnace and the fans, the 1D equation for heat flow gives Equation 2.1, where: Q is the heat flux through the piston; k is the thermal conductivity of the pistons (18.7 W/m.K at 500 °C); S is the surface area of the 40 mm diameter piston; T_f is the furnace temperature (700 °C); T_{AE} is the desired temperature at the fans (30 °C); and l is the distance between the fans and the furnace (30 mm). with these parameters, the heat flux, Q, to be dissipated by the cooling system is 35 W—less than the 100 W dissipation capacity of a single heat sink.

$$Q = \frac{kS(T_f - T_{\mathrm{AE}})}{l} \tag{2.1}$$

Figure 2.2 shows the temperature recorded within the furnace, within the AE sensor housing, below the lower piston, and below the lower ceramic baseplate (see Figure 2.1 for the schematic of the press) when the furnace was heated to 620 °C and cooled, at a rate of 1 °C/min. The temperature within the AE housing

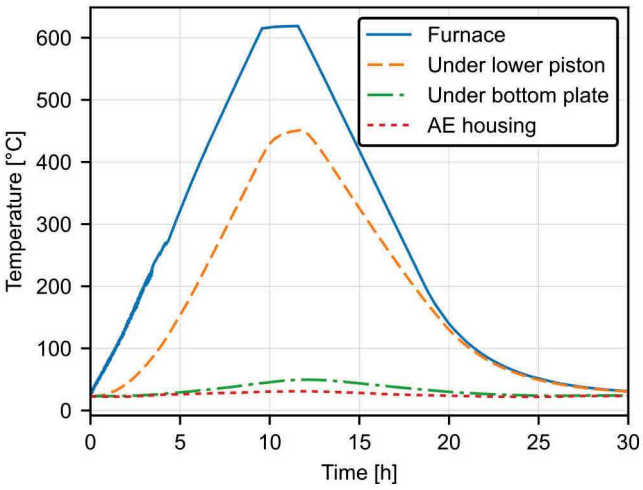

Figure 2.2: Temperature distribution at various locations of the setup.

is increased by less than 10 °C when the furnace is at 620 °C, sufficiently low for the AE transducer.

- Thermal insulation—A 50 mm thick ceramic plate was placed between the moving platen and the lower piston to avoid the body of the press from heating (Figure 2.1). Superwool Plus Blanket from Morgan Thermal Ceramics was used for insulation of the upper piston between the top of the furnace and the air-cooling system, and between the bottom of the furnace and the ceramic plate. The Superwool insulation has a continuous working temperature of 1000 °C.

To measure the deformation of the pistons due to thermal expansion and contraction, a sample of 310 steel was heated to 700 °C under a servo-controlled load of 100 N. The aim was to measure the displacement of the platen during the experiment and, knowing the thermal expansion coefficients of the sample, calculate the thermal expansion of the piston for future calibration of tests on rock samples. However, variations in the deformation of the upper and lower pistons with temperature between experiments were greater than the thermal expansion of the sample. Changes in the thermal expansion within the piston between tests were likely caused by fluctuations of ambient temperature (which could change by several °C over 24 hours) and their influence on the efficiency of the cooling system. The thermal strain of the pistons during heating and cooling due to thermal expansion could therefore not be measured, and so the thermal expansion of the sample during an experiment was unknown.

2.1.3 *Experimental methods*

2.1.3.1 *AE monitoring*

AE SENSOR AND LOCATION Ideally, the AE sensor should be in contact with the sample, to obtain a more representative AE signal. However, the high temperature transducers used for the velocity measurements were particularly sensitive to electrical noise, owing to their metal casing, and their sensitivity was reduced once they had been heated to 450 °C. Therefore, it was decided to use the AE transducer within the upper piston to capture the AE hit rate and amplitude rather than the temporal characteristics of the AE waveforms, as metrics for microcracking.

A single Micro80 AE sensor from Physical Acoustics was used for all AE monitoring experiments, its small size (10 mm diameter and 12 mm height) allowing it to be embedded within the 40 mm diameter steel upper piston (see Figure 2.3 for an schematic of the AE housing design). The sensor has a frequency response in the range of 200–900 kHz and a resonant frequency of 325 kHz. The ceramic piezo-transducer is housed within a stainless-steel case and therefore, to avoid picking up electrical noise, the case was insulated using electrical tape.

To test the influence of the AE transducer location on signal quality, a granite sample (Lanhélin Granite from Brittany, France, see Chapter 4), of 20 mm diameter and 40 mm length was loaded to 100 N. The AE produced by a Hsu-Nielson source (breaking a pencil lead on the sample surface) was recorded simultaneously by one Micro80 AE sensor within the AE housing (Figure 2.3), and one adjacent, attached to the side of the piston. Figure 2.4 shows the recorded AE waveforms and their frequency spectrograms. The AE signal recorded by the sensor within the piston contains more energy across a larger frequency range than the sensor attached to the side of piston. This supports the choice for embedding the AE sensor within the piston.

To test the influence of the applied load on the AE detection threshold, another cylindrical granite sample (Westerly Granite this time, from Rhode Island, USA; see Chapter 4), of 20 mm diameter and 40 mm length, was loaded to uniaxial stresses of 1, 2.5, 5 and 10 MPa. Again, AE issuing from a Hsu-Nielson source on the sample surface was recorded, and Figure 2.5 shows the amplitude and energy of the detected AE hit with the stress applied on the sample. The amplitude and energy are increased with load applied on the sample. For AE hits near the detection threshold of the apparatus, changes in coupling may determine whether they are detected or not, endangering the interpretation of AE data. Note, for AE monitoring, the applied stress was chosen to be 1 MPa or less depending on the type of experiment. A preliminary study of the influence of axial load on thermal microcracking and its consequences is presented in Chapter 6.

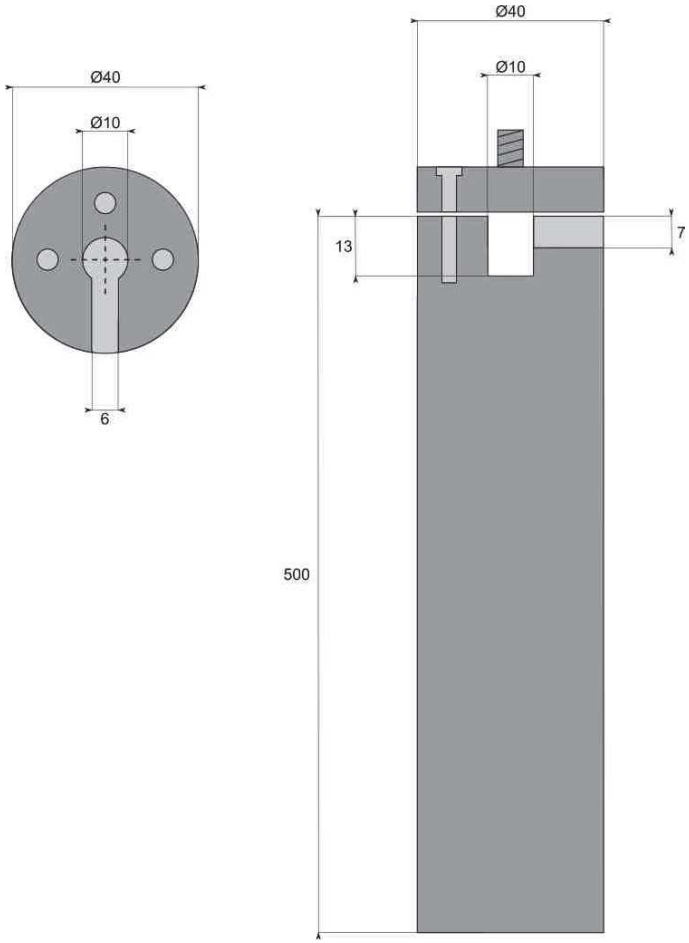

Figure 2.3: Schematic of the design for the acoustic emission (AE) sensor housing within the top of the steel upper piston (see Figure 2.1 for an illustration of the entire system).

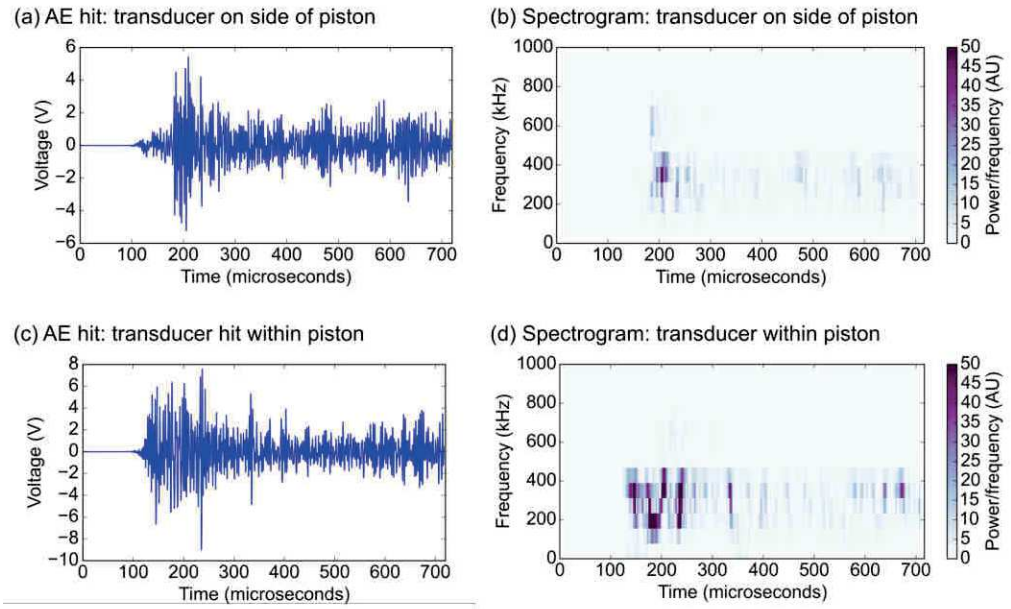

Figure 2.4: Acoustic emission (AE) waveforms and their power spectrograms recorded simultaneously on two Micro80 AE sensors, one embedded within the upper piston (as per the experimental procedure used throughout this thesis) and one adjacent, attached to the side of the piston. The AE source was a single Hsu-Nielson lead break source on the sample (of Westerly Granite) surface.

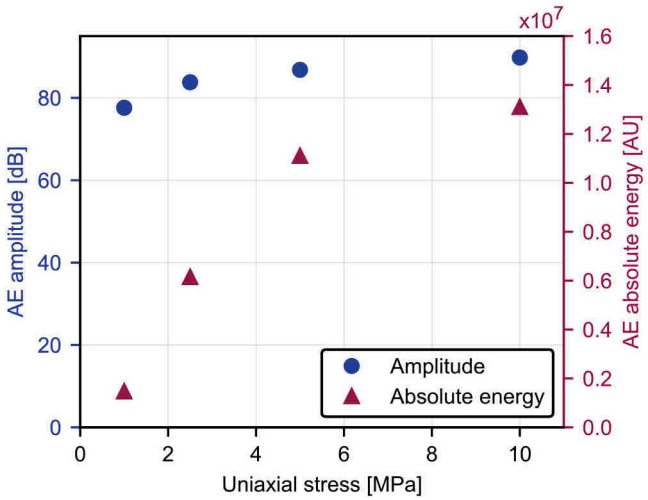

Figure 2.5: Acoustic emission (AE) amplitude and absolute energy (root mean square of the waveform, in arbitrary units) recorded for a Hsu-Nielson lead break test on a sample of Westerly Granite under uniaxial stresses of 1, 2.5, 5, and 10 MPa.

Peak definition time (PDT)	200 µs
Hit definition time (HDT)	400 µs
Hit lockout time (HLT)	1000 µs

Table 2.1: Settings for acoustic emission (AE) detection. See Figure 2.6 for an illustration of their use.

AE ACQUISITION The AE sensor was connected to a 1283 USB AE Node: a single channel acoustic emission digital signal processor with a built-in 26 dB pre-amplifier and integrated analogue low- and high-pass filters. The AEWin software from Physical Acoustics was used to control acquisition at the Mistras AE node, and to visualise and export the AE data for post-processing.

The AE node analogue filters were set to 20 kHz (low-pass) and 1 MHz (high-pass) to be close to the frequency range of the sensor. When the pre-amplified voltage across the transducer crossed the detection threshold, an AE hit was registered (see Figure 2.6 for an illustration of an AE hit and the acquisition parameters). Generally, the amplitude threshold was set to 40 dB, to be above the background level of noise (mostly coming from the uniaxial press itself). Following the trigger, subsequent oscillations of the voltage across the threshold are counted (also known as ring-down counts Figure 2.6). The AE trigger system parameters, illustrated in Figure 2.6, were set to: 400 µs peak definition time (PDT: the time following detection within which the peak voltage—and therefore the AE amplitude—may be determined); 400 µs hit definition time (HDT: the maximum time between consecutive threshold crossings, above which they are considered as part of separate hits); and a 1000 µs hit lockout time (HLT: the minimum time between consecutive hits). These parameters (Table 2.1) were selected to correctly capture the AE produced by a Hsu-Nielson source (lead break) on the surface of a rock sample. For example, a lead break on the surface of the Westerly Granite produces an AE hit of amplitude 79 dB when under 300 N load.

When triggered, the 1283 USB AE Node could also be set to record 7000 time samples at a maximum sampling rate of 10 MHz. This proved useful to set the AE acquisition parameters (PDT, HDT, HLT), as the AE waveforms could be visualised and checked for truncation. During experiments, to capture the majority of the AE signal whilst retaining a reasonable resolution, a sampling rate of 5 MHz was chosen, with a 100 µs pre-trigger. This allowed for the post-processing of AE, to pick out signals which were the result of electrical or mechanical noise—i.e. sudden high amplitude spikes, or low amplitude oscillations, respectively. Where any post-processing was required to filter signals due to noise, this is indicated in the text.

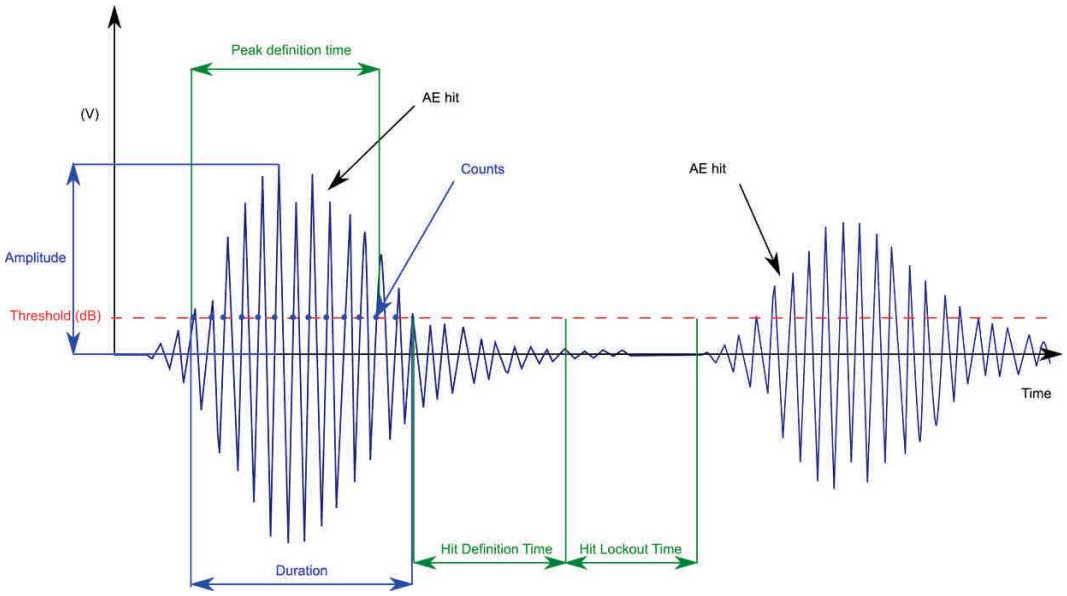

Figure 2.6: Illustration of an AE waveform (voltage with time), annotated with the AE acquisition parameters: amplitude threshold, peak definition time (PDT), hit definition time (HDT), and hit lockout time (HLT). Also shown are some AE characteristics: amplitude, duration, and counts (or "ring-down" counts). This figure is reproduced from Unnþórsson (2013).

2.1.3.2 *In situ velocity measurements*

After proving the apparatus for AE monitoring, a new configuration was developed to perform ultrasonic wave velocity measurements during heating and cooling, commonly used during mechanical testing of rock to assess damage. Two techniques were chosen to quantify changes in the velocity of the medium. The first was by measurements of the direct P-wave travel time to calculate the P-wave velocity (v_P)—commonly performed at ambient temperature conditions and more rarely at elevated temperatures. The second method was Coda Wave Interferometry (Snieder, 2002), a technique less commonly used in the laboratory, by which minute changes within the microstructure may inferred from small delays in the travel time of scattered elastic waves.

For both methods, S9215 high temperature AE sensors (Physical Acoustics) were used, which have a maximum operating temperature of 540 °C, allowing them to be contained within the furnace. They have a resonant frequency of 100 kHz (52 dB), and an operating frequency range of 80–560 kHz. The sensors were in direct contact with opposing faces of a rock sample. Coupling was ensured, and kept constant by, a servo-controlled axial force of 100 N (~0.3 MPa) on the sample. Without the servo-control, the load oscillates dramatically as the pistons thermally expand and contract (by up to 6 mm at 700 °C), which risks both damaging the sensors and influencing their

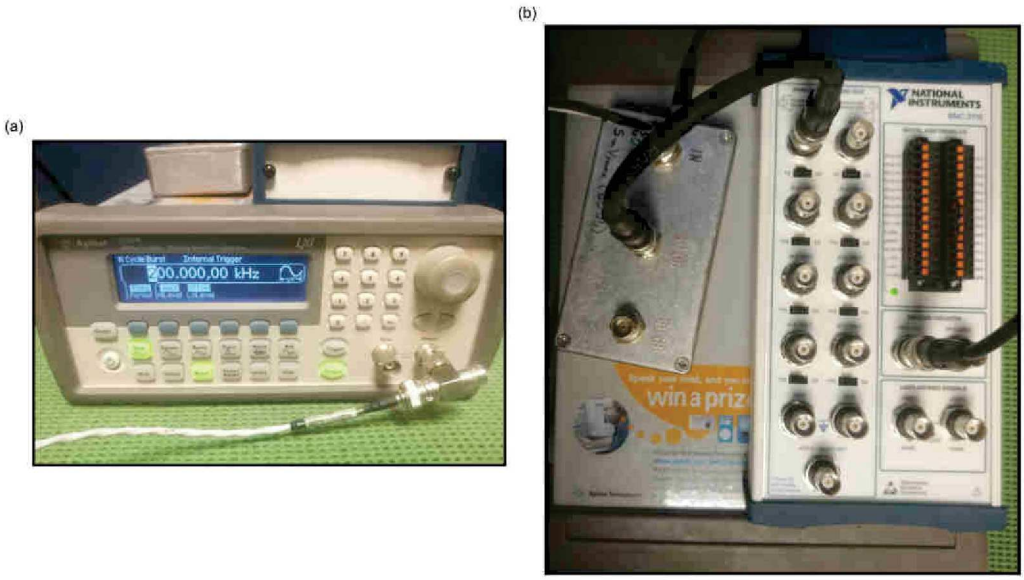

Figure 2.7: (a) Waveform generator used for velocity measurements, emitting a single period of a 200 kHz sinusoidal pulse. (b) The 40 dB pre-amplifier and BNC input board to a National Instruments BNC 2110 acquisition card.

coupling with the sample. In this configuration, measurements were made at temperatures of up to 450 °C.

One sensor acted as a source (the upper sensor) and the other as a receiver (the lower sensor), both housed within each piston—see Figure 2.1 for a schematic of the press, and Figure 2.8a for a close-up of sensors within each piston. The upper sensor was chosen to be the emitter, as its location is more susceptible to noise than the sensor within the lower piston, which is in direct contact with only the sample and the ceramic base-plate. During heating and cooling, a signal generator (Agilent 33220A, Figure 2.7a) connected to the upper transducer emitted a 200 kHz sinusoidal pulse every 50 ms. The generator simultaneously triggered a National Instruments BNC 2110 acquisition card to record the pre-amplified (+40 dB pre-amplifier with a flat response above 2 kHz) voltage across the receiving transducer (Figure 2.7b).

Each recorded waveform was 2 ms in duration: 4000 samples at a sampling rate of 2 MHz, including a pre-trigger recording time of 0.05 ms. The trigger system was a "soft" trigger, programmed in Matlab to allow a voltage input channel, rather than a dedicated trigger channel, to start the acquisition. In this way, it was possible to set a recording buffer, to provide the pre-trigger data, which could not be performed using the standard acquisition functions provided by the National Instruments. Excitation and acquisition were repeated 50 times in succession and the recorded waveforms were stacked to increase the signal-to-noise ratio. A waiting time of 10 s was imposed between

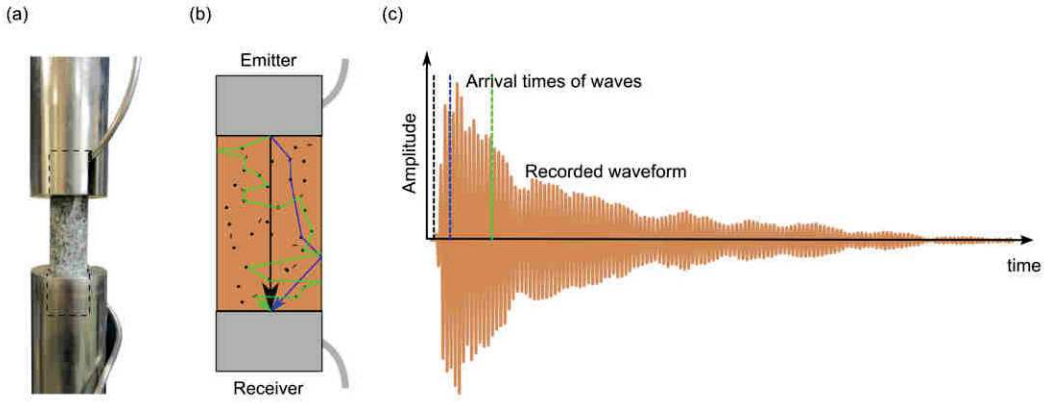

Figure 2.8: (a) Photo of the sensor configuration for P-wave velocity and Coda Wave Interferometry measurements, whereby acoustic sensors are in direct contact with opposing ends of the sample (here Lanhélin Granite) (b) Illustration of ray-paths of the direct P-wave (black), and of scattered and reflected waves (blue and green). (c) An example of a recorded waveform and a schematic illustration of the increased travel time with increasing distance travelled within the sample.

stacks. The resulting waveform data was used for both v_P and CWI calculations, which are detailed below. The results are shown in Chapter 4 (on granite) and Chapter 5 (on volcanic rock).

DIRECT P-WAVE VELOCITY To calculate the shift in P-wave arrival time, the waveforms were first spliced to contain only the first arrivals. Next, the cross-correlation functions between consecutive waveforms were calculated in the frequency domain. The cross-correlation functions were then interpolated by piece-wise quadratic interpolation around their maximum, and the lag time at the maximum of th newly interpolated cross-correlation functions provided the shift in P-wave arrival time. Calculating the cumulative of these time-shifts throughout an experiment gave the time shift with respect to the initial waveform prior to heating. The code (in Matlab) for the v_P calculation is provided in Section B.1. The P-wave velocity could then be calculated from the time shift, calibrated to the velocity measured using a separate, dedicated apparatus for measurements at room temperature (details given below in Section 2.2.2).

CODA WAVE INTERFEROMETRY CWI considers an ultrasonic wave that becomes scattered and reflected multiple times by the boundaries of, or the heterogeneities within a medium (Snieder, 2002). Figure 2.8b illustrates the different paths that may be taken by the acoustic waves within the sample, as they are reflected on sample boundaries, scattered by heterogeneities. The resulting waveform at a given location is the contribution of many scattered waves that have trav-

elled along different ray paths (illustrated in Figure 2.8c). Following changes in the medium—which include velocity changes, the displacement of scatterers due to thermal or mechanical deformation, and the development of new scatterers—the travel time of these scattered waves becomes delayed (Snieder, 2006). In the case of a velocity perturbation, Snieder (2002) showed that the shift in travel time of the wave is proportional to the time travelled (Equation 2.2), and therefore may be significantly greater than the delay observed in the direct arrivals.

$$\frac{\delta v}{v} = -\frac{\delta t}{t} \tag{2.2}$$

The scattered waves arrive later or earlier following a change in velocity, and the resulting waveform becomes elongated (apparent increase in velocity) or compressed (apparent increase in velocity) in time. For a given velocity change, the ratio between time shift and travel time is constant(Equation 2.2): stretching of the waveform increases with travel time as later arrivals have travelled for longer at the new velocity. This is illustrated by an example of a granite sample (Lanhélin Granite), heated to 100 °C and cooled at a rate of 1 °C/min (Figure 2.9). There is a positive time shift between the waveform recorded prior to heating, and following heating (once cooled), which becomes greater with increased arrival time. The stretching of the waveform indicates an apparent decrease in the velocity of the sample following heating and cooling.

There are two main methods used in CWI to calculate the relative time shift between waveforms. The first—and original—method involves calculating the cross-correlation function between the two waveforms in windows centred at different travel times (Snieder, 2002). The lag of the maximum of each cross-correlation function provides the time shift for a given travel time, and their linear regression yields the relative time shift, $\frac{\delta t}{t}$. An illustration of this method applied to the granite heated to 100 °C is shown in Figure 2.9d. However, a potential problem with this method is that it approximates the time shift as a constant within each window (Larose and Hall, 2009).

The second approach for calculating $\frac{\delta t}{t}$—and the method used herein—is the stretching method, whereby an array of relative time shifts is applied to the first waveform and the values of $\frac{\delta t}{t}$ for which the stretched first waveform correlates most with the second are selected (Larose and Hall, 2009; Sens-Schönfelder and Wegler, 2006) (see Figure 2.9d for an illustration). Following Larose and Hall (2009), a spline interpolation is used in the time domain to stretch each waveform, noted h_k, onto a series of new time vectors $t(1-a)$, where a is a value of the relative time shift, $\frac{\delta t}{t}$. The cross-correlation function is then calculated (in the frequency domain) between a reference waveform h_0 and the shifted waveform $h_k[t(1-a)]$, and the relative time shift is equal to the value of a for which the peak of the cross-correlation function is

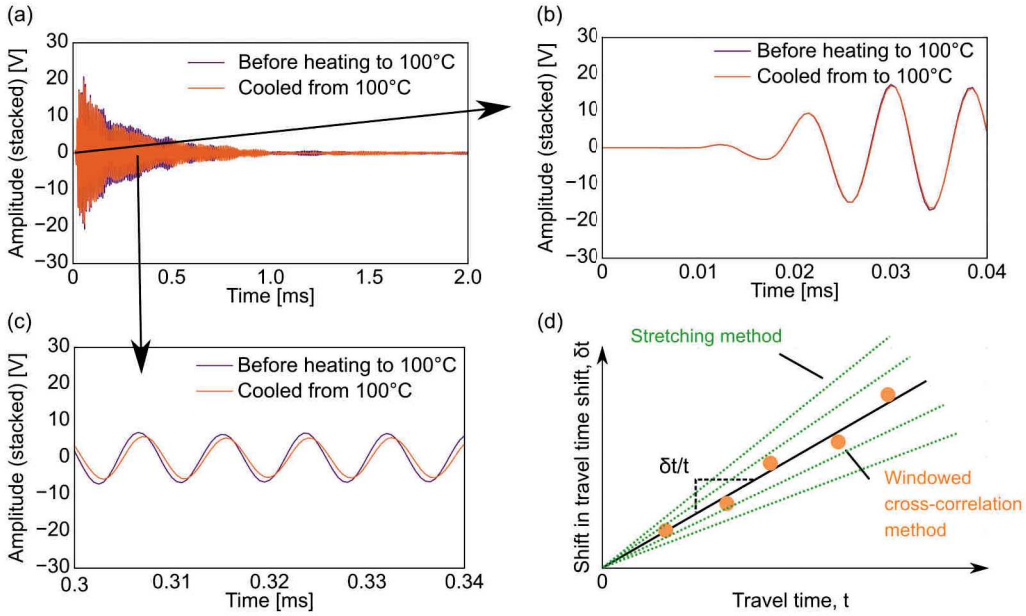

Figure 2.9: Illustration of CWI performed on a sample of Lanhélin Granite, before and following heating to 100 °C and cooling. (a) shows the recorded waveforms pre- and post- heating. (b) shows a zoom on the P-wave first arrival. (c) shows a zoom on a later part of the wave, where a time delay is visible following heating. (d) illustrates the windowed-cross correlation method (linear regression of the time delay calculated in windows) and the stretching method (applying a range of relative time shifts to one waveform, and selecting that which results in the best correlation).

maximal, noted $a_{k,0}$ (T is the length in time of the waveforms, here 0.5 ms).

The correlation between the reference waveform, h_0, and subsequent waveforms, h_k, was observed to deteriorate with temperature due to the strong perturbation of the medium. To counter this, the relative time shift $a_{k,k-1}$ between consecutive waveforms h_k and h_{k-1} was calculated instead. In this case, a scaling factor is required to infer the relative time shift with respect to the reference waveform, $a_{k,0}$ (Equation 2.3). The scaling factor is a function of the previous relative time shifts $a_{i,i-1}$.

$$a_{k,0} = \prod_{i=1}^{k} (a_{i,i-1} + 1) - 1 \tag{2.3}$$

The Matlab functions used to calculate the relative time shift between waveforms are provided in Section B.2. Functions for both the windowed cross-correlation and stretching methods are included.

Changes in the electro-elastic response of the piezo-ceramic transducers with temperature were observed and required calibration. A cylindrical sample of fused quartz (20 mm diameter, 40 mm length) was heated to 450 °C and cooled, at a rate of 1 °C/min. Figure 2.10b shows the original waveform data used for CWI during a single heating and cooling cycle of a fused quartz sample to a maximum temperature of 450 °C (the furnace temperature with time is shown in Figure 2.10a). The change in travel time with temperature is illustrated by the white lines in Figure 2.10b, the result of applying the relative time shift to different initial arrival times. There is a stretching of the waveforms with temperature: a positive relative time shift (Figure 2.10b), equating to an apparent decrease in the CWI wave velocity of the sample when heated (Equation 2.2). Changes in the wave velocity of fused quartz with temperature are low (Fukuhara and Sanpei, 1994) and were considered negligible. It was expected that the source of the relative time shift was wave scattering occurring within the steel casings of the sensors, and a change in the electro-elastic response of the piezo-ceramic transducers themselves with temperature. The signal measured on the fused quartz sample contains all of these possible influences, which are not to be considered in the rock samples. To compensate for these effects, the relative time shifts calculated for the quartz sample (the mean values over five heating and cooling cycles) were subtracted from those on rock samples.

2.1.3.3 *Thermal stressing conditions*

AE AND VELOCITY DURING THERMAL CYCLING TO 450 °C Measurements of v_P and the CWI relative time shift of waveforms (see previous Section 2.1.3.2 for details) were made on samples during three heating cycles to a maximum temperature of 450 °C, with a two-hour dwell time at the peak temperature, and at a rate of 1 °C/min.

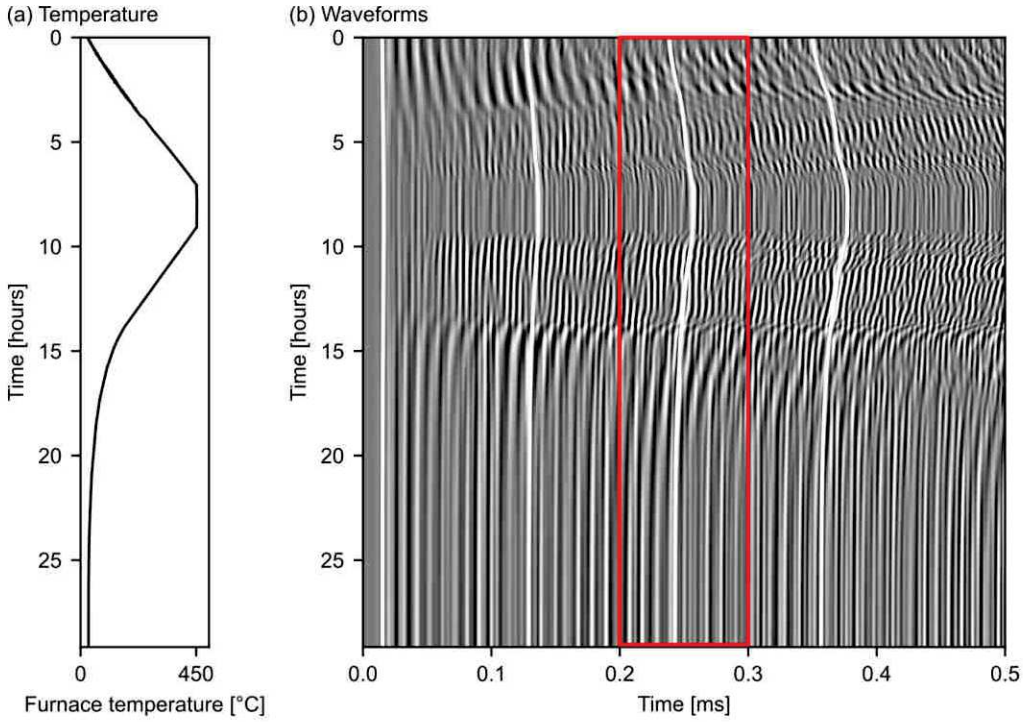

Figure 2.10: CWI performed on a sample of fused quartz during heating to 450 °C and cooling. (a) Furnace temperature against experiment time. (b) The first 0.5 ms of the recorded waveforms with experiment time. White lines show the calculated relative time shift (stretching method) applied to four distinct initial arrival times. A zoomed image on the red square is shown in Figure 2.11.

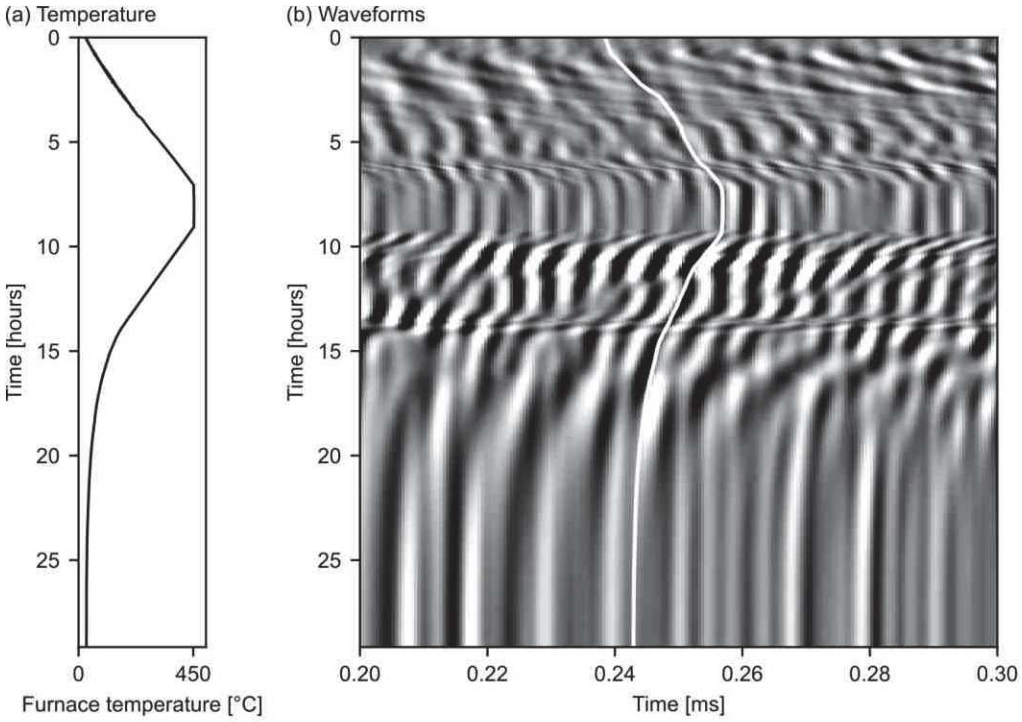

Figure 2.11: CWI performed on a sample of fused quartz during heating to 450 °C and cooling (zoom on the red box shown in Figure 2.10). (a) Furnace temperature against experiment time. (b) The first 0.3 ms of the original recorded waveforms with experiment time. The white line shows the calculated relative time shift (stretching method) applied to an arrival time of 0.24 ms.

During heating and cooling, a constant load of 100 N (~0.3 MPa) was applied on the sample to ensure coupling with the AE transducers on either side, embedded within the pistons. Furnace temperature was measured by a thermocouple at 10 mm from the sample surface and, in most cases, temperature was measured at the centre of the sample (except when samples were rare and the risk of breakage was avoided, and is indicated in the text) through a 1.7 mm diameter hole drilled radially into the side of the sample.

AE monitoring (see Section 2.1.3 for details) was performed on samples from the same block, under the same uniaxial load and thermal stressing conditions as for the velocity measurements. A constant load of 100 N (~0.3 MPa) was applied on the sample to follow the same experiment procedure as for the velocity measurements. To avoid any spurious AE due to friction between the thermocouple and the sample, the thermocouple was placed outside of the sample, at 1 cm from its surface.

Note, it has been found that the difference in temperature between the furnace and the centre of the sample does not have a material affect on the interpretation of data. Figure 2.12 shows the variation of the sample temperature and the furnace temperature with time during the heating of a Westerly Granite sample to 450 °C and cooling. Typically, the temperature between the furnace and the centre of the sample was found to be around 10 °C (20 °C maximum) during heating, and 5 °C during cooling.

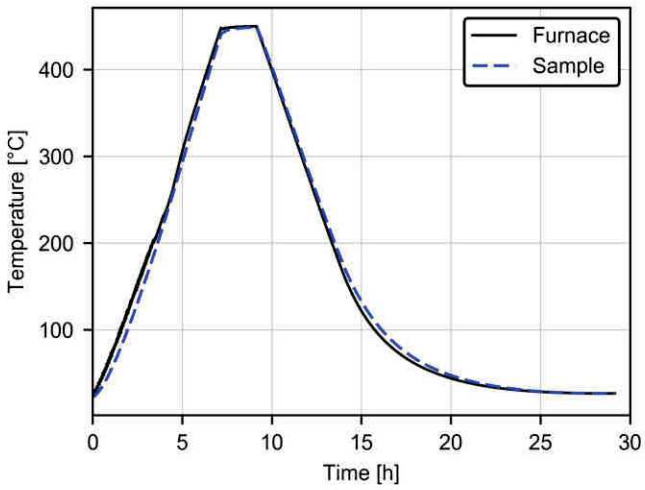

Figure 2.12: Sample temperature and furnace temperature during heating and cooling of Westerly Granite to and from 450 °C.

AE MONITORING UP TO 700 °C AE monitoring was performed during heating to 700 °C and cooling, at a rate of 1 °C/min, and with a dwell time of two hours at the peak temperature. As for the AE monitoring to 450 °C, the thermocouple was placed outside of

the sample, at 1 cm from its surface. During heating and cooling, a constant load of 310 N (1 MPa) was applied to the sample. The load was greater than previous (100 N) to improve coupling between the piston and the sample, which was possible as direct comparison with the velocity data was not required.

2.2 PETROPHYSICAL MEASUREMENTS

All petrophysical measurements were performed on cylindrical samples of 20 mm diameter, cored and ground to nominally 40 mm in length. Samples were then dried in a vacuum oven for at least 48 hours prior to measurements and experimentation.

2.2.1 *Porosity*

The connected porosity of samples was measured using one of two methods:

- The triple-weight water saturation method involved first weighing samples dried in vacuo for their dry mass (m_{dry}). Next, samples were kept overnight in a Bell jar under vacuum, before distilled water was passed into the Bell jar through tubing connected to a water aspirator pump, immersing the samples and saturating them. Samples were then left for several hours, before their water-saturated mass (m_{sat}) and suspended Archimedes mass (m_{Arch}) were measured. The porosity (ϕ_{water}) may then be calculated by Equation 2.4:

$$\phi_{\text{water}} = \frac{m_{\text{sat}} - m_{\text{dry}}}{m_{\text{sat}} - m_{\text{Arch}}} \tag{2.4}$$

- Porosity was also measured using helium pycnometry. An AccuPyc II 1340 pycnometer from Micromeritics first provided the volume of the rock matrix, and the porosity (ϕ_{gas}) was then calculated using Equation 2.5, from both the matrix volume (V_{matrix}) and the total sample volume (V_{sample}), given by the sample dimensions (measured using callipers):

$$\phi_{\text{gas}} = \frac{V_{\text{sample}} - V_{\text{matrix}}}{V_{\text{sample}}} \tag{2.5}$$

2.2.2 *Ultrasonic wave velocity*

Room temperature measurements of the ultrasonic P-wave (v_P) and S-wave (v_S) velocities were made along the sample length. The sample was placed in a jig between two steel end-caps, which both contained either the P- or S-wave piezo-transducers. One sensor was excited by

a 10 V sinusoidal pulse (700 kHz for P-wave, and within the range of 100–500 kHz for S-wave), and the opposing sensor acted as a receiver. The total travel time—the difference in time between the pulse and the P-wave and S-wave arrival time—was observed on an oscilloscope (at 10 MHz sampling rate), and corrected for the travel time of the wave within each end-cap. Finally, the velocity was calculated from the corrected travel time and the length of the sample measured using callipers.

2.2.3 *Permeability*

Measurements of permeability were made with nitrogen as the permeant, under a confining pressure of 1 MPa, and one of two methods—depending on the permeability of the sample—were used:

- The pulse decay method (Brace et al., 1968) was used on samples with permeabilities of less than 10×10^{-15} m^2 using a modified bench-top permeameter (Farquharson et al., 2016) from Vinci Technologies, along the length of the oven-dried samples. A gradient of 0.2 MPa, was imposed across the sample, before arresting the gas supply and recording the upstream pressure decay with time using a manometer (Keller LEX 1). Permeabilities were calculated by fitting the pressure-time curves (Brace et al., 1968), taking in to account the Klinkenberg correction for gas slippage (Klinkenberg, 1941).
- The steady-state method was used for higher permeability samples ($>10 \times 10^{-15}$ m^2), whereby a constant gas pressure gradient was imposed across the sample and, once stabilised, the flow rate was measured using a volumetric mass flow meter (Bronkhorst EL-Flow F-111B-050-AAD-22-V, with a maximum flow rate of 50 mln/min). Flow rates were measured for several pressure gradients within the range of 0.001–0.2 MPa, and the permeability was calculated from the linear regression of flow with pressure and Darcy's law, again applying the correction for gas slippage (Klinkenberg, 1941).

2.2.4 *Thermal properties*

The thermal diffusivity, conductivity, and specific heat (heat capacity), of samples were measured using a Hot Disk TPS 500 Thermal Constants Analyser. The analyser uses the Transient Plane Source method, whereby a Hot Disk sensor of 3.189 mm radius acts simultaneously as a heat source and a thermocouple. The "single-sided" configuration was used here (illustration shown in Figure 2.13), the sensor placed between a face of the cylindrical sample on one side, and an insulating foam of known thermal properties on the other. The analyser

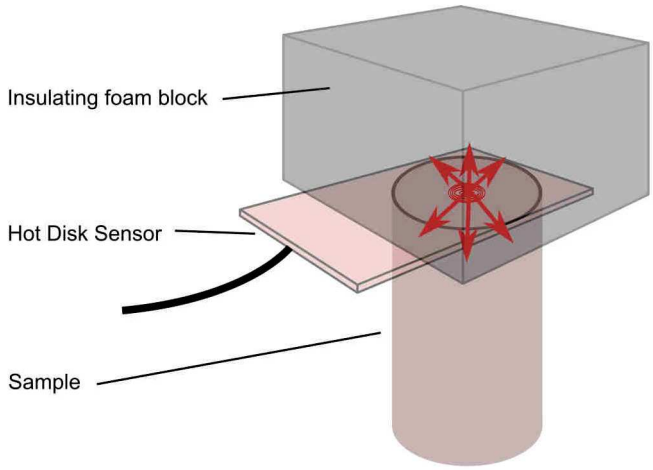

Figure 2.13: Configuration for measurements of thermal diffusivity, thermal conductivity, and specific heat, using the Hot Disk TPS 500 Thermal Constants Analyser and the transient plane source method. The one-sided configuration is shown here, whereby a Hot Disk 3.18 mm radius sensor—acting simultaneously as heat source and thermocouple—is placed between one face of the cylindrical rock sample and a block of insulating foam.

was programmed to supply a constant power output to the sensor coil over a fixed duration—5 s at 150 mW for the Westerly Granite (unheated, 400 and 700 °C samples) and 5 s at 90 mW for the Lanhélin and Garibaldi Grey Granites—whilst recording the resistance of the coil with time. The sensor temperature was calculated from measurements of resistance, and the thermal diffusivity and conductivity were then inferred from the transient temperature change by and the thermal conductivity equation (assuming that the heat source is within an infinite medium). The parameters for these measurements are: the duration of heating, which must be low enough to ensure a heat penetration depth within the sample boundaries (at 10 mm distance from the centre of the sensor); and the power output, to control the amplitude of the temperature increase.

2.2.5 *Mechanical tests*

For all mechanical tests, a lubricating wax was applied to both faces of dried samples (under vacuum at 40 °C for at least 24 h) to limit their friction with the pistons (Bésuelle et al., 2000).

Uniaxial Compressive Strength (UCS) tests were carried out using another uniaxial press of the Rock Deformation Laboratory at Strasbourg University. Tests were performed at a constant strain rate of 1×10^{-5}/s until failure, whilst measuring axial load and displace-

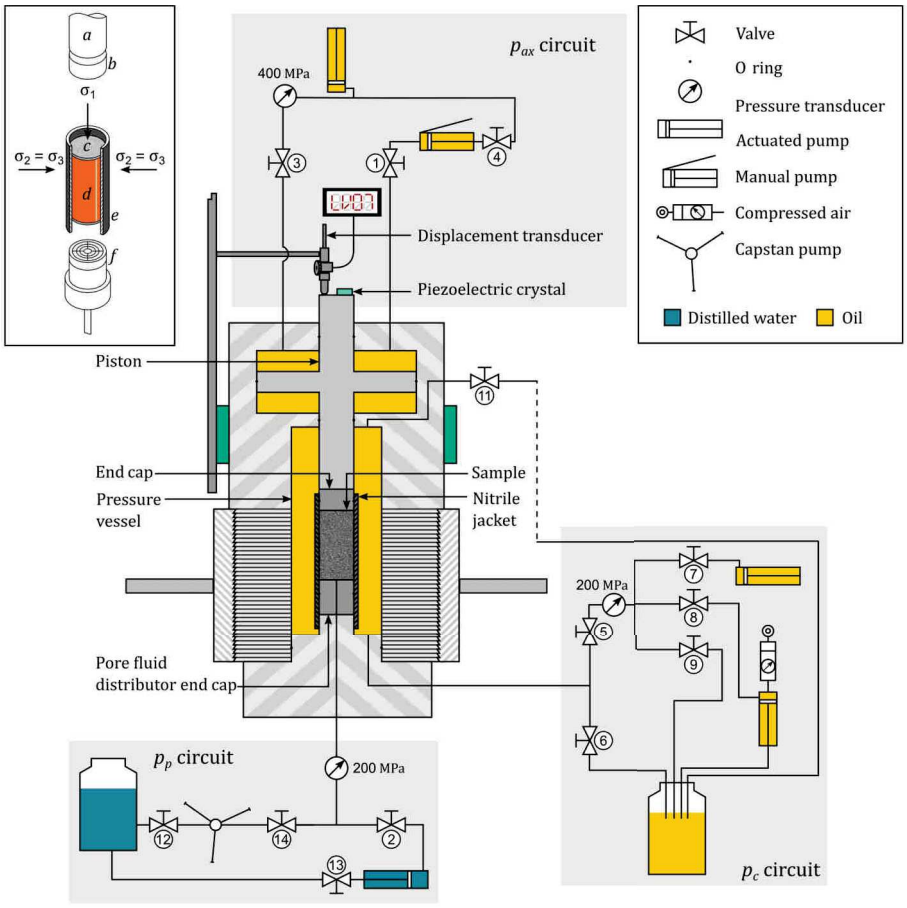

Figure 2.14: Schematic of the conventional triaxial apparatus of the Rock Deformation Laboratory at Strasbourg University (from Farquharson et al. (2017)). Note that triaxial tests performed here were under dry conditions.

ment. Strain was calculated from the voltage across a linear variable differential transducer (LVDT) monitoring the displacement of the piston relative to the static base plate, and corrected for the strain of the load-train.

Triaxial tests were also performed on dry samples, in the conventional triaxial apparatus of the Rock Deformation Laboratory (Klein and Reuschlé, 2004), of which a schematic is shown in Figure 2.14 from Farquharson et al. (2017). Confining pressure was regulated by a servo-controlled stepping motor connected to a pressure transducer with an accuracy of 0.05 MPa. Axial load was applied by a piston and regulated by a second computer-controlled stepping motor. Axial displacement was measured with an accuracy of 0.2 μm outside the pressure vessel, with a capacitive transducer mounted on the moving piston, which was servo-controlled to advance at a fixed rate (corresponding to a nominal strain rate of 1×10^{-5}/s).

3

NEW PROCEDURE FOR QUANTIFICATION OF THERMAL MICROCRACKS AND MICRO-MECHANICAL MODELLING

Alongside the new experimental tool to monitor thermal microcracking in rock, a numerical tool was developed, to rapidly assess the microcrack damage within rock from images of the microstructure. This new method, which consists of processing optical micrographs for analysis of crack properties, is applied to a thermally-cracked, fine-grained granite. These results have been published as presented in:

L. Griffiths, M. J. Heap, P. Baud, and J. Schmittbuhl (2017a). 'Quantification of microcrack characteristics and implications for stiffness and strength of granite.' In: *International Journal of Rock Mechanics and Mining Sciences* 100, pp. 138–150. ISSN: 13651609. DOI: 10.1016/j.ijrmms.2017.10.013

ABSTRACT

Microcracks can affect the mechanical properties of rocks, such as their stiffness and strength. To provide a link between the microstructural parameters and the mechanical behaviour of rock, micromechanical models use parameters that represent a quantitative description of the microcrack population. However, these parameters are difficult to constrain. With the aim of better constraining micromechanical models for rock strength and stiffness, we provide here robust measurements of microcrack characteristics. We developed an algorithm to process optical micrographs of rock, automatically creating binary images of the microcrack network. We applied this procedure to optical micrographs of fine-grained granite samples that have undergone varying degrees of thermal microcrack damage. From these processed images, we calculate the mean microcrack length and the number of microcracks per unit area (and therefore the 2D microcrack density). We also create heat maps showing the spatial distribution of microcracks and their lengths. The results of our automated image analysis are in very good agreement with those of widely-used stereological techniques, and we show that our method can be applied to other rock types (sandstone and andesite) that contain microcracks. Using the measured microcrack characteristics as inputs for the Ashby and Sammis (1990) 2D micromechanical sliding wing crack model, we predict the uniaxial compressive strength of the granite and compare the

predictions with strength measurements made in the laboratory. We find good agreement between the model and the experimental data for granite heated to temperatures below the alpha-beta transition of quartz (~573 °C). Rock strength is overestimated above this threshold, possibly due to variations in fracture toughness, which is considered constant in our modelling. Finally, we use the 2D sliding crack model of David et al. (2012) to infer microcrack density and aspect ratio from the mechanical response of the thermally microcracked samples to cyclic stressing. We show a good agreement between inferred and measured crack densities if a scaling factor is introduced.

3.1 INTRODUCTION

Rocks commonly contain microscopic cracks (Kranz, 1983; Simmons and Richter, 1976). Microcracks in rock have a length of typically 0.1 mm or less (Simmons and Richter, 1976) and an aspect ratio, i.e. the ratio of their aperture and their length, of less than 10^{-2} generally in the range of 10^{-3}–10^{-5}. They can be mechanically, chemically, or thermally induced and significantly affect the thermal (Kant et al., 2017) and transport (Le Ravalec et al., 1996; Nasseri et al., 2009a; Siratovich et al., 2015) properties of rock, which may have important implications for geothermal or hydrocarbon reservoirs, or for the underground storage of nuclear waste (Paterson and Wong, 2005). Microcracks also reduce the stiffness (Budiansky and O'Connell, 1976; Jaeger et al., 2009; Simmons et al., 1975; Walsh, 1965; Zimmerman, 1985) and strength (Jaeger et al., 2009; Paterson and Wong, 2005) of rocks, an important consideration for industrial geomechanical problems such as borehole breakouts (Bérard and Cornet, 2003) and natural geophysical phenomena, including the formation and properties of fault zones (Mitchell and Faulkner, 2009).

As a result, the detailed microscale characterisation of rock must inform on the mechanical response at the laboratory scale and beyond, and numerous micromechanical models exist to perform such a function. For example, one type of upscaling model relies on the scale invariance of fracture processes (Bonnet et al., 2001). Another type assumes a clear representative elementary volume at the micro-scale and upscales to greater lengthscales using micromechanical damage mechanics models. Examples of the latter include micromechanical models that explore the influence of microcracks on rock stiffness (Budiansky and O'Connell, 1976; David et al., 2012; Walsh, 1965) and strength (Ashby and Sammis, 1990; Griffith, 1921; McClintock and Walsh, 1962; Murrell and Digby, 1970). The reliability of these micromechanical models depends on the accuracy of the micro-scale characterisation, along with the adequacy of the model assumptions for a given rock. For instance, micromechanical models for failure require an accurate description of the initial microcrack density and

geometry. In the case of Ashby and Sammis' 2D sliding wing crack model (Ashby and Sammis, 1990), which predicts the compressive failure of microcracked materials and has been widely applied to the failure of rocks (Baud et al., 2014, 2000; Rawling et al., 2002), an initial crack damage parameter is required, itself a function of the microcrack length and the number of microcracks per unit area (herein referred to as the number density). However, these micromechanical models typically show some limitations when the crack density becomes large and multiple crack interactions are in play up to the limit of the microcrack coalescence (Hansen and Schmittbuhl, 2003; Ortiz, 1988; Wong et al., 2001). A central issue of modelling damage mechanics is the consideration of microcrack interactions for high microcrack densities (e.g. Hashin (1988), Horii and Nemat-Nasser (1986), and Kemeny and Cook (1991)).

To obtain information on the microcrack distribution, microscopy is one of the most commonly used tools. For example, a quantification of the microcrack density may be obtained "manually" using the stereological techniques of Underwood (1967) (see Fredrich et al. (1989), Heap et al. (2009b, 2014a), Tapponnier and Brace (1976), Wong (1985), and Wu et al. (2000)). These established techniques involve placing a grid over a microscope image and counting intersections between microcracks and the grid to calculate their area density. However, this manual approach can be time consuming and is open to subjectivity. Microcrack characteristics can also be determined numerically from digital images of the microcrack network (dedicated analysis tools are available, for example FracPaq Healy et al. (2017)). These images can be generated manually by tracing over micrographs (which has subjectivity and reproducibility issues) or automatically, using image segmentation techniques to create binary images of the microcracks. For example, Arena et al. (2014) and Delle Piane et al. (2015) used image processing software to segment backscattered Scanning Electron Microscopy (SEM) micrographs of Carrara Marble. From the processed SEM micrographs, they are able to calculate the microcrack length, aspect ratio and surface density. For studying microcracks, SEM micrographs have the advantage over optical micrographs in that they are sensitive to mass density. However, compared to optical microscopy, SEM is more expensive, time consuming, and technically demanding. For analyses of large sets of micrographs, it is therefore of interest to develop an automated and robust procedure targeting optical micrographs.

In this study, we aim to address the influence of microcrack density on the mechanical response of rock. To keep other rock attributes such as the mineralogy and grain size constant, we selected a fine-grained granite (Garibaldi Grey Granite) in which we induced varying amounts of thermal microcracking by heating samples to temperatures ranging from 100 to 900 °C. To assess the thermal micro-

crack damage on the microscale, we present here a new automatic procedure, coded in Python, that rapidly extracts quantitative microcrack statistics from optical microscope images. The details of the micrograph processing stage, which produces binary images of the microcracks, are described in Appendix A. From the processed images, we calculate the microcrack length and number density, thus quantifying the microcrack damage present within the rock (scripts for both the image processing and the microcrack quantification are available on demand from the corresponding author). We then performed uniaxial deformation experiments to study the influence of thermal microcracking on rock stiffness and uniaxial compressive strength (UCS). We compare our experimental UCS measurements on the thermally microcracked granite samples with the upscaled predictions from Ashby and Sammis' micromechanical sliding wing crack model (Ashby and Sammis, 1990) (using data from our quantitative microcrack analysis). Finally, we followed a downscaling approach by using the sliding crack model of David et al. (2012) to infer values of the microcrack density and aspect ratio using data from stress-cycling experiments on the thermally microcracked granite, and we compare these values to the direct microscale measurements.

3.2 MATERIALS AND METHODS

Previous studies that focus on the influence of microcrack density on the physical and mechanical properties of rock have performed experiments on variably thermally microcracked samples of the same rock (e.g. David et al. (1999) and Wang et al. (2013)). In this way, the microcrack density may vary, whilst other rock properties such as composition and grain size remain constant. Here we follow the same approach by preparing a suite of variably thermally microcracked granite samples for our measurements.

3.2.1 *Sample preparation*

Garibaldi Grey Granite from British Columbia, Canada, was chosen for this study due its homogeneity and small crystal size (between 0.5 and 1 mm) with regards to the dimensions of a thin section and a laboratory sample. The composition of the granite, estimated from an optical micrograph of the unheated granite (a cropped micrograph is shown in Figure 3.1) is 45 % quartz, 45 % feldspar, and 10 % mica. For the laboratory measurements, we prepared 11 cylindrical samples of 20 mm diameter and nominally 40 mm in length and thermally microcracked them to varying degrees by heating them in a furnace at room pressure to temperatures of 100, 200, 400, 500, 550, 600, 650, 750, 800, and 900 °C. One sample was left intact. The heating procedure consisted of drying the rock in a vacuum pump at 40 °C over 24 h

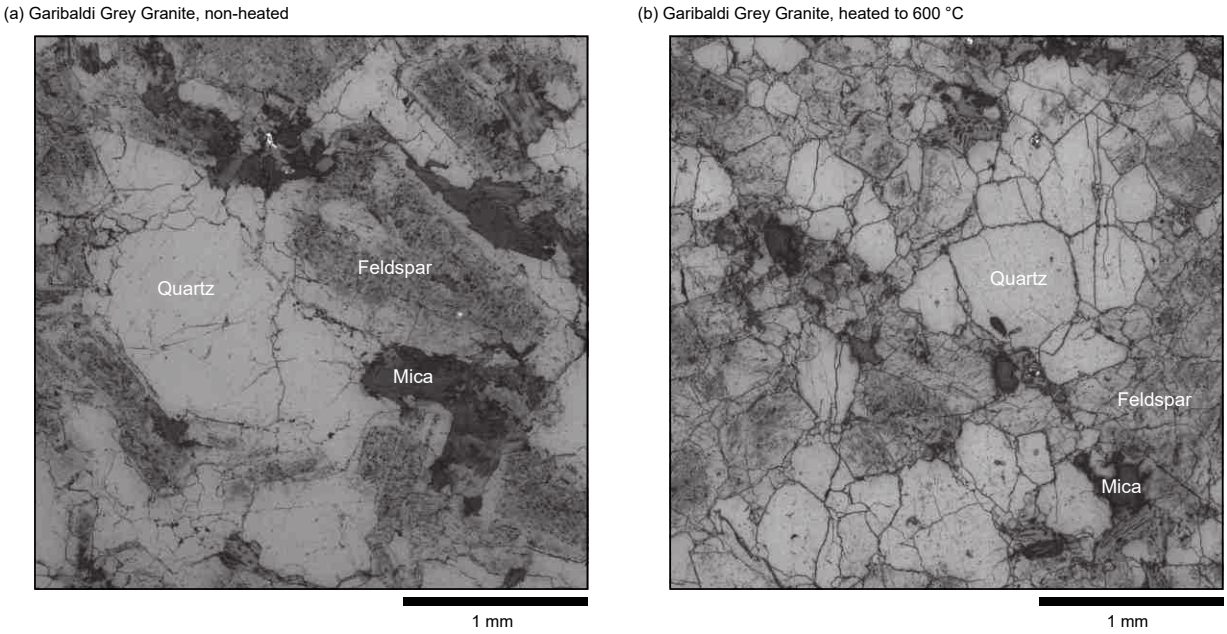

Figure 3.1: Cropped 3 mm × 3 mm optical micrographs of Garibaldi Grey Granite: (a) a thin section of the unheated granite and (b) a thin section of the granite which has been heated to 600 °C.

before placing the sample in the furnace, programmed to heat at 1 °C/min to the desired maximum temperature. The rock remained at the target temperature for a dwell time of two hours before being cooled at 1 °C/min back to room temperature. Considering the low heating and cooling rate of 1 °C/min, we assume that the temperature gradient across our samples to be negligible. Indeed, the time constant for thermal equilibrium of a cylindrical sample is equal to r^2/d where r is sample radius and D is the thermal diffusivity (Wang et al., 2013). If we take the diffusivity of our 20 mm diameter granite samples to be that of Westerly Granite ($1 \times 10^{-6}\,\mathrm{m}^2/\mathrm{s}$; Clauser and Huenges (1995), Vosteen and Schellschmidt (2003), and Wang et al. (2013)), the time constant is equal to 100 s. The time constant is within an order of magnitude of the 60 s the furnace takes to heat by 1 °C and, as such, we can expect a low thermal gradient across the sample. Figure 3.1 shows cropped optical micrographs of the intact granite (Figure 3.1a) and the granite heated to 600 °C (Figure 3.1b). The granite heated to 600 °C clearly contains more microcracks than the intact sample (Figure 3.1b).

3.2.2 *Crack density and crack length measurements*

Thin sections of the granite samples were prepared in a plane parallel to the sample axis. Optical microscope images at 2500× optical zoom (2592 × 1944 pixels, or 5.2 × 3.9 mm) were taken across the entirety

of each of the thin sections (that have an area of roughly 20 × 25 mm, i.e. 100 % of the sample width and 62 % of the sample length). Figure 3.1 shows examples of cropped micrographs of the intact sample and the sample heated to 600 °C. All the cropped micrographs were processed to create binary images of the microcracks, following the filtering and segmentation procedure described in detail in Appendix A. Microcracks were automatically identified and characterized in the processed images in windows of 1 × 1 mm and their lengths were approximated by the distance between their end points.

Examples of entire thin section of the granite heated to 550, 600, and 650 °C are shown in Figure 3.2. Figure 3.2 also shows the spatial distributions (heat maps) of the number of cracks per unit area (or number density), N_A, and the mean microcrack length, calculated from the processed optical micrographs in windows of 1 × 1 mm. We see no spatial preference for the location of microcracking, which supports our conclusion that the heating/cooling rate is sufficiently low to ensure a homogeneous temperature distribution within the sample. If this was not the case, we might expect a higher number of microcracks per unit area at the periphery of the sample. In these examples, we generally observe an increase in N_A and a decrease in the mean microcrack length with temperature (Figure 3.2).

The final results of the image analysis are shown in Figure 3.3: the mean number of cracks per unit area, or number density N_A, and the mean microcrack length as a function of thermal stressing temperature (data also available in Table 3.1). Error rs represent one standard deviation from the mean microcrack length and number density. We see that N_A remains constant (~75/mm^2) up to a temperature of 550 °C. N_A is doubled from 550 to 600 °C (from ~75 to ~150/mm^2), but remains approximately constant (between ~150 and ~175/mm^2) between 650 and 900 °C (Figure 3.3). The calculated values of the microcrack lengths (100 µm or less) are compatible with values of microcrack lengths in the literature (see Kranz (1983) and Simmons and Richter (1976) and references therein). The mean microcrack length increases slightly with temperature up to around 550 °C (Figure 3.3). Above 550 °C, the mean microcrack length decreases to ~60 µm and remains constant up to the maximum temperature of 900 °C (Figure 3.3).

To validate the proposed automatic procedure, we compared our analysis to the widely-used manual stereological techniques of Underwood (1967). The latter technique extracts information on the 3D microstructure from 2D microscope images to provide the surface area per unit volume, S_V (mm^{-1}). For this, parallel test lines are drawn across the 2D image and the number of intersections between these lines and the features are counted. The number of intersections per unit length of test line is written P_L (mm^{-1}). Assuming that the surfaces of the feature are randomly distributed within the volume and

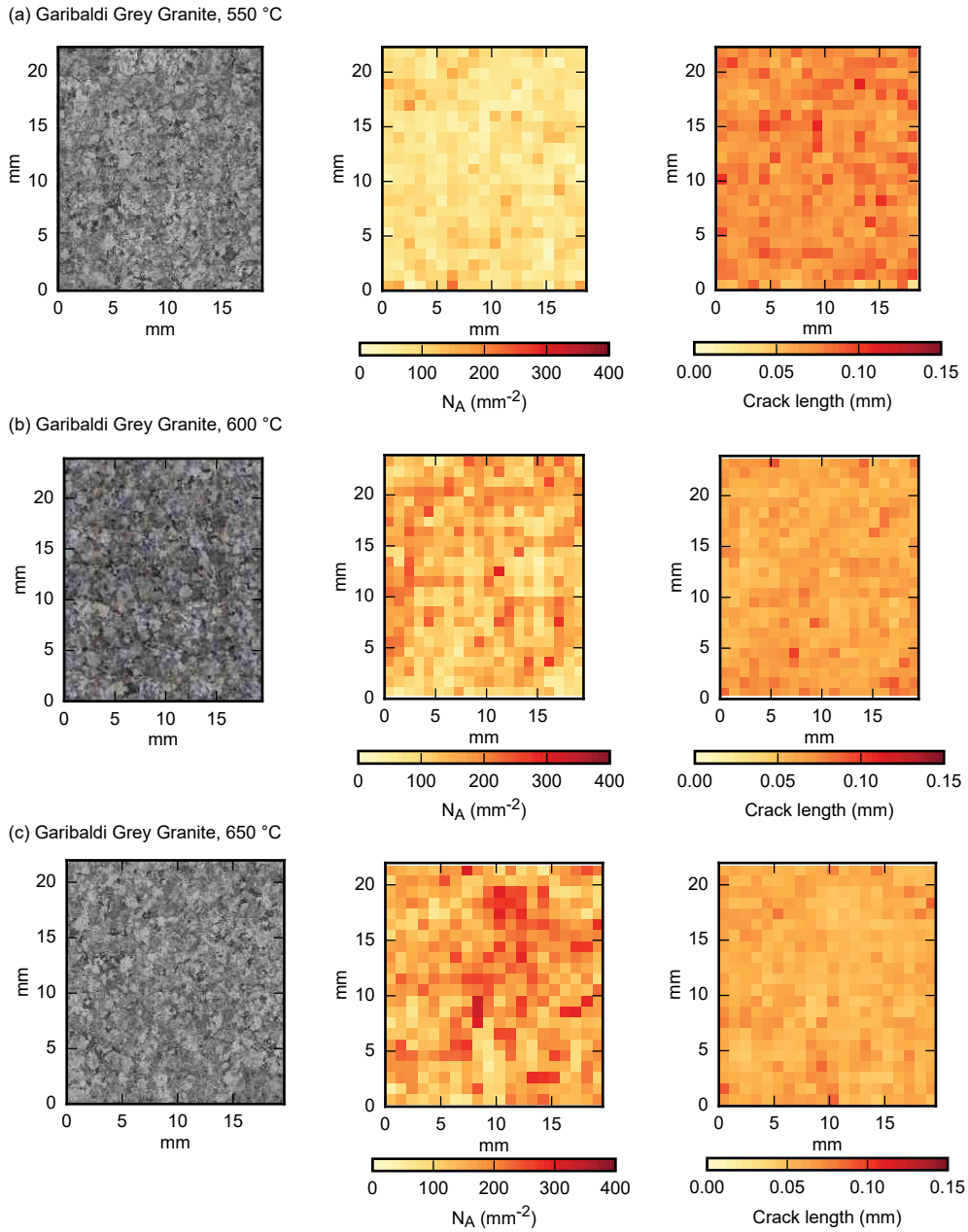

Figure 3.2: Original optical micrographs of thin sections of Garibaldi Grey Granite samples heated to (a) 550, (b) 600, and (c) 650 °C, alongside heat maps of the number of microcracks per unit area (N_A) and the mean microcrack length ($2c$) over a 1 × 1 mm area, as calculated from the processed micrographs (data given in Table 3.1).

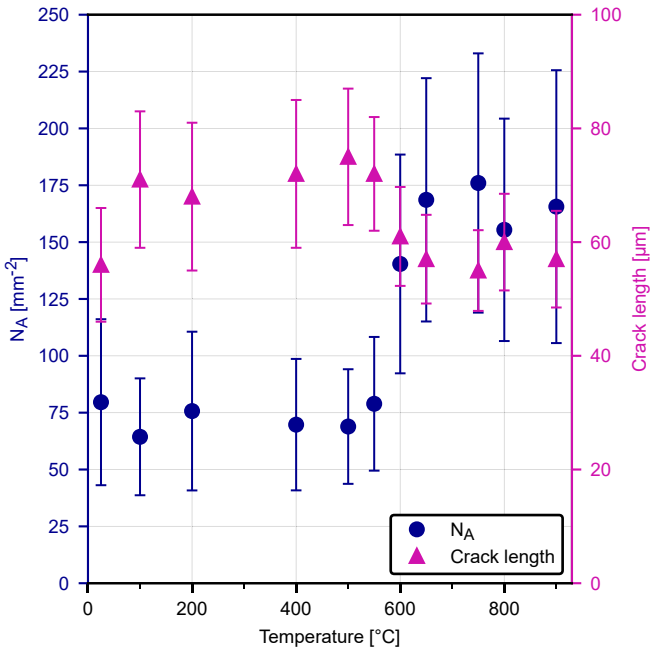

Figure 3.3: Results of the micrograph analysis of all Garibaldi Grey Granite thin sections. Shown are the mean number of microcracks per unit area (N_A) and mean microcrack lengths ($2c$) as a function of the maximum temperature to which the sample was heated. Error bars give one standard deviation from the mean number of cracks and their average lengths per mm² across each thin section.

that a large number of parallel test lines are drawn, we have Equation 3.1 (Saltykov, 1958).

$$S_V = 2P_L \tag{3.1}$$

If we now consider two sets of test lines drawn in perpendicular directions, we have two values, P_I, the number of intersections per test line length in the first direction, and P_{II}, the number of intersections per test line length in the second direction. S_V is then equal to the sum of the intersections per unit length in both directions (Equation 3.2).

$$S_V = P_I + P_{\mathrm{II}} \tag{3.2}$$

In our case, the features we consider are microcracks, and Figure 3.4a shows a grid of test lines overlaying a 2 × 2 mm micrograph of the granite sample heated to 600 °C. Here the grid test lines are spaced at regular intervals of 0.1 mm, as used in Heap et al. (2009a) and Heap et al. (2014b). This example micrograph has also been processed following our algorithm (Figure 3.4b) and the resulting microcrack network is shown in green. In this way, we can compare the S_V values from manually counting intersections between test lines and the microcracks in the original (i.e. unprocessed) microscope image with S_V values resulting from the automatic counting of intersections with the microcracks in the processed image. The result of this analysis is presented in Figure 3.5a. We see that S_V values obtained from manually counting intersections in the original image are very similar to those obtained by counting intersections programmatically in the processed image (Figure 3.5a). We note that the manual method is open to subjectivity and that results may vary from user to user.

For our analysis method, rather than use a grid, we chose to directly calculate N_A by automatically locating and counting cracks within 1 × 1 mm windows of the processed micrographs. To compare the two methods, S_V can be related to N_A through the Walsh (1965) 2D crack density, γ, which is defined by Equation 3.3, where c is the crack half-length.

$$\gamma = N_A c^2 \tag{3.3}$$

Through direct measurements of the mean crack length, $2c$, and N_A, Hadley (1976) showed an agreement between the product of these two values and the microcrack length per unit area of Underwood (1967) (Equation 3.4).

$$L_A \approx 2cN_A \tag{3.4}$$

L_A is related to S_V via Equation 3.5 (Underwood, 1967) and therefore S_V can be used to calculate the 2D crack density, γ (Equation 3.6).

$$L_A = \frac{\pi}{4} S_V \tag{3.5}$$

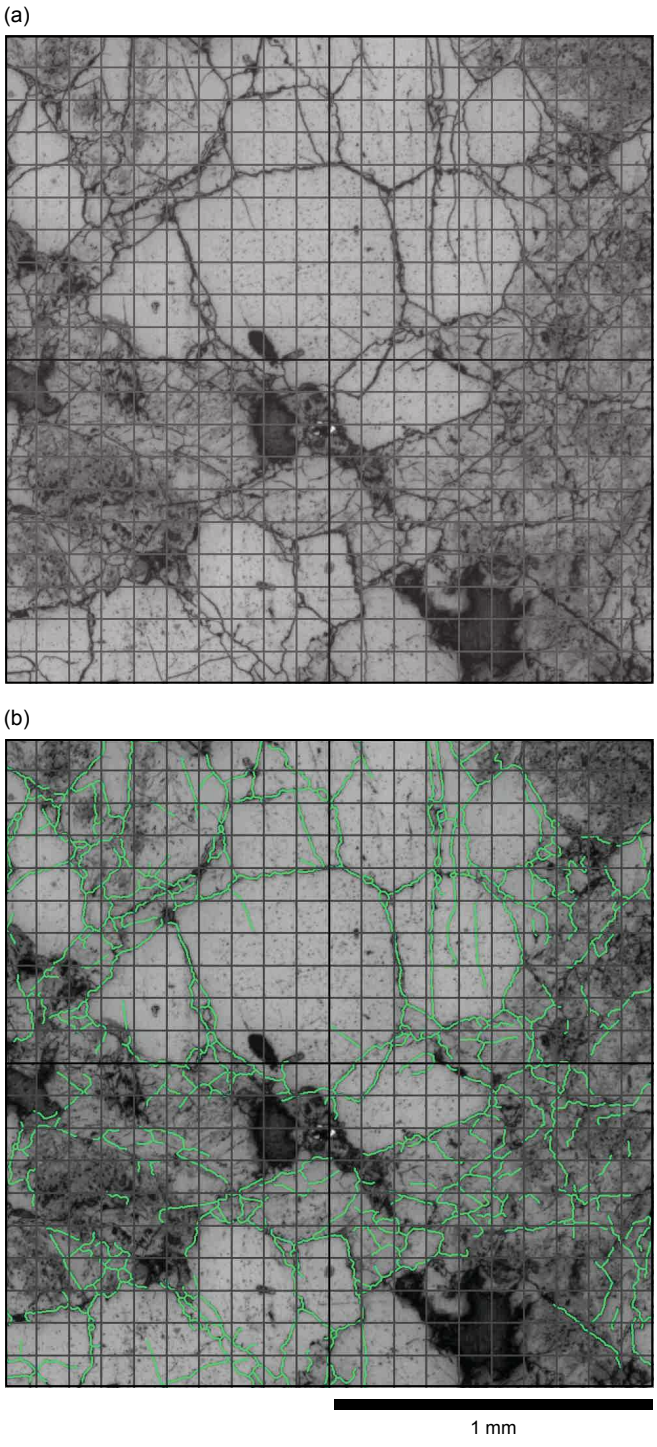

Figure 3.4: (a) Cropped micrograph of the thin section of Garibaldi Grey Granite sample heated to 600 °C. A grid has been superposed to show the working of the stereological method of Underwood (1967). (b) The same micrograph as in panel (a) with the results of micrograph processing (details provided in Appendix A) superposed in green.

Thermal stressing temperature [°C]	Cracks per unit area N_A [mm^{-2}]	Mean crack length $2c$ [µm]	2D crack density γ
ambient	79.6	56	0.062
100	64.4	71	0.081
200	75.7	68	0.088
400	69.7	72	0.090
500	68.9	75	0.097
550	78.9	72	0.102
600	140.4	61	0.131
650	168.6	57	0.137
750	176.0	55	0.133
800	155.4	60	0.140
900	165.6	57	0.135

Table 3.1: The results of the micrograph analysis of all Garibaldi Grey Granite thin sections. For each thermal stressing temperature, we report the calculated mean crack number density, N_A, and mean crack length, $2c$. From these values, we calculate the crack density, γ (Equation 3.3).

$$\gamma \approx \frac{\pi S_V c}{8} \tag{3.6}$$

For all thin sections, γ was calculated from both N_A and S_V (Figure 3.5b). Both methods give similar results, especially for lower values of γ. The strong agreement between the calculated values of N_A and S_V serves to validate the method (including the crack length approximation) and the accuracy of the stereological methods.

3.2.3 *Physical properties (porosity and P-wave velocity)*

The connected porosities of all granite samples were measured using the triple weight water saturation method. The P-wave velocities, noted v_P, were measured under ambient pressure and temperature conditions along the length of the oven-dried cylindrical samples (placed in a vacuum oven for at least 24 h at 40 °C). The porosity and v_P of the 11 samples were measured following the heating procedure and ranged, respectively, from 0.009 and 4.37 km/s for the intact rock to 0.037 and 1.48 km/s for the sample heated to 900 °C (Table 3.2; Figure 3.6a). The porosity increases with the maximum heating temperature, whilst v_P decreases with temperature (Figure 3.6a). In both measurements, large changes are observed from 500 to 600 °C (Figure 3.6a). Since we observe no pores in the microstructural images (Figure 3.1) we assume that all porosity is cracks.

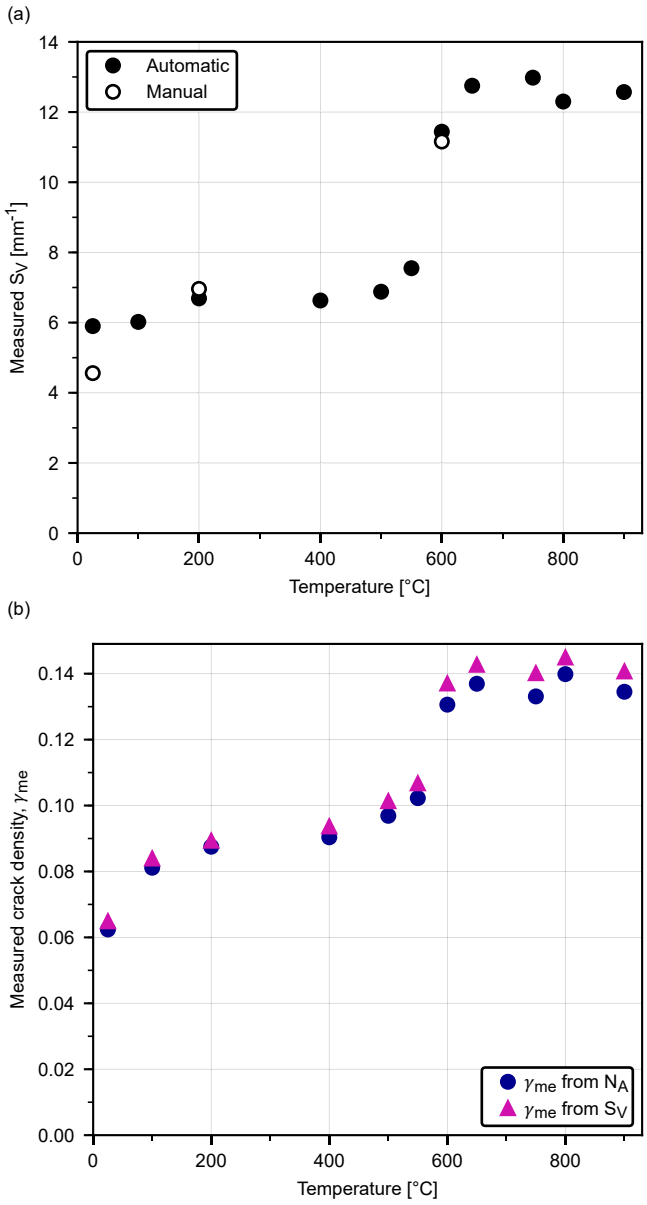

Figure 3.5: (a) Comparison between the mean crack surface area per unit volume (S_V) from manually counting intersections between microcracks and test lines in the original 25, 200, and 600 °C micrographs (cropped to 10 x 10 mm) and S_V given by the number of intersections between the generated microcrack network and the test lines across the entire thin section. (b) The measured microcrack density (γ_{me}) for each thin section of Garibaldi Grey Granite as calculated from both the microcrack number density N_A (Equation 3.3), and the crack surface per unit volume S_V (Equation 3.6).

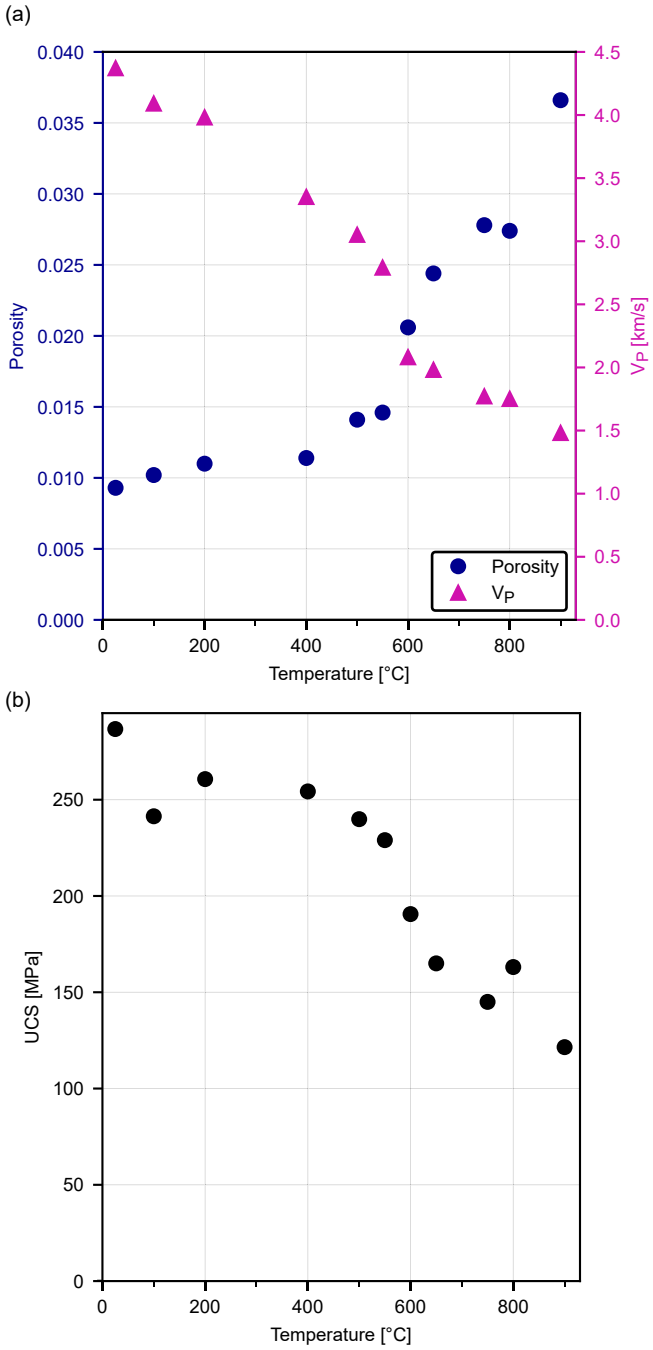

Figure 3.6: Physical and mechanical properties of the Garibaldi Grey Granite samples as a function of thermal stressing temperature: (a) the measured values of connected porosity and P-wave velocity, and (b) the uniaxial compressive strength (UCS).

Thermal stressing temperature [°C]	Connected porosity	v_P [km/s]	Measured UCS [MPa]
ambient	0.009	4.37	287
100	0.010	4.09	241
200	0.011	3.98	261
400	0.011	3.35	254
500	0.014	3.05	240
550	0.015	2.79	229
600	0.021	2.08	191
650	0.024	1.98	165
750	0.028	1.77	145
800	0.027	1.75	163
900	0.037	1.48	122

Table 3.2: The physical and mechanical properties of all Garibaldi Grey Granite samples measured at room temperature and pressure. For each maximum heating temperature, we report the connected porosity, the P-wave velocity, v_P, and the measured uniaxial compressive strength (UCS).

3.2.4 *Stiffness measurements*

We conducted a series of deformation experiments in which we uniaxially loaded and unloaded each of the 11 oven-dry (under vacuum at 40 °C for at least 24 hours) samples (examples of these curves are shown in Figure 3.7a. Samples were loaded up to a maximum stress (within the elastic domain) at a constant strain rate of 10^{-5} /s. The maximum stresses for cycling were therefore chosen to be well below the UCS of the rock as not to induce cracking: 100 MPa for all samples heated up to 650 °C and less, and 75 MPa for the samples heated to 750, 800, and 900 °C. The axial strain was measured using a single strain gauge (Vishay Micro-Measurements 125UT general purpose strain gauge) glued halfway along the length of the sample, this way we eliminate any deformation of the load-train from the recorded data. A lubricating wax was applied to either end of the samples to limit any stress due to friction between the rock and the pistons (Bésuelle et al., 2000).

3.2.5 *Uniaxial compressive strength (UCS) measurements*

UCS tests were conducted on the 11 oven-dry (under vacuum at 40 °C for at least 24 h) granite samples at a constant strain rate of 10^{-5}/s until failure, whilst measuring axial stress and strain (Figure 3.7b).

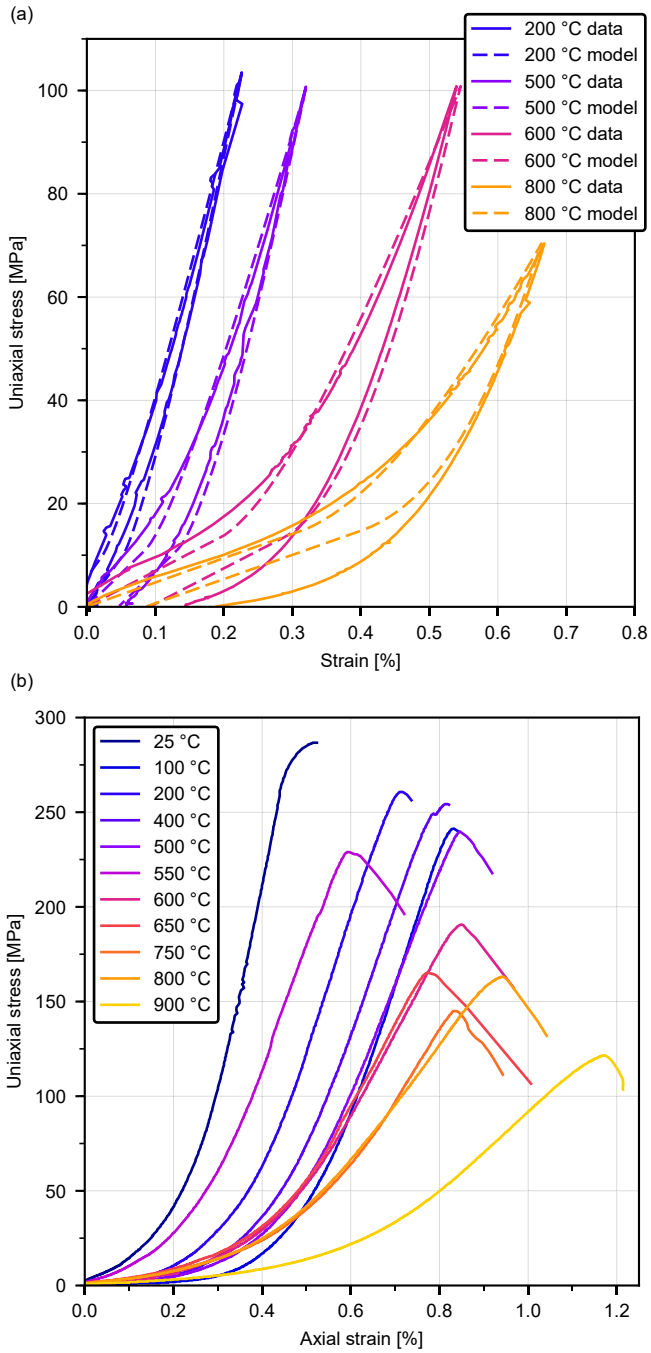

Figure 3.7: Mechanical testing of thermally stressed Garibaldi Grey Granite samples. (a) Axial stress against axial strain during uniaxial stress-cycling tests on samples heated to 200, 500, 600, and 800 °C. The 200, 500, and 600 °C samples were loaded to a maximum uniaxial stress of around 10 MPa, the 800 °C sample was loaded to a maximum stress of around 75 MPa. (b) Axial stress against axial strain for all uniaxial compressive strength (UCS) tests on the thermally stressed samples (25–900 °C).

Strain was calculated using data from a linear variable differential transducer (LVDT) that monitored the displacement of the piston relative to the static base plate. Displacement measured by the LVDT was corrected for the strain accumulated in the load-train. For all UCS tests, a lubricating wax was again applied to both ends of the sample to limit friction at the piston/sample interfaces. The measured values of UCS (Table 3.2) are shown in Figure 3.6b as a function of thermal stressing temperature. UCS generally decreases with temperature. For example, UCS was decreased from 287 MPa for the ambient sample to 122 MPa for the sample thermally stressed to 900 °C (Figure 3.6b). As for the porosity and v_P measurements (Figure 3.6a), we observe a notable change in UCS from 550 to 600 °C (Figure 3.6b).

3.3 MICROMECHANICAL MODELLING

3.3.1 *Upscaling using the Ashby and Sammis 2D sliding wing crack model*

Brittle failure is the result of the propagation, interaction, and coalescence of microcracks and as such, micromechanical models of rock failure, which are based on the work of Griffith (1921), must consider microcrack geometry. This is achieved by considering a certain microcrack density, often expressed as a single damage parameter, which evolves during brittle deformation. One of the most popular models is the 2D sliding wing crack model of Ashby and Sammis (1990). This model is based on linear elastic fracture mechanics applied to the failure of rocks in compression (Baud et al., 1996; Horii and Nemat-Nasser, 1986; Kemeny and Cook, 1991). It considers a planar far-field stress in which there is a microcrack of half-length c at a given angle to the maximum principal stress direction. As the far-field axial stress increases, the Coulomb condition for sliding is satisfied. The microcrack tips locally concentrate the tensile stress, which increases further with frictional slip along the microcrack. In this case, wing cracks may nucleate from each tip when the mode I (opening) stress intensity factor reaches a critical value, noted K_{IC}. The wing cracks then follow a curved path before aligning with the principal stress direction.

The sliding wing crack model (Ashby and Sammis, 1990) was developed for brittle failure of a material containing a certain density of microcracks, which propagate in the direction of the major principal stress if the material is loaded in compression. For geometrical simplicity, the model considers that all microcracks have the same half-length and the same orientation of 45 ° to the principal stress direction. Then, if the wing cracks become sufficiently proximal, microcrack interactions will lead to microcrack coalescence and, ultimately, macroscopic failure. For uniaxial compression, the sliding wing crack model (Ashby and Sammis, 1990) gives an expression for the applied

stress σ_1 as a function of μ, the friction coefficient of the fracture, K_{IC}, the fracture toughness, c, the crack half-length, D the damage parameter, and D_0 the initial damage parameter Equation 3.7b:

$$\sigma_1 = \frac{\frac{C_4}{\cos(45°)} \frac{K_{IC}}{\sqrt{\pi c}} \sqrt{\sqrt{\frac{D}{D_0}} - 1 + \frac{0.1}{\cos(45°)}}}{1 + \frac{\sqrt{\pi D_0}}{1-\sqrt{D}} \left(\sqrt{\frac{D}{D_0}} - 1 \right)} \tag{3.7}$$

Where $C_4 = \frac{\sqrt{30}\cos(45°)}{\sqrt{1+\mu^2}-\mu}$. The initial damage parameter D_0 is proportional to the 2D microcrack density, γ, of Walsh (1965) by Equation 3.8b, which is in turn a function of the microcrack half-length, c, and the microcrack number density, N_A (Equation 3.3).

$$D_0 = \frac{\pi}{2}\gamma \tag{3.8}$$

The applied stress, σ_1, is therefore a function of the microcrack density, as the interaction between microcracks is important in the deformation process. The model predicts that for a certain level of damage D (increasing with the wing crack length), the applied stress, σ_1, will reach a peak: the UCS of the rock. An cedure is therefore necessary to determine the UCS using this model.

However, the initial damage in the rock, D_0, is often ill-constrained in studies that use the Ashby and Sammis model (Ashby and Sammis, 1990) as it requires knowledge of the microcrack distribution. Here we determine D_0 from the rock microstructure by processing optical micrographs to calculate the mean microcrack length ($2c$) and number density (N_A). From the mean values of N_A and c, D_0 was calculated using Equation 3.3 and Equation 3.8 for each thin section (Table 3.3). We include all cracks, regardless of their orientation, in the calculation of D_0, and the sliding crack model assumes that they are all at 45 ° to the stress direction. We find that the unheated granite has a D_0 of 0.098, which is comparable to that of Westerly Granite, a granite with similar porosity and crystal size, at 0.13 (Brace et al., 1966). D_0 increases with temperature up to a temperature of 650 °C, after which D_0 remains roughly constant up to the maximum temperature of 900 °C (Table 3.3).

The sliding wing crack model (Ashby and Sammis, 1990) (Equation 3.8) was then used to predict the UCS of the 11 samples (Figure 3.8). The value of the fracture toughness K_{IC} and the friction coefficient, μ, for the unheated granite were inferred by fitting the wing crack model to triaxial deformation experiments on unheated, oven-dry samples of Garibaldi Grey Granite at confining pressures of 0, 5, and 10 MPa. The calculated values of K_{IC} and μ are 0.54 MPa.m$^{1/2}$ and 0.7, respectively, and were assumed constant for all samples. The values of D_0 that result from our microstructural analysis are given in Table 3.3. We highlight that under some conditions, 2D modelling may require particular care when applied to 3D fracture processes

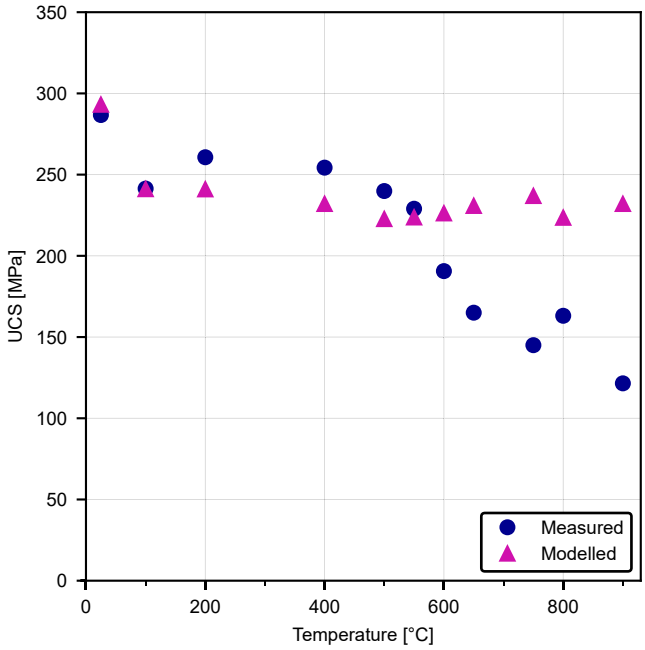

Figure 3.8: The laboratory-measured uniaxial compressive strength (UCS) and the UCS predicted by the sliding wing crack model (Ashby and Sammis, 1990) as a function of thermal stressing temperature for Garibaldi Grey Granite.

(Germanovich et al., 1994), however, for predicting the stiffness, mechanical behaviour, and failure of 3D rock samples, 2D modelling has been used to great effect in a range of rock types (Baud et al., 2014; Griffiths et al., 2017b; Heap et al., 2016).

3.3.2 *Downscaling using the David et al. (2012) sliding crack model for the stiffness of damaged rock*

The stiffness of rock is strongly influenced by microcracking (see Figure 3.7). During the uniaxial loading of microcracked rock, the stress-strain curves are characterized by a strong non-linearity and hysteresis (David et al., 2012; Walsh, 1965). With increasing uniaxial load, the first microcracks to close are those perpendicular to the direction of the applied stress, followed by those at lower angles. Once microcracks are closed they may begin to slide if the friction between the faces of the crack is overcome, meaning that the rock is always less stiff than it would be in the absence of microcracks (David et al., 2012; Walsh, 1965). The Walsh 2D sliding crack model (Walsh, 1965) provides the stiffness of a microcracked material during uniaxial compression as a function of the mean microcrack and microcrack density. The model was recently extended by David et al. (2012) to include the unloading of the material.

Thermal stressing temperature [°C]	D_0	$\frac{K_{IC}}{\sqrt{\pi c}}$ [MPa]	Predicted UCS [MPa]
Ambient	0.098	58.0	293.0
100	0.127	51.5	241.0
200	0.137	52.6	240.9
400	0.142	51.2	231.9
500	0.152	50.1	222.6
550	0.161	51.2	223.6
600	0.205	55.6	226.1
650	0.215	57.5	230.7
750	0.209	58.5	236.8
800	0.220	56.0	223.4
900	0.211	57.5	231.9

Table 3.3: The calculated values of the initial damage parameter D_0, $\frac{K_{IC}}{\sqrt{\pi c}}$, and the predicted uniaxial compressive strength (UCS) provided by the sliding wing crack model (Ashby and Sammis, 1990) for temperatures between ambient and 900 °C.

For a given uniaxial stress, a microcrack may be open, closed, or closed and sliding. If the microcrack is open or sliding, then it contributes to the stiffness of the rock. The contribution of the microcrack to the bulk Young's modulus depends on its aspect ratio, its orientation with regards to the applied stress direction, and the friction coefficient on the crack face. During loading, the effective Young's modulus is a function of the intact Young's modulus of the uncracked rock E_0, and the sum of the compliances of the open (C_{open}) and sliding ($C_{sliding}$) microcracks (Equation 3.9):

$$E_{loading} = \frac{E_0}{1 + C_{open} + C_{sliding}} \tag{3.9}$$

The Young's modulus during unloading is a function of the intact Young's modulus of the uncracked rock E_0, and the sum of the compliances of the open (C_{open}) and reverse sliding ($C_{reverse}$) microcracks (Equation 3.10):

$$E_{unloading} = \frac{E_0}{1 + C_{open} + C_{reverse}} \tag{3.10}$$

During loading, a microcrack may begin sliding once the applied stress reaches a certain value, depending on the crack orientation with regards to the stress and the friction coefficient. The stress-strain curve is initially steeper than previous because, for the microcracks to slide back towards their initial position, the Coulomb criteria along

the crack face must be fulfilled in the opposite direction, thereby overcoming resistance to frictional sliding twice. Microcracks that were closed and sliding are now stuck and do not contribute to the effective Young's modulus. As a result, the slope of the curve at the very beginning of unloading is closer to the Young's modulus of the uncracked rock (Walsh, 1965). Microcracks begin sliding in the opposing direction only once the applied stress is sufficiently decreased and as such, this model predicts the hysteresis that we observe experimentally (Figure 3.7a).

To infer the microcrack density and aspect ratio of microcracks in the thermally stressed granite samples, we used the (David et al., 2012) to fit our uniaxial cyclic loading experimental curves (Figure 3.7a). The intact Young's modulus, equal to 65 GPa, was provided by the slope at the beginning of the unloading cycle. For comparison, the Voigt-Reuss-Hill average estimate (Hill, 1952) of the intact Young's modulus is 76 GPa if we assume: no porosity; a mineralogical composition in volume of 45 % quartz, 45 % feldspar and 10 % mica; and the elastic moduli of the minerals provided from Mavko et al. (2009). The Voigt-Reuss-Hill estimate is similar but greater than the measured value as it does not account for any microstructural elements which may contribute to rock stiffness (e.g. grain boundaries or pressure-independent microporosity), justifying our value of 65 GPa for the intact Young's modulus. The friction coefficient was set to 0.7, as for our UCS modelling. The microcrack aspect ratio and microcrack density were then selected manually to best fit the shape of the stress-strain curve. Figure 3.7a shows examples of the experimental curves (solid curves) and the best-fit curves (dashed curves) predicted by the model.

The inferred microcrack aspect ratios using the David et al. (2012) range from 2.4×10^{-4} to 5×10^{-4}, within the typical 10^{-3}–10^{-4} range for microcracks (Kranz, 1983) (Figure 3.9). The inferred microcrack densities range from 0.5 to 4.9 (noted γ_{mo} in Figure 3.9) and are similar to those inferred by David et al. (2012) from uniaxial cycling data of thermally stressed La Peyratte granite, which range from 0.2 for an intact sample to 4.4 for a sample heated to 600 °C. We see that both the inferred microcrack densities and aspect ratios increase with temperature, showing a marked increase between 550 and 650 °C (Figure 3.9).

3.4 DISCUSSION

3.4.1 *Automated procedure for quantifying microcrack characteristics*

We present here a new automated procedure (described in detail in Appendix A) for rapidly processing optical micrographs of microcracked materials to quantify their microcrack characteristics. We cal-

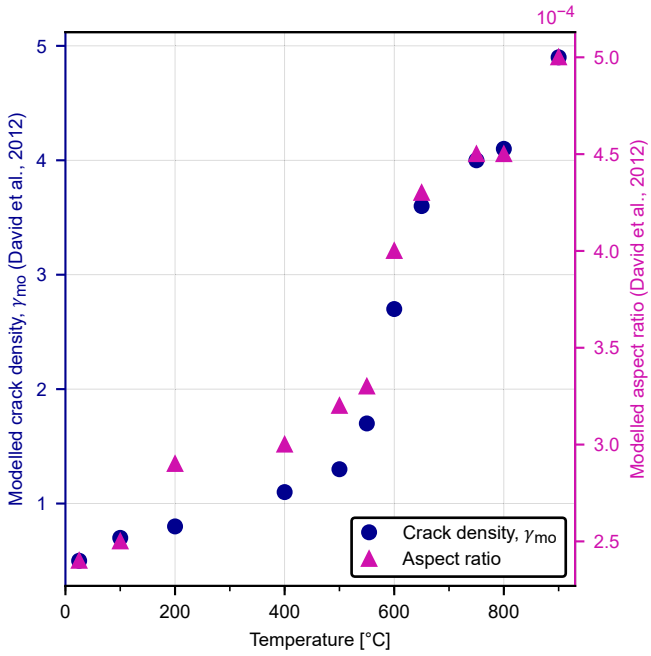

Figure 3.9: The mean microcrack density (γ_{mo}) and aspect ratio in the thermally stressed Garibaldi Grey Granite, as inferred from the rock compressibility using the sliding crack model (David et al., 2012), against thermal stressing temperature. Some example experimental and modelled stress-strain curves are shown in Figure 3.7a.

culate the mean microcrack length and number density to obtain the mean microcrack density (Equation 3.2). Further, we can create heat maps showing the spatial distribution of microcracks and their lengths (Figure 3.2). We found that for a suite of thermally microcracked granites, our automated procedure provides microcrack characteristics in very good agreement with those measured using widely-used stereological techniques (Underwood, 1967) (Figure 3.5). Our program therefore offers a reliable method to quickly and robustly determine microcrack characteristics of microcracked granites from optical micrographs. Although automated programs exist that can extract microcrack characteristics from images (e.g. Arena et al. (2014) and Delle Piane et al. (2015)) they, so far, have relied on SEM images, which are more time-consuming to collect and more expensive than optical microscope images.

We have shown that our automated image analysis procedure works for optical micrographs of granite. To explore whether our algorithm works well for rock types with different microstructures, we analysed two additional thin sections: a deformed sample of Darley Dale Sandstone and an intact (but naturally microcracked) andesite from Volcán de Colima (Mexico). Unlike the granites analysed herein, the Darley Dale Sandstone sample (Figure 3.10a) contains pores (high aspect ratio features) and was deformed triaxially in the brittle regime until failure (under a confining pressure of 50 MPa and a pore fluid pressure (distilled water) of 20 MPa) in an experiment from Heap et al. (2009b). In this regime, failed samples of Darley Dale Sandstone typically show a shear band (that hosts intensely comminuted grains) and microcracks preferentially aligned to the direction of maximum principal stress outside the band (Wu et al., 2000). We find that the image processing performs well outside the shear band, isolating inter- and intra-granular microcracks (Figure 3.10b). We notice that the extent of microcracking increases with proximity to the shear band (Figure 3.10b). Inside of this shear band, however, no microcracks are located because the shear band constitutes a zone of crushed grains, rather than discrete fractures (the quantification of crack density within areas of grain crushing, automatically or otherwise, is beyond the scope of this study).

The andesite from Volcán de Colima was selected for analysis because it contains a network of naturally occurring microcracks within a groundmass that hosts crystals and irregularly-shaped pores (Farquharson et al., 2015; Heap et al., 2014a) (Figure 3.11a). Our algorithm works well at locating microcracks and crystal boundaries are correctly ignored (Figure 3.11b). However, the algorithm is unable to distinguish between pore boundaries and microcracks, which appear similar in this case. The algorithm will therefore overestimate the microcrack density and would need further development to avoid counting pore boundaries as microcracks. An alternative solution would be

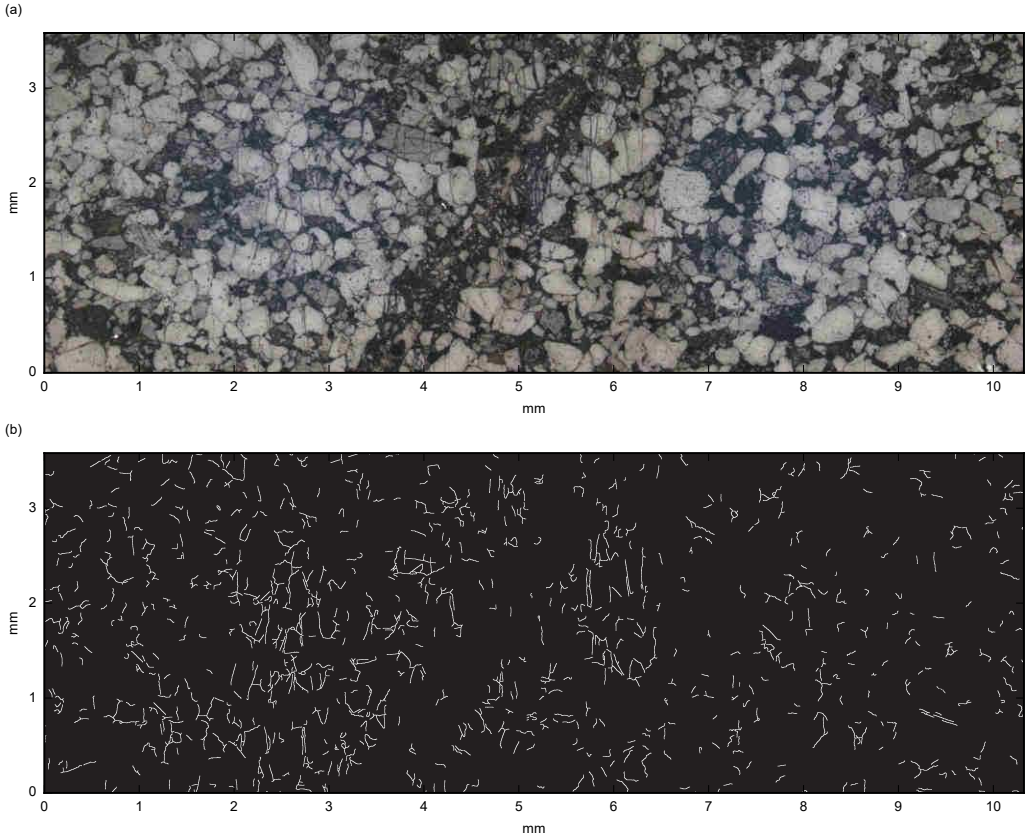

Figure 3.10: (a) Micrograph of Darley Dale Sandstone exhibiting strain localisation. The sandstone was deformed under a confining pressure of MPa and a pore pressure of 20 MPa pore pressure until failure (Heap et al., 2009b). (b) The results of the image analysis procedure. Cracks have been dilated to improve visibility for the reader.

to use SEM micrographs of the andesite, where pore boundaries will appear much sharper.

Overall, we find that the procedure works well for microcracked rocks and therefore is useful for a wide range of applications.

3.4.2 *Evolution of microcrack characteristics and physical properties with thermal stressing temperature*

Our microstructural characterisation of the thermally microcracked granites shows that the mean microcrack length increases slightly between the unheated and the 550 °C sample (from 56 to 72 μm), but the number of microcracks per unit area remains roughly constant (within the range of 64.4–79.6 mm^{-2}), as the thermal stressing temperature is increased to 550 °C (Figure 3.3). Between 550 °C and 600 °C, the microcrack number density sharply increases to 140.4 mm^{-2} and the mean length sharply decreases to 61 μm (Figure 3.3). The 2D microcrack density, γ, is proportional to both the microcrack number density and the square of the microcrack length (Equation 3.3). We found that the measured microcrack density increases with temperature up to 600 °C (from 0.062 for the unheated sample to 0.131 for the 600 °C sample) and is roughly constant above 600 °C (between 0.13 and 0.14) (Figure 3.5b).

For temperatures of up to 600 °C, the aforementioned increase in microcrack density manifests as changes to the rock physical properties. In agreement with previous studies of the physical properties of thermally microcracked granite, our measurements (Figure 3.6) show that porosity increases (Chaki et al., 2008; David et al., 1999; Géraud, 1994; Nasseri et al., 2009a; Reuschlé et al., 2006) whilst v_P decreases (Chaki et al., 2008; David et al., 1999; Nasseri et al., 2007; Reuschlé et al., 2006), and that the UCS decreases (Homand-Etienne and Houpert, 1989), as a function of thermal stressing temperature. Further, we observe a large increase in porosity and a large decrease in v_P and UCS between the samples heated to 550 and 600 °C (Figure 3.6). This latter observation is due to the alpha-beta transition of quartz at around 573 °C, which is accompanied by a large expansion in volume and therefore increased intergranular thermal stresses (Fredrich and Wong, 1986; Glover et al., 1995; Jones et al., 1997; Nasseri et al., 2007). Although we see a decrease in UCS with thermal stressing temperature, it is worth noting that the influence of thermal microcracks on compressive strength decreases significantly under confinement (Violay et al., 2017; Wang et al., 2013).

Above 600 °C, the physical properties (porosity, v_P, and UCS) continue to evolve (Figure 3.6) whilst the measured microcrack density is almost constant (Figure 3.5b). One explanation for the constant microcrack density between thermal stressing temperatures of 600 and 900 °C is that cracks grow to a maximum length, depending on the length-

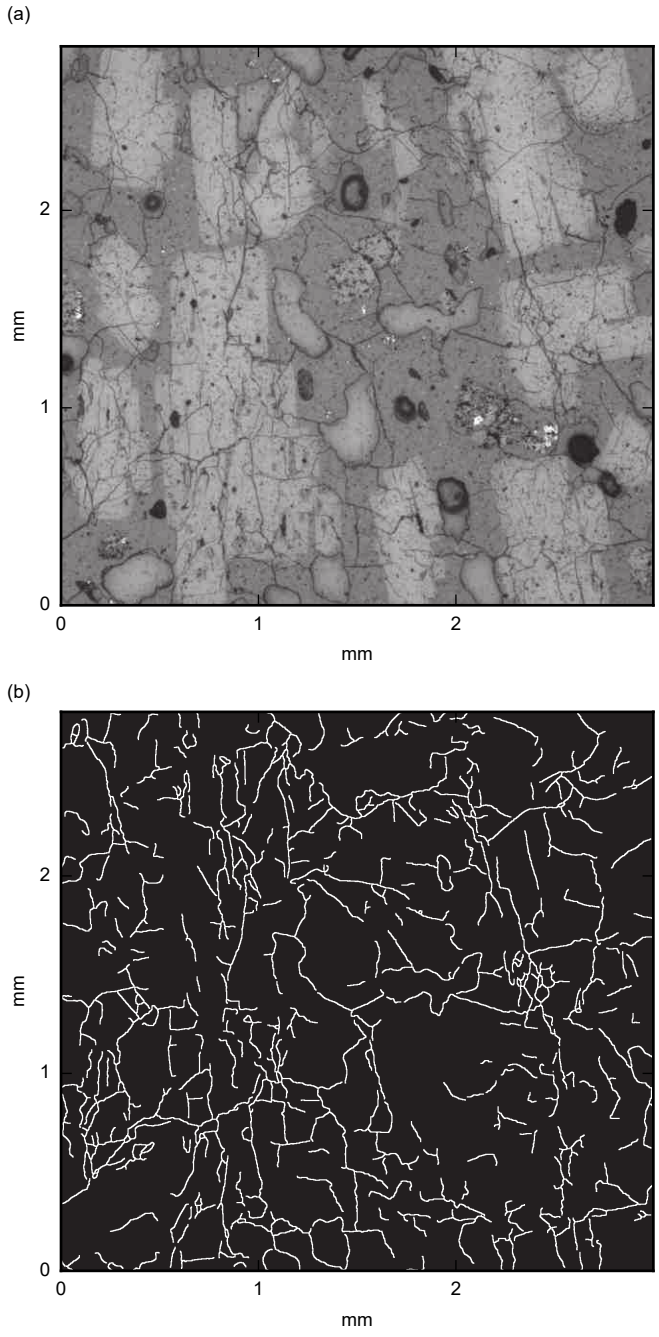

Figure 3.11: (a) Micrograph of thin section of andesite from Volcán de Colima (Mexico). (b) The results of the image analysis procedure. Cracks have been dilated to improve visibility for the reader.

scale of the microstructure (i.e. the grain size). This does not seem to be the case, however, as the mean microcrack length (~60 µm) is much lower than the average grain size (~1 mm, Figure 3.1a). The low value for the mean microcrack length, compared to the average grain size, is likely due to the presence of intracrystalline microcracks, which are usually much smaller than the crystals (Kranz, 1983). Another possible explanation for the constant measured microcrack density could be that, at these high temperatures, microcracks are growing into one other, creating a mesh of microcracks that are considered as many individual microcracks by the algorithm. This would result in a decrease in microcrack length, but it would also result in an increase in microcrack number density, which we do not observe (Figure 3.3).

Another explanation for the low variation in the measured microcrack density values at high temperature could be that there is much less microcracking between temperatures of 600 and 900 °C. Although this explanation appears unlikely, because we observe changes to both the porosity and v_P between 600 and 900 °C (Figure 3.6a), perhaps there is an increase in the aperture of microcracks between these temperatures, rather than an increase in the number of microcracks. We can explore this further by plotting v_P and porosity as a function of the measured microcrack density (noted γ_{me} in Figure 3.12). We find that as microcrack density increases, we see a decrease in v_P and an increase in porosity. More specifically, the increase in porosity accelerates at higher microcrack densities. This observation could be explained by an increase in the aspect ratio of microcracks, rather than the growth of new microcracks. Indeed, studies of thermal microcracking in Westerly Granite suggest that thermal microcrack aperture greatly increases as temperature is increased above the quartz alpha-beta transition (Johnson et al., 1978; Nasseri et al., 2007). Qualitatively, we observe this increase in microcrack aperture in the micrographs of samples heated to temperatures of 600 °C and above. The increase in microcrack aperture would explain how physical properties (Figure 3.6) continue to evolve as temperature is increased beyond 600 °C whilst the microcrack density (a function of the number of microcracks and their lengths) shows much less variation (Figure 3.5b).

3.4.3 *Upscaling: predicting uniaxial compressive strength from microstructural measurements*

We used the Ashby and Sammis (1990) micromechanical model to predict the UCS of the thermally microcracked granite from the microcrack characteristics determined by our image analysis. These predicted values are in good agreement with our measured values for temperatures of up to 550 °C. However, the model overestimates the strength for 600 °C and above (Figure 3.8).

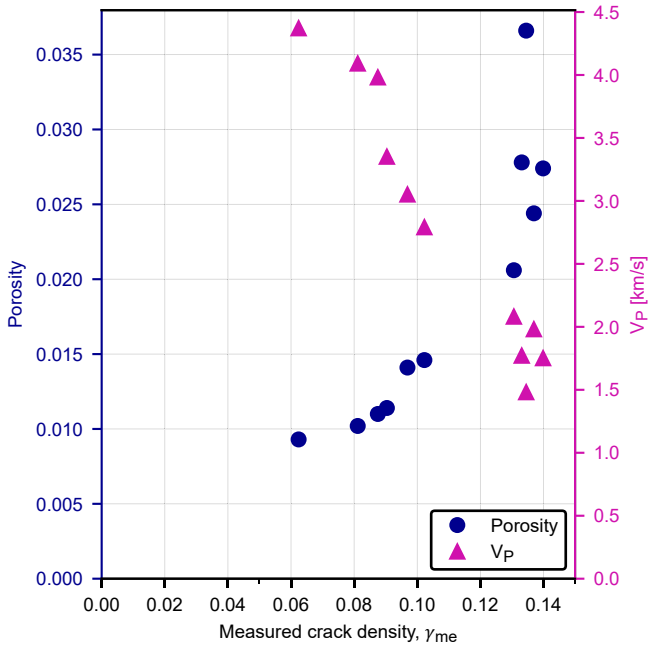

Figure 3.12: The measured porosity and P-wave velocity (v_P) of the 11 Garibaldi Grey Granite samples against the measured crack density.

Our quantitative microstructural analysis shows that the number of microcracks per unit area and the microcrack length do not change significantly from 600 to 900 °C (Figure 3.3). Thus, the calculated values of microcrack density (Figure 3.5b) and therefore D_0 (Figure 3.13) also do not change significantly from 600 to 900 °C. Since D_0 and c are the only model parameters we update for in Equation 3.7, if they show no variation then neither will the predicted UCS (as shown in Figure 3.8).

A possible explanation for the overestimation of UCS for temperatures of 600 to 900 °C is that the fracture toughness K_{IC}, which we kept constant at 0.54 MPa.m$^{1/2}$, decreases with temperature. Indeed, Nasseri et al. (2007) show the fracture toughness of thermally microcracked Westerly Granite to decrease with thermal stressing temperature from 1.43 MPa.m$^{1/2}$ at ambient temperature, to 0.22 MPa.m$^{1/2}$ at 850 °C. They observe a large decrease in K_{IC} for temperatures above that of the quartz alpha-beta transition, which in our case would lead to a decrease in the predicted UCS (Equation 3.5). Below 600 °C, the difference between the measured and predicted UCS due to smaller variations in K_{IC} is small and likely therefore hidden by the natural sample variability.

3.4.4 *Downscaling: predicting microcrack characteristics from stress cycling experiments*

We used the David et al. (2012) sliding crack to infer the microcrack characteristics of the rock using mechanical data from stress cycling experiments (example stress-strain curves are shown in Figure 3.7a). We find that the microcrack densities inferred from the model follow a similar trend to the direct measurements (Figure 3.13), despite a difference in magnitude. If we plot the inferred microcrack density (γ_{mo}) against the measured microcrack density (γ_{me}) (Figure 3.13b) we see a linear trend whereby the David et al. (2012) model overestimates the actual microcrack density systematically by a constant factor of around 55 (Figure 3.13). An explanation for the difference in magnitude could be that the model does not account for microcrack interactions, which may become significant at high crack densities. Indeed, David et al. (2012) also infers unexpectedly high microcrack densities from the sliding crack model and highlights the importance of selecting an adapted effective medium theory to account for microcrack interaction.

The inferred microcrack aspect ratio inferred from the sliding crack model increases with temperature, and continues to do so for temperatures above the alpha-beta transition in quartz (~573 °C). As discussed previous, this increase in aspect ratio could explain why we continue to measure large changes in the physical properties of the rock for thermal stressing temperatures higher than 600 °C (Figure 3.6) whilst the measured microcrack density (a function of the length and number of cracks) shows much less variation (Figure 3.5b).

3.5 CONCLUSION

To look specifically at the role of microcrack density on the stiffness and strength of rock whilst keeping other rock attributes constant (such as the mineralogy and grain size), we chose to study a fine-grained granite (Garibaldi Grey Granite) in which we induced varying degrees of thermal damage (up to a temperature of 900 °C). We then quantified the 2D microcrack density using a newly developed algorithm to process optical micrographs to provide measurements of the number of microcracks per unit area and their lengths.

We measured an increase in microcrack density with thermal stressing temperature for temperatures of up to 600 °C. Above 600 °C, the measured microcrack density within the granite is roughly constant. Measurements of the physical properties of the granite showed an increase in porosity and a decrease in v_P with heating temperature for temperatures of up to 900 °C. We therefore measure variations in physical properties where the microcrack density (a function of the number and length of microcracks) shows little variation. We suggest

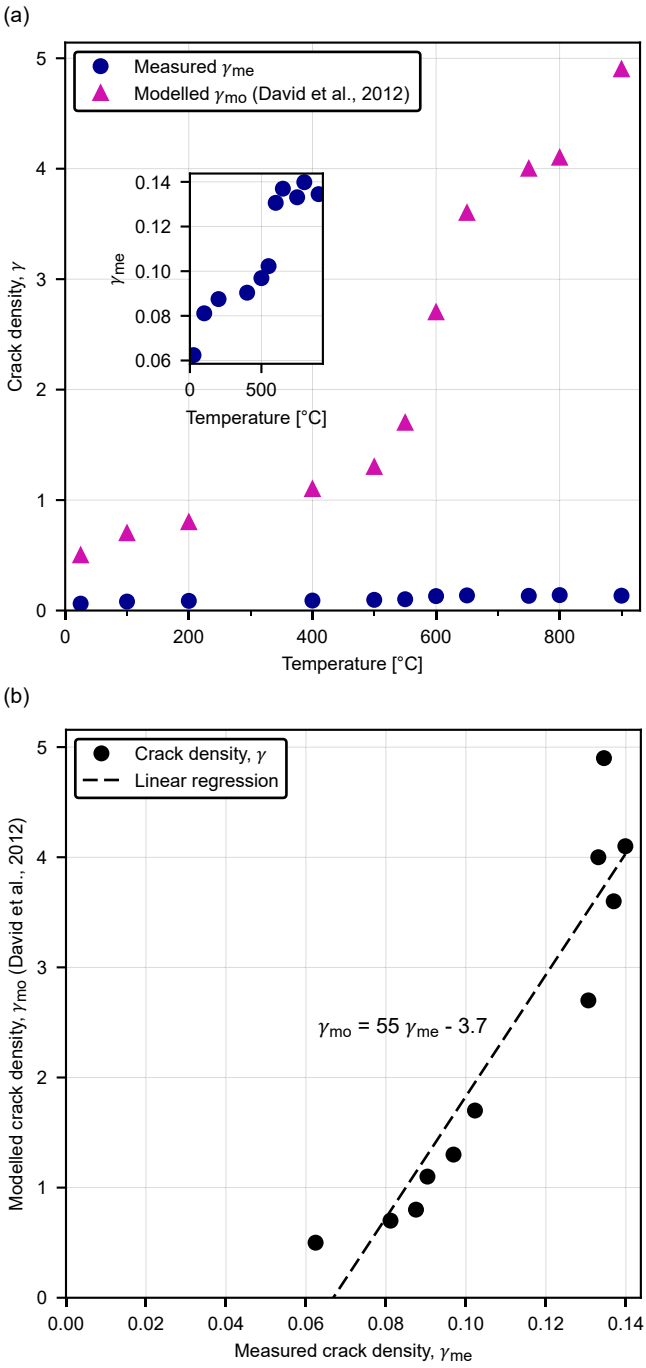

Figure 3.13: Comparison between crack densities from the David et al. (2012) sliding crack model and the optical measurements. (a) Inferred and measured microcrack densities as a function of thermal stressing temperature. Inset is a zoomed plot of the measured crack densities. (b) The inferred crack densities against the measured crack densities; the dashed line is their least squares linear regression.

that the continued evolution of physical properties at temperatures of

600 °C and above is due to a widening of existing microcracks rather than their formation or propagation.

Using a combined experimental and modelling approach, we bridge the gap between our measurements of microcrack density at the microscale, and our measurements of mechanical properties at the sample scale. First, we applied an upscaling approach using our calculated microcrack densities as an input in Ashby and Sammis (1990) sliding wing crack model to predict the uniaxial compressive strength of the granite. The UCS predictions are comparable with our laboratory measurements for granite thermally stressed to temperatures of below 600 °C. For the granite heated to 600 °C and above, the compressive strength is overestimated by the model, perhaps due to a decrease in fracture toughness above the alpha-beta transition of quartz. Next, we took a downscaling approach by using the sliding crack model of David et al. (2012) to infer microcrack density and mean microcrack aspect ratio from laboratory measurements of stiffness. Whilst the inferred microcrack density (γ_{mo}) is proportional to the measured microcrack density (γ_{me}), the inferred values are greater by a factor of around 55 (Figure 3.13). A possible explanation for the difference is that the model does not account for microcrack interactions, which amplify their influence on rock stiffness.

Although we focused on the case of a fine-grained granite in this study, we propose the use of our image analysis procedure (see Appendix A for details) for quantifying microcrack damage in rock types with vastly different microstructures. To demonstrate the power of the model, we analysed optical micrographs of a triaxially deformed sandstone (Darley Dale Sandstone) and a naturally microcracked andesite (from Volcán de Colima). Our method can accurately find the microcracks in both samples, although it falls short of characterising the grain crushing within the shear band of the sandstone sample, and treats some pore boundaries as microcracks in the andesite sample. Nevertheless, we anticipate that the image processing algorithm presented here will emerge as a useful tool in the quantification of microcrack characteristics in a range of microcracked materials and may be used provide input images for dedicated fracture pattern quantification tools such as FracPaq (Healy et al., 2017).

Through the measurements and modelling presented in this study, we demonstrate how the micro scale can inform on the laboratory or sample scale, and vice-versa. Uniting laboratory scale and microstructural observations through constrained up- and downscaling methods permits a deeper understanding of the mechanical behaviour of rocks.

4

THERMAL MICROCRACKING IN GRANITE

The influence of temperature on rock is of interest to a wide range of geoscience and engineering domains. Where thermal stresses result in microcracking, these small cracks have a strong influence on the physical, thermal, transport, and mechanical properties of rock. Thermal microcracking is significant for underground resource management, including at sites for radioactive waste disposal and geothermal reservoirs.

Often, laboratory studies of thermal microcracking have quantified microcrack damage through measurements of the physical properties of rock before and after heating, and a common metric has been the ultrasonic wave velocity. For the monitoring of thermal microcracking in real-time, Acoustic Emission (AE) monitoring has been used to observe the onset of AE due to heating. The influence of repeated thermal stressing, and thermal stresses during to cooling have had less attention. Where velocity measurements have been made on rock samples at elevated temperatures, they have generally shown the velocity of rock to decrease with temperature, underlining the need to understand how rock properties are changed at temperature conditions seen within Earth's crust.

To monitor thermal microcracking in granite during repeated heating and cooling cycles, the newly developed apparatus described in Section 2.1 is first put to use on the well-studied Westerly Granite. This study is followed by a comparison with results of the same procedure on two other granites of different grain sizes. This chapter concludes with the study of the influence of thermal stressing on the properties of granite. For which, measurements of the physical, mechanical, transport, and thermal properties were made on a suite of variably thermally-stressed samples, for comparison with results of the AE and velocity monitoring experiments.

4.1 THERMAL MICROCRACKING IN WESTERLY GRANITE MONITORED USING DIRECT WAVE VELOCITY, CODA WAVE INTERFEROMETRY AND ACOUSTIC EMISSIONS

The following work has been published in:

L. Griffiths, O. Lengliné, M. J. Heap, P. Baud, and J. Schmittbuhl (2018). 'Thermal Cracking in Westerly Granite Monitored Using Direct Wave Velocity, Coda Wave Interferometry, and Acoustic Emissions.' In: *Journal of Geophysical Research: Solid Earth* 0.0. ISSN: 2169-9313. DOI: 10.1002/2017JB015191

The influence of temperature on the physical and mechanical properties of rock is of interest to many areas of Earth science and engineering, and at a wide range of scales. In granite, the thermal expansion of minerals results in the build-up of thermal stresses during heating and may lead to thermal microcracking (Kranz, 1983). Thermal microcracking has been shown to increase porosity (Chaki et al., 2008; David et al., 1999; Nasseri et al., 2007; Reuschlé et al., 2003; Wang et al., 2013), increase permeability (Chaki et al., 2008; Glover et al., 1995; Jones et al., 1997; Meredith et al., 2012; Wang et al., 2013) and reduce uniaxial strength (Nasseri et al., 2007) and stiffness (David et al., 2012; Walsh, 1965).

Fredrich and Wong (1986), for example, studied the micromechanics of thermal cracking in three crustal rocks, including Westerly Granite, in which—through microscopic observation of a suite of thermally stressed samples—they found that thermal microcracking occurs from temperatures within the range of 100–165°C and found that all crystal boundaries were cracked in the granite heated to 500 °C. Using a 2D square inclusion model, they link these threshold temperatures for thermal microcracking to the thermal expansion mismatch between the inclusion and the surrounding material. In another study of thermal microcracking in granite, Thirumalai and Demou (1974) measured the thermal dilation of two granites (Halecrest and Charcoal) during cyclical heating and cooling. They observed a permanent dilation of the granites following the first cycle, due to an increase in thermal microcrack porosity. However, they found the magnitude of microcracking with subsequent cycles to be much diminished, with no permanent dilation following the third heating/cooling cycle.

In the laboratory, a common technique to detect microcracking is acoustic emission (AE) monitoring. AE are transient elastic waves produced during microcrack extension, and AE monitoring has been applied to thermal microcracking in granite (Chen et al., 2017; Glover et al., 1995; Jones et al., 1997; Siratovich et al., 2015; Todd, 1973). For example, Glover et al. (1995) heated La Peyratte granite at 1 °C/min to 900 °C while monitoring AE and observed an onset of AE at around

80 °C, and a spike in the AE rate at 573 °C. Around 573 °C corresponds to the temperature of the alpha/beta transition of quartz at room pressure, which is accompanied by a marked thermal expansion, thus increasing thermal stresses and leading to further thermal microcracking. Todd (1973) also used AE monitoring to study the influence of multiple heating and cooling cycles (to a maximum temperature of 300 °C) on Westerly Granite. Todd (1973) observed AE mostly as the unheated rock was heated for the first time; very few AE were observed during cooling or during repeated thermal stressing cycles. Another example of AE monitoring during cooling (which we note are rare in the literature) is a study by Browning et al. (2016), who monitored thermal microcracking in volcanic rocks (a basalt and a dacite). Browning et al. (2016) found the vast majority of AE to occur during cooling, which they attribute to thermal microcracking, underlining the merit for further study of AE monitoring during cooling.

The P (pressure) wave and S (shear) wave ultrasonic velocities of rock (herein v_P and v_S, respectively) are particularly sensitive to microcracking and have been shown to permanently decrease when the build-up of thermal stresses leads to thermal microcracking (Chaki et al., 2008; David et al., 1999; Johnson et al., 1978; Jones et al., 1997; Nasseri et al., 2007). David et al. (1999) found the v_P of La Peyratte granite to decrease from roughly 5.5 to 3.7 km/s when heated to 450 °C and cooled back to room temperature. The same thermal stressing procedure was applied by Nasseri et al. (2007) to Westerly Granite, following which they observed a decrease in v_P from roughly 4.5 to 3.0 km/s. There is, however, a lack of direct wave velocity measurements performed above room temperature in the literature. Examples include Zappone and Benson (2013), who measured v_P and v_S of a metapelite from the southern Alps in northern Italy during heating to 750 °C under high confining pressures of 200, 300, and 400 MPa, revealing the temperature of the quartz α/β transition. To examine the influence of temperature on the matrix velocity of rock, Kern (1982) measured v_P and v_S of samples of various rocks under a high confining pressure of 600 MPa and temperatures of up to 600 °C. Confining pressure was applied with the aim of closing all microcracks, and the wave velocities were seen to decrease with increasing temperature. Wang et al. (1989) measured v_P of Westerly Granite during heating to 300 °C and cooling under confining pressures of 7, 28, and 55 MPa, finding v_P to decrease with increasing temperature, from ~4.5 km/s at room temperature to ~3.4 km/s at 300 °C. Wang et al. (1989) found that for all confining pressures v_P decreased during heating and increased during cooling, returning to the velocity of the unheated rock.

Grêt et al. (2006) used another method, coda wave interferometry (CWI), to measure the influence of temperature on the wave velocity of Elberton Granite when heated to 90 °C. CWI is a technique to infer small changes in wave velocity from assessments of small relative

delays in multiply scattered waves using high-resolution cross correlations of waveforms (Snieder, 2002, 2006). Grêt et al. (2006) observed increasing time delays during heating, corresponding to an apparent decrease in wave velocity. Between 70 and 90 °C they observed a strong nonlinear decrease in the apparent velocity with temperature, a result of thermal microcracking. During a second heating and cooling cycle, they observed a reversible thermo-elastic response of the waveforms to temperature. CWI, however, has yet to be used to monitor changes in rock microstructure resulting from thermal microcracking when heated to and cooled from higher temperatures.

Here we use a new approach, combining AE monitoring, measurements of v_P, and CWI to monitor microstructural changes in Westerly Granite during three heating and cooling cycles to a maximum temperature of 450 °C. Through repeated heating and cooling cycles, we quantify the influence of the irreversible (thermal microcracking) and reversible (thermo-elastic deformation) changes in microstructure on the velocity of granite.

4.1.1 *Materials and methods*

4.1.1.1 *Materials*

We selected Westerly Granite (from Rhode Island, USA) for this study as its physical and mechanical properties are well known, near isotropic (Lockner, 1998), and have been shown to exhibit permanent changes—through thermal microcracking—when heated (Nasseri et al., 2009a; Nasseri et al., 2007; Wang et al., 1989; Yong and Wang, 1980). Westerly Granite has a mineralogical composition in volumetric fraction of 27% quartz, 36% microcline, 30% plagioclase, 6% phyllosilicates, and 1% others, and a mean crystal size of 0.75 mm (Meredith and Atkinson, 1985). We show a backscattered scanning electron microscope (SEM) micrograph of a thin section of Westerly Granite in Figure 4.1. Labeled are grains of quartz (Qtz), microcline (Mc), plagioclase (Pl), and phyllosilicate (here biotite, Bt).

We cored three cylindrical samples of Westerly Granite in the same orientation and precision-ground their end-faces flat and parallel (diameter of 20 mm and a nominal length of 40 mm). Samples were oven-dried at 40 °C in-vacuo for at least 48 hr prior to experimentation. We assume that the granite block is sufficiently homogeneous and isotropic (Lockner, 1998) and that the influence of thermal stressing is sufficiently repeatable to compare measurements on different samples cored from the same block.

4.1.1.2 *Experimental procedure*

EXPERIMENTAL SETUP The experimental setup (Figure 4.2)–designed specifically for acoustic measurements at high temperature–consists

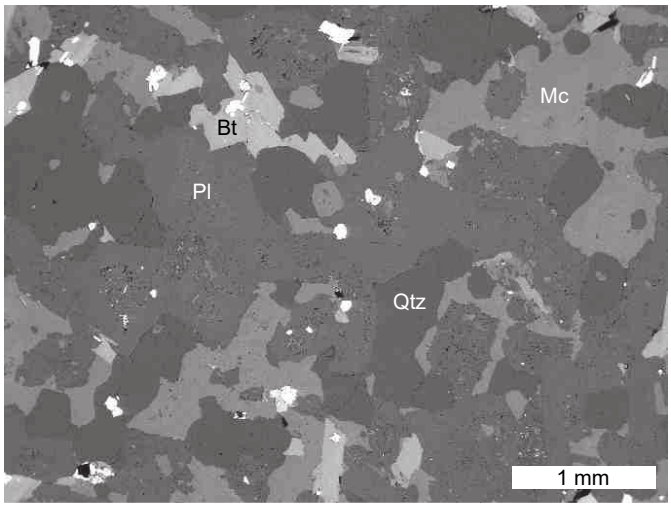

Figure 4.1: Backscattered scanning electron microscope micrograph of unheated Westerly Granite. Labeled are grains of quartz (Qtz), microcline (Mc), plagioclase (Pl), and phyllosilicate (here biotite, Bt).

of a LoadTrac II servo-controlled uniaxial press, in which a rock sample is held between two vertical pistons made from heat resistant stainless steel (grade 310). A GSL-1100X tube furnace (MTI Corporation), which has a constant temperature zone of 80 mm in length, surrounds the sample. A custom-built air-cooling system is attached around the top of the upper piston to avoid exposing the AE transducer embedded within the upper piston and the load cell to potentially-damaging high temperature.

THERMAL LOAD In each experiment, a sample is subject to three heating and cooling cycles, at rate of 1 °C/min, with a dwell time of 2 hr at the maximum temperature of 450 °C. The maximum temperature is limited by the operating range of the acoustic transducers within the furnace (Figure 4.2)). We performed in situ measurements of P wave traveltime and CWI on the first Westerly Granite sample, and for a second sample we monitored AE. During both experiments, the furnace temperature was recorded at 10 mm from the sample surface. During the first experiment (the velocity measurements), we also recorded the temperature at the center of the sample using a thermocouple (of diameter 1.5 mm) inserted through a 1.7 mm hole drilled radially, halfway along the sample length. A third granite sample was subject to the same thermal stress cycling procedure, and we performed "static" measurements of v_P and v_S at room temperature using a separate dedicated device before and after each cycle, for comparison with our in situ measurements.

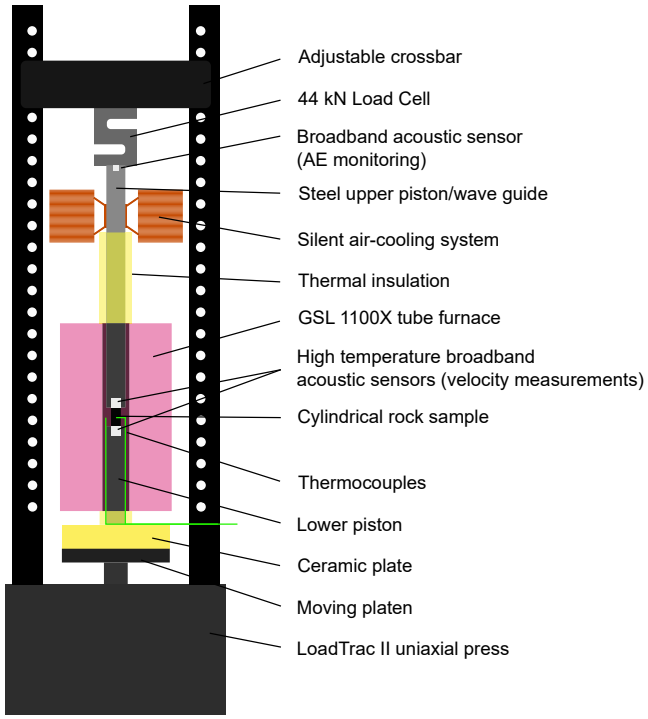

Figure 4.2: Schematic of the experimental setup for acoustic emission monitoring and velocity measurements. The setup consists of a LoadTrac II uniaxial press and a GSL 1100X tube furnace. For AE monitoring, a single acoustic sensor is embedded within the top of the upper piston. For CWI and P wave travel time measurements, a pair of high-temperature sensors are in direct contact with opposing ends of the sample.

4.1.2 *Measurements*

4.1.2.1 *P-wave velocity*

For the in situ v_P measurements we used two acoustic sensors, a source and receiver, housed within each piston (Figure 4.2). The sensors were in direct contact with opposing faces of the granite sample and coupling was ensured, and kept constant by, a servo-controlled axial force of 100 N (~0.3 MPa) on the sample (coupling otherwise oscillates dramatically as the pistons thermally expand and contract). The sensors were S9215 high-temperature sensors from Physical Acoustics, which have a resonant frequency of 100 kHz (52 dB) and an operating frequency range of 80–560 kHz. During the three heating and cooling cycles, a signal generator connected to the upper transducer emitted a 200 kHz sinusoidal pulse every 50 ms and simultaneously triggered a National Instruments BNC 2110 acquisition card to record the preamplified (+40 dB preamplifier with a flat response above 2 kHz) voltage across the receiving transducer. Each recorded waveform was 2 ms in duration: 4000 samples at a sampling rate of 2 MHz, including a pretrigger recording time of 0.05 ms. The acquisition was repeated 50 times in succession, and the 50 recorded waveforms were stacked to increase the signal-to-noise ratio. We set a waiting time of 10 s between stacks, and acquisition continued throughout the three heating and cooling cycles.

To calculate the shift in P wave arrival time, we spliced the first 30 μs of the recorded waveforms and calculated the cross-correlation functions (in the frequency domain) between pairs of waveforms throughout the experiment. Next, in the time domain, we performed a piecewise quadratic interpolation of each cross-correlation function around its maximum, and we calculated the time shift at the maximum of the newly interpolated cross-correlation function. We calculated the cumulative shift in P wave arrival time with experiment time to obtain the time shift with respect to the initial waveform.

At room temperature, and on a separate, dedicated, and calibrated setup, we made static measurements of v_P and v_S at ambient pressure and temperature, both before and following heating and cooling. We used two pairs of piezo-transducers in contact with opposing faces of the sample (each pair oriented either parallel or perpendicular to the sample length for P wave and S wave, respectively), with one emitting an ultrasonic wave (excited by a sinusoidal pulse: 700 kHz for P wave and multiple frequencies within the range of 100–500 kHz for S wave), and the other receiving. The velocities were calculated from the direct wave arrival times observed on an oscilloscope. Using the static v_P measurement of the unheated granite prior to heating and the shift in P wave arrival time measured during heating and cooling, we calculated v_P during the entire experiment.

4.1.2.2 *Coda Wave Interferometry (CWI)*

CWI considers an ultrasonic wave that becomes scattered and reflected multiple times by the boundaries of, or the heterogeneities within a medium (Snieder, 2002). The resulting waveform at a given location is the contribution of many scattered waves that have traveled along different raypaths. Following changes in the medium—which include velocity changes, the displacement of scatterers due to thermal or mechanical deformation, and the development of new scatterers—the traveltime of these scattered waves becomes delayed (Snieder, 2006). In the case of a velocity perturbation, Snieder (2002) showed that the shift in traveltime of the wave is proportional to the time traveled (Equation 4.1) and therefore may be significantly greater than the delay we observe in the direct arrivals.

$$\frac{\delta v}{v} = -\frac{\delta t}{t} \tag{4.1}$$

The scattered waves arrive later or earlier following a change in velocity, and the resulting waveform becomes elongated (apparent decrease in velocity) or compressed (apparent increase in velocity) in time. For a given velocity change, the ratio between time shift and traveltime is constant (Equation 4.1): the stretching of the waveform increases with increasing traveltime as later arrivals have traveled for longer at the new velocity.

There are two main methods used in CWI to calculate the relative time shift between waveforms. The first—and original—method involves calculating the cross-correlation function between the two waveforms in windows centered at different traveltimes (Poupinet et al., 1984; Snieder, 2002). The lag of the maximum of each cross-correlation function provides the time shift for a given traveltime, and their linear regression yields the relative time shift, $\frac{\delta t}{t}$. However, a potential problem with this method is that it approximates the time shift as a constant within each window (Larose and Hall, 2009).

The second approach for calculating $\frac{\delta t}{t}$–and the method used herein–is the stretching method, whereby we apply an array of relative time shifts to the first waveform and we select the value of $\frac{\delta t}{t}$ for which the stretched first waveform correlates most with the second (Larose and Hall, 2009; Sens-Schönfelder and Wegler, 2006). Following Larose and Hall (2009), we use a spline interpolation in the time domain to stretch each waveform, noted h_k, onto a series of new time vectors $t(1-a)$, where a is a value of the relative time shift, $\frac{\delta t}{t}$. We then calculate the cross-correlation function (in the frequency domain), between a reference waveform ho and the shifted waveform $h_k[t(1-a)]$, and the relative time shift is equal to the value of a for which the peak of the cross-correlation function is maximal, noted $a_{k,0}$ (T is the length in time of the waveforms, here 0.5 ms).

In our experiments, the correlation between the reference waveform, h_0, and subsequent waveforms, h_k, deteriorates with temperature due to the strong perturbation of the medium. To counter this, we calculate instead the relative time shift $a_{k,k-1}$ between consecutive waveforms h_k and h_{k-1}. In this case, a scaling factor is required to infer the relative time shift with respect to the reference waveform, $a_{k,0}$ (Equation 4.2). The scaling factor is a function of the previous relative time shifts $a_{i,i-1}$.

$$a_{k,0} = \prod_{i=1}^{k} (a_{i,i-1} + 1) - 1 \tag{4.2}$$

With our limited sampling of the wavefield, we cannot clearly identify the wave path, which mostly contribute to the coda. Here as the wavelength is of the same order of magnitude as the sample dimensions, we expect that the coda is dominated by surface waves traveling around the cylindrical sample (as concluded by Grêt et al. (2006), under similar experimental conditions). It is also possible that multiple-reflected waves contribute to the coda, as the pulse wavelength is slightly less than the sample dimensions.

4.1.2.3 *Calibration of the acoustic sensors*

It is important to account for apparent time shifts due to external biases of the experimental procedure, including whether the response of the acoustic sensors is sensitive to temperature. Zhang et al. (2013) applied CWI to the mechanical deformation of concrete and, to quantify the influence of fluctuations in ambient temperature on the relative time shift, they simultaneously performed CWI on a second, un-stressed concrete sample. Zhang et al. (2013) calculated the relative time shift from the two experiments to isolate the influence of mechanical deformation on $\frac{\delta t}{t}$.

Here we performed both CWI and v_P measurements on a sample of fused quartz (with the same dimensions as the granite samples). We expected to see a low time shift in both the direct P wave and CWI measurements due to the low changes in v_P and v_S with temperature (measured to increase by ~2% and ~3%, respectively, when heated to 450 °C; Fukuhara and Sanpei (1994)), and because of the low thermal expansion coefficient of fused quartz. Regarding the influence of thermal expansion, if we assume that the relative time delay is equal to the relative elongation of raypaths, which is in turn equal to the linear thermal expansion coefficient of fused quartz, we find a low $\frac{\delta t}{t}$ of $5.4 \times 10^{-7}/°C$. Any deviation from these relative time shifts is expected to originate from external factors, including the sensor response, which must be corrected for when measurements are made using the same experimental apparatus on rock samples of the same geometry.

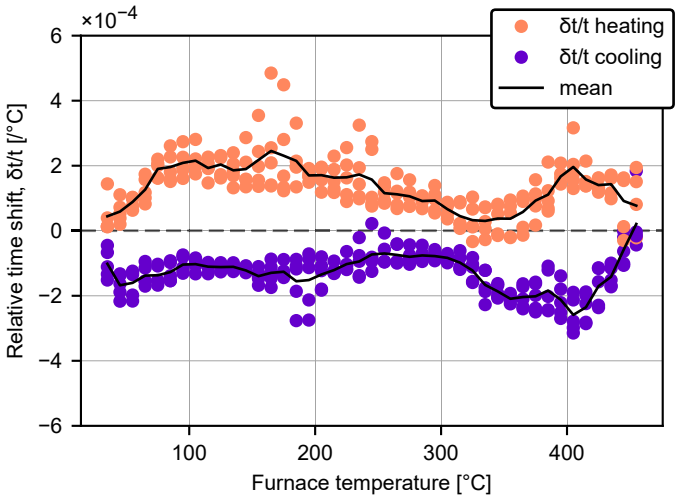

Figure 4.3: The CWI relative time shift per °C with temperature (averaged over intervals of 10 °C) calculated from waveforms recorded over three cycles of heating and cooling of a fused quartz sample. The black solid line represents the mean relative time shift with temperature, which we used to calibrate our CWI measurements on the Westerly Granite sample.

We observed an increase in v_P of the fused quartz sample by around 2.7% at 450 °C (similar to the ~3% increase measured by Fukuhara and Sanpei (1994)). However, we measured a positive relative time shift using CWI (~1.5×10^{-4}/°C; Figure 4.3), indicating an apparent decrease in the CWI wave velocity with temperature (Equation 4.1) significantly greater than that due to the linear thermal expansion coefficient of quartz. We expect that the observed relative time shift (Figure 4.3) may be due to wave scattering/reflection within the steel casings of the sensors, and sensitivity of the electro-elastic response of the piezo-ceramic transducers to temperature. The signal we measured for the fused quartz sample contains all these possible influences, which we correct for in the measurements made on the granite sample. Note that we expect the hysteresis of the relative time shift with respect to furnace temperature (Figure 4.3) to be due to the temperature of the acoustic sensors, which is lower during heating and higher during cooling.

Figure 4.4 shows the Westerly Granite sample temperature with time (Figure 4.4a) and the amplitudes in greyscale of the first 0.5 ms of the recorded waveforms (Figure 4.4b), which we used for both CWI and v_P measurements. In Figure 4.4c, we show the same waveforms but stretched by applying the mean relative time shift with temperature measured on the sample of fused quartz (Figure 4.3), to illustrate the relative time shift correction.

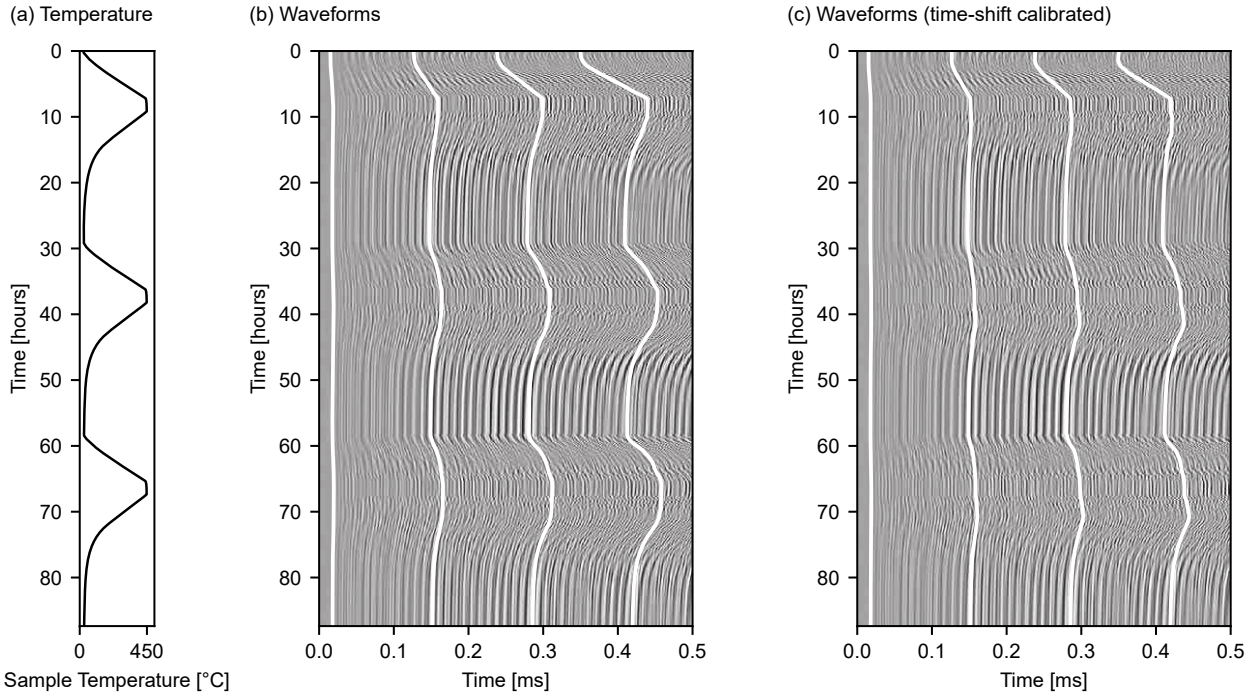

Figure 4.4: CWI during three heating and cooling cycles. (a) Westerly Granite sample temperature against experiment time. (b) The first 0.5 ms of the original recorded waveforms with experiment time. (c) The first 0.5 ms of the time shift corrected waveforms with experiment time. The white lines illustrate the stretching of the waveform with time, by applying the non-calibrated and calibrated cumulative time shifts measured with CWI to four distinct initial arrival times.

4.1.2.4 *Acoustic Emission (AE) monitoring*

For AE monitoring, a single broadband AE sensor is housed facing toward the sample within the center of the upper piston (Figure 4.2) to best capture the AE energy. To test this configuration, we simultaneously recorded the AE produced by a Hsu-Nielsen lead break source—a 0.5 mm diameter 2H pencil lead of approximately 3 mm in length broken by pressing it against the surface of the granite sample—using two identical sensors, one within the piston (as in Figure 4.2) and one adjacent, attached to the outside of the piston (details of the AE acquisition are described in the paragraph below). We observed a greater amplitude and improved frequency content using the AE sensor embedded within the piston. The piston, acting as a continuous waveguide (thus avoiding problems associated with attenuation at surface interfaces), applied a servo-controlled load of 100 N (~0.3 MPa) on the sample to ensure a constant coupling between the sensor and the sample. Without the servo-controlled load, the coupling oscillates dramatically as the pistons deform with temperature, ultimately influencing the AE detection threshold.

The AE sensor was a micro80 miniature sensor from Physical Acoustics, which has a bandwidth of 200–900 kHz and a resonant frequency of 325 kHz. The sensor was connected to a 1283 USB AE Node: a single-channel AE digital signal processor with a built-in 26 dB preamplifier and integrated analogue low- and high-pass filters (set to 20 kHz and 1 MHz, respectively). When the preamplified voltage across the transducer crossed the 40 dB detection threshold (with respect to a 1 μV reference voltage), an AE "hit" was registered, and the system then counted the subsequent number of oscillations across the voltage threshold (also known as ring-down counts). The AE trigger system parameters were set to 400 μs peak definition time (the time following detection within which the peak voltage—and therefore the AE amplitude—may be determined), 400 μs hit definition time (the maximum time between consecutive threshold crossings, above which they are considered as part of separate hits), and a 1000 μs hit lockout time (the minimum time between consecutive hits). These parameters were selected to correctly capture the AE produced by a Hsu-Nielson source (lead break) on the surface of the granite sample, which produces an AE hit of amplitude 79 dB. When triggered, the 1283 USB AE Node also recorded the first 7 ms of each AE waveform (7000 time samples at 1 MHz sampling rate) with a 100 μs pretrigger. Studying the waveforms, we postprocessed the AE data to remove any hits resembling electrical spikes, which corresponded to all hits that had both an amplitude greater than 55 dB and a number of ring-down counts lower than 60. For comparison, genuine AE hits of more than 55 dB in amplitude had a mean number of ring-down counts of 460. The number of discounted hits corresponded to 105 out of 596,

	v_P [km/s]	v_S [km/s]	AE hits during heating	AE hits during cooling
unheated	4.89	2.7	-	-
Heated to 450 °C	2.95	-	224	267
2× heated to 450 °C	2.77	-	19	73
3× heated to 450 °C	2.71	2.2	22	24

Table 4.1: P-wave and S-wave velocities, measured before and following the heating/cooling cycles to 450 °C, and number of detected AE hits during heating and cooling of each cycle.

45 out of 137, and 43 out of 89 AE hits over the course of the first, second, and third cycles, respectively.

4.1.3 *Results*

4.1.3.1 *P-wave velocity at temperature*

Table 4.1 shows the measurements of v_P and v_S made at room temperature on a thermally stressed Westerly Granite sample using a separate dedicated setup. Before heating, v_P was 4.89 km/s, decreasing to 2.95 km/s following the first heating and cooling cycle. We measure smaller decreases, from 2.95 to 2.77 km/s, and finally to 2.71 km/s following the second and third cycles, respectively (Table 4.1). We measure a decrease in v_S from 2.7 km/s before heating to 2.2 km/s following the third cycle (Table 4.1).

Figure 4.5 shows the in situ measurements of v_P against sample temperature during each heating and cooling cycles. The initial value of v_P ("v_P preheat" in Figure 4.5a) is the value measured using a separate calibrated device at room temperature prior to heating (4.97 km/s), which is then recalculated taking in to account the measured traveltime shift during heating and cooling. As the sample is first heated to 50 °C, v_P initially shows a slight increase (Figure 4.5a). Between 100 and 450 °C v_P shows a continuous decrease to 2.50 km/s at 450 °C. During cooling, v_P recovers to 3.01 km/s, resulting in a permanent net decrease of 1.96 km/s over the first cycle. A similar permanent decrease in v_P following a single heating/cooling cycle is also observed in our room temperature measurements on another thermally stressed sample of Westerly Granite (Table 4.1) and in the literature: Nasseri et al. (2009b) measured at room temperature a similar decrease in v_P of Westerly Granite when heated to 450 °C from 4.5 to 3.0 km/s. Agreement with these standard room temperature measurements adds veracity to our in situ measurement method.

During the second cycle, the in situ v_P decreases from 3.01 to 2.44 km/s at 450°C and increases back to 2.90 km/s upon cooling (0.11 km/s net decrease; Figure 4.5a). Finally, during the third cycle, v_P

decreases to 2.42 km/s at 450 °C, returning to 2.85 km/s upon cooling (0.05 km/s net decrease; Figure 4.5a). The v_P of the sample was remeasured using a separate device following all cycles (black circle in Figure 4.5a), which is the same as the final value of v_P calculated from the cumulative time shift.

4.1.3.2 *Coda Wave Interferometry*

We calculated the relative time shift between the first 0.5 ms of consecutive waveforms (Figure 4.4b) using the stretching method (Larose and Hall, 2009; Sens-Schönfelder and Wegler, 2006) as described previously, before correcting for the relative time shift measured on the fused quartz sample (Figure 4.3). In Figure 4.4b and Figure 4.4c, the white solid lines illustrate the stretching of the waveform during heating and cooling by applying the noncalibrated and calibrated CWI time shifts, respectively, to four distinct initial arrival times. We see that these lines follow the shift in the peaks and troughs of the waveforms. Overall, we observe an elongation of the waveforms during heating and a compression during cooling—a positive and negative relative time shift respectively—corresponding to an apparent decrease in velocity with increasing temperature (Equation 4.1).

Figure 4.5b shows the calibrated relative time shift per °C, $\frac{\delta t}{t}$, averaged over a 10 °C increase/decrease in sample temperature during each cycle. As the rock is heated for the first time, the relative time shift is initially negative (Figure 4.5b), corresponding to an apparent increase in velocity with temperature up until 60 °C. Between 60 and 150 °C the relative time shift is positive and increases linearly with sample temperature. Above 150 °C, the time shift is constant with temperature, remaining roughly between 5×10^{-4}/°C and 7.5×10^{-4}/°C. Measurements of relative time shift are greater in amplitude than those measured on the sample fused quartz sample (~1.5×10^{-4}/°C; Figure 4.3). During cooling, $\frac{\delta t}{t}$ remains positive between 440 and 400 °C, before becoming negative and showing a linear decrease as the sample cools (an apparent increase in velocity). The amplitude of the relative time shift during cooling remains below 4×10^{-4}/°C, lower than during heating. Overall, we find similar values to those of Grêt et al. (2006)—$\frac{\delta t}{t}$ of between 2×10^{-4}/°C and 6×10^{-4}/°C—when they heated and cooled Elberton Granite to a maximum temperature of 90 °C, confirming our approach.

In the following cycles the relative time shift is initially positive during heating (apparent decrease in velocity), at around 2×10^{-4}/°C throughout cycle 2 and 3.5×10^{-4}/°C during cycle 3 (Figure 4.5b). The time shift decreases with temperature, remaining lower than during the first cycle between 150 and 450 °C. During the cooling phase of cycles 2 and 3, the relative time shifts are very similar. Initially close to zero, $\frac{\delta t}{t}$ increases to around 2.5×10^{-4}/°C at 420 °C and then decreases during the rest of each cooling phase, becoming negative

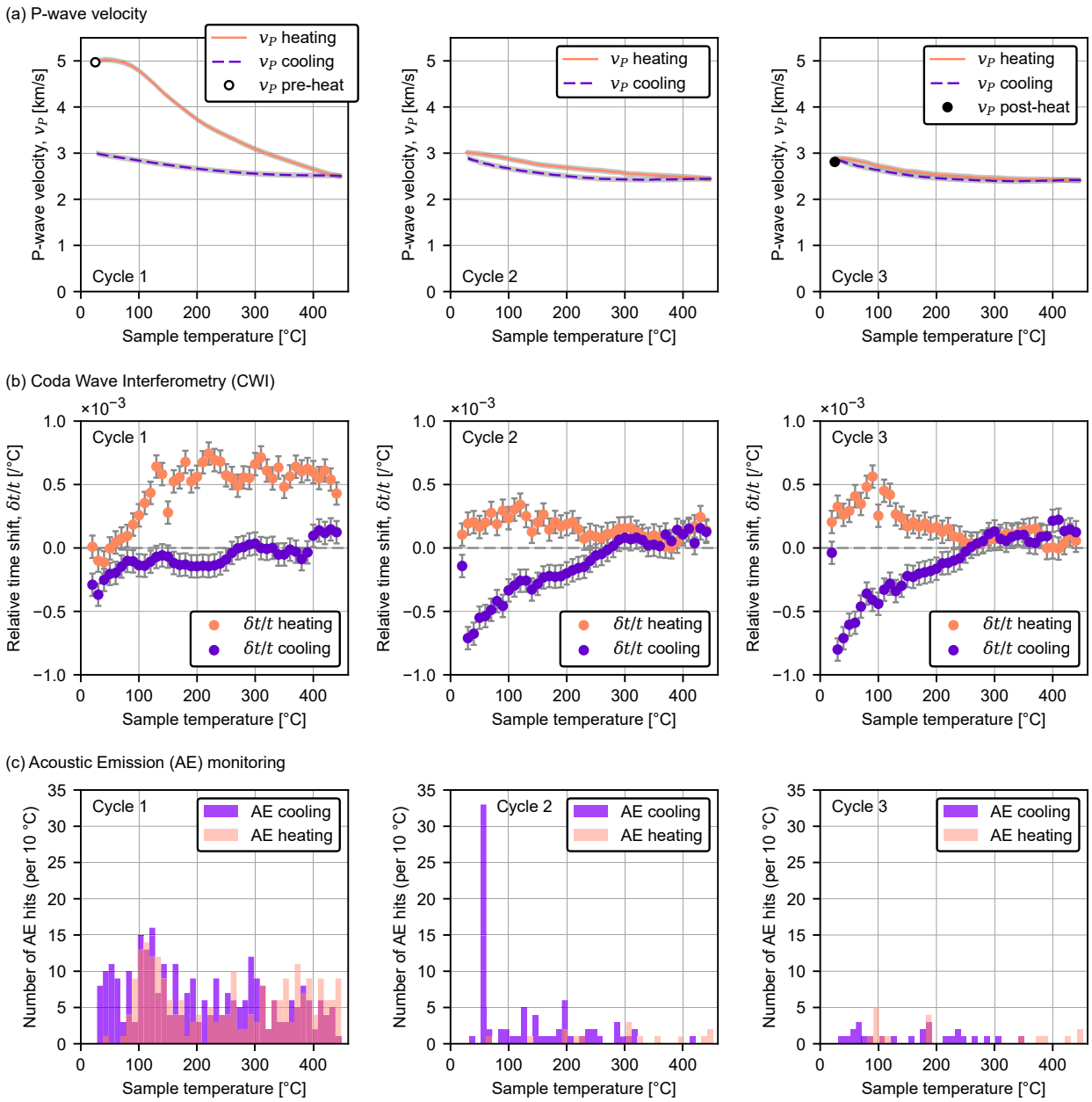

Figure 4.5: Measurements made during three heating/cooling cycles of Westerly Granite to a maximum temperature of 450 °C. (a) P wave velocity: the circles represent v_P measurements made at room temperature before (open) and after heating (filled). The lines represent v_P against sample temperature during heating (solid) and cooling (dashed), calculated from the cumulative shift in P wave arrival time with temperature and the initial v_P of the unheated rock, measured prior to heating (4.97 km/s). Error (shaded grey) is equal to the precision of the initial v_P measurement. (b) CWI: the relative time shift per °C (averaged over 10 °C intervals) against sample temperature. The error bars represent the potential variability, equal to two standard deviations from the mean of the relative time shifts measured on the fused quartz sample (Figure 4.3). (c) AE monitoring: the bars show the number of AE hits in bins of 10 °C against sample temperature during heating and cooling.

at around 300 °C. This corresponds to an acceleration of the apparent wave velocity as the granite cools.

Regarding the influence of deformation on traveltime, we can apply the same calculation as for the fused quartz, equating the relative time shift due to the relative elongation of raypaths to the linear thermal expansion coefficient of roughly 1.2×10^{-5}/°C (19–300 °C; Heard and Page (1982)). The relative time shift due to thermal expansion is therefore likely small in comparison to our measurements (Figure 4.5b).

THERMAL CYCLING TO 450 °C he total number of AE hits recorded during the first heating/cooling cycle (491) is greater than during the second (92) and third (46) cycles (Table 4.1). Figure 4.5c shows the number of AE hits against sample temperature in intervals of 10 °C. We observed no significant variation in the amplitude or energy of AE hits during heating and cooling, and therefore, we report only the number of detected AE. The sample temperature was not recorded during the AE monitoring experiment to avoid noise from friction between the thermocouple and the sample. Instead, we calculate the sample temperature from the furnace temperature, and the sample and furnace temperatures measured during the CWI experiment. During the first heating cycle (Figure 4.5c), we begin to observe AE once the sample temperature exceeds 70 °C, reaching a peak AE rate at 110 °C. We see an increase in AE activity at around 250 °C, and a second, larger increase between 310 and 450 °C. During cooling, we record roughly the same number of AE hits as during heating (267 compared to 224; Table 4.1), and the AE rate is constant with temperature (Figure 4.5c). During the second cycle, the AE rate is lower overall than during the first cycle (Figure 4.5c) (with the exception of the larger number of hits as the sample reaches room temperature). During the third cycle, we record even fewer AE hits during both heating and cooling (Figure 4.5c).

4.1.4 *Discussion*

4.1.4.1 *Thermal microcrack monitoring*

THE ONSET OF THERMAL MICROCRACKING As we heat the Westerly Granite sample for the first time, we observe a slight increase in v_P and an increase in the CWI apparent velocity up until a sample temperature of roughly 60 °C. From 70 °C we detect AE (Figure 4.5c) as a result of thermal microcracking, a threshold consistent with previous observations: 70–130 °C in Westerly Granite (Bauer et al., 1979; Hall and Bodnar, 1989; Johnson et al., 1978; Yong and Wang, 1980). The onset of AE marks the start of a significant decrease in v_P from 4.97 to 2.50 km/s at 450 °C (Figure 4.5a), and an increase in the CWI relative time shift (Figure 4.5b). We continue to record AE

throughout heating (Figure 4.5c), as previously observed in experiments on granite (Glover et al., 1995; Johnson et al., 1978), and we link the simultaneous velocity decrease and AE hits to the creation and propagation of thermal microcracks. Figure 4.6 shows SEM micrographs of an unheated sample of Westerly Granite, and a sample heated to and cooled from 450 °C. Qualitatively, we observe more microcracks—both intragranular (through grains) and intergranular (along grain boundaries)—within the heated granite than within the unheated granite. We expect that in our case, thermal microcracking results from the build-up of mechanical stresses due to the differential thermal expansion of neighboring crystals rather than due to thermal gradients within the sample. Following the calculation of Wang et al. (2013), assuming a thermal diffusivity of granite of $10 \times 10^{-6}\,m^2/s$, the time constant for thermal equilibrium in our samples of radius 10 mm (the characteristic length) is 100 s. We assume that the thermal gradient within the sample is therefore negligible when heating and cooling at a rate of 1°C/min.

(THERMAL) KAISER MEMORY EFFECT During cooling of the first cycle, we observe an increase in wave velocity (e.g., v_P increases from 2.5 to 3.0 km/s; Figure 4.5a and Figure 4.5b), which we attribute to the closure of microcracks as crystals contract. Following the first heating/cooling cycle, we heated the granite a second time (examples of repeated thermal stressing; e.g., Todd (1973) and Yong and Wang (1980), are rare in the literature). AE hits, observed from around 80 °C, are far less frequent than during the first cycle (Table 4.1 and Figure 4.5c). From the beginning of heating we measure an immediate decrease in v_P, which continues throughout heating from 3.01 km/s at room temperature to 2.44 km/s at 450 °C (Figure 4.5a) and, in the CWI measurements, a positive relative time shift (Figure 4.5b). This suggests that crystals are not as tightly interlocked as in the unheated granite and may expand owing to the presence of new microcracks along grain boundaries following the first cycle ((Homand-Etienne and Houpert, 1989). During cooling of cycle two, v_P increases from 2.44 to 2.90 km/s (Figure 4.5a). The 0.11 km/s permanent decrease in velocity—also seen in our benchtop measurements of v_P at room temperature on another sample (Table 4.1)—is evidence of further microcracking (albeit much reduced) during the second cycle. Thermal microcracking during repeated heating cycles is in conflict with the Kaiser memory effect (Kaiser, 1953) whereby, to sustain damage, a material must be subject to stresses greater than those it has already experienced. The Kaiser memory effect has previously been observed during the thermal stressing of rock and concrete (Choi et al., 2005; Heap et al., 2013a; Yong and Wang, 1980; Zuberek et al., 1998). We suggest that thermal microcrack formation during the second cycle may be due to remnant stresses within the granite following the first

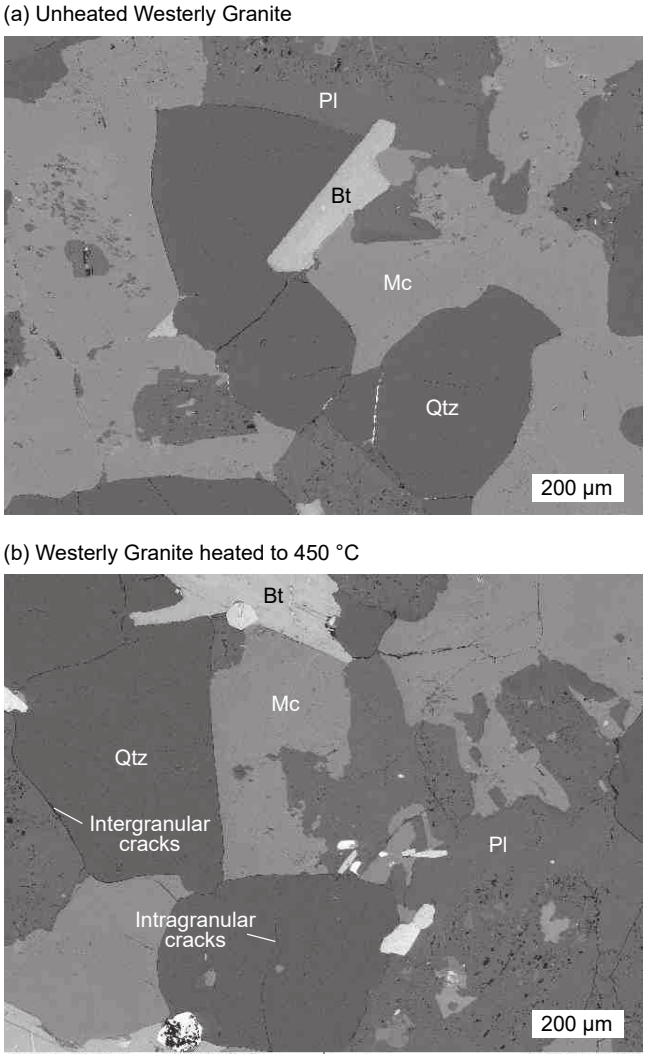

Figure 4.6: Backscattered scanning electron microscope micrographs of samples of Westerly Granite both (a) unheated and (b) heated to 450 °C and cooled. Labeled are grains of quartz (Qtz), microcline (Mc), plagioclase (Pl), phyllosilicate (biotite, Bt), and intergranular and intragranular microcracks.

cycle. As the granite is heated for the third time, AE begins later still, at around 100 °C, and we observe fewer AE than during the previous two cycles (Table 4.1 and Figure 4.5c). We measure a decrease in v_P from 2.90 to 2.42 km/s (Figure 4.5a) during heating and an increase from 2.42 to 2.85 km/s during cooling—0.05 km/s less than before heating. Again, these values are similar to our room temperature v_P measurements on another Westerly Granite sample (Table 4.1). During the third cycle, as the velocity change is almost entirely recovered, owing to the reversible opening and closing of microcracks, we expect very little thermal microcracking to have occurred. Thirumalai and Demou (1974), who performed thermal dilation measurements during repeated heating and cooling of granite, also observed no evolution in microcrack damage from the third thermal stressing cycle.

THERMAL MICROCRACKING DURING COOLING During the first cycle, we detected a similar number of AE hits during cooling as during heating (4.1). Browning et al. (2016), who heated two volcanic rocks (a basalt and a dacite) to 1100 °C, found that the majority of the detected AE occurred during cooling, which they attributed to cooling-induced thermal microcracking. For Westerly Granite, the increase in v_P (from 2.50 km/s at 450 °C to 3.01 km/s at room temperature; Figure 4.5a) and the CWI negative time shift (an increase in apparent velocity; Figure 4.5b) during cooling indicate that thermal microcracking is much less significant than during heating, despite the slightly greater number of AE hits detected during cooling (4.1 and Figure 4.5c). However, we do still expect that some of the cooling AE is due to microcracking, as the velocity recovery during cooling is slightly less than during cycles 2 and 3, where velocity changes are near elastic (Figure 4.5a and Figure 4.5b). Taken together, these observations suggest that although there was likely some thermal microcracking occurring during the cooling phase of cycle one, it is not easy to attribute the large number of recorded AE during cooling to microcracking. We therefore speculate that a large portion of the AE activity during the first cooling cycle was not associated with microcracking, but rather friction on microcrack surfaces as the crystals cool and contract. Although this is in conflict with the conclusion of Browning et al. (2016), we note that the process of thermal microcracking may differ between a crystalline rock (granite) and a volcanic rock that consists of phenocrysts within an amorphous groundmass.

4.1.4.2 *P- and S-wave velocity*

Assuming that thermal microcracking in Westerly Granite is isotropic and homogeneous (Nasseri et al. (2009b); and also shown to be the case in La Peyratte granite by David et al. (1999)), and ignoring thermal strain effects, the relative time shift in the arrival times of scattered waves may be equated to a change in the velocity of the rock.

We expect the coda to contain surface waves and multiple-reflected waves, which are both sensitive mostly to changes in v_S (Grêt et al., 2006; Snieder, 2002). First, the velocity of surface waves travelling around the sample is directly proportional to the shear wave velocity (typically 0.9 v_S). Second, as waves are scattered and reflected multiple times, they are converted from P to S waves, and vice versa. Snieder (2002) showed that once the P and S wave energies have reached equilibrium, the CWI apparent velocity change (provided by Equation 4.1) is more sensitive to changes in the velocity of S waves than P waves (Equation 4.3 for a Poisson medium). For our CWI measurements, if we consider an S wave of velocity 2.7 km/s (v_S of the unheated granite; Table 4.1), waves may travel a distance of up to 1.35 m, traversing the sample multiple times. We therefore assume that the P and S wave energies are equilibrated, which is the case following a few reflections/scatterings (Trégourès and Tiggelen, 2002).

$$\frac{\delta v}{v} = 0.09\frac{\delta v_P}{v_P} + 0.91\frac{\delta v_S}{v_S} \tag{4.3}$$

Therefore, with CWI, the same waveform data used for our v_P measurements may inform on changes in v_S. Assuming that apparent changes in CWI velocity are equal to changes in v_S, in Figure 4.7, we calculate the pseudo S wave velocity, noted v_{CWI}, from the measurement of v_S at room temperature prior to heating, and the CWI relative time shift (similar to our approach for calculating v_P). Our room temperature measurements show a decrease in v_S from 2.7 km/s before heating to 2.2 km/s following all three heating/cooling cycles (Table 4.1). This is the same 17% decrease as observed by CWI (Figure 4.7) and is also compatible with the 15% permanent decrease in v_S measured by Nasseri et al. (2009a) when they heated Westerly Granite to 450 °C (a single heating/cooling cycle).

Also in Figure 4.7, we show v_P and the ratio $\frac{v_P}{v_{\mathrm{CWI}}}$, analogue to the $\frac{v_P}{v_S}$ ratio. The $\frac{v_P}{v_S}$ ratio is known to be sensitive to microcrack orientation and density (a function of the number and size of microcracks). In the case of isotropic thermal microcracking in dry granite, we expect $\frac{v_P}{v_S}$ to decrease with microcrack density (Wang et al., 2012). During the first cycle, we calculate a permanent decrease in $\frac{v_P}{v_{\mathrm{CWI}}}$ from 1.84 to 1.34 (Figure 4.7) due to thermal microcracking. We note that a $\frac{v_P}{v_{\mathrm{CWI}}}$ ratio of less than $\sqrt{2} \approx 1.41$ results in a negative Poisson's ratio and, although theoretically plausible (Case, 1984; Walsh, 1965), is rare among isotropic materials. Homand-Etienne and Houpert (1989) also found a negative Poisson's ratio for two thermally microcracked granites (Senones Granite and Remiremont Granite heated to 200–600 °C); they suggested that residual stresses during cooling are the cause of this unexpected mechanical behavior.

During cycles 2 and 3, we observe a near reversible decrease in $\frac{v_P}{v_{\mathrm{CWI}}}$ with increasing temperature (Figure 4.7). We expect that the evolution of $\frac{v_P}{v_{\mathrm{CWI}}}$ with temperature during the second and third cycles is due

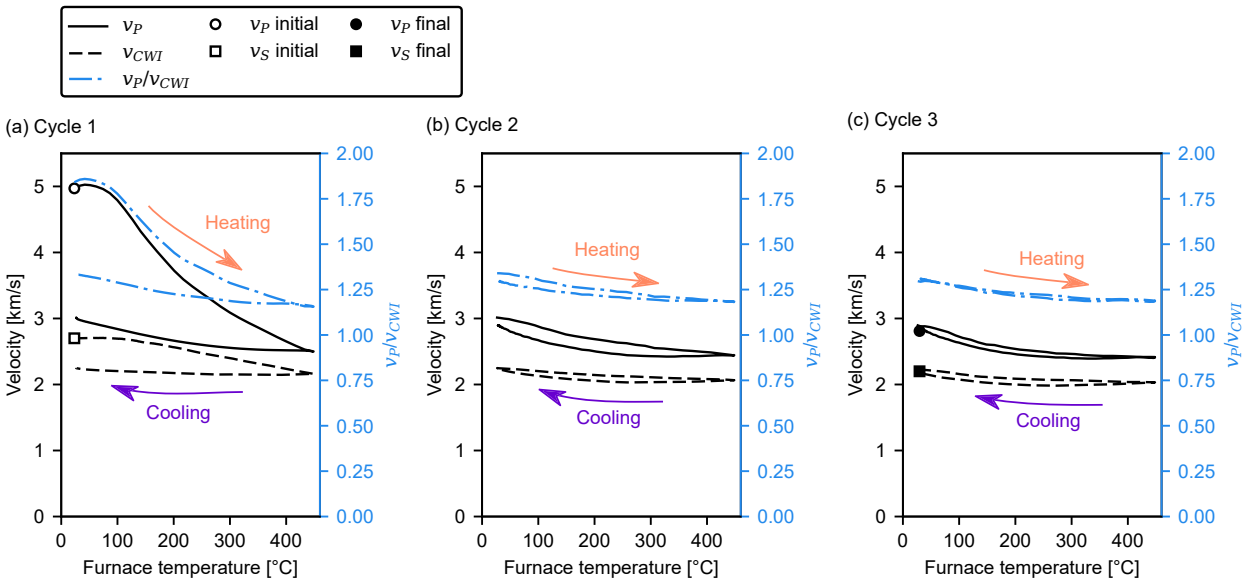

Figure 4.7: Wave velocity of Westerly Granite against sample temperature during (a–c) three heating and cooling cycles to a maximum temperature of 450 °C. The symbols show static measurements of v_P (circles) and v_S (squares) made at room temperature using a separate device both before (open symbols) and following thermal stressing (closed symbols). The curves represent v_P (black solid), the CWI pseudo S wave velocity, v_{CWI}, (black dashed), and their ratio (blue dot-and-dashed). The v_P and v_{CWI} are calculated respectively from the time shift of the P wave first arrivals and the CWI relative time shift (Equation 4.1), scaled to the static v_P (4.97 km/s) and v_S (2.7 km/s) measurements of the unheated granite.

to the thermo-elastic deformation of crystals. The decrease in $\frac{v_P}{v_{CWI}}$ with temperature could be due to a widening of preexisting microcracks as crystals expand: assuming that cracks are dry and elliptical, an increase in crack aspect ratio corresponds to an increase in crack density and, in turn, a decrease in $\frac{v_P}{v_S}$ ratio (O'Connell and Budiansky, 1974). A dedicated study would be needed to further assess the influence of temperature on the elastic moduli of Westerly Granite.

4.1.4.3 *Geothermal implications*

Thermal microcracking in granite is known to lower stiffness and strength (Wong, 1982), lower thermal diffusivity (Heuze, 1983; Kant et al., 2017), and increase permeability (Darot et al., 1992; David et al., 1999; Heard and Page, 1982; Nasseri et al., 2009a; Violay et al., 2017): all parameters that can influence the exploitation and modeling of geothermal resources. Granite is the reservoir rock for the many geothermal projects in the Upper Rhine Graben, including those at Soultz-sous-Forêts (France) (e.g., Gérard and Kappelmeyer (1987) and Gérard et al. (2006)) and Rittershoffen (France) (e.g., Baujard et al. (2017)). In such a thermally dynamic environment, it is important to consider the evolution of the intrinsic mechanical and transport properties of rock with temperature. Our velocity measurements of granite are strongly dependent on temperature—due to the thermal expansion and contraction of crystals and the formation and propagation of thermal microcracks—and highlight the importance of performing measurements under in situ temperature conditions. Potential differences in rock properties with temperature should be understood when applying laboratory measurements made under ambient conditions to the modeling of and monitoring of geothermal systems.

While our results exhibit (to a degree) a Kaiser memory effect—whereby repeated thermal stressing does not further induce thermal microcracking (Figure 4.5)—reservoir conditions may favor repeated thermal microcracking, over longer durations. First, thermal stresses further accumulate over time and space in a geothermal reservoir, as fluid penetrates deeper into the rock mass through the newly created crack porosity (Dempsey et al., 2015; Murphy, 1978). Thermal stresses may also contribute to stress-induced subcritical crack growth within the reservoir and around the borehole, leading to damage accumulation over time (Bérard and Cornet, 2003). Finally, our short-term (and dry) experiments do not allow for crack sealing due to hydrothermal precipitation, which is known to occur in geothermal reservoirs (Batzle and Simmons, 1976; Griffiths et al., 2016). Crack sealing increases rock cohesion and strength, allowing cracks to recrack (Engelder, 1987)—a phenomenon which has been reproduced in the laboratory (Karner et al., 1997). In a geothermal environment, thermal stresses may therefore play an important role in the evolution of crack damage over time.

Our velocity measurements are also relevant for geothermal reservoir monitoring. During the hydraulic stimulation (through water injection) of the Soultz-sous–Forêts geothermal reservoir, earthquake tomography inversions revealed changes in v_P, which coincided with changes in the injection flow rate (Calò et al., 2011). From our results, we speculate that a significant portion of velocity changes may be a consequence of temperature changes due to the circulating fluids. CWI, through correlation of ambient seismic noise, has been used to link velocity changes to geothermal reservoir activities (Lehujeur et al., 2017; Obermann et al., 2015). At a geothermal reservoir, v_P, v_S, and their ratio are often interpreted in terms of fluid saturation; however, our results suggest that temperature effect of circulating fluids may also play a significant role. Note that at the scale of the geothermal reservoir, the wave velocity of rock may be lower than velocities measured in the laboratory due to the lower frequency of seismic waves compared to ultrasonic waves (Zoback, 2010). Further, within a geothermal reservoir, changes in temperature and related changes in velocity are localized, whereas here the temperature varied throughout the sample. At the reservoir scale there will be a limit in the resolution of seismic tomography depending on the amplitude of the localized velocity changes and the affected volume.

We chose to perform these measurements on the well-studied Westerly Granite; however, many geothermal reservoirs are hosted in volcanic rock (Grant, 2013), and we may expect differences in the mechanisms for thermal microcracking in such rock due to differences in microstructure and porosity. For example, there is evidence to suggest that thermal microcracking in volcanic rocks occurs primarily during cooling (Browning et al., 2016), and volcanic rocks with a high preexisting crack density prior to heating are thought to exhibit less thermal microcracking during heating/cooling (Heap et al., 2009a; Vinciguerra et al., 2005). The influence of temperature on thermal microcracking and velocity in different rock types merits further study.

Through our experiments, in which we heated granite samples from ambient temperature, we offer insight into the potential for thermal microcracking in a geothermal environment. However, thermal microcracking may also be induced by the quenching of hot rock by cooler fluids (Siratovich et al., 2015). For example, the use of cool drilling fluid in geothermal wells has been shown to induce borehole breakouts (Bérard and Cornet, 2003), and the injection of cool water has even been actively used to enhance permeability within the reservoir, in a technique known as thermal stimulation (Grant, 2013; Jeanne et al., 2017; Kitao et al., 1995). Further research into the particularity of cooling-induced cracking would complement our study.

A final research perspective is the influence of confining pressure on thermal microcracking and ultrasonic velocity. At the Soultz-sous-Forêts geothermal site, for example, the pressure increase in the ver-

tical stress component increases by around 25 MPa per kilometer depth, and the horizontal components are of a similar order of magnitude (Cornet and Bérard, 2003; Genter et al., 2010; Valley and Evans, 2007). During heating, thermal microcracking may be inhibited by high confining pressures (Molen, 1981; Siddiqi and Evans, 2015; Wong and Brace, 1979) and, at room temperature, the v_P and v_S of thermally microcracked Westerly Granite have been shown to increase with confining pressure (Nasseri et al., 2009a). Wang et al. (1989) measured v_P of Westerly Granite during heating to and cooling from 300 °C, under confining pressures of 7, 28, and 55 MPa. Wang et al. (1989) found that for all confining pressures, v_P decreased during heating and increased during cooling, back to the velocity of the unheated rock. For example, under 7 MPa confining pressure, v_P decreased from ~4.5 km/s at room temperature to ~3.4 km/s at 300 °C and increased back to ~4.5 km/s during cooling. Violay et al. (2017) performed high-temperature (up to 1000 °C), high-pressure (130 MPa) triaxial experiments on Westerly Granite samples to emulate conditions within the ductile crust. Violay et al. (2017) found that when samples were heated to the target temperatures under a confining pressure, their permeabilities (at pressure and temperature) were higher when the temperature was higher, interpreted by these authors as a result of thermal microcracking. The results of Violay et al. (2017) and Wang et al. (1989) show that thermal microcracks in granite may open (and remain open) when heated under confining pressure. Further experiments are now required to better understand thermal microcracking under a confining pressure.

4.1.5 *Conclusions*

Through the combined use of AE monitoring and in situ v_P and CWI measurements, we observed both permanent (microcracking) and nonpermanent (crack opening and closing) changes in the microstructure of Westerly Granite when repeatedly heated and cooled, at ambient pressure, to a maximum temperature of 450 °C. Following a slight initial increase in velocity with temperature during heating, from the onset of AE at around 70 °C, we observed a large– and mostly permanent–reduction in velocity with temperature due to thermal microcracking. Thermal microcracking is a result of the build-up of mechanical stresses due to the mismatch in thermal expansion of crystals. During cooling we detected AE (slightly more than during heating) but the measured increase in velocity suggests that the source of AE cannot be entirely attributed to thermal microcracking: AE may instead be due to friction on microcrack surfaces as crystals cool and contract. We observed some, but less microcracking during the second cycle, and less again during the third cycle. During these two cycles, the reversible change in velocity with heating and cooling

is nonnegligible: v_P decreased by roughly 10% of the initial velocity when heated to 450 °C. We attribute the reversible increase/decrease in velocity to the elastic expansion/contraction of crystals, and the associated opening/closing of microcracks. We show how CWI can be used to monitor microcracking at high temperature and, in the case of isotropic and homogeneous microcracking, provide a measure of v_S. Our velocity measurements made during the thermal stressing of Westerly Granite—which add to existing measurements in the literature made on thermally–stressed rock under ambient conditions—highlight the value of performing measurements of rock properties under in situ temperature conditions, to provide more relevant data for seismic and geomechanical modeling.

4.2 THE INFLUENCE OF MICROSTRUCTURE AND COOLING RATE ON THERMAL MICROCRACKING IN GRANITE

Continuing from the study of the Westerly Granite, two other granites, Garibaldi Grey Granite from British Columbia, Canada and Lanhélin Granite from Brittany, France, were selected to establish the effect of microstructure on thermal microcracking, and thermal microcracks on the physical, thermal, transport, and mechanical properties of rock properties of the rock.

To assess the temperature conditions required for thermal microcracking and their influence on the velocities for the two granites, samples of each rock were subject to the same cyclic heating to 450 °C as previously in Section 4.1. Acoustic emission (AE) monitoring and wave velocity measurements were performed during heating and cooling. To examine the incidence of thermal microcracking at higher temperatures, AE monitoring was performed on all three granites during heating to 700 °C and cooling.

Whilst there exists a wealth of data on the properties of thermally-microcracked granite within the literature, it was useful to perform an exhaustive characterisation of the two granites presented here, to better inform any conclusions drawn. A suite of samples of both granites were slowly heated to temperatures of up to 900 °C and cooled. To assess the influence of cooling rate, additional samples were heated to 300 °C and 700 °C and cooled rapidly through immersion in water. Measurements were made of their microcrack density, microcrack length, and their physical, mechanical, thermal, and transport properties.

4.2.1 *Materials and experiments*

4.2.1.1 *Materials*

Optical micrographs of thin sections of the unheated Garibaldi Grey Granite, Lanhélin Granite, and Westerly Granite are presented in Figure 4.8. Compared with the Westerly Granite, which has an average grain size of 0.75 mm diameter (Meredith and Atkinson, 1985), the grain size is around 1 mm diameter in Garibaldi Grey Granite, and around 2 mm in the Lanhélin Granite. The unheated Garibaldi Grey Granite, containing both intra- and inter-granular microcracks, appears more microcracked than the unheated Lanhélin, where microcracks are mostly visible along grain boundaries (Figure 4.8). Table 4.2 reports the mineralogical composition of the two new granites, calculated from 2D optical micrographs of thin sections, above that of Westerly Granite (Chayes, 1952). Cylindrical samples of each rock were cored and their ends ground (20 mm diameter and nominally 40 mm in length). Samples were dried in vacuo for at least 48 hours prior to experimentation.

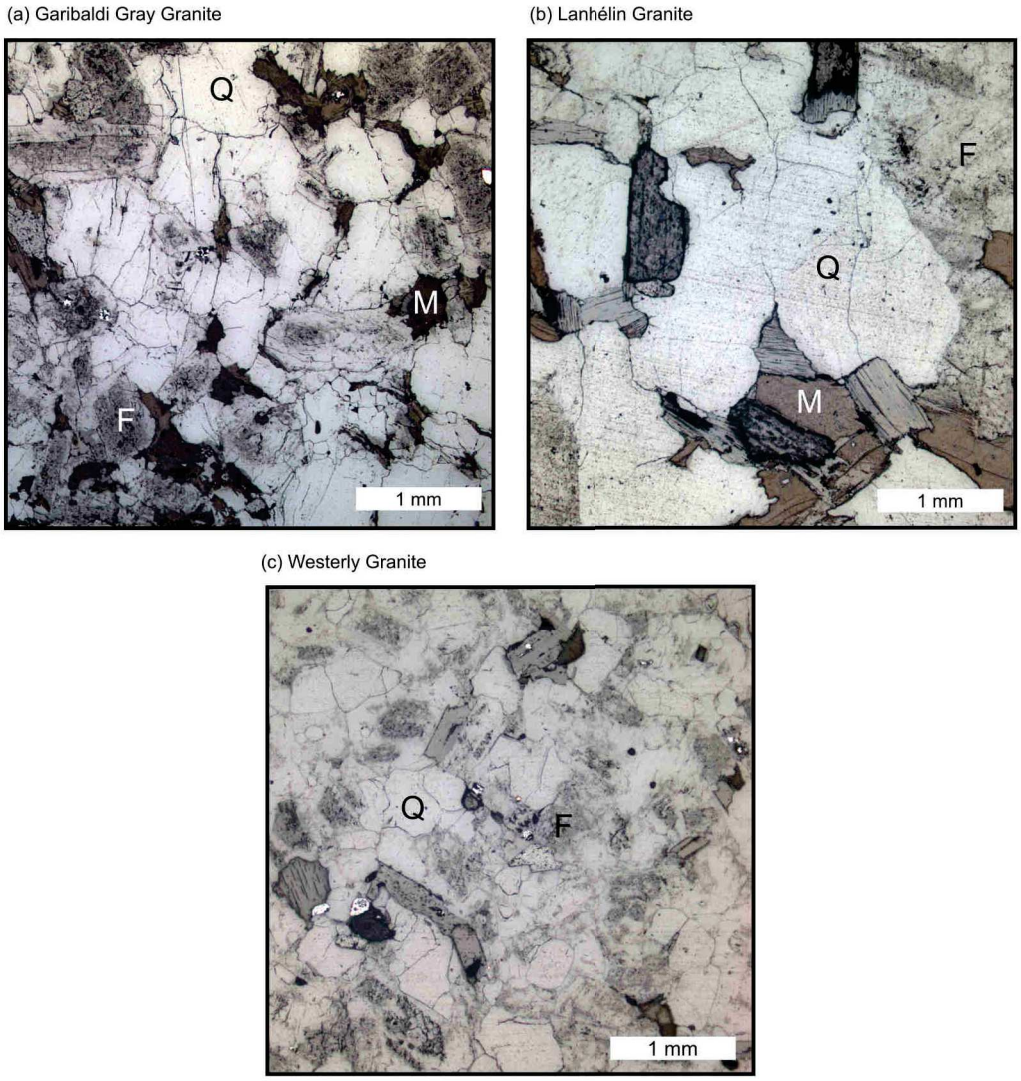

Figure 4.8: Optical micrographs of (a) Garibaldi Grey Granite, (b) Lanhélin Granite, and (c) Westerly Granite (shown again for comparison). Labelled in the granites are quartz (Q), feldspar (F), and mica (M).

	Composition	Grain size
Garibaldi Grey granite	43 % quartz 47 % feldspar 10 % mica	1 mm
Lanhélin granite	38 % quartz 45 % feldspar 17 % mica	2 mm
Westerly Granite (Chayes, 1952)	28 % quartz 65 % felsdpar 4 % biotite 2 % muscovite 1 % other	0.75 mm

Table 4.2: The mineralogical compositions of Garibaldi Grey Granite and Lanhélin Granite as calculated from optical micrographs of thin sections, and the composition of Westerly Granite (Chayes, 1952), for comparison.

4.2.1.2 *Experiments*

MONITORING EXPERIMENTS Measurements of v_P and the CWI relative time shift of waveforms were made on Garibaldi Grey and Lanhélin granite samples during three heating cycles to a maximum temperature of 450 °C (see methods Section 2.1.3.2 for details). AE monitoring was performed on Garibaldi Grey and Lanhélin granite samples during three heating cycles to a maximum temperature of 450 °C, and on samples of Garibaldi Grey Granite, Lanhélin Granite, and Westerly Granite during a single cycle up to 700 °C (methods Section 2.1.3.3). For comparison with the high temperature results, room temperature measurements of v_P were made on the samples used for AE monitoring, using a separate dedicated apparatus (methods Section 2.2.2). These values are shown alongside the high temperature measurements where available.

The characteristic time-scales for heat diffusion within the samples (following the calculation in Section 4.1 and Wang et al. (2013) for Westerly Granite and using measurements of the thermal diffusivity (Figure 4.17), are 68 s for the unheated Garibaldi Grey Granite and 51 s for the unheated Lanhélin Granite. These times increase to 111 and 109 s for samples heated to 700 °C and cooled. As these characteristic times are of the same order of magnitude as the 60 s taken by the furnace to heat by 1 °C, it is assumed that the heating rate is low enough to consider that the thermal gradient with the sample is negligible when heated to 700 °C at 1 °C/min.

THERMAL STRESSING CONDITIONS Cylindrical samples of each rock—20 mm diameter and nominally 40 mm in length—were prepared and dried. The samples were then heated without load at room pressure to 100, 200, 300, 400, 500, 600, 700, 800, and 900 °C and cooled. The furnace was set to heat and cool at a rate of 1 °C/min, remaining at the target temperature for a dwell period of two hours. Note: data on the Westerly Granite presented in this section was obtained from other thermal stressing experiments, where samples were heated to 400, 450, and 700 °C under a small load.

Additional samples of Garibaldi Grey and Lanhélin granite samples were also "shock-cooled" from temperatures of 300 and 700 °C by immersing them in cool water (~15 °C) following the two-hour dwell period at the target temperature.

MEASUREMENTS The following measurements were taken:

- Crack density microanalysis (see Chapter 3)—Thin sections of the intact rock, and of samples heated to 300 and 700 °C (both slow- and shock-cooled) were prepared in a plane parallel to the sample axes. Optical micrographs were stitched together to form a 10 x 10 mm window at the centre of the thin section. Binary images of microcracks were produced by manually tracing them using Inkscape (a vector graphics editor). Note: the automated procedure for binary segmentation of micrographs presented in Chapter 3 (Griffiths et al., 2017a) could not be used, as the images of the Lanhélin granite include the marks of feldspar etching. However, the method for processing binary images of microcracks presented in Chapter 3 (Griffiths et al., 2017a) was used to calculate in windows of 1 × 1 mm:
  - The mean crack length, $2c$ (approximated as the geometric distance between crack end points);
  - The number of cracks per unit area (N_A);
  - The Walsh (1965) 2D crack density ($\gamma = N_A c^2$)
  - The surface area per unit volume, S_V (Underwood, 1967).
- Connected porosity (triple-weight method, Section 2.2.1).
- Ultrasonic P-wave velocity (Section 2.2.2).
- Gas permeability (Section 2.2.3)—Permeabilities of samples were measured using one of two methods described in Section 2.2.3. The Lanhélin 800 and 900 °C, and Garibaldi Grey 900 °C samples were measured using the steady-state method (owing to their high permeability; $>1 \times 10^{-15}\,\mathrm{m}^2$). Other samples were measured using the pulse-decay method, with exception of the Garibaldi Grey Granite unheated, 100 °C, and Lanhélin Granite

unheated, 100 °C, 200 °C, the permeabilities of which were too low ($<1 \times 10^{-20}\,m^2$) to be measured using this apparatus.

- Thermal diffusivity, conductivity and specific heat—A Hot Disk TPS 500 analyzer (Figure 2.13), with power output settings of: 150 mW during 5 s for the Westerly Granite (unheated, 400 and 700 °C samples), and 90 mW during 5 s for the Lanhélin and Garibaldi Grey Granites.

- Mechanical tests (Section 2.2.5)—Uniaxial Compressive Strength (UCS) tests were conducted on dry unheated samples and samples of Garibaldi Grey and Lanhélin granites heated to 300 °C and 700 °C, both slow- and shock- cooled (under vacuum at 40 °C for at least 24 h prior). Dry triaxial tests at confining pressures of 5 and 10 MPa were performed on the Garibaldi Grey Granite samples heated to 300 and 700 °C (cooled both at 1 °C/min and shock-cooled).

4.2.2 *Results*

4.2.2.1 *AE and velocity during thermal cycling to 450 °C*

P-WAVE VELOCITY Figure 4.9a shows the in-situ v_P of Garibaldi Grey Granite against sample temperature during each of the three heating and cooling cycles to a peak temperature of 450 °C.

During heating of the first cycle, v_P decreases from 4.21 at room temperature, to 2.93 km/s at 450 °C. Initially, the rate of change of v_P accelerates, before becoming linear with temperature at around 200 °C. v_P increases to 3.25 km/s upon cooling: a net decrease of 0.96 km/s.

During heating of cycle two, v_P decreases again to 2.79 km/s at 450 °C, and increases to 3.08 km/s upon cooling: a smaller net decrease of 0.16 km/s. Following cycle three, however, v_P is permanently decreased by only 0.01 km/s. For comparison, the room temperature measurement of v_P made following all cycles on the sample used for the AE monitoring experiment (Figure 4.9c) is very close to the value issuing from the in-situ v_P measurements.

Figure 4.10a shows the in-situ v_P of the Lanhélin Granite against sample temperature during each of the three heating and cooling cycles. From the initial velocity of 5.72 km/s, v_P shows a near linear decrease to 3.00 km/s at 450 °C (Figure 4.10a). During cooling, v_P increased to 3.77 km/s, resulting in a permanent net decrease of 1.95 km/s over the first cycle. During cycle two, v_P decreases again during heating, but by only 1 km/s, and shows a net decrease of 0.20 km/s upon cooling. Similar behaviour is seen during cycle 3, again resulting in a 0.20 km/s permanent decrease in v_P (Figure 4.10a). v_P was measured on the sample used for AE monitoring following heat-

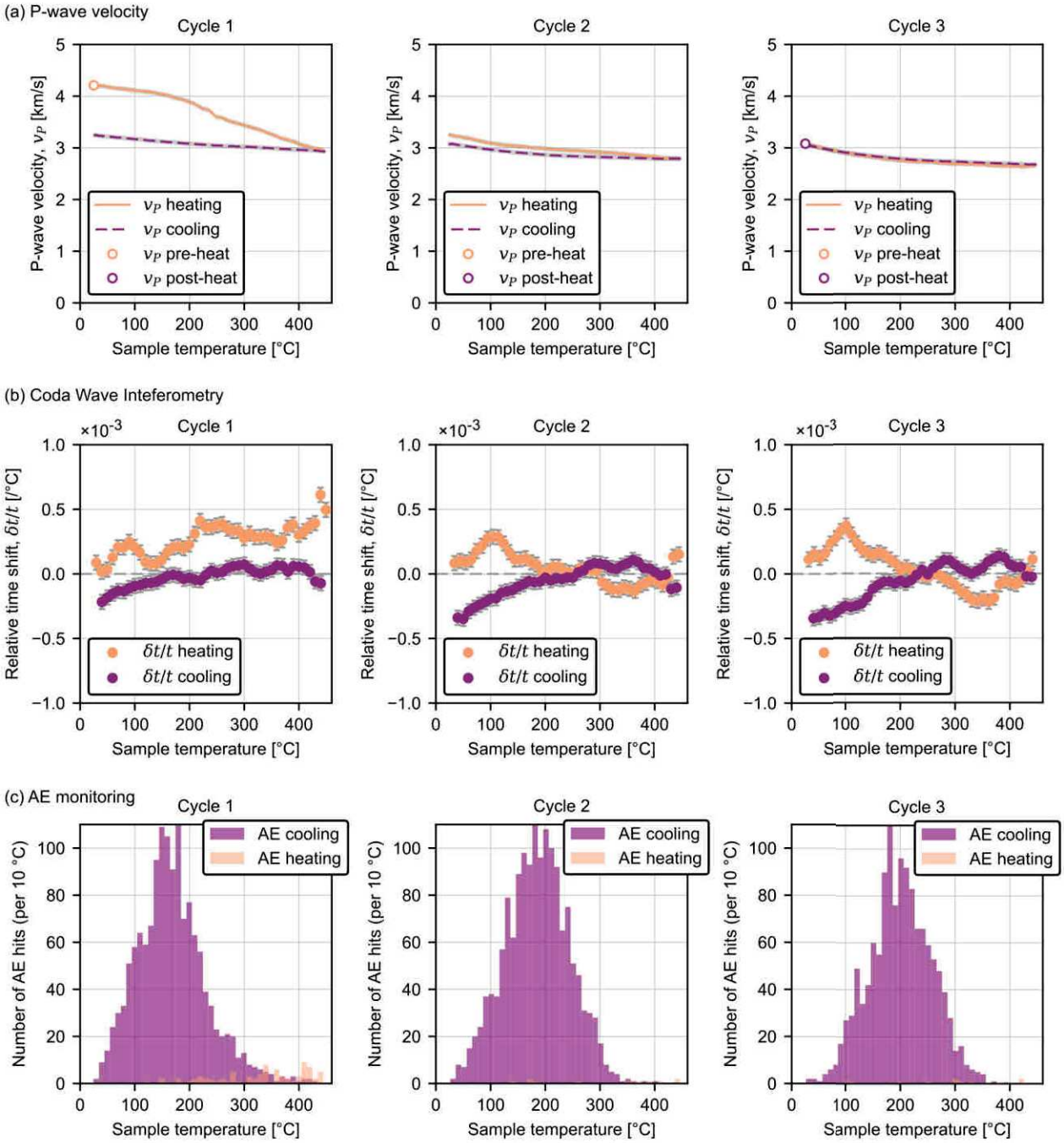

Figure 4.9: Measurements made during three heating/cooling cycles of Garibaldi Grey Granite to a maximum temperature of 450 °C. (a) P-wave velocity: lines represent v_P against sample temperature during heating (solid) and cooling (dashed), calculated from the cumulative shift in P-wave arrival time with temperature and the initial v_P of the rock measured prior to heating. Error (shaded grey) is equal to the precision of the initial v_P measurement. (b) CWI: the relative time shift per °C (averaged over 10 °C intervals) against sample temperature. (c) AE monitoring: the number of AE hits per 10 °C against sample temperature.

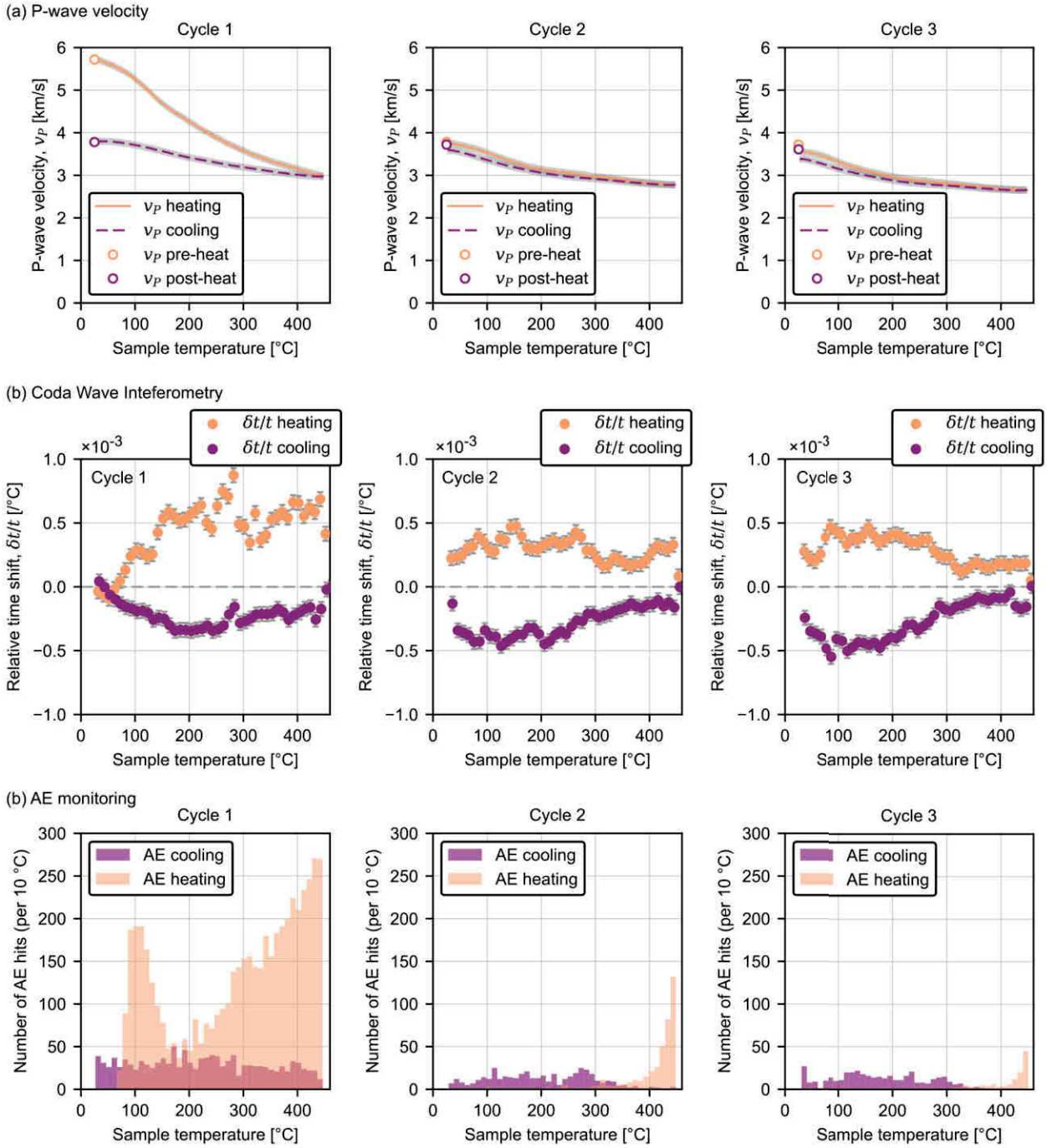

Figure 4.10: Measurements made during three heating/cooling cycles of Lanhélin Granite to a maximum temperature of 450 °C. (a) P-wave velocity: lines represent v_P against sample temperature during heating (solid) and cooling (dashed), calculated from the cumulative shift in P-wave arrival time with temperature and the initial v_P of the rock measured prior to heating. Error (shaded grey) is equal to the precision of the initial v_P measurement. (b) CWI: the relative time shift per °C (averaged over 10 °C intervals) against sample temperature. (c) AE monitoring: the number of AE hits per 10 °C against sample temperature.

ing/cooling cycles, and the values correspond well with those issuing from the in-situ velocity measurements (circles in Figure 4.10a).

CODA WAVE INTERFEROMETRY The relative time shift, $\frac{\delta t}{t}$, between waveforms was calculated using the *stretching* method (Larose and Hall, 2009; Sens-Schönfelder and Wegler, 2006), as for the Westerly Granite sample and described in Figure 2.1.3.2.

Figure 4.9b shows the calibrated relative time shift ($\frac{\delta t}{t}$) per °C for the Garibaldi Grey Granite against sample temperature, averaged in bins of 10 °C. During heating of cycle one, $\frac{\delta t}{t}$ shows an overall increase throughout, from $8 \times 10^{-5}/°C$ to $5 \times 10^{-4}/°C$ at 450 °C (Figure 4.9b), corresponding to an apparent decrease in velocity with temperature (as observed for the Westerly Granite in Figure 4.5). During cooling, $\frac{\delta t}{t}$ oscillates around zero, until 160 °C where it becomes negative, decreasing as the sample cools; indicating a velocity increase.

During heating cycles two and three of the Garibaldi Grey Granite, $\frac{\delta t}{t}$ is initially positive as the sample is heated, increasing at 100 °C to $3.5 \times 10^{-4}/°C$ to $4 \times 10^{-4}/°C$, before decreasing and becoming negative at around 250–300 °C. These values correspond to low amplitude changes in velocity, initially decreasing during heating, then increasing up to 450 °C. During cooling the trend is reversed, corresponding to an apparent decrease in velocity down to 250 °C, followed by an increase in velocity as the sample reaches room temperature.

Figure 4.10b shows $\frac{\delta t}{t}$ for the Lanhélin Granite. As the rock is heated for the first time, $\frac{\delta t}{t}$ is initially negative and low in amplitude (Figure 4.10b), corresponding to a small apparent increase in velocity with temperature up to 60 °C (as observed in the Westerly Granite in Figure 4.5). Between 60 °C and 150 °C, $\frac{\delta t}{t}$ is positive and increases linearly with sample temperature. Between 150 and 450 °C, $\frac{\delta t}{t}$ is near constant. During cooling of the Lanhélin Granite, $\frac{\delta t}{t}$ is negative throughout, decreasing from zero at 450 °C to around $-4 \times 10^{-4}/°C$ at 200 °C, before increasing to near zero at room temperature. This negative $\frac{\delta t}{t}$ corresponds to an apparent increase in velocity during cooling.

For the Lanhélin Granite, during cycles two and three, from the beginning of heating, the $\frac{\delta t}{t}$ is positive (~$2.5 \times 10^{-4}/°C$) but lower than during heating (~$5 \times 10^{-4}/°C$). During cooling, $\frac{\delta t}{t}$ decreases to a minimum of $-5 \times 10^{-4}/°C$ between 200 and 100 °C, before increasing slightly to $-1 \times 10^{-4}/°C$ and $-2.5 \times 10^{-4}/°C$ during cycles two and three respectively.

For the Garibaldi Grey and Lanhélin Granite; the CWI apparent velocity, as for v_P (Figure 4.10a), decreases during heating and increases during cooling.

AE MONITORING Figure 4.9c and Figure 4.10c show the number of AE hits against sample temperature in intervals of 10 °C during each cycle for the Garibaldi Grey and Lanhélin granites, respectively.

The onset of AE is less well defined in the Garibaldi Grey Granite data (Figure 4.9c) than it was for the Westerly Granite (Figure 4.5c). Few AE were detected, the first from around 100 °C sample temperature (Figure 4.9c). From 200 °C the AE rate increased, but remained below 10 hits /10 °C. During cooling from 450 °C, however, AE activity increased from 400 °C and reached a peak of more than 100 hits /10 °C at 150 °C. From 150 °C, the AE rate then decreased as the rock cooled to room temperature. During cycles two and three, very few AE were detected during heating and during cooling, however, AE activity was similar to the first cycle.

During the first heating cycle of the Lanhélin Granite (Figure 4.10c), the AE rate increased from 70 °C, reaching a peak at 110 °C. AE activity then decreases to around 40 hits/10 °C at 190 °C, before increasing steadily with temperature up to the 450 °C, where is reaches more than 250 hits/10 °C. During cooling from 450 °C, the number of AE hits with temperature was constant at around 30 hits /10 °C. For the Lanhélin Granite, during heating of cycles two and three, AE was detected from around 300 °C increasing significantly up to 450 °C. During cooling of cycles two and three, AE was observed from around 350 °C, and from 350 °C it remained near constant at 10-20 hits/10 °C. The number of detected AE for the Lanhélin Granite was greater than for the Garibaldi Grey (Figure 4.9c) and Westerly Granites (Figure 4.5c).

4.2.2.2 *AE monitoring to 700 °C*

The mean AE amplitudes detected during heating to 700 °C and cooling, were 46 dB for the Westerly, 49 dB for the Garibaldi Grey, and 53 dB for the Lanhélin Granite. Figure 4.11 shows the number of AE hits per 10 °C and the analogue seismic b-values against furnace temperature. The analogue seismic b-value is the negative slope of the log-linear AE amplitude-frequency distribution, and was calculated using Aki's maximum likelihood estimate (Aki, 1965). The b-values were calculated for every 200 AE hits, in 100 hit intervals (as in Heap et al. (2013a)). A relatively high b-value indicates a greater proportion of low amplitude AE, and a relatively high b-value indicates a greater proportion of low amplitude AE.

For the Westerly Granite (Figure 4.11a), the onset of AE was detected at around 70 °C (as seen previously in Figure 4.5, and a similar temperature to the 60–70 °C observed by Yong and Wang (1980)). AE activity increased significantly from 300 °C, increasing to a peak at around 570 °C. Following this, the AE rate decreased sharply, before rising again as the sample heats to 700 °C (Figure 4.11b). The analogue seismic b-value for the Westerly Granite was near constant

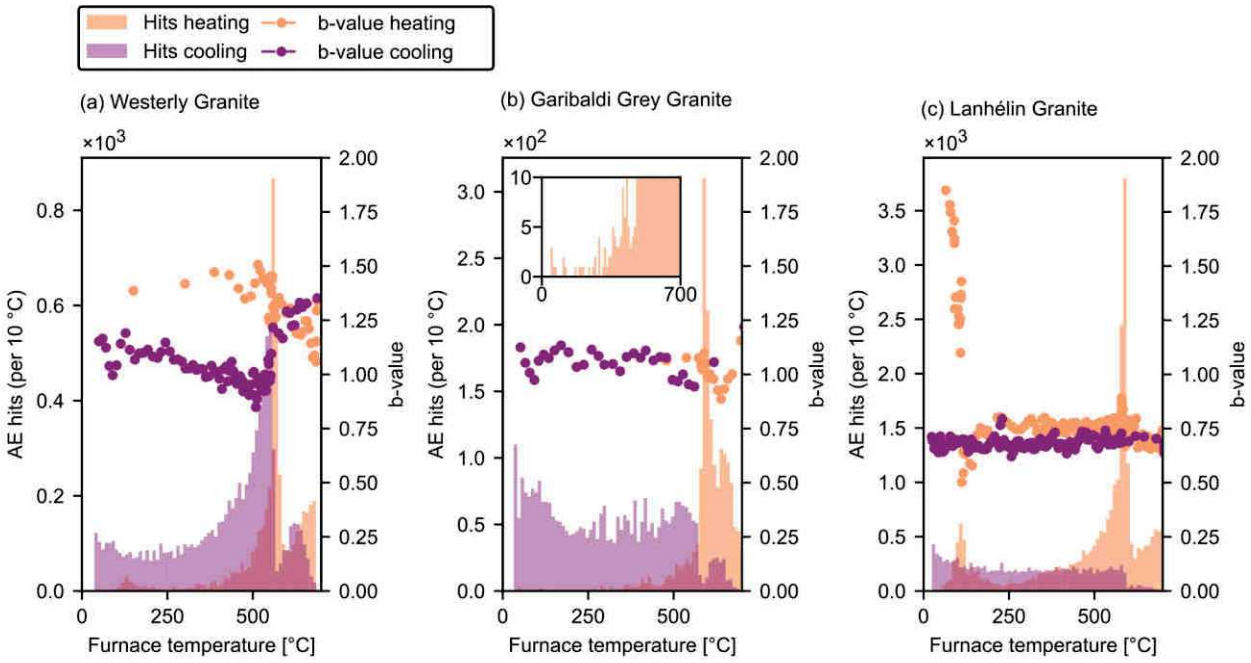

Figure 4.11: Acoustic Emission (AE) hit rate and analogue seismic b-values against furnace temperature in bins of 10 °C during heating and cooling of samples of (a) Westerly Granite, (b) Garibaldi Grey Granite, and (c) Lanhélin Granite to a maximum temperature of 700 °C. The b-values were calculated using the Aki (1965) maximum likelihood method. Note the differences in the y-axis scale (hit rate).

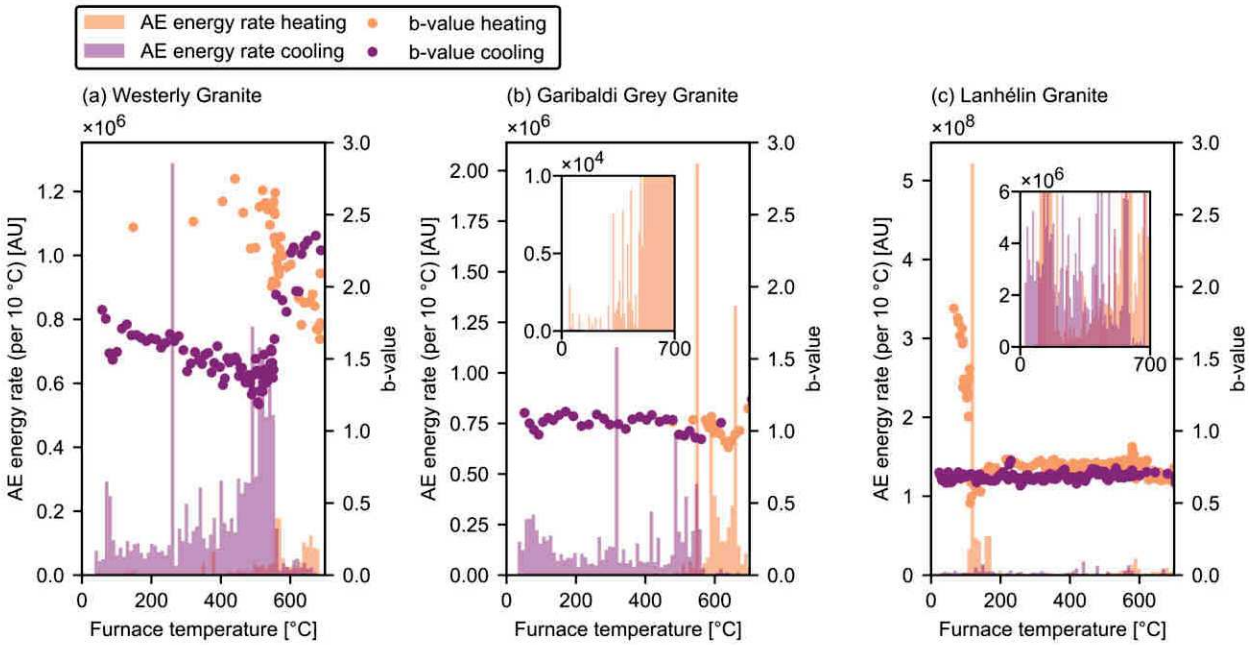

Figure 4.12: Acoustic Emission (AE) energy rate and b-value against furnace temperature in bins of 10 °C during heating and cooling of samples of (a) Westerly Granite, (b) Garibaldi Grey Granite, and (c) Lanhélin Granite to a maximum temperature of 700 °C. Analogue seismic b-values were calculated using the Aki (1965) maximum likelihood method. Note the differences in scale along the y-axis (energy rate).

during heating, at around 1.4 until 500 °C, where it fluctuates before decreasing to near 1 at 700 °C.

For the Westerly Granite during cooling, the AE rate, initially low, increased slightly to 100 hits/10 °C at 630 °C before decreasing again. At around 570 °C AE activity increased suddenly, reaching a peak of around 500 hits/10 °C. From this peak, as the Westerly Granite cooled, the number of AE with temperature decreased as the rock cooled, stabilising at 100 hits/10 °C at 250 °C. During cooling, the b-value for the Westerly Granite was initially higher than during heating, at 1.3, and decreased sharply across 570 °C to 1. Throughout the rest of cooling the b-value increased gradually, reaching 1.1 at room temperature.

Although the onset of AE for the Garibaldi Grey Granite was observed at a similar temperature (see inset of Figure 4.11b), a low number were detected during heating between room temperature and 250 °C. From 250 °C, the AE rate increased, reaching a peak of 250 hits/10 °C at around 570 °C (note the difference in the y-axis scale between the granites), and remained high throughout the rest of heating. Similar to the Westerly Granite, a bump in AE activity for the Garibaldi Grey Granite was observed during cooling at around 630 °C. AE activity increased to 50 hits/10 °C at 550 °C, and remained constant

throughout the rest of cooling (Figure 4.11b). The b-value could only be calculated from around 400 °C during heating due to the low number of AE hits detected. The b-value is near constant during heating and cooling (1–1.1), apart from a slight decrease at 600 °C during heating (Figure 4.11b).

The onset of AE activity for the Lanhélin Granite is observed at around 60 °C, and reaches a local peak of around 500 hits/10 °C at 100 °C (Figure 4.11c). From 250 °C, AE activity increased up to a maximum of ~3500 hits 10/ °C at 570 °C. As for the other granites, the AE rate decreased above 600 °C (to ~500 hits/10 °C). As the Lanhélin Granite cooled, the AE rate was initially low, and increased to 2500 hits/10 °C at 570 °C, where it remained during the rest of cooling (Figure 4.11c). Initially high at 1.75, the b-value showed a sharp decrease to 0.5 at around 100 °C. The b-value then increased to around 0.75, remaining around this value throughout heating, with a small increase at 570 °C, and subsequent decrease between 600 °C and 700 °C. During cooling, the b-value was near constant, at around 0.7, slightly lower than during heating.

Figure 4.12 shows the AE energy rate (given in arbitrary units) with furnace temperature for all three granites. As high energy hits have high amplitudes, they therefore contribute to a decrease in the b-value, meaning that in this case, the AE energy offers no additional information to the AE amplitude data. For this reason, only the number of AE hits and the analogue seismic b-value are discussed.

4.2.2.3 *Microcrack density microanalysis*

Following the methodology presented in Chapter 3 (Griffiths et al., 2017a), the mean crack length ($2c$), the number of cracks per unit area (N_A), the 2D crack density ($\gamma = N_A c^2$; Walsh (1965)), and the surface area per unit volume (S_V; Underwood (1967)) were calculated from optical micrographs of thin sections of Garibaldi Grey Granite and Lanhélin Granite. Un-heated samples, and samples heated to 300 and 700 °C (both slow and shock-cooled) were analysed. Results are shown in Figure 4.15.

Figure 4.13 and Figure 4.14 and show the distributions of the number of intersections of microcracks within the thin sections of the thermally-stressed Garibaldi Grey and Lanhélin samples with horizontal, P_I, and vertical, P_{II} test lines (see Chapter 3 for details). S_V is equal to their sum (Underwood, 1967). As for the processed micrographs of Garibaldi Grey Granite in Chapter 3, no spatial preference for thermal microcracking or microcrack orientation was observed within the thin sections.

For the Garibaldi Grey Granite slow-cooled samples, the microcrack length decreased slightly with thermal stressing temperature, from 0.073 mm in the unheated sample to 0.062 mm in the sample heated to 700 °C (Figure 4.15). The crack lengths in the shock-cooled

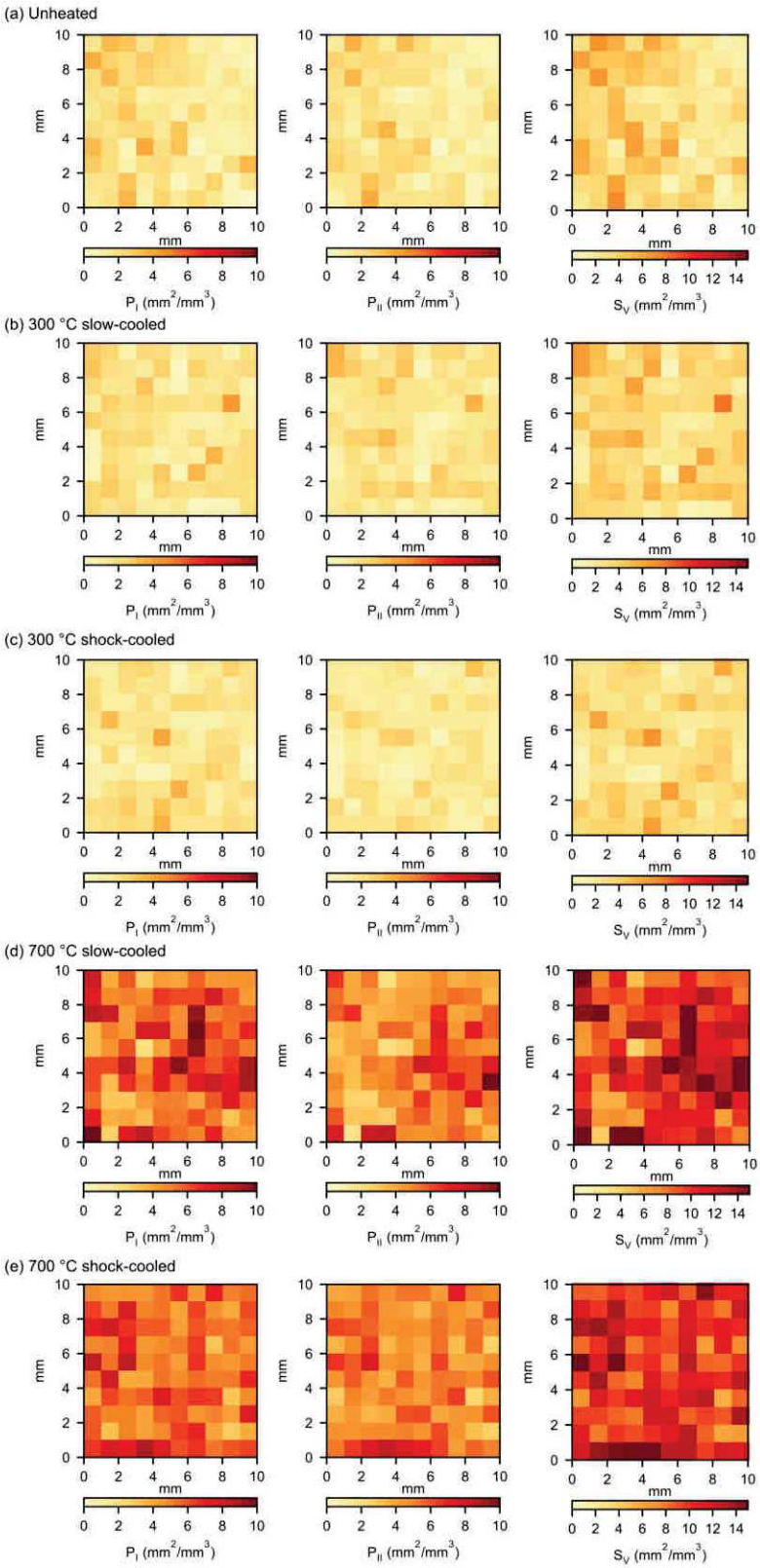

Figure 4.13: Number of intersections of microcracks with the horizontal (P_I) and vertical (P_{II}) test lines and their sum, the crack surface area per volume, S_V (Underwood, 1967), for thin sections of Garibaldi Grey Granite samples heated to 300 °C and 700 °C (both cooled at 1 °C and shock-cooled by quenching).

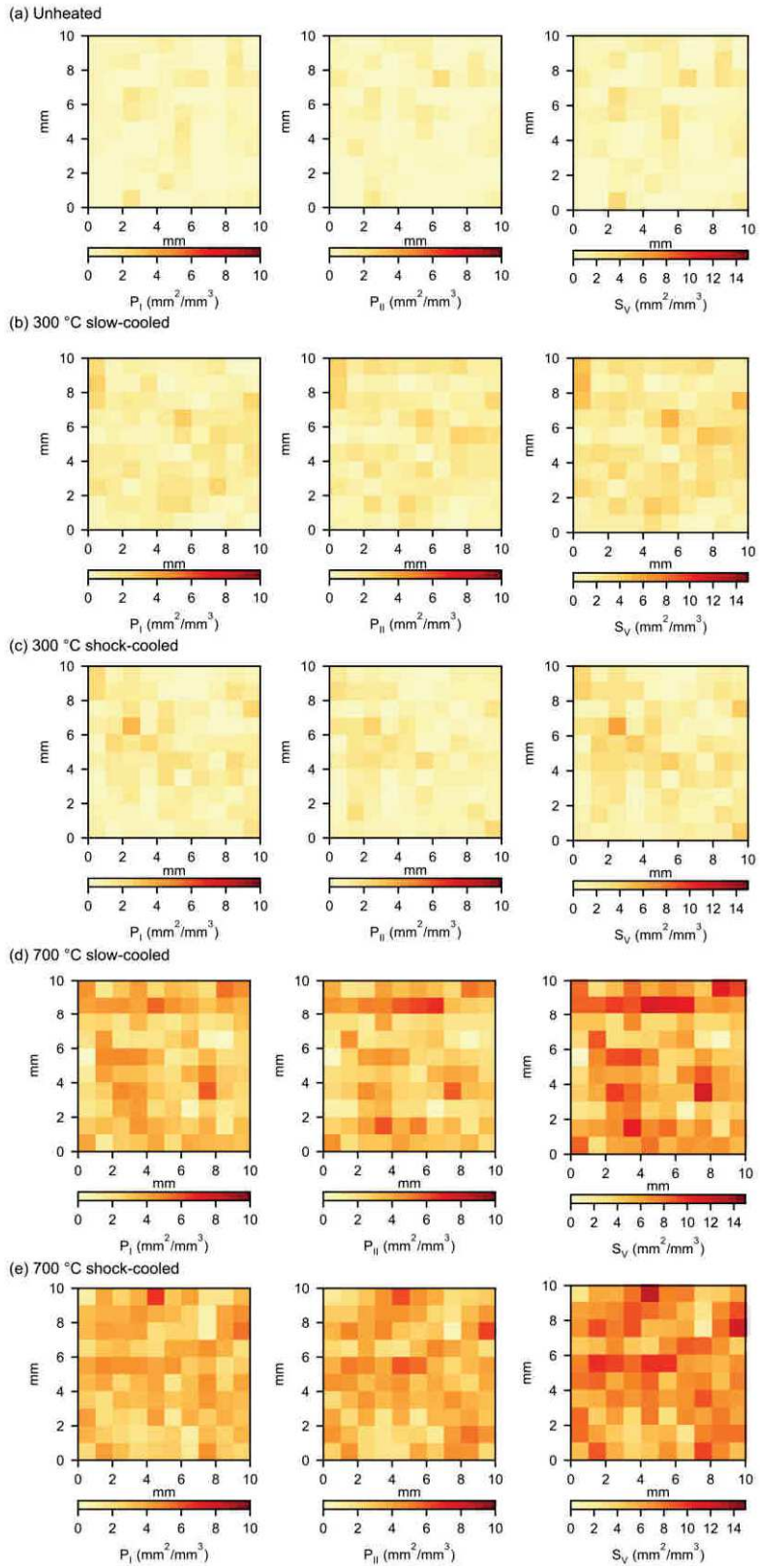

Figure 4.14: Number of intersections in the horizontal (P_I) and vertical (P_{II}) test lines and their sum, the crack surface area per volume, S_V (Underwood, 1967), for thin sections of Lanhélin Granite samples heated to 300 °C and 700 °C (both cooled at 1 °C and shock-cooled by quenching).

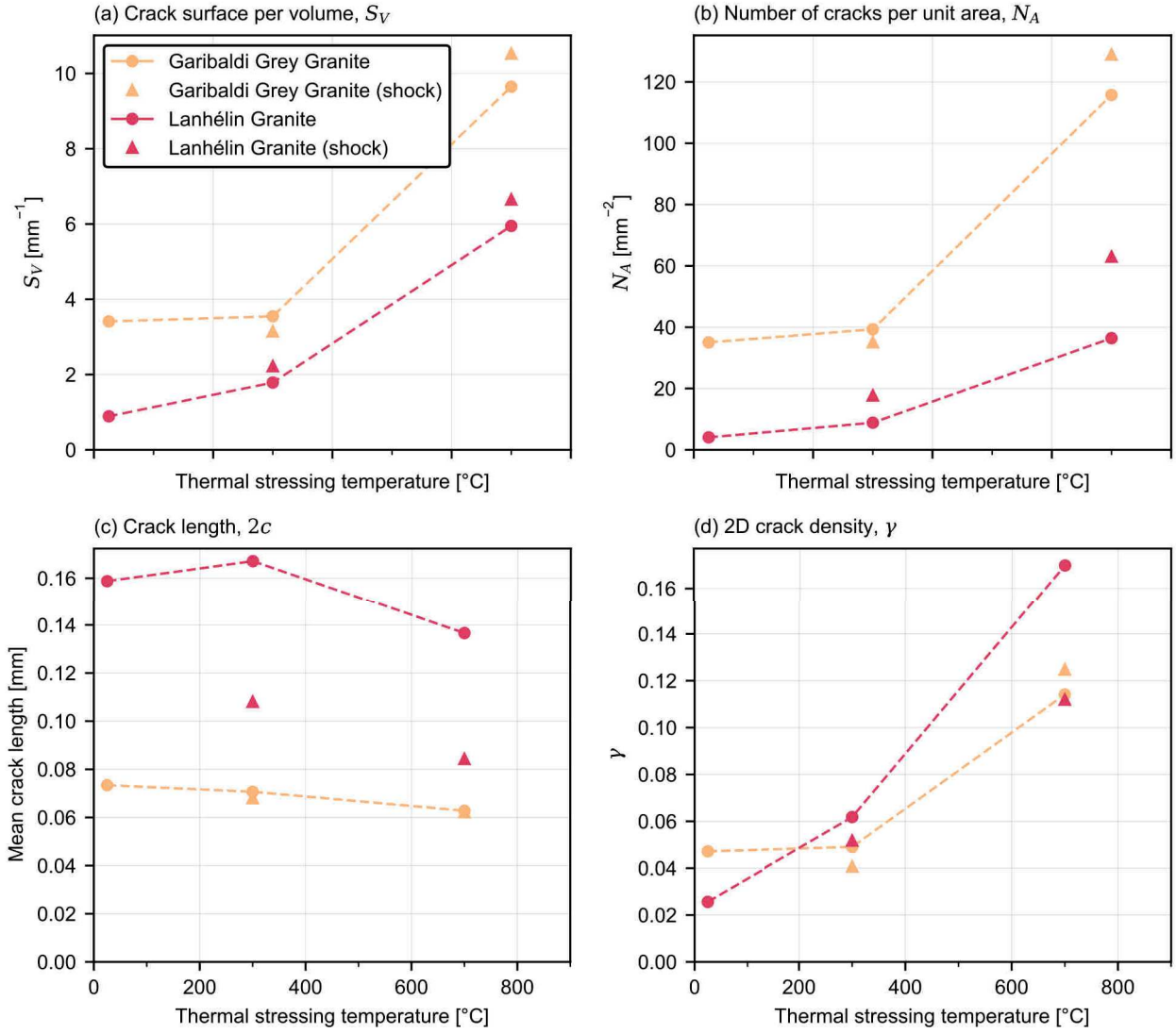

Figure 4.15: (a) Calculated crack surface area per volume (S_V; Underwood (1967)), (b) number of cracks per unit area (N_A) (c) mean crack length ($2c$) and (d) crack density (γ) against maximum heating temperature for samples of Garibaldi Grey Granite, Lanhélin Granite, intact samples and samples heated to 300 °C and 700 °C (both cooled at 1 °C (circles) and "shock" cooled by quenching (triangles). Dashed lines simply join the data points for the samples cooled at 1 °C/min to improve visibility.

samples are similar to their slow-cooled counterparts. These crack lengths are about half of those reported by Hadley (1976) for unheated Westerly Granite (~0.018 mm). Between the intact and 300 °C samples, S_V (3.4 mm^{-1}), N_A (35 mm^{-2}), and γ (0.047) show little changes from their initial values. Between the 300 °C and 700 °C samples, however, S_V increased to 9.6 mm^{-1}, N_A increased to 116 mm^{-2}, and γ increase to 0.11 (Figure 4.15). The extent of microcracking for the 700 °C shock-cooled samples is greater still (S_V of 10.5 mm^{-1}, N_A of 129 mm^{-2}, and γ of 0.124).

The mean microcrack length is greater in the unheated Lanhélin Granite at 0.16 mm than in the unheated Garibaldi Grey Granite (Figure 4.15), which is closer to the values reported by Hadley (1976) for Westerly Granite. In the slow-cooled Lanhélin Granite, the mean crack length increases to 0.17 mm in the 300 °C sample, and decreases to 0.14 mm in the 700 °C sample (Figure 4.15). The crack lengths of the shock-cooled Lanhélin samples are significantly lower than the slow-cooled equivalents, at 0.11 mm and 0.084 mm in the 300 and 700 °C samples respectively.

As $\gamma = N_A c^2$ (Walsh, 1965), the crack length, lower for the shock-cooled samples, influences γ more strongly than the number of microcracks, whereas S_V is a function of the total microcrack length. As microcracks within the binary image are separated at junction points, the crack density is artificially decreased when cracks meet. For this reason, S_V is a more reliable metric for quantifying the microcrack damage here. A similar conclusion was made by Homand-Etienne and Houpert (1989), who preferred S_V over the number of cracks per unit area, N_A, as the latter favours small cracks.

For the Lanhélin Granite, S_V increases with temperature to 1.79 /mm in the 300 °C slow-cooled sample, then to 5.95 /mm in the 700 °C slow-cooled sample.

4.2.2.4 *Physical, transport and thermal properties*

POROSITY AND v_P AND PERMEABILITY Figure 4.16 reports the measurements of the connected porosity, v_P, and permeability of the thermally-stressed samples of Garibaldi Grey and Lanhélin granites. Also shown are measurements for the Westerly Granite samples: unheated, and heated to 400, 450, and 700 °C.

For the Garibaldi Grey Granite, with thermal stressing temperature, measurements show: a porosity increase from 0.93 % (unheated) to 3.70 % (900 °C; Figure 4.16a); a permeability increase from 4.11×10^{-18} m^2 (300 °C) to 2.20×10^{-15} m^2 (900 °C; Figure 4.16c); and a decrease in v_P from 4.37 km/s (unheated) to 1.38 km/s (900 °C; Figure 4.16b).

For the Westerly Granite, porosity and v_P follow a similar trend to the Garibaldi Grey Granite (Figure 4.16d), except for the porosity at 700 °C, which is greater (3.08 % for the Westerly Granite, compared to 2.45 % for the Garibaldi Grey Granite).

For the Lanhélin Granite, the change with temperature is significant: porosity increases from 0.35 % (unheated) to 4.29 % (900 °C); permeability increases from 1.8×10^{-18} m^2 (300 °C) to 2.81×10^{-14} m^2 (900 °C); and v_P decreases from 6.00 km/s (unheated) to 1.21 km/s (900 °C).

THERMAL PROPERTIES Figure 4.17 shows the thermal diffusivity, the thermal conductivity, and the specific heat of the thermally-stressed samples of Westerly, Garibaldi Grey, and Lanhélin granites against thermal stressing temperature. The thermal diffusivity an conductivity of the Garibaldi Grey Granite decrease from 1.46×10^{-6} m/s^2 and 2.78 W/mK in the unheated sample, to 0.79 mm^2/s and 1.42 W/mK in the 900 °C sample, respectively.

For the Westerly Granite, the thermal diffusivity decreased from 1.25×10^{-6} m/s^2 in the intact sample to 1.01×10^{-6} m/s^2 in the sample heated to 700 °C, and the conductivity decreased from 2.52 W/mK (intact) to 2.11 W/mK (700 °C).

The Lanhélin Granite shows a decrease from the initially higher diffusivity and conductivity of the unheated sample of 1.97×10^{-6} m/s^2 and 3.17 W/mK, to 0.70 mm^2/s and 1.45 W/mK in the sample heated to 900 °C (Figure 4.17). Regardless of thermal stressing, the specific heat remains near constant, at 1.9 MJ/m^3.K, 2.0 MJ/m^3.K, and 2.1 MJ/m^3.K for the Garibaldi Grey, Westerly, and Lanhélin granite samples respectively.

4.2.2.5 *Mechanical properties*

Figure 4.18 shows the uniaxial stress-strain curves of the mechanical tests performed on the unheated, 300 °C, 700 °C (slow- and shock-cooled) samples of Garibaldi Grey Granite and Westerly Granite. The peak stresses (UCS) of the stress-strain curves (Figure 4.18) are shown in Figure 4.19. The UCS of the Garibaldi Grey Granite is seen to decrease with thermal stressing temperature—from 287 MPa (unheated) to 122 MPa (900 °C) (Figure 4.19d). The UCS of the Lanhélin Granite unheated samples and the sample heated to 300 °C are similar, at around 150 MPa, and both the 700 °C samples are weaker (UCS of 60-70 MPa; Figure 4.18). The largest decrease in UCS is observed in the granite samples heated to 600 °C and above, in which the quartz has undergone the α/β transition (Glover et al., 1995).

The Young's moduli of the thermally-stressed samples were calculated from the linear section of the stress-strain curves (Figure 4.18) and are given in Table 4.3. The Young's modulus of the Garibaldi Grey Granite decreased with heating temperature, from 74 GPa for the unheated rock, to 68 GPa for the 300 °C sample, and 39 GPa for the 700 °C sample (Table 4.3). The Garbaldi shock-cooled samples were also less stiff than the slow-cooled: 63 GPa for the shock-cooled 300 °C sample; and 28 GPa for the shock-cooled 700 °C sample. The stiffness

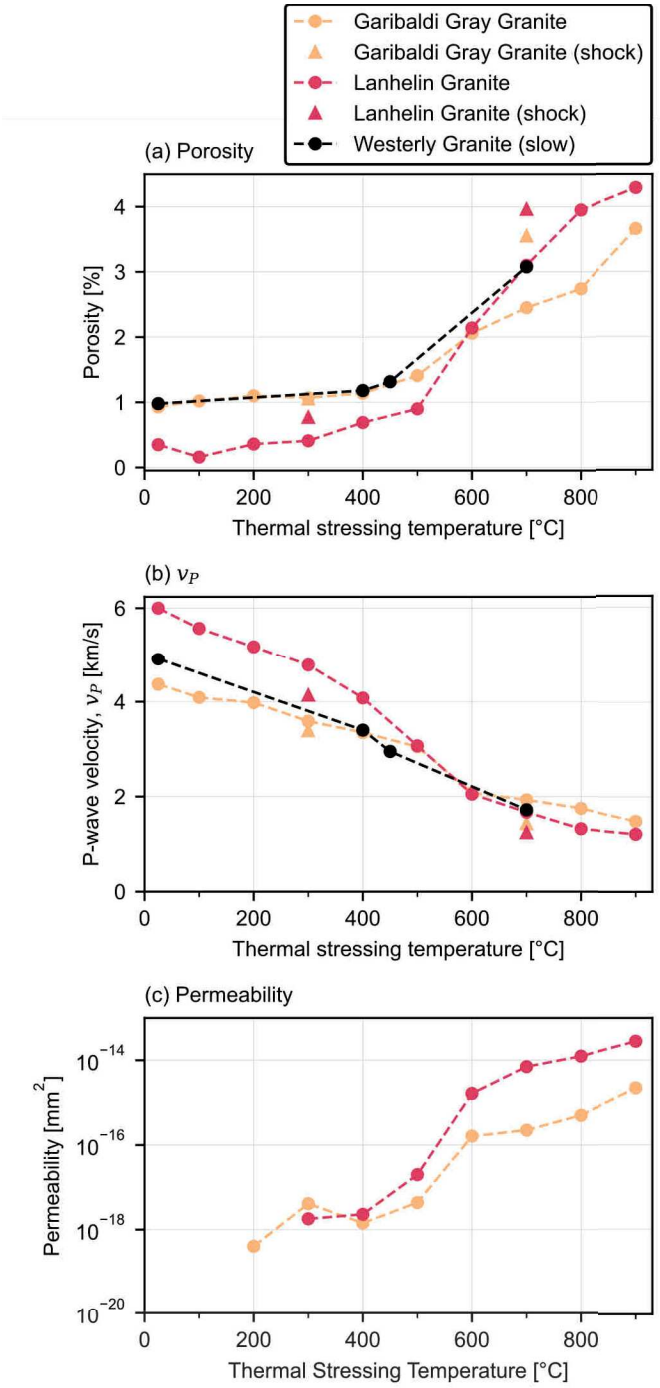

Figure 4.16: (a) Porosity, (b), P-wave velocity (v_P), and (c) permeability. Circles represent the samples cooled at 1 °C/min, and triangles represent the samples "shock"-cooled by quenching. Dashed lines simply join the slow-cooled data points for each rock to improve visibility.

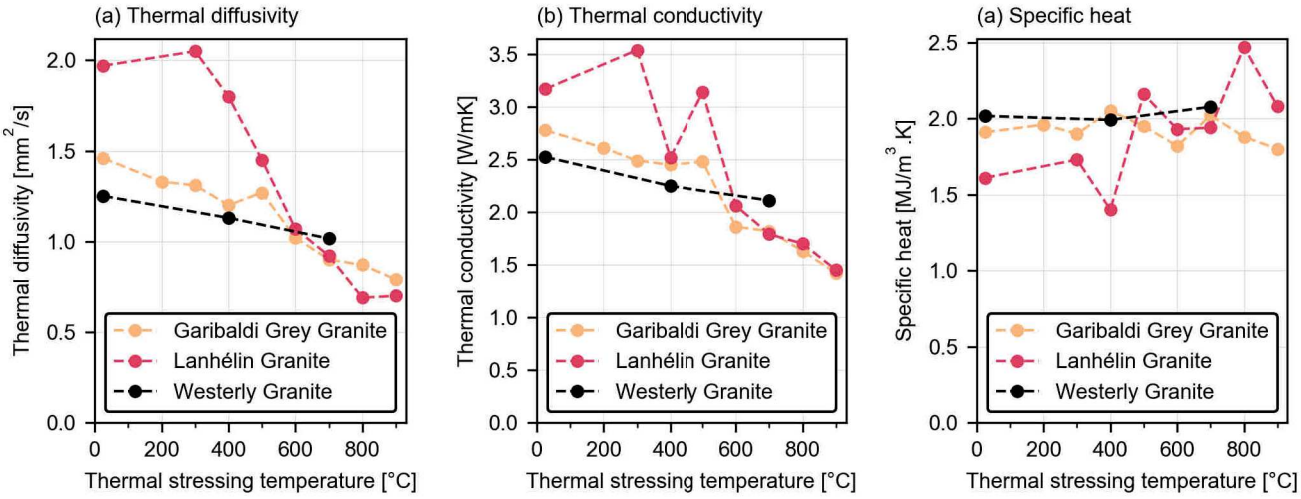

Figure 4.17: (a) Thermal diffusivity, (b) conductivity and (c) specific heat of thermally-stressed samples of Westerly Granite, Garibaldi Grey Granite and Lanhélin Granite against thermal stressing temperature (cooled at 1 °C/min). Measurements were made using a Hot Disk TPS 500 Thermal Constants Analyser. Dashed lines simply join the data points to improve visibility.

of the Lanhélin Granites heated to 300 °C (64 GPa for the slow-cooled, and 58 GPa for the shock-cooled) are similar to the 54 GPa calculated for the unheated sample (Table 4.3). The Young's moduli of the 700 °C samples are lower, at 14 GPa for the slow-cooled sample, and 11 GPa for the shock-cooled.

Triaxial tests were performed on dry samples of thermally-stressed and unheated Garibaldi Grey Granite. These tests were performed to examine the effect of microcrack closure on their influence on the strength of the Garibaldi Grey Granite. Wang et al. (2013) previously observed the influence of thermal microcracks within Westerly Granite on mechanical failure to decrease when confining pressure was applied. Figure 4.20 shows the differential stress (the difference between the axial stress σ_1 and the confining pressure σ_3) against strain, under uniaxial conditions (Figure 4.20a), and under confining pressures of 5 and 10 MPa (Figure 4.20b and c). At 5 MPa, the peak stress for the 300 and 700 °C samples increases to roughly 275 MPa, which is similar to the UCS of the unheated sample. At 10 MPa confining pressure, the peak stress is again similar between samples, but greater than at 5 MPa (around 350 MPa; Figure 4.20c).

As under uniaxial conditions, the elastic modulus (from the slope of the linear section of the stress-strain curves in Figure 4.20) of the 700 °C sample when deformed under 5 MPa confining pressure (57 GPa) is lower than the 300 °C (72 GPa), which is in turn lower than the unheated rock (84 GPa; Table 4.3). At 10 MPa, the unheated and

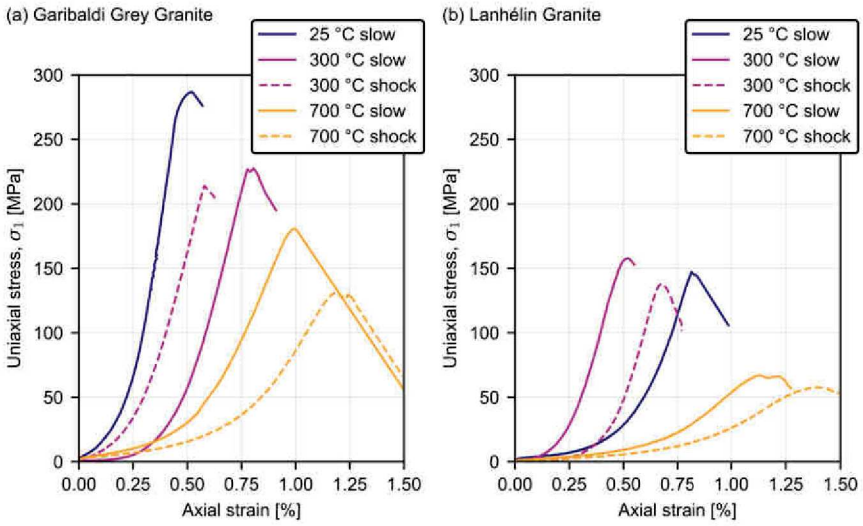

Figure 4.18: Uniaxial stress against axial strain measured during uniaxial tests to failure on non-heated, 300 °C and 700 °C (cooled at 1 °C/min and shock-cooled) samples of (a) Garibaldi Grey Granite, and (b) Lanhélin Granite.

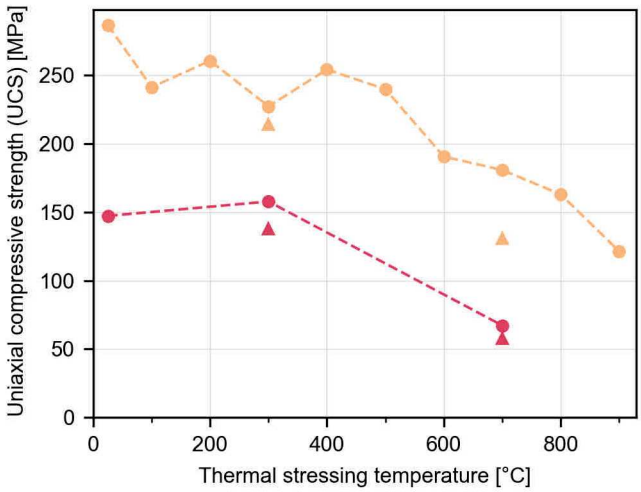

Figure 4.19: Uniaxial Compressive Strength (UCS) of Garibaldi Grey Granite and Lanhélin Granite against maximum heating temperature (25–900 °C). Circles represent the samples cooled at 1 °C/min, and triangles represent the samples "shock"-cooled by quenching. UCS was measured for samples heated to temperatures ranging from 25 to 900 °C for Garibaldi Grey Granite and temperatures of 25, 300 and 700 °C for Lanhélin Granite. Dashed lines simply join the data points for the samples cooled at 1 °C/min to improve visibility.

Granite	Temperature	Heating rate	Confining pressure [MPa]	Elastic modulus [GPa]
Garibaldi Grey	Unheated	-	-	74
	Unheated	-	5	84
	Unheated	-	10	86
	300 °C	1 °C/min	-	68
	300 °C	Shock	-	63
	300 °C	1 °C/min	5	72
	300 °C	1 °C/min	10	93
	700 °C	1 °C/min	-	39
	700 °C	Shock	-	28
	700 °C	1 °C/min	5	57
	700 °C	1 °C/min	10	62
Lanhélin	Unheated °C	1 °C/min	-	54
	300 °C	1 °C/min	-	64
	300 °C	Shock	-	58
	700 °C	1 °C/min	-	14
	700 °C	Shock	-	11

Table 4.3: Elastic moduli of the thermally-stressed granite samples, calculated from uniaxial stress-strain data for Garibaldi Grey Granite and Lanhélin Granite (Figure 4.18), and from stress-strain data under confinement on Garibaldi Grey Granite (Figure 4.20).

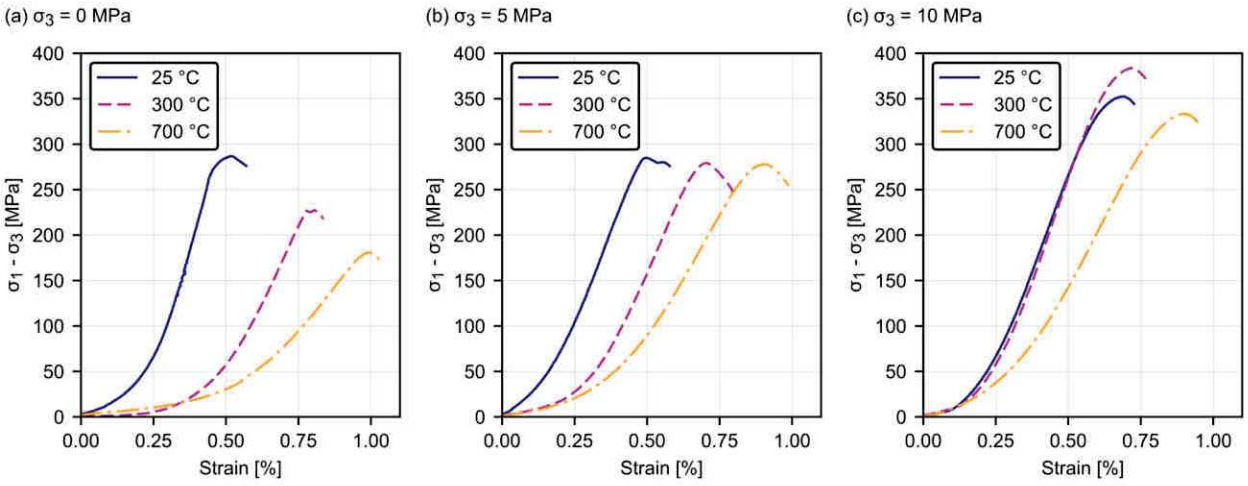

Figure 4.20: Differential stress against axial strain for triaxial tests on non-heated, 300 °C and 700 °C (cooled at 1 °C/min) Garibaldi Grey Granite samples, at confining pressures of (a) 0 MPa, (b) 5 MPa, and (c) 10 MPa.

300 °C samples are of a similar stiffness (86 and 93 GPa respectively), and the 700 °C sample is less stiff (62 GPa).

4.2.3 *Discussion*

4.2.3.1 *Monitoring thermal microcracking*

THE ONSET OF AE In all the AE monitoring experiments to 700 °C under 310 N load (1 MPa), the onset of AE was observed at around 80 °C for the Westerly Granite, 65 °C for the Lanhélin Granite, and 100 °C for the Garibaldi Grey Granite (Figure 4.11 and Table 4.4). In the Westerly and Lanhélin Granites, there was a clear peak in the number of detected AE with temperature at around 100 °C. This was also observed by Glover et al. (1995) when they performed AE monitoring during heating of La Peyratte Granite to 900 °C, which has a grainsize of 1.5 mm in diameter Glover et al. (1995). This peak was also observed for the Westerly Granite (Figure 4.5) and the Lanhélin Granite (Figure 4.10) while heating to 450 °C.

For the Garibaldi Grey Granite, the number of AE hits detected at the onset of thermal microcracking was much lower than for the Lanhélin Granite (see Figure 4.11b). This suggests that thermal microcrack events during the first 200 °C are few in number, low in amplitude, or both. The large decrease in v_P during heating (Figure 4.9) does suggest, however, that thermal microcracks extended or widened during heating, and therefore the associated AE hits may have been below the detection threshold of the experimental apparatus.

Granite	Onset of AE	Porosity (unheated)	Grain size
Westerly	80 °C	1.18 %	0.75 mm (Fredrich et al., 1989)
Garibaldi Grey	100 °C	0.93 %	1 mm
Lanhélin	65 °C	0.35 %	2 mm
La Peyratte	70 °C (Glover et al., 1995)	0.435 % (David et al., 1999)	1.5 mm (Glover et al., 1995)
Ailsa Craig	125 °C (Jones et al., 1997)	0.9 % (Odling et al., 2007)	0.25 mm (Odling et al., 2007)

Table 4.4: The temperature of the onset of AE during heating, porosity and grain size of Westerly, Garibaldi Grey, Lanhélin, La Peyratte and Ailsa Craig granites, from results of this study and David et al. (1999), Fredrich et al. (1989), Glover et al. (1995), Jones et al. (1997), and Odling et al. (2007)

Table 4.4 reports the temperature of the onset of AE during heating, the porosity and the grain size of Westerly, Garibaldi Grey, Lanhélin granites, and the La Peyratte (David et al., 1999; Glover et al., 1995) and Aisla Craig (Jones et al., 1997; Odling et al., 2007) granites. There is no apparent correlation between the grain size and the temperature at the onset of AE. However, the onset is generally at lower temperatures in the granites which have lower initial porosities (Lanhélin and La Peyratte; Table 4.4). This could be due to where initial microcrack porosity is lower, there is less void space within the rock to accommodate the thermal expansion of grains, resulting in microcracking at lower temperatures. It should be noted, however, the temperature of the onset of AE observed using different systems may vary (Yong and Wang, 1980).

Note also that the onset of AE in granite has also been linked to fluid decrepitation (the fracturing of grains containing fluid inclusions), which may occur between 75 °C and 573 °C in Westerly Granite, and is thought to be one of the main causes of intragranular cracking in granite below the α/β transition of quartz (Hall and Bodnar, 1989). Detected AE hits may therefore include microcracking events due to fluid decrepitation.

A greater number of AE was detected at the onset of AE for the Lanhélin Granite than for the Westerly and Garibaldi Grey granites (Figure 4.11). The analogue seismic b-value could therefore be calculated throughout the initial heating of the Lanhélin Granite (Figure 4.11). The Lanhélin Granite b-value was seen to decrease sharply between 70 and 110 °C (Figure 4.11), indicating that microcrack events at the onset of AE (at 70 °C) were smaller in amplitude than the AE detected at 100 °C, at which temperature a peak in AE rate was observed. The Lanhélin Granite b-value subsequently increases to around 1.5.at 110–150 °C. This suggests that at the onset of thermal microcracking, microcracks propagate over smaller distances compared to at higher temperatures, and that the largest cracks are formed at around 110 °C. The lower number of detected AE for the Garibaldi Grey and West-

erly granites meant that the amplitude distribution at the onset of AE could not be established.

To study the temperature conditions required for thermal microcracking in multi-phase rock, Fredrich and Wong (1986) proposed a micromechanical model, considering a 2D square inclusion (of side equal to the diameter of a grain). They linked the thermal expansion mismatch and anisotropy of the inclusion to the stress intensity factor at microcrack tips, both inter- and intra-granular. Fredrich and Wong (1986) then calculated the threshold temperatures for thermal microcrack propagation, i.e. the temperature increase required for the stress intensity factor to reach the fracture toughness.

Equation 4.4 gives the expression of the stress intensity factor as a function of a, the initial microcrack length, and the normal stresses to the crack, σ_{yy}.

$$K_I = \left(\frac{2}{\pi a}\right)^{1/2} \int_0^a \frac{\sigma_{yy}(x) x^{1/2}}{(a-x)^{1/2}} dx \tag{4.4}$$

Equation 4.5 is the normal stress along the length of an intragranular microcrack, and Equation 4.6 is the normal stress on the grain boundary, both due to a thermal expansion mismatch ($\Delta\alpha$) (Fredrich and Wong, 1986). Equation 4.7 is the normal stress along the length of an intragranular microcrack, and Equation 4.8 is the normal stress on the grain boundary due to a thermal expansion mismatch caused by a thermal expansion anisotropy ($\Delta\alpha'$).

$$\sigma_{yy\ \text{intra}} = \frac{E\Delta\alpha\Delta T}{2\pi(1-\nu)} \ln\left[\frac{(x+\sqrt{2}L)^2 + 2L^2}{x(x+2\sqrt{2}L)}\right] \tag{4.5}$$

$$\sigma_{yy\ \text{inter}} = \frac{E\Delta\alpha\Delta T}{2\pi(1-\nu)} \left[\arctan\left(\frac{x}{2L}\right) + \arctan\left(1-\frac{x}{2L}\right) - \pi\right] \tag{4.6}$$

$$\sigma'_{yy\ \text{intra}} = \frac{E\Delta\alpha'\Delta T}{2\pi(1-\nu^2)} \ln\left[\frac{(x+\sqrt{2}L)^2 + 2L^2}{x(x+2\sqrt{2}L)}\right] \tag{4.7}$$

$$\begin{aligned}\sigma'_{yy\text{inter}} = {} & \frac{E\Delta\alpha'\Delta T}{2\pi(1-\nu^2)} \frac{4L^2}{4L^2+(2L-x)^2} \\ & - \frac{4L^2}{4L^2+x^2} + \ln\left(\frac{2L-x}{x}\right) \\ & - \frac{1}{2}\ln\left(\frac{4L^2+(2L-x)^2}{4L^2+x^2}\right)\end{aligned} \tag{4.8}$$

The normal stresses are a function of the change in temperature (ΔT), the thermal expansion mismatch $\Delta\alpha$), the grain size (L, equal to half the grain size), the Young's modulus (E), and the Poisson's ratio (ν) of the rock are also required by the model.

Here, a square inclusion was considered of side 1 mm ($2L$) for the Garibaldi Grey Granite, and 2 mm for the Lanhélin Granite (the

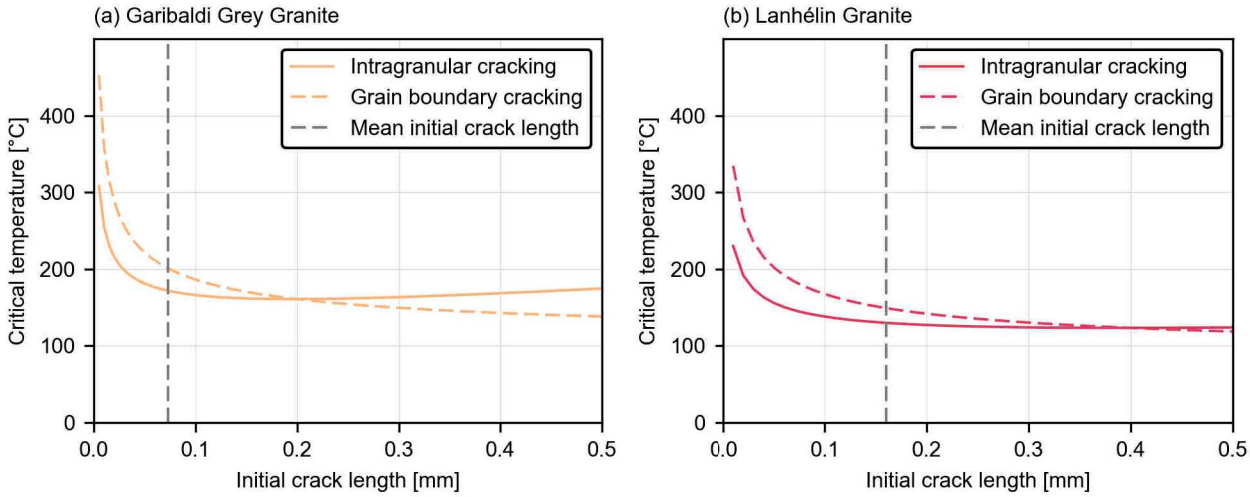

Figure 4.21: The modelled temperature (Fredrich and Wong, 1986) for intragranular (solid lines) and grain boundary (dashed lines) microcrack propagation due to the thermal expansion mismatch and anisotropy (using the values for a quartz inclusion, reported by Fredrich and Wong (1986)) against the initial microcrack length of (a) Garibaldi Grey Granite and (b) Lanhélin Granite.

grain diameter). The Young's modulus of each granite were calculated by the slope of the stress-strain curves during uniaxial deformation of unheated samples of Garibaldi Grey and Lanhélin Granites (Figure 4.18), finding values of 74 GPa and 54 GPa respectively. The Poisson's ratio was taken to be 0.1, the value for Westerly Granite (Brace and Jones, 1971). The thermal expansion mismatch ($\delta\alpha$) between grains and the bulk rock matrix, could not be calculated here as the thermal expansion of the rock matrix is unknown. Instead, values for a quartz inclusion in Westerly Granite are used: the difference in thermal expansion due to mismatch, $3.3 \times 10^{-6}/°C$, and anisotropy, $3.4 \times 10^{-6}/°C$ (Fredrich and Wong (1986)). As such, these calculations should only be interpreted qualitatively.

Figure 4.21 shows the critical temperature for crack propagation as a function of the initial crack length (a) for both inter and intragranular microcracking—when K_I is equal to the critical stress intensity factor, K_{IC} ($0.3\,\mathrm{MPa\,m^{0.5}}$; Atkinson (1984)). The initial mean microcrack lengths of each granite (Figure 4.15) are shown by vertical dashed grey lines. The model predicts a lower temperature threshold for thermal microcracking with increasing grain size, and hence the temperature required for thermal microcrack propagation in the coarser grained Lanhélin Granite is lower than for the Garibaldi Grey Granite, as was observed during AE monitoring (Figure 4.11).

Taking in to account the mean initial crack lengths, the temperature for intragranular thermal microcracking is slightly lower than for intergranular (grain boundary) microcracking (Figure 4.21). Qual-

itatively, significant intra-granular cracking was observed in thin sections of Garibaldi Grey Granite and Lanhélin Granites heated to temperatures of 300 °C and below, where multiple fractures traverse grains (the crack analysis procedure did not differentiate grain boundary and intragranular cracks). Fluid decrepitation likely contributed to the high amount of intra-granular cracking observed here within the samples heated to temperatures of 300 °C and below. Fredrich and Wong (1986) used their model to predict intra-granular microcracks to form at lower temperatures than inter-granular cracks when considering a microcline inclusion. Mineralogy is therefore a strong factor for the onset of thermal microcracking in granite.

It should also be noted that the stresses and stress intensity factors may be up to four times greater for multi-grain structures (i.e. rock) than for a single grain, and depend greatly on the distribution of grain size and geometry, and their mechanical and thermal properties (Evans, 1978b).

AE AT THE α/β TRANSITION OF QUARTZ For all granites, the rate of AE accelerates as the sample temperature reaches around 570 °C (Figure 4.11). This is the temperature of the quartz α/β transition (573 °C at room pressure; Glover et al. (1995)), during which quartz undergoes a rapid thermal expansion, amplifying thermal stresses within the rock, and resulting in increased thermal microcracking. Glover et al. (1995) previously observed the peak in AE rate at 573 °C when monitoring AE during the heating of La Peyratte Granite to 900 °C.

For all granites, the analogue seismic b-value was seen to show a slight increase prior to the α/β transition, and then a decrease at the transition (Figure 4.11). This indicates the formation of many small cracks at the quartz transition. Similar behaviour was observed at the onset of thermal microcracking for the Lanhélin Granite, where microcracking events were initially low in amplitude, becoming larger in amplitude when the AE rate peaked (Figure 4.11). Glover et al. (1995) observed no change in the analogue seismic b-value during heating, however, and it was suggested that during thermal microcracking, the length scale of microcrack events does not change, as it depends on the grain size throughout heating and cooling. Here, results seem to favour the slight increase in b-value with thermal stressing observed by Atkinson et al. (1984).

AE DURING COOLING AE monitoring has rarely been performed on granite during cooling, however, AE activity during cooling is significant for all granites (Figure 4.11). This is contrary to the findings of Todd (1973), who heated Westerly Granite to 300 °C at rates of 2, 5 and 8 °C/min before cooling. Whilst Todd (1973) observed very little AE during cooling and no significant AE during heating at 2 °C/min,

AE was observed during heating at 5 and 8 °C/min. This, and the low number of AE hits detected overall (~200 and ~700 at 5 and 8 °C/min, respectively), suggest that the AE detection threshold was higher than for the experiments presented here.

For all granites, AE during cooling between 700 °C and 570 °C (the temperature of the α/β transition of quartz; Glover et al. (1995)) is lower than during heating in the same temperature range. Above the α/β transition of quartz, the thermal expansion coefficient of β quartz is near zero or negative (Ackermann and Sorrell, 1974) and therefore it may be expected that the AE rate is less as the quartz grains undergo no thermal contraction.

For all granites, AE activity during cooling was highest between the temperature of the quartz α/β transition and room temperature (Figure 4.11). For the Garibaldi Grey and Lanhélin Granite, unlike the AE rate during heating, the AE rate during cooling between 570 °C and room temperature is consistent, suggesting that AE may be due to the frictional sliding of grains, as they contract in a near linear fashion.

During cooling of the Westerly Granite, the b-value showed a strong decrease across the α/β transition, whereas the b-values for the Garibaldi Grey and Lanhélin Granites were constant (Figure 4.11). The decrease in b-value in the Westerly Granite indicates an increase in the length-scale of the AE events. This may be due to the thermal contraction of the quartz as it returns to its α phase, which causes higher amplitude thermal microcracking events. The AE rate during cooling of the Westerly Granite also peaked at this temperature (unlike the other two granites, where AE during cooling was near constant from 570 °C to room temperature) and is indicative of thermal microcracking during cooling. The b-value increased during the rest of cooling, becoming stable at around 250 °C. It is unclear, however, why there is a difference in the AE activity between the Westerly Granite, and the Lanhélin and Garibaldi Grey granites during cooling.

AE PARAMETER ANALYSIS The mean AE amplitudes during heating and cooling are 46 dB for the Westerly, 49 dB for the Garibaldi Grey, and 53 dB for the Lanhélin Granite. This is reflected in the seismic analogue b-values (a decrease in b-value indicates an increasing proportion of high amplitude AE), which are on average lower in the Lanhélin than the Garibaldi Grey Granite, and lower again in the Westerly Granite (Figure 4.11). The Lanhélin granite has the largest average crystal size (Figure 4.8): ~2 mm compared to ~1 mm in the Garibaldi Grey Granite, and 0.75 mm in the Westerly Granite (Meredith and Atkinson, 1985). As the amplitude of AE is characteristic of the size of microcracks (Evans, 1978a), and many cracks form along grain boundaries and across grains, the AE amplitude distributions

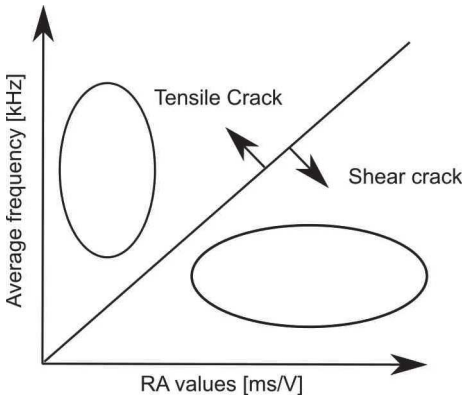

Figure 4.22: Classification of tensile and shear cracks from the relationship between the average frequency and RA values. (adapted from Ohtsu et al. (2007).

are controlled by the grain size, as is the case for the mechanical testing of rock (Evans, 1978a).

It was attempted to differentiate between the AE hits during heating and during cooling by means of the AE parameters (ring-down counts, amplitude, duration, rise time, energy etc.; see Chapter 2). For concrete, a common way to distinguish tensile from shear events is by comparing the average frequency (the number of ring-down counts divided by the duration) with the RA value (which is the rise time, i.e. the time of the peak amplitude, divided by the amplitude) (Ohno and Ohtsu, 2010; Ohtsu et al., 2007). Figure 4.22 provides an illustration: tensile cracks have a higher frequency content overall and reach their peak amplitudes over a shorter duration than shear cracks. Aggelis (2011) used this classification when deforming concrete, to differentiate between tensile cracks prior to failure and mixed-mode fractures at failure. Figure 4.23 shows the average frequency against the RA values during the heating and cooling of the three granite samples, however, there is no clear distinction between the modes of the heating (orange) and cooling (purple) cracks.

Ring-down counts can provide another possible comparison of AE parameters. Figure 4.24 shows the AE ring-down counts during heating (orange) and cooling (purple), against the amplitude of the AE hit for all three granites. Overall, the number of AE counts increases with amplitude, which is expected as higher amplitude hits are detectable for increased durations. The amplitude range of the Westerly and Garibaldi Grey Granites AE are similar—between 40 dB and 80 dB (Figure 4.24)—and there is no clear difference between the AE during heating and cooling. AE from the Lanhélin Granite has a wider range of amplitude, from 40 dB up to 100 dB (Figure 4.24c). During heating, AE hits of a given amplitude seem to have more ring-down counts than during cooling (Figure 4.24). This suggests that during heating, hits are longer in duration. Within the Lanhélin Granite data there

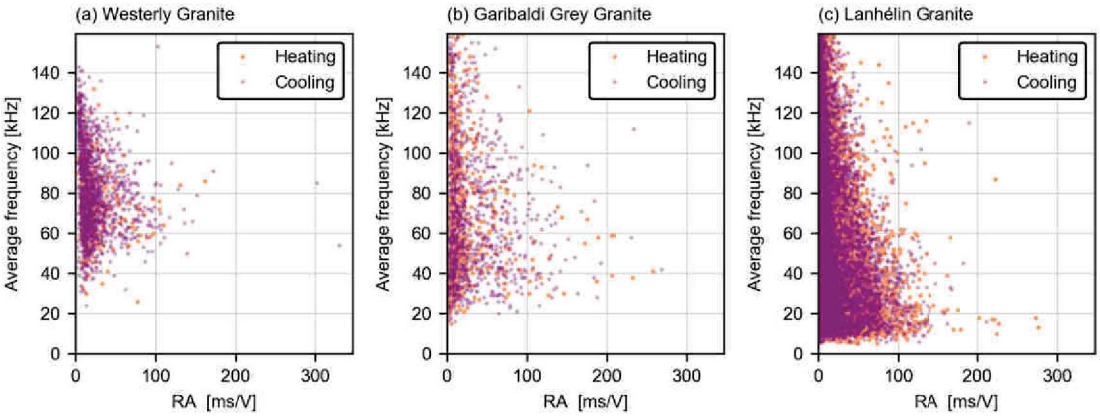

Figure 4.23: Average frequency of AE hits against AE RA values during heating to 700 °C and cooling of samples of (a) Westerly Granite, (b) Garibaldi Grey Granite, and (c) Lanhélin Granite.

are also several AE hits with comparatively low ring-down counts for their amplitudes, which are outside of the main population. The AE waveforms within this group appear similar to the majority (Figure 4.25); their decreased duration may be due to an earlier drop-off in amplitude to below the AE detection threshold.

Baud (1995), who monitored AE during the heating of granite to 900 °C, found two populations of AE hits when ring-down counts were plotted against amplitude (as in Figure 4.24). Whilst there may be an evolution of the AE characteristics during different phases of thermal microcrack development, another possible cause is suggested to be a change in the load on the sample during heating, influencing the coupling with the AE sensor, which is not the case here, as the load is servo-controlled.

IN-SITU VELOCITY MEASUREMENTS For all granites, v_P decreases with increasing temperature; the velocity measured at 450 °C is lower than the v_P when cooled to room temperature (Figure 4.26).

Figure 4.26 shows the relative change in v_P of the three granites with temperature during the cyclic heating and cooling. The decrease in v_P with temperature is greatest for the Westerly and Lanhélin granites, which show a similar relative decrease at 450 °C of around 50 %. The v_P of the Garibaldi Grey Granite is decreased by 30 % at 450 °C. Together with the AE data, this suggests that less thermal microcracking occurred in the Garibaldi Grey Granite during heating to 450 °C.

During cycles two and three, the velocity decrease with temperature is between 10 and 18 %. This difference highlights the value of performing velocity measurements under in-situ repeated thermal stress conditions. Velocity changes are inferred at geothermal reservoirs to monitor reservoir activity (Lehujeur et al., 2017; Obermann

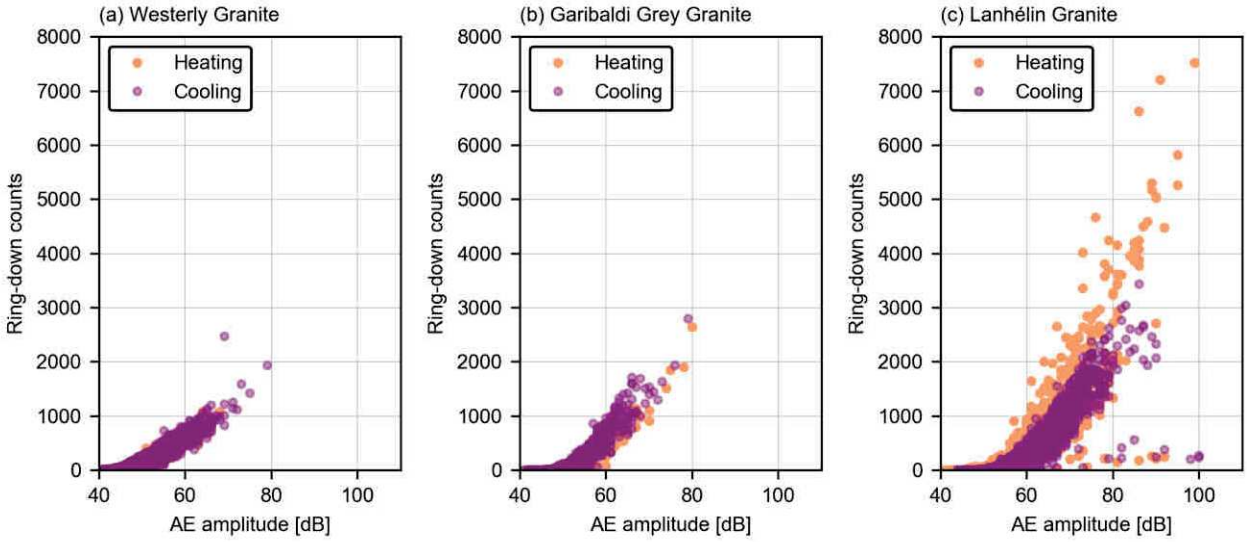

Figure 4.24: Acoustic Emission ring down counts against amplitude during heating and cooling of samples of (a) Westerly Granite, (b) Garibaldi Grey Granite, and (c) Lanhélin Granite to a maximum temperature of 700 °C.

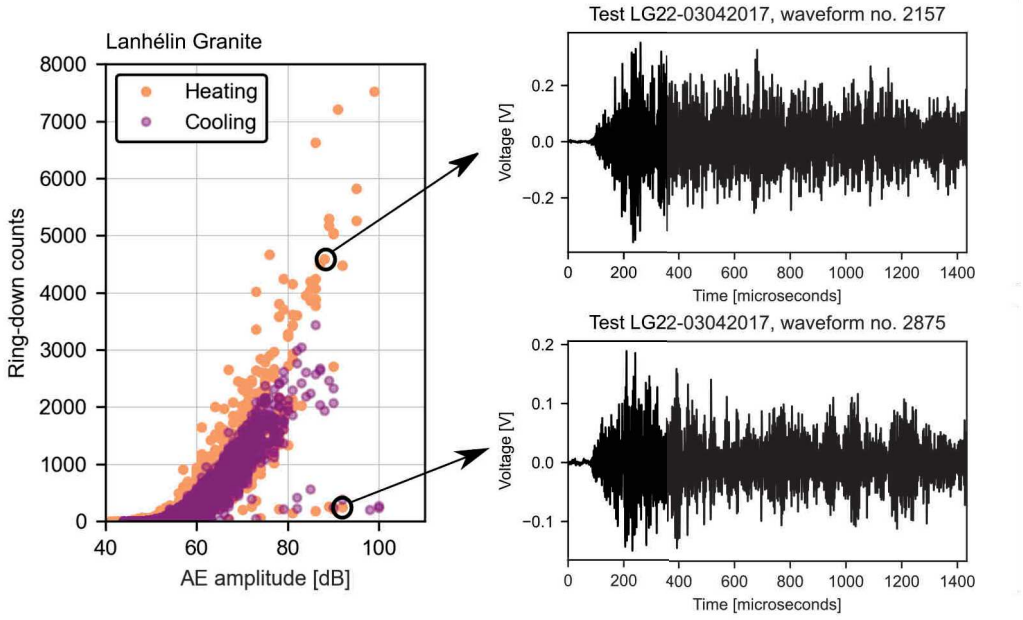

Figure 4.25: Acoustic Emission ring down counts against amplitude during heating and cooling of samples of Lanhélin Granite, alongside two AE waveforms recorded during heating.

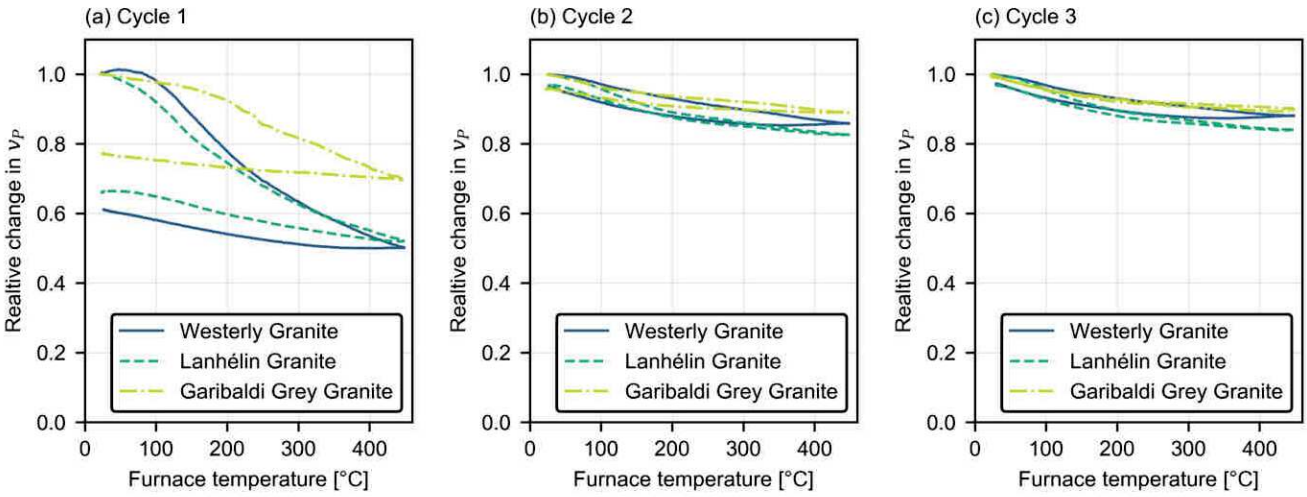

Figure 4.26: Relative change in P-wave velocity (v_P)—normalised to the velocity at the beginning of each cycle—against sample temperature during three heating and cooling cycles of samples of Westerly Granite, Garibaldi Grey Granite, and Lanhélin Granite to a maximum temperature of 450 °C.

et al., 2015), and are often interpreted as changes in fluid saturation. The results here suggest that the temperature component may be significant in such a thermally dynamic environment.

As the increase in v_P during cooling is of a similar amplitude during all three cycles, the AE hits detected during cooling of the first cycle are not expected to be entirely the result of thermal microcracking. It was suggested for the Westerly Granite (Section 4.1) that AE during cooling may be due to the frictional sliding of crystals as they contract, and is applicable also to the Garibaldi Grey and Lanhélin granites. A similar phenomenon was observed by Choi et al. (2005) when they performed AE monitoring during three repeated heating and cooling of composite laminates to a maximum temperature of 160 °C. They attributed AE during the second and third cycles to frictional sliding as the material adjusts to temperature changes.

4.2.3.2 *The influence thermal microcracking on rock properties*

COMPARISON WITH MONITORING DATA In the Garibaldi Grey and Lanhélin granites, with thermal stressing, v_P, the thermal diffusivity, the thermal conductivity and the UCS decrease, while the porosity and permeability increase (Figure 4.16).

Samples heated to just beyond the onset of thermal microcracking (~100–300 °C; Figure 4.11) show an increase in v_P, but little change in porosity (Figure 4.16). The AE and velocity data (Figure 4.11 and Figure 4.26) show that thermal microcracking occurs at these temperatures, but microcracks have a low aperture and contribute little the

crack porosity of the rock. As the granites are heated further, thermal microcracking continues and microcracks widen. Marked changes in v_P (decrease) and porosity (increase) are observed between samples heated to 500 and 600 °C (Figure 4.16). This is due to the increased thermal microcracking caused by the thermal expansion of quartz across the α/β transition (Glover et al., 1995) (Figure 4.11). Large increases in porosity and decreases in permeability have been previously observed in granites heated beyond the α/β transition (Chaki et al., 2008; Glover et al., 1995; Nasseri et al., 2007)

The thermal diffusivity and conductivity of the granites decreased strongly with thermal stressing temperature from 400 °C (Figure 4.17). Thermal properties of cracked materials are strongly influenced by porosity (Zimmerman, 1989), and the 400 °C threshold corresponds to the temperature of the significant porosity increase seen in both granites (Figure 4.16). Kant et al. (2017) measured the thermal diffusivity, conductivity and specific heat of a granite (from the Aare massive of the Swiss Central Alps) during heating to 500 °C and cooling. They found a decrease in thermal diffusivity from 1.7 mm/s^2 to 0.7 mm/s^2 at 500 °C, increasing to 1.3 mm/s^2 when the rock cooled to room temperature (25 % permanent decrease). A similar decrease in thermal diffusivity was measured for the Garibaldi Grey Granite (14 %) and the Lanhélin Granite (30 %) when heated to 500 °C and cooled (Figure 4.17). Kant et al. (2017) also measured an increase in the specific heat with temperature, from around 0.7 kJ/kg/°C to 1.1 kJ/kg/°C at 500 °C. Upon cooling, the specific heat returned to its initial value, resulting in no significant permanent change, as seen for the granites, here (Figure 4.17).

The Garibaldi Grey Granite showed a general decrease in UCS (Figure 4.19). For the Lanhélin Granite, a decrease in UCS observed for the 700 °C samples, but not for the 300 °C samples. When heated to above 600 °C, the significant thermal microcracking, observed by AE monitoring (Figure 4.11), had an increased effect on the strength of both granites under uniaxial conditions.

COMPARISON WITH MICROCRACK DENSITY Figure 4.27 shows the porosity, v_P, permeability, and UCS of the unheated, and 300 °C, and 700 °C (both shock and slow-cooled) samples against the crack surface density, S_V (Underwood, 1967).

The Lanhélin Granite, which contains the lowest initial crack density (Figure 4.15) and has the lowest initial porosity (Figure 4.16), exhibits the greatest relative change in crack density, and physical and mechanical properties with thermal stressing (Figure 4.30 and Figure 4.31).

In the Garibaldi Grey and Lanhélin granites, for a given increase in S_V, the increase in porosity and permeability is greater for the coarser grained Lanhélin Granite (Figure 4.27a and c). This may be due to

the larger aperture of thermal microcracks in the heated Lanhélin Granite, as observed in the microstructure (Figure 4.28). A widening of microcracks increases the porosity and permeability (Guéguen and Dienes, 1989) for a fixed microcrack length.

v_P is less affected by microcrack aperture and, as such, v_P follows a similar linear trend with S_V in both granites (Figure 4.27b). Generally, the evolution of UCS with S_V is less clear, however at high crack densities, a decrease in strength is observed (Figure 4.27d).

Note: the conclusion that microcracking occurs during heating also means that the cracks observed within the heated samples were present when the rock was at the peak temperature which, for example, has implications for modelling of the physical properties of granite at elevated temperatures.

To establish a relationship between measurements of the crack surface per unit volume, S_V, within thermally-stressed Westerly Granite samples and the thermal stressing temperature, Fredrich and Wong (1986) extended the model of Davidge (1981) for grain boundary cracking in polycrystalline materials. The model considers a 2D spherical inclusion and equates the thermoelastic strain energy due to heating to the fracture energy per unit volume. This results in a quadratic relationship between S_V and temperature (Equation 4.9). In Equation 4.9, T is the temperature, and T_0 and S_{V_0} are the initial temperature and crack surface per unit volume, respectively.

$$S_V - S_{V_0} = k(T - T_0)^2 \tag{4.9}$$

Equation 4.9 relates the change in S_V to a quadratic function of the change in temperature, and a multiplicative factor $k = E(\Delta\alpha)/[8(1-\nu)G_{1c}]$. Here, E is the Young's modulus, ν is the Poison's ratio, $\Delta\alpha$ is the average mismatch in thermal expansion, and G_{1c} is the fracture energy parameter. Figure 4.29 shows the values of S_V against thermal stressing temperature and a quadratic fit (Equation 4.9) to the data (by linear regression). Also shown are the data of Fredrich and Wong (1986) for Westerly Granite. Note that the values of Fredrich and Wong (1986) are greater than those measured here. This is in part due to the higher resolution SEM micrographs used by Fredrich and Wong (1986). Here it was decided to use optical micrographs, to facilitate crack mapping over larger areas of thin sections, and for a large number of thin sections (see Chapter 3). The values of S_V calculated here for the Garibaldi Grey Granite are closer to the values of Nasseri et al. (2009a) using optical micrographs of thermally-stressed Westerly Granite: 5.4 mm^2/mm^3 for the intact Westerly Granite and 9.4 mm^2/mm^3 following heating to 650 °C.

The average thermal expansion mismatch, $\Delta\alpha$, for each rock was calculated from: the Young's Modulus of the intact samples of Garibaldi Grey and Lanhélin Granites (74 GPa and 54 GPa, respectively; Table 4.3); the Poisson's ratio of Westerly Granite (0.1; Brace and Jones

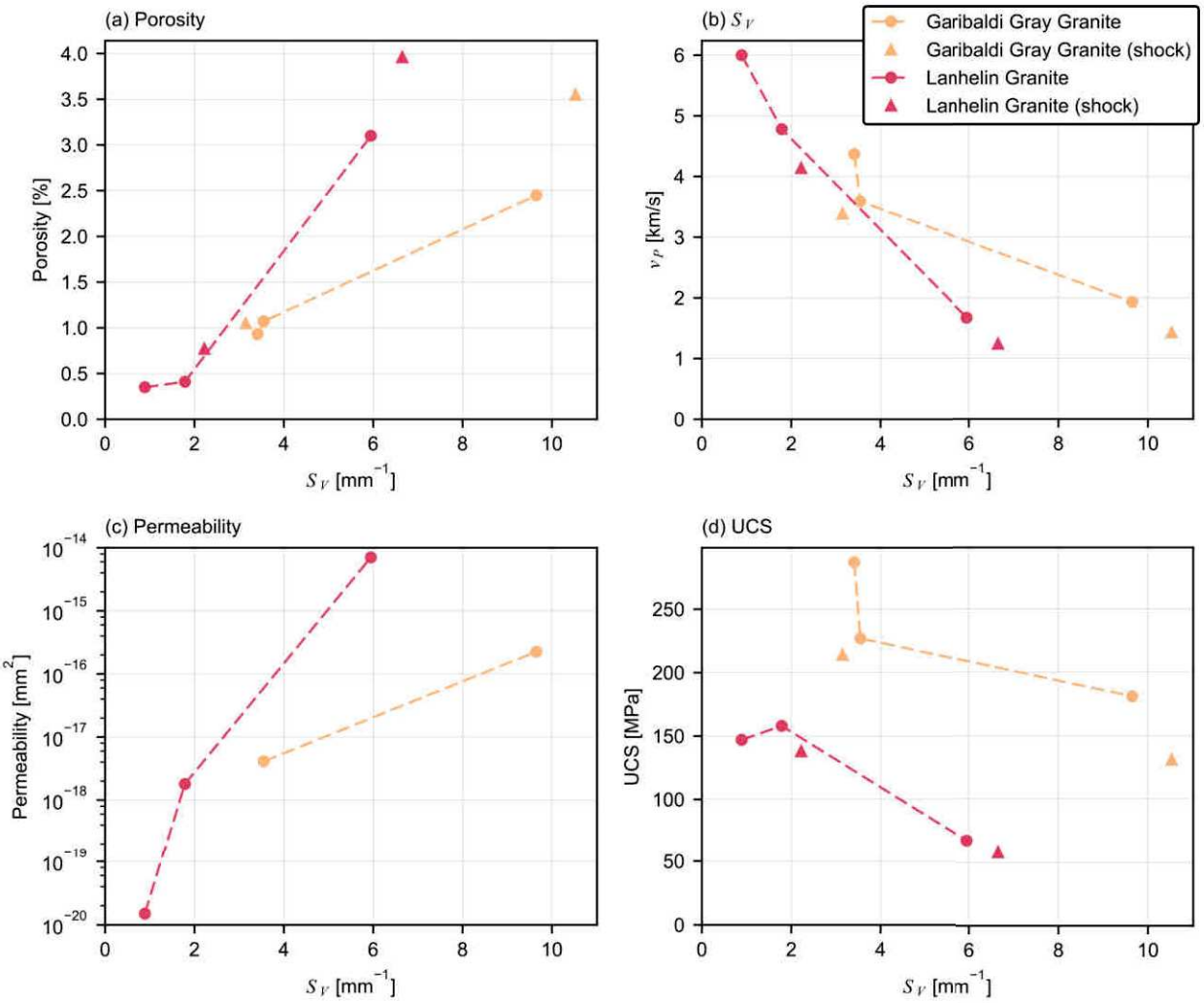

Figure 4.27: Room temperature measurements of (a) porosity, (b) v_P, (c) permeability, and (d) UCS against the crack surface area per volume, S_V (Underwood, 1967) of samples of Garibaldi Grey Granite and Lanhélin Granite intact samples and samples heated to 300 °C and 700 °C (both cooled at 1 °C (circles) and "shock" cooled by quenching (triangles). Dashed lines simply join the data points for the samples cooled at 1 °C/min to improve visibility.

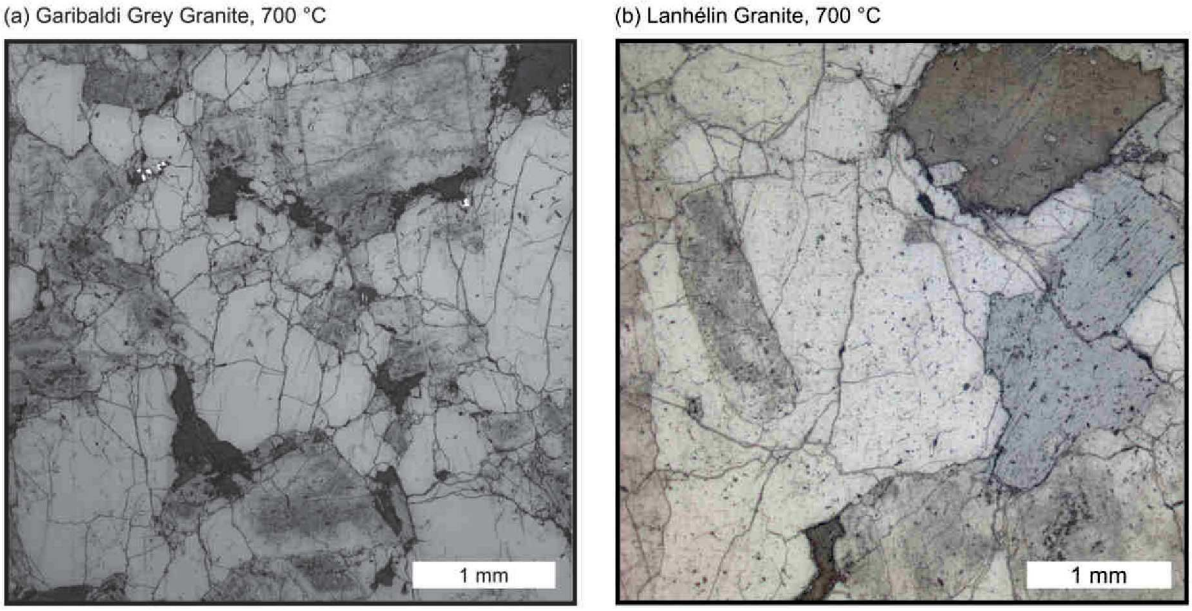

Figure 4.28: Optical micrographs of thin sections of (a) Garibaldi Grey Granite and (b) Lanhélin Granite samples heated to 700 °C and cooled at a rate of 1 °C/min.

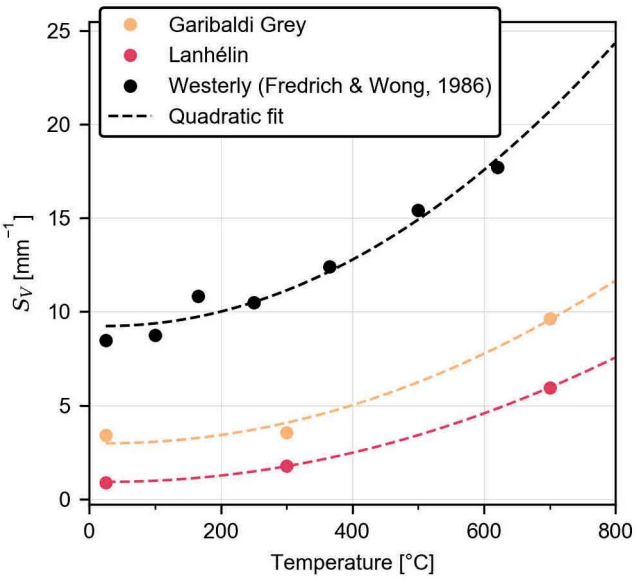

Figure 4.29: S_V measurements of thermally-stressed samples of Garibaldi Grey Granite and Lanhélin Granite against thermal stressing temperature. Also shown are data from Fredrich and Wong (1986) on Westerly Granite. The dashed curves represent the fit by linear regression of Equation 4.9 to the measurements.

(1971)). This results in an average thermal expansion mismatch of $7.1 \times 10^{-6}/°C$ for the Garibaldi Grey Granite and $9.5 \times 10^{-6}/°C$ for the Lanhélin Granite; and the average value of G_{1c} for granite (Atkinson, 1984). The value of $7 \times 10^{-6}/°C$ found by Fredrich and Wong (1986) for Westerly Granite (calculated within the range of 20 - 620 °C, from the data shown in Figure 4.29) is similar to that of the Lanhélin Granite and particularly the Garibaldi Grey Granite. The model required a higher average thermal expansion mismatch in the Lanhélin Granite to explain the greater increase in S_V with temperature.

Edwards (1951) found the thermal stress around an isotropic inclusion to be proportional to: the change in temperature; the mismatch in thermal expansion; and the Young's modulus of the inclusion. The thermal stresses between grains during heating may also be of a similar magnitude in each granite. These models do not account for the relaxing of stresses by frictional sliding along interfaces (Ghahremani, 1980) or the presence of porosity to accommodate for thermal expansion. Therefore, the stress-accumulation along grain boundaries in the less porous Lanhélin Granite can be expected to be greater than for the Garibaldi Grey Granite, and lead to an earlier onset of thermal microcracking, as observed in the AE monitoring data (Figure 4.11).

COMPARISON WITH PUBLISHED DATA Figure 4.30 shows the changes in porosity (difference with the porosity of the unheated sample) and v_P (normalised to v_P of the unheated sample) of the granites with thermal stressing temperature. Also shown are measurements on: v_P of Westerly granite from Nasseri et al., 2009a; La Peyratte granite (0.5–1.5 mm grainsize) from David et al. (1999) and Glover et al. (1995); and the v_P of Remiremont (1.45 mm) and Senones (7.2 mm) granites from Homand-Etienne and Troalen (1984).

Figure 4.31 shows the relative changes in permeability and UCS of the granites, normalised to measurements of the unheated rock. However, the permeability of the Garibaldi Grey and the Lanhélin granites are normalised to the permeabilities of the samples heated to 200 °C and 300 °C, respectively.

Overall, measurements of the physical, transport, and mechanical properties are in agreement with data from the literature.

- The increase in porosity with thermal stressing temperature is low up to 600 °C, where it is increased by about 50 % for all granites. From 600 °C the porosity increase is more dramatic, especially for the Lanhélin and Westerly Granites, for which the porosity is increased by more than a factor of three at 800 and 900 °C.

- The decrease in v_P is generally linear with thermal stressing temperature for all granites (Figure 4.30a), with the exception of a greater decrease across the α/β transition. The decrease

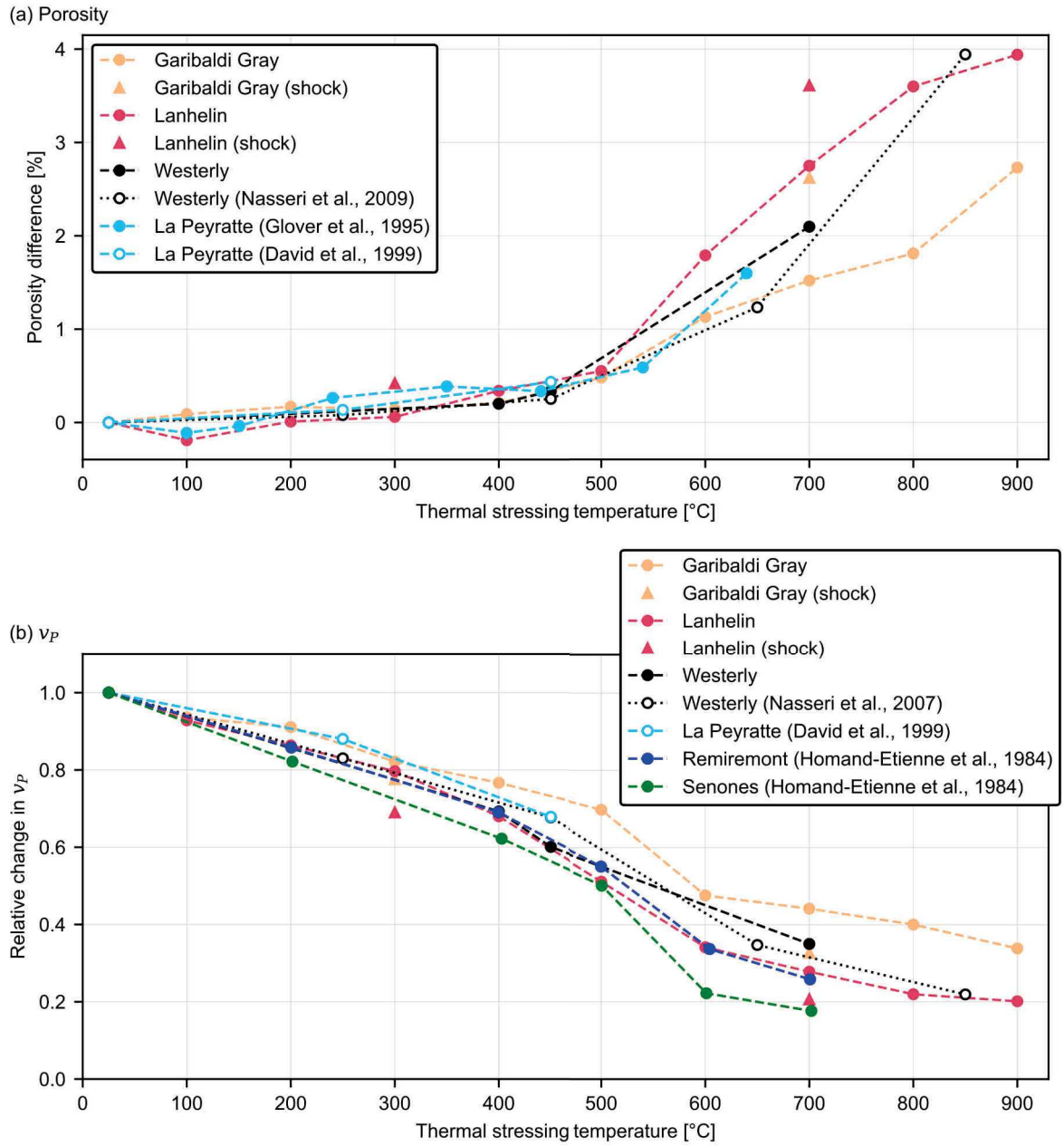

Figure 4.30: Relative changes (normalised to the value for the unheated sample) in (a) porosity, (b) v_P, (c) permeability, and (d) uniaxial compressive strength (UCS) with temperature for Garibaldi Grey Granite Lanhélin Granite, Westerly Granite (this study and Nasseri et al. (2009b)), La Peyratte Granite (David et al., 1999; Glover et al., 1995), and Remiremont and Senones granites (Homand-Etienne and Troalen, 1984), heated to temperatures between 100 and 900 °C.

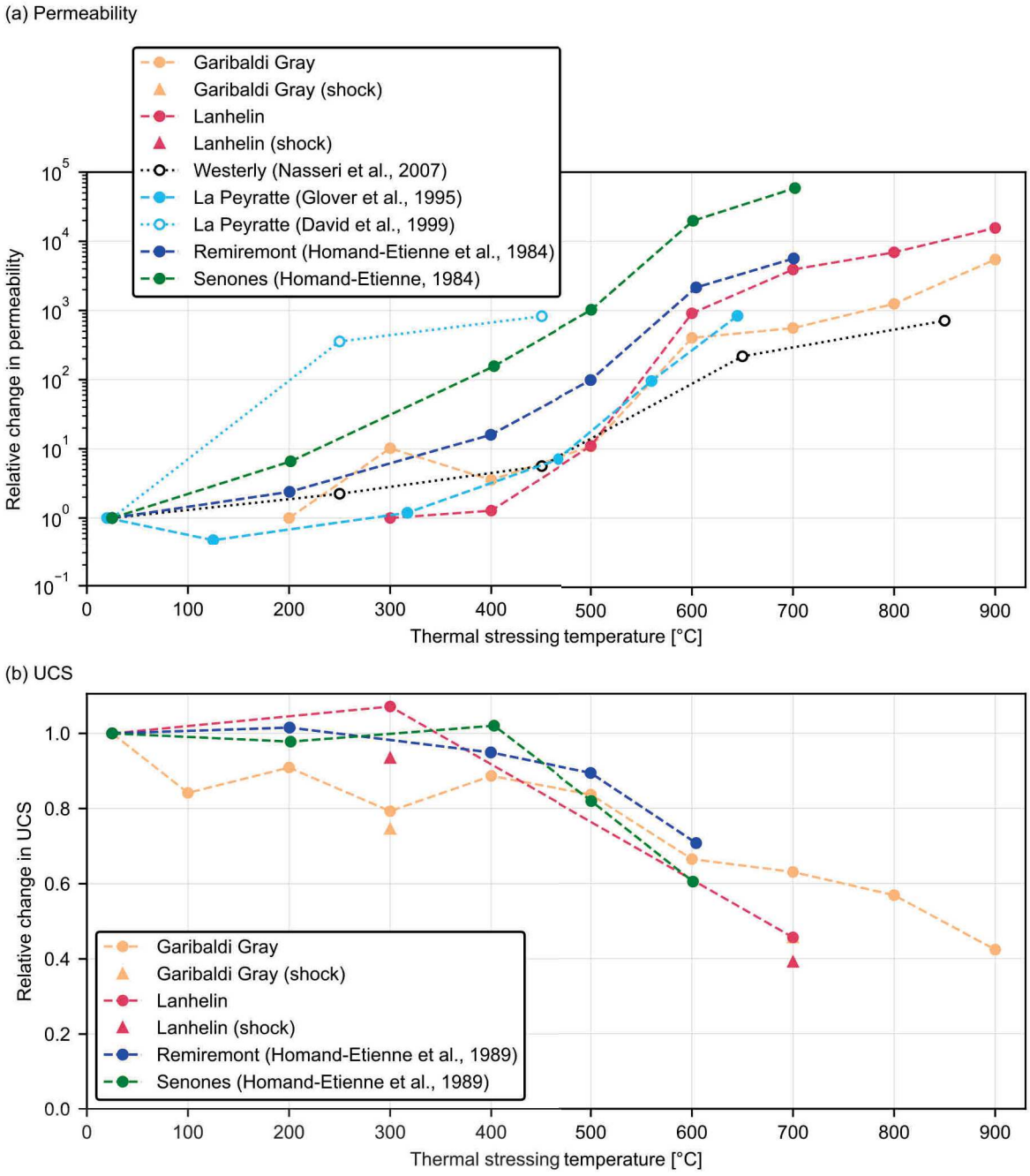

Figure 4.31: Relative changes in: (c) permeability, normalised to the value for the unheated sample (or 200°C for Garibaldi Grey and 300 °C for the Lanhélin Granites), and (d) uniaxial compressive strength (UCS) with temperature for Garibaldi Grey Granite and Lanhélin Granite, Westerly Granite (this study and Nasseri et al. (2007)), La Peyratte Granite (David et al., 1999; Glover et al., 1995), and Remiremont and Senones granites (Homand-Etienne and Houpert, 1989; Homand-Etienne and Troalen, 1984), heated to temperatures between 100 and 900 °C.

is greatest for Senones Granite, followed by Remiremont and Lanhélin granites, Westerly, La Peyratte, and finally Garibaldi Grey Granite (Figure 4.30). This generally follows the order of decreasing grain size (with exception of the Westerly Granite, which has a slightly smaller grain size than the La Peyratte granite. Figure 4.32 shows the relative change in v_P against grain size (diameter) for thermally-stressed samples of Garibaldi Grey Granite and Lanhélin granites, and Senones and Remiremont granites (Homand-Etienne and Troalen, 1984). The relative decrease in v_P is greater in the coarser grained granites, which is more accentuated at higher temperatures.

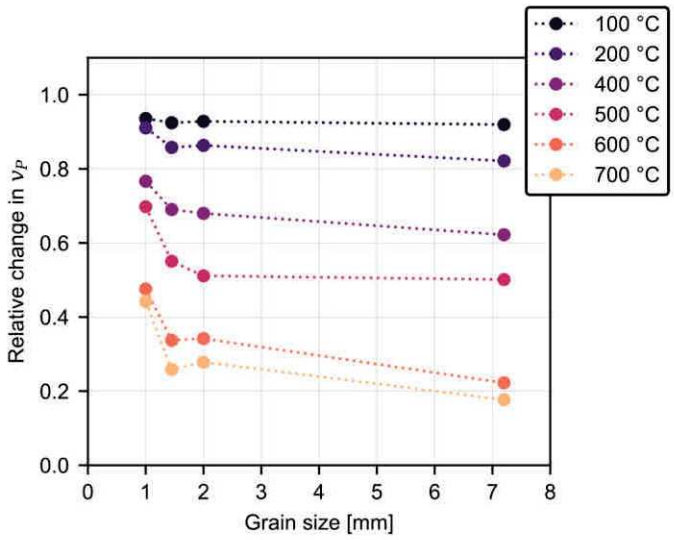

Figure 4.32: Relative change in P-wave velocity (v_P) against grain size (diameter) for thermally-stressed samples of Garibaldi Grey and Lanhélin granites, and Senones and Remiremont granites (Homand-Etienne and Troalen, 1984) heated to temperatures of 100, 200, 300, 500, 600 °C.

- The permeability of La Peyratte granite as measured by David et al. (1999) shows the greatest increase with thermal stressing temperature up to 450 °C. The unheated La Peyratte granite was measured by David et al. (1999) to be 1.9×10^{-21} m^2, although it was significantly higher for Glover et al. (1995) at 8.4×10^{-17} m^2. The low permeability rock is more sensitive to additional microcracking than the higher permeability rock, which may already contain a well-connected microcrack network.

  For all granites, the relative increase in permeability (Figure 4.31a) are spread wider than the porosity and v_P (Figure 4.30). The permeability increase across the α/β transition is greater. Above 600 °C, the permeability change is greater for granites with larger grains. This is also the case below 600 °C, with the ex-

ception of the Lanhélin Granite (which could be due to the normalisation of the Lanhélin data to the 300 °C sample rather than the unheated sample). The permeability change may be due to a larger microcrack aperture in the coarser-grained rock.

- The UCS of the Lanhélin, Remiremont and Senones granites (Homand-Etienne and Houpert, 1989) shows no real change when heated to temperatures of 400 °C and less. Here, the UCS of Garibaldi Grey Granite shows a slight decrease with thermal stressing temperatures within this range. The UCS of the coarser grained granites appears to be less affected by temperature up to 400 °C, which may be due to larger pre-existing flaws (such as intra-granular microcracks) than in the Garibaldi Grey Granite.

  From 500 °C, the UCS of all granites is decreased. Extensive thermal microcracking at these temperatures influences failure under uniaxial conditions. Data is too sparse, however, to make any firm conclusions on the influence of grain size on the amplitude of the strength reduction.

THERMAL SHOCK COOLING Here, when samples were shock-cooled (by water quenching) from 300 and 700 °C, the increase in porosity and decrease in v_P were greater than for the slow-cooled samples (Figure 4.16), indicating increased thermal microcracking due to shock-cooling, particularly for the 700 °C samples. The stiffness of the shock-cooled samples were lower than for the slow-cooled samples (Table 4.3). The additional thermal microcrack damage is expected to be due to the high temperature gradient within the sample. Despite the high thermal gradient across the sample radially, no clear anisotropy or heterogeneity of microcracking was observed within the thin sections (Figure 4.13 and Figure 4.14).

Zhou et al. (2018) showed, through high temperature hydraulic fracturing tests in the laboratory, that above 300 °C, contact between the borehole wall and the fracturing fluid created thermal and elastic shock waves, resulting in tensile stresses around the borehole sufficient to cause fracturing. This suggests that the additional thermal microcracking observed here due to the shock cooling of the 300 and 700 °C samples may have been caused by thermal and mechanical shock waves.

When plotted as a function of the crack surface density (S_V), the porosity and v_P of the shock-cooled and slow-cooled samples aligned (Figure 4.27), suggesting that the thermal microcracks in the shock-cooled samples have a similar aperture to their slow-cooled counterparts. Of the two granites, the Lanhélin was more sensitive to shock-cooling (Figure 4.16). This could be explained by the larger grain size and lower initial crack density, yielding a lower microcrack surface area to accommodate thermal strain.

As here, Siratovich et al. (2015) measured an increase in permeability and a decrease v_P with thermal stressing of granite Lanhélin Granite heated to 325 °C when the rock was cooled rapidly by contact with cool water. Siratovich et al. (2015) measured the permeability of the unheated granite to be $1.35 \times 10^{-18}/\mathrm{m}^2$, and $7.48 \times 10^{-18}/\mathrm{m}^2$ for the slow-cooled sample, and $4.87 \times 10^{-17}/\mathrm{m}^2$ for the shock-cooled sample. v_P was decreased by 4–6 % for the slow-cooled sample and by 11 % in the shock-cooled sample. Here, a greater relative decrease in v_P of the Lanhélin Granite was observed with thermal stressing: v_P decreased by 14 % when heated to 300 °C and slow-cooled, and decreased by 26 % when shock-cooled. Results show that the presence of cool fluid within hot geothermal reservoirs may induce thermal microcracking due to rapid cooling.

MICROCRACKS UNDER PRESSURE Here, thermal stressing and thermal microcrack monitoring was performed under ambient pressure conditions. It is important to understand how the results shown here may be applied to the thermal stressing of rock at depth. Wang et al. (1989) made several measurements of v_P of Westerly Granite during heating to 300 °C and cooling, under confining pressures of 7, 28, and 55 MPa. Under 7 MPa confining pressure, they measured a decrease in v_P from around 4.7 km/s to 3.4 km/s at 300 °C—slightly higher than the 3.1 km/s measured here at 300 °C and ambient pressure (Figure 4.5). However, upon cooling, they found that v_P returned to the value prior to heating, which they attributed to the closure of the new microcrack porosity by the confining pressure. This indicates that thermal microcracks formed under confinement will remain open only when the temperature remains elevated.

Violay et al. (2017) found that when Westerly Granite samples were heated to temperatures of up to 1000 °C under a confining pressure of 130 MPa, their permeability (at pressure and temperature) was higher when the temperature was higher, due to thermal microcracking, which formed and remained open under confining pressure.

Wang et al. (2013) heated samples of La Peyratte granite to 700 °C and deformed them under triaxial conditions at room temperature. They found that the permeability of the heated rock remained significantly higher than the permeability of the unheated rock (1×10^{-21} m^2), by 4–5 orders of magnitude at confining pressures of up 90 MPa. However, under 30 MPa effective pressure, the strength of the heated La Peyratte Granite was the same as that the unheated granite when deformed. This showed that cracks remained open to facilitate fluid flow, but they were too small compared with the pre-existing flaws in the granite which were controlling strength.

Here, under uniaxial conditions and at 5 MPa confinement, the stiffness of the 700 °C sample was lower than the 300 °C sample, which was in turn lower than the unheated sample (Figure 4.20, Table 4.3).

At 10 MPa, the unheated and 300 °C samples had a similar stiffness, however the 700 °C sample was less stiff. This suggests that some high aperture thermal microcracks in the granite are still open and contribute to the stiffness.

4.2.3.3 *Implications for geothermal reservoirs*

The results presented here are relevant to geothermal reservoirs hosted within granitic rock (e.g. Soultz-sous-Forêts (France), Gérard and Kappelmeyer (1987) and Gérard et al. (2006); and Rittershoffen (France), Baujard et al. (2017)). Results suggest that grain size may be a key factor in influencing the effect of temperature on thermal microcracking and hence on rock properties. The Soultz-sous-Forêts geothermal reservoir is hosted within granite composed of larger grains than the granites studied here: quartz crystals within the granite average 5 mm across (Dezayes et al., 2010), and may be larger than 10 cm in diameter. Changes in temperature within the coarser grained granite may lead to significant changes in rock properties, including the permeability, a key parameter for the functioning of geothermal reservoirs, and which influences large scale fluid convection (Magnenet et al., 2014).

The thermal diffusivity and conductivity of the thermally-stressed samples were seen to decrease significantly with thermal stressing temperature. These thermal properties are highly important for the behaviour of geothermal reservoirs (Grant, 2013), and field measurements of thermal conductivity at the well by means of thermal response tests are being performed increasingly often (Signorelli et al., 2007). Laboratory measurements may compliment the field measurements by quantifying the potential variation in thermal properties of granite due to thermal stressing, and help constrain the modelling of heat flow around the borehole, and within the geothermal reservoir itself.

At geothermal sites, cold water has previously been injected in to the reservoir to open fractures and increase permeability around the borehole (Grant et al., 2013; Jeanne et al., 2017; Kitao et al., 1995). Here, the physical properties of the coarser-grained Lanhélin Granite were the most sensitive to shock-cooling. Thermal microcracking due to contact with cool water at the Soultz-sous-Forêts site could be accentuated by the larger crystal size.

At the Soultz-sous-Forêts geothermal site, earthquake tomography inversions revealed changes in v_P coinciding with changes in the injection flow rate (Calò et al., 2011), and the correlation of ambient seismic noise has been used to link velocity changes to geothermal reservoir activities (Lehujeur et al., 2017; Obermann et al., 2015). Results show that the rock microstructure may be a consideration when interpreting velocity changes. For example, the decrease in the wave velocities of the Garibaldi Grey Granite with temperature were 20 %

less than for the coarser-grained Lanhélin Granite, which was less again than for coarser grained granites in the literature (Figure 4.32).

As at depth rock is subject to pressure, it is important to understand how thermal microcracks behave under such conditions. Whilst the influence of thermal microcracks on the strength of Garibaldi Grey Granite were seen to decrease with confining pressure, they still had some effect on rock stiffness (Figure 4.20, Table 4.3), which is a key parameter factor for the hydraulic fracturing of geothermal wells (Legarth et al., 2005), and for the thermo-hydro-mechanical behaviour of geothermal reservoirs (Brownell et al., 1977). De Simone et al. (2013) performed coupled thermo-hydro-mechanical simulations to study rock stability during injection of cold water into geothermal rock. The conditions for rock instability due to the combined thermal and mechanic stresses showed a high sensitivity to the stiffness parameters. The influence of microcracks on rock stiffness also suggests that some thermal microcracks may remain open under confinement, and therefore may contribute to the permeability of the bulk rock.

4.3 CONCLUSION

- During repeated heating and cooling cycles to a maximum temperature of 450 °C, AE monitoring and in-situ measurements of wave velocity were performed on samples of Westerly Granite, Garibaldi Grey Granite and Lanhélin Granites. Results showed the velocity of the granite to decrease with temperature during all thermal stressing cycles, and especially during the first cycle (by 30–50 %).
- Through combined velocity measurements and AE monitoring, it could be showed that when the granites were heated to 450 °C and cooled, thermal microcracking occurred during heating. The number of detected AE during heating was seen to increase with the size of the velocity decrease due thermal microcracking.
- AE during cooling was observed for all granites and was concurrent with an increase in velocity. For all cycles, during cooling, the increase in wave velocity was of a similar amplitude, which indicated that little microcracking occurs during cooling. It is suggested that AE during cooling of the first cycle is due to frictional sliding along crack faces rather than microcracking.
- AE monitoring experiments during heating to 700 °C and cooling showed that the analogue seismic b-value, calculated from the AE amplitudes, can be used to distinguish the different stages of thermal stressing, i.e. :the onset of thermal microcracking; the quartz α/β transition; and AE during cooling. AE amplitudes were shown to be greater with increasing grainsize. In

the Lanhélin Granite, the amplitude of microcrack events was seen to decrease significantly following the onset of AE, indicating the formation and extension of small microcracks first, followed by larger microcracks.

- The temperature for the onset of AE increased with increasing porosity, and is explained by the accommodation of thermal strain by the void space. The amplitude of AE events increased with the grain size, due to the control of grain size on the length-scale of microfractures.

- Measurements made at room temperature of the microcrack density and lengths, physical, transport, thermal, and mechanical properties of variably thermally-stressed samples showed the Lanhélin Granite—which is the coarser-grained granite and contains the lowest initial microcrack porosity—to be the most sensitive to thermal stressing. The Lanhélin Granite samples exhibited the greatest relative increase in crack density, porosity, and permeability, and decrease in v_p, thermal diffusivity and UCS with thermal stressing. Overall, measurements of the granites are comparable with existing studies, however grain size appears to amplify the effect of thermal stressing on rock properties.

- For both the Lanhélin and Garibaldi Grey granites, the influence of shock-cooling by immersion in water increased thermal microcracking. This suggests that thermal microcracking may occur in granite during cooling if thermal gradients are sufficiently great.

5 THERMAL MICROCRACKING IN VOLCANIC ROCK

5.1 INTRODUCTION

The influence of thermal microcracking on the physical and transport properties of volcanic rock plays an important role for geo-engineering projects such as geothermal reservoirs, which are often hosted in volcanic rock (Grant, 2013). Locations of geothermal reservoirs hosted in volcanic rock include: the Ethiopian Rift valley, where geothermal production began in 1998 (Teklemariam et al., 2000), exploiting the upflow of geothermal fluids through low permeability basaltic lava flows (Battistelli et al., 2002); New Zealand, including the Rotokawa reservoir in andesitic rock (McNamara et al., 2016b; Siratovich et al., 2014); and Iceland, the basaltic Krafla and Námafjall geothermal sites have been exploited since the 1970s (Björnsson et al., 1977; Thór Gudmundsson and Arnórsson, 2002). Additionally, the influence of microcracks on volcanic rock permeability may determine whether or not gas can escape from a given volcanic system. Permeability and gas pressure are assumed to exert a first-order control over the eruptive behaviour of a volcano (Eichelberger et al., 1986; Farquharson et al., 2017; Melnik et al., 2005; Sparks et al., 1997).

The influence of temperature on the seismic velocity of rock is also important, as velocity models inferred from seismic monitoring are used to understand the structure of volcanoes. Examples include: Mt. Erebus volcano, Antarctica (Grêt, 2005); Merapi volcano, Indonesia (Sens-Schönfelder and Wegler, 2006); and Mt. Etna, Italy (Patane et al., 2002). Changes in the seismic velocity of rock over time may be due to a number of factors, including changes in temperature, porosity, crack density, confining pressure, pore fluid pressure, fluid saturation, and fluid viscosity (Sanders et al., 1995). At geothermal sites, changes in seismic velocity may provide valuable information on changes within the reservoir due to fluid circulation (e.g., Calò et al. (2011), Lehujeur et al. (2017), and Obermann et al. (2015)). In both cases, it is important have some understanding of the potential impact of temperature on the seismic velocity.

In the laboratory, to establish the occurrence of thermal microcracking in volcanic rock, Bauer and Handin (1983) measured the thermal expansion coefficient of three rocks (Mt. Hood Andesite, Cuerbio Basalt and Charcoal Granodiorite) during heating to 800 °C at a rate of 5 °C/min, under confining pressures of 5, 50 and 100 MPa. They found that the thermal expansion of the bulk rock sample was greater than the theoretical contribution of each mineral phase, and they at-

tributed this difference to the opening of thermal microcracks during heating.

Thermal microcrack damage due to heating and cooling has been shown through measurement to change the physical and transport properties of volcanic rock. For example, Jones et al. (1997) measured an increase in the permeability of Seljadur Basalt (Iceland) following heating to temperatures between 400 and 700 °C (by around a factor of 9 when heated to 700°C), coinciding with a decrease in the P-wave (v_P) and S-wave (v_S) velocities due to an increase in microcrack density. Vinciguerra et al. (2005) measured a decrease in v_P of Seljadur Basalt by more than 40 % following heating to 900 °C, due to the formation of thermal microcracks. Again, for Seljadur basalt, Nara et al. (2011) measured a permeability increase by almost three orders of magnitude, and a decrease in P-wave velocity from 5.65 to 4.33 km/s when heated to 800 °C, owing to thermal microcracking.

Not all studies have found the same behaviour with thermal stressing. Vinciguerra et al. (2005) measured no significant change in the v_P of basalt from Mt. Etna from the initial v_P of around 3.2 km/s following heating to 900 °C and cooling. Heap et al. (2009a) also found no change in the elastic moduli of basalt from Mt. Etna heated to 900 °C. Vinciguerra et al. (2005) suggested that the high pre-existing crack density within the Etna basalt explained the lack of further thermal microcracking during their experiments. Following exposure to high-temperature, no significant changes were detected either in the physical and mechanical properties of: andesites from Volcán de Colima, Mexico (Heap et al., 2014a); the strength of dacite from Mt. St. Helens, USA (Kendrick et al., 2013); or the strength of basalt from Pacaya volcano, Guatemala (Schaefer et al., 2015).

Studies have used AE monitoring to study thermal microcracking within volcanic rock. Jones et al. (1997) performed acoustic emission (AE) monitoring of Seljadur Basalt during heating to 800 °C, observing a constant AE rate throughout, which they attributed to thermal microcracking. Vinciguerra et al. (2005) report AE monitoring data during the heating of Etna Basalt to 600 °C and Seljadur Basalt to 900 °C, in which they observed a continuous increase in the number of AE during heating of the Seljadur Basalt, which was highly thermally microcracked upon cooling, and bursts of AE for the Etna Basalt, which underwent little microcracking. It has also been suggested that thermal microcracking in some volcanic rocks may occur during cooling. Browning et al. (2016) heated and cooled two volcanic rocks (a basalt and a dacite) to a maximum temperature of 1100 °C whilst monitoring AE. They detected significantly more AE during cooling, which they attributed to thermal microcracking. By contrast, Heap et al. (2014a) found no systematic difference between the number of AE during heating and during cooling of andesites from Volcán de Colima (up to a maximum temperature of 450 °C).

For volcanic rock, it can be concluded for the above-mentioned studies that the influence of temperature on thermal microcracking varies, and seems to depend strongly upon the rock microstructure. Here, to look at the effect of temperature on volcanic rock, a selection of rocks was made, each with different microstructures:

- A basalt from Mt. Etna (porosity ~4 %).
- A basalt ("Rubble Creek") from British Columbia, Canada (porosity ~1 %).
- A porous andesite ("La Lumbre"; Farquharson et al. (2017)) from Volcàn de Colima, Mexico (porosity ~23 %).

In terms of classification, the main difference between the basalt and the andesite is the silica content (45–55 % for a basalt, and 57–63 % for an andesite). Samples of each rock were subjected to heating and cooling cycles at temperatures of up to 450 °C whilst monitoring AE and changes in wave velocity (v_P and Coda Wave Interferometry (CWI); Chapter 2). To examine the behaviour at higher temperatures, samples of the Etna Basalt and the Rubble Creek Basalt were also heated to 700 °C again monitoring AE. The peak temperature of 700 °C here was a self-imposed maximum, to allow comparison with AE monitoring data recorded for the granites (Chapter 4).

For the Rubble Creek Basalt, a suite of thermally-stressed samples were prepared for measurement of their physical, mechanical, transport and thermal properties. The analysis of physical and mechanical properties were performed uniquely on the Rubble Creek Basalt, as the porosity was similar to that of the granites, within the range of 0.3–1.5 % (Chapter 4). Further, the Rubble Creek Basalt was an interesting comparison with the granites due to its porphyritic texture, containing isolated phenocrysts within a groundmass. Measurements of porosity and ultrasonic wave velocities showed the Rubble Creek Basalt to be less heterogeneous than the Etna Basalt (Heap et al., 2009a; Vinciguerra et al., 2005) and La Lumbre Andesite (Farquharson et al., 2017), allowing for a better comparison between samples, to highlight the influence of thermal microcracks on rock properties.

Following a presentation of each rock, the results of thermal stressing experiments are shown, and finally a discussion of the influence of rock microstructure on thermal microcracking and the implications for volcanic and geothermal environments.

5.2 MATERIALS

ETNA BASALT Over the past ten years, several studies have focused on basalt from Mt. Etna: Heap et al. (2009a), Stanchits et al. (2006), Vinciguerra et al. (2005), and Zhu et al. (2016). Backscattered Scanning Electron Microscopy (SEM) micrographs of the basalt collected

from Mt. Etna and used in this study are shown in Figure 5.1. The basalt has a porphyritic texture consisting of a completely crystallised groundmass hosting pores and phenocrysts (Figure 5.1).

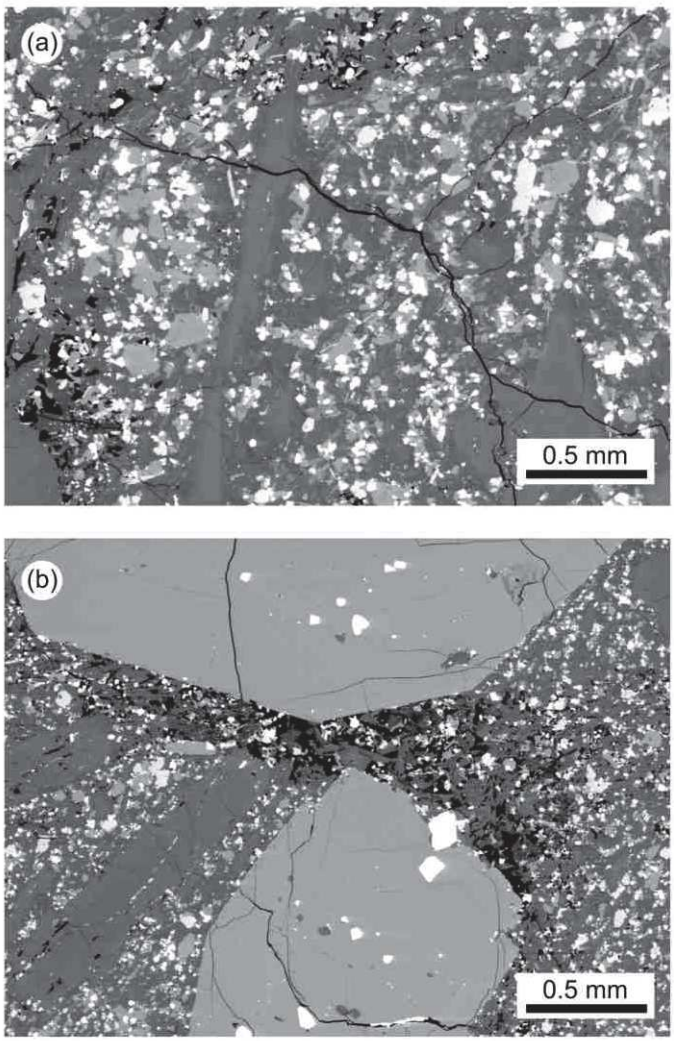

Figure 5.1: Backscattered scanning electron microscope micrographs of the Etna Basalt used in this study. Cracks traverse the groundmass (a) and phenocrysts (b).

Qualitatively, the microcracks in the basalt may be several mm in length (Figure 5.1a) and traverse both the crystallised groundmass and the large phenocrysts (Figure 5.1b). The connected porosity of the basalt was measured to be around 4 % on average (measured by helium pycnometry, see Chapter 2), and the pores (typically less than 100 microns in diameter) are collected in pockets, not uniformly distributed throughout the sample (Figure 5.1b). These pockets form the volume between microlites where the groundmass is absent: a diktytaxitic texture (see, for example, Kushnir et al. (2016)).

RUBBLE CREEK BASALT Backscattered Scanning Electron Microscopy (SEM) micrographs of a basalt from Rubble Creek, British Columbia, Canada (which has not previously been studied) is shown in Figure 5.2a. This basalt has a porosity of 1.06 % (measured by helium pycnometry; Chapter 2), and consists of isolated phenocrysts (50–200 µm length) within a crystallized groundmass. Whilst fewer pores are visible than in the Etna Basalt, a high number of pre-existing microcracks may be observed (Figure 5.2a), traversing both the groundmass and the phenocrysts. Figure 5.2b shows an SEM micrograph of the Rubble Creek Basalt heated once to 450 °C and cooled, at room pressure.

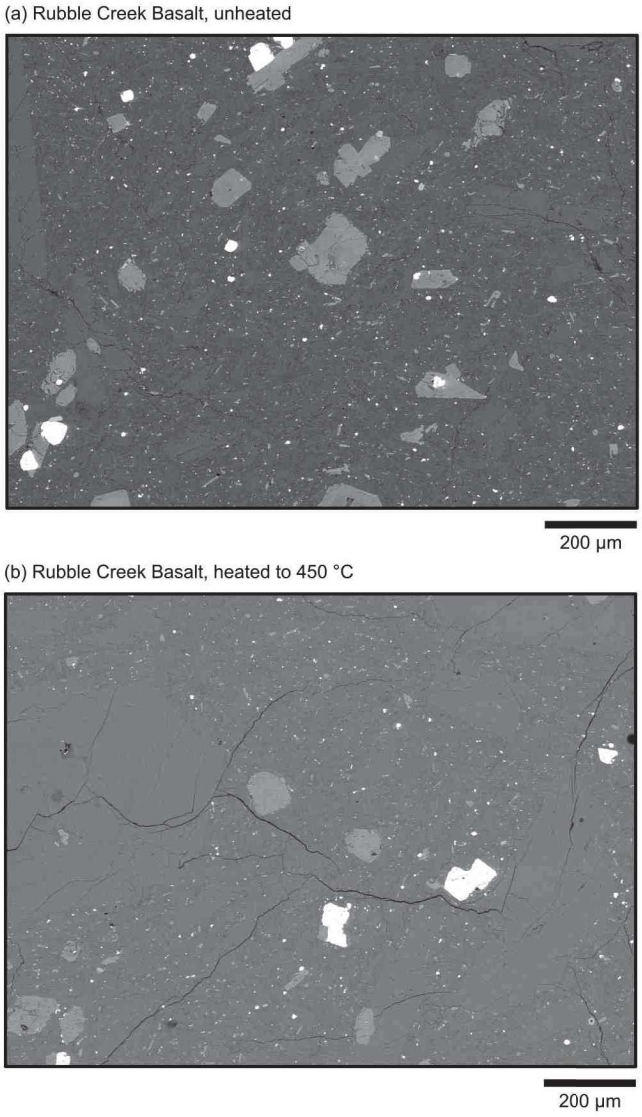

Figure 5.2: Backscattered scanning electron microscope micrographs of (a) the unheated Rubble Creek Basalt, and (b) heated to 450 °C.

LA LUMBRE ANDESITE Rocks studied previously in this work have contained porosity consisting mostly of microcracks. As an extension of the results presented thus far, a more porous andesite was chosen, to gain preliminary insight into the influence of pores on thermal microcrack formation. The andesite was collected from the La Lumbre debris-flow track on the southwestern flank of Volcàn de Colima for a study by Farquharson et al. (2017) on the influence of mechanical deformation on permeability. It is of interest to study whether any thermal microcracking may occur due to temperature changes within the volcano.

A backscattered Scanning Electron Microscopy (SEM) micrograph of the andesite from Volcàn de Colima, Mexico is shown in Figure 5.3 (Farquharson et al., 2017). The andesite is a vesicular poryphyritic andesite, containing both phenocrysts and microphenocrysts (Figure 5.3; Farquharson et al. (2017)), and has a porosity of around 23 % (measured by helium pycnometry; Chapter 2). The andesite contains a glassy groundmass with an abundance of microlites, unlike the basalts which are entirely crystallised.

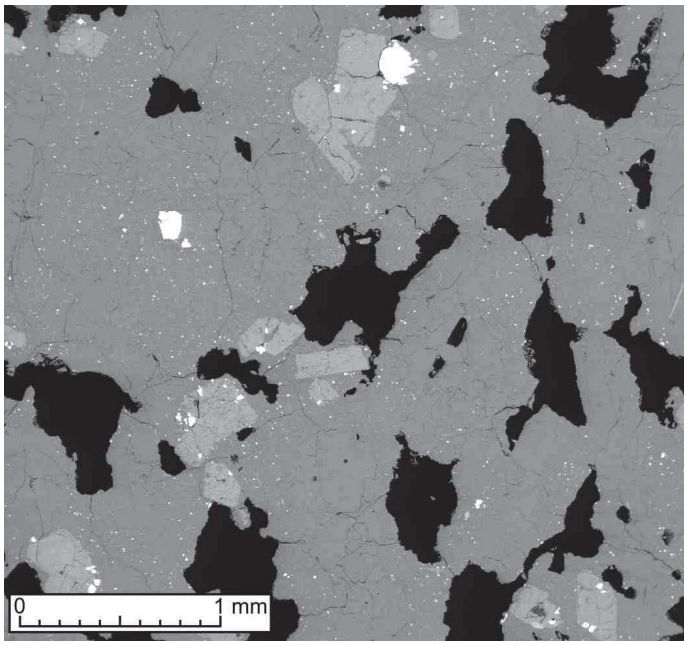

Figure 5.3: Backscattered scanning electron microscope (SEM) micrograph of La Lumbre Andesite from Volcàn de Colima (from Farquharson et al. (2017)).

5.3 RESULTS

5.3.1 *AE monitoring and velocity measuements*

THERMAL CYCLING OF ETNA BASALT Figure 5.4 shows the measurements of v_P and the CWI relative time shift ($\frac{\delta t}{t}$) with temperature

during three heating and cooling cycles of Etna Basalt to a maximum temperature of 450 °C. As the Etna Basalt was heated for the first time, v_P increased from 3.36 km/s at room temperature to 3.76 km/s at 450 °C (Figure 5.4a). During cooling, v_P decreased from 3.76 km/s at 450 °C to 3.29 km/s at room temperature.

For the Etna Basalt, during the first cycle, the increase in v_P during heating (~11 %) was slightly less than the decrease in v_P during cooling (~−13 % of the initial value), resulting in a small permanent drop in v_P of 0.07 km/s (~2 %). Similarly, during cycles two and three, v_P was permanently decreased by 0.13 km/s and 0.03 km/s, respectively, so over all cycles, v_P decreased from 3.36 to 3.13 km/s. As an additional verification, the v_P of the second sample used for AE monitoring was measured between cycles using a separate benchtop apparatus (see Chapter 2). v_P of the second sample was found to decrease from 3.05 km/s prior to heating, to 2.88 km/s (following cycle one), 2.82 km/s (cycle two), and 2.58 km/s (cycle three). The permanent decrease in v_P measured on both samples is similar.

The CWI relative time shifts with temperature are similar during each cycle, generally negative during heating, and positive during cooling, remaining below 5×10^{-4}/°C throughout; an apparent increase in velocity with increasing temperature. The relative time shifts during the first cycle are, however, slightly lower in amplitude than during the following two cycles, where they are near identical.

During heating and cooling of the Etna Basalt, around 5 AE hits per 10 °C were detected during the first cycle, and fewer during cycles two and three (Figure 5.4c). A similar number of AE hits were detected during heating and cooling of the first cycle, but during cycles two and three the number of AE during cooling was greater than during heating.

Figure 5.5 shows the number of AE hits per 10 °C, during heating of a sample of Etna Basalt to a maximum temperature of 700 °C. The analogue seismic b-value was also calculated, using the Aki (1965) maximum likelihood estimate in windows of 200 hits at 100 hit intervals. AE was detected during heating from around 120 °C up to 700 °C (Figure 5.4), although the AE rate was low, between 10 and 100 hits per 10 °C. AE activity was observed to be greater throughout cooling, reaching a peak of around 500 hits per 10 °C at 550 °C (Figure 5.5).

The b-value for the Etna Basalt was near constant, at around 0.9, although it showed a slight increase during heating at 500–550 °C and 650–700 °C, and decrease during cooling between 700 and 400 °C, temperatures where AE activity was seen to increase. Changes in b-value have previously been seen to accompany thermal microcracking in the granites (Chapter 4), suggesting that, at the higher temperatures, thermal microcracking occurred during the heating and cooling of the basalt. Whilst in-situ velocity measurements could not be performed above 450 °C, the v_P of the sample heated to 700 °C was seen to de-

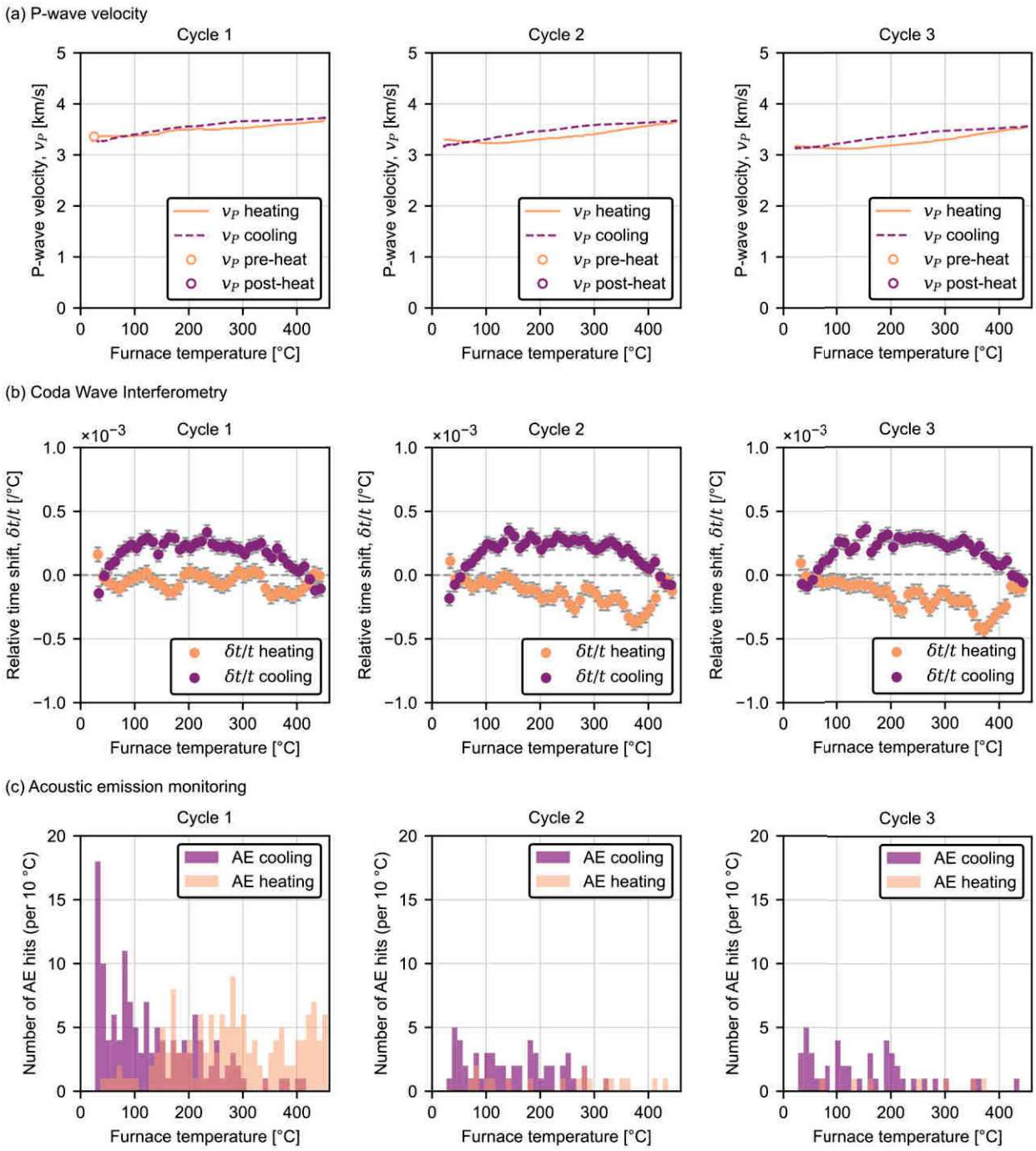

Figure 5.4: Comparison between (a) direct P-wave velocity (v_P), (b) coda wave interferometry (CWI) measurements, and (c) acoustic emissions (AE), made on samples of Etna Basalt when heated to 450 °C and cooled over three cycles. (a) P-wave velocity: symbols represent v_P measurements made at room temperature before and after cycles; lines represent v_P against furnace temperature during heating (solid) and cooling (dashed), calculated from the shift in P-wave arrival time with temperature and the initial v_P of the intact rock, measured prior to heating. (b) CWI: the relative time shift per °C (averaged over 10 °C intervals) against furnace temperature. (c) AE monitoring: bars shows the number of AE hits per 10 °C against furnace temperature.

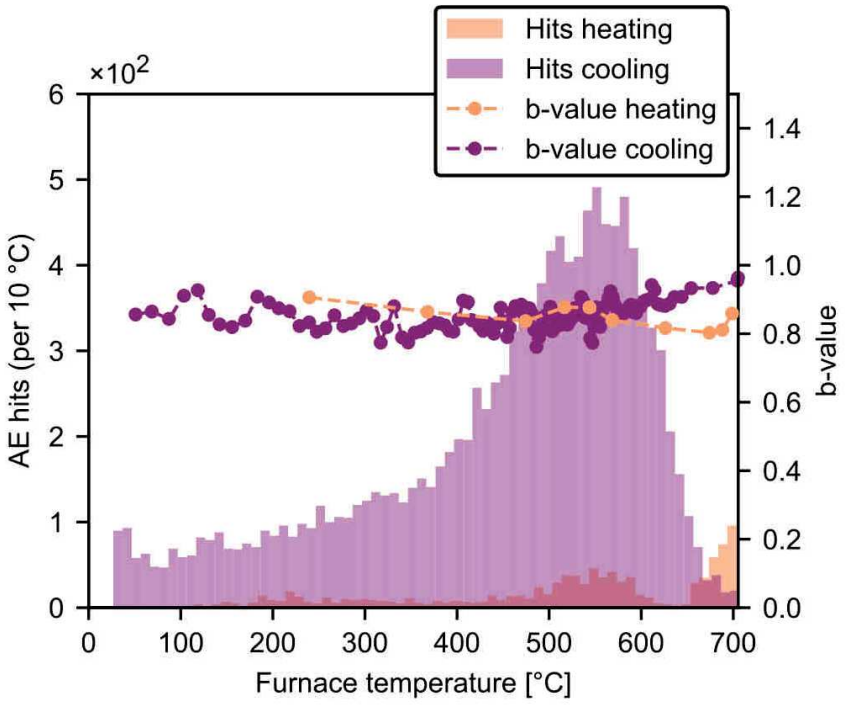

Figure 5.5: Number of acoustic emission (AE) hits and analogue seismic b-value against furnace temperature in bins of 10 °C during heating and cooling of samples of Etna Basalt to a maximum temperature of 700 °C. The b-values were calculated using the Aki (1965) maximum likelihood estimate.

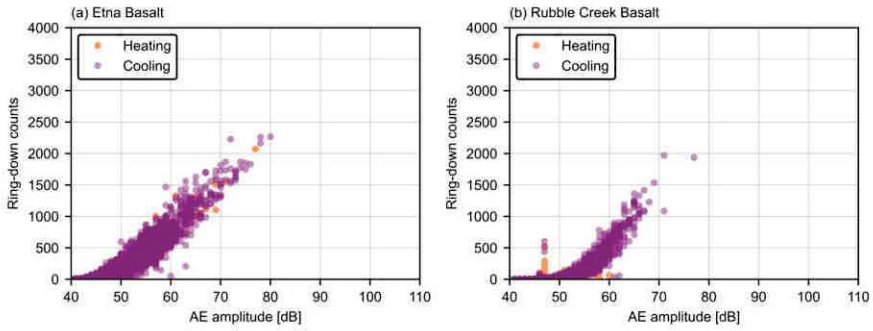

Figure 5.6: Acoustic Emission ring down counts against amplitude during heating and cooling of samples of (a) Etna Basalt and (b) Rubble Creek Basalt.

crease by 12 % from 2.95 km/s prior to heating, to 2.59 km/s upon cooling.

To examine whether the AE during heating and cooling have different characteristics, Figure 5.6 shows the number of AE ring-down counts against amplitude during heating to 700 °C and cooling of the Etna Basalt and the Rubble Creek Basalt (as was shown for the granite in Chapter 4). Overall, the AE amplitudes for the Etna Basalt are greater than for the Rubble Creek basalt, although no clear difference is observed between the AE detected during heating, and the many AE hits detected during the cooling of both rocks.

THERMAL CYCLING OF RUBBLE CREEK BASALT Figure 5.7 shows the measurements of v_P, the number of AE hits per 10 °C, and the CWI relative time shift with temperature during three heating and cooling cycles of the Rubble Creek Basalt to a maximum temperature of 450 °C. As the Rubble Creek Basalt was heated for the first time, very few AE hits were detected during heating, and v_P decreased from 4.57 at room temperature to 4.2 km/s at 200 °C (Figure 5.7a). However, between 200 °C and 450 °C, v_P of the Rubble Creek Basalt was constant.

For the Rubble Creek Basalt, the CWI relative time shift, initially low in amplitude, increased at 70 °C to 1×10^{-4}/°C–2×10^{-4}/°C, and remained constant up to 200 °C, corresponding to an apparent decrease in velocity with heating. From 200 °C, the relative time shift decreased, becoming negative at roughly 300 °C, reflecting the low amplitude fluctuations observed in v_P (Figure 5.7a). The very low number of AE and the low apparent velocity decrease suggest that very few thermal microcracks formed during heating to 450 °C.

During cooling, v_P remained near constant, and the relative time shift was low until around 200 °C (Figure 5.7). From 200 °C an apparent decrease in velocity in both the v_P and CWI measurements was observed (Figure 5.7a). From 120 °C there was a strong decrease in

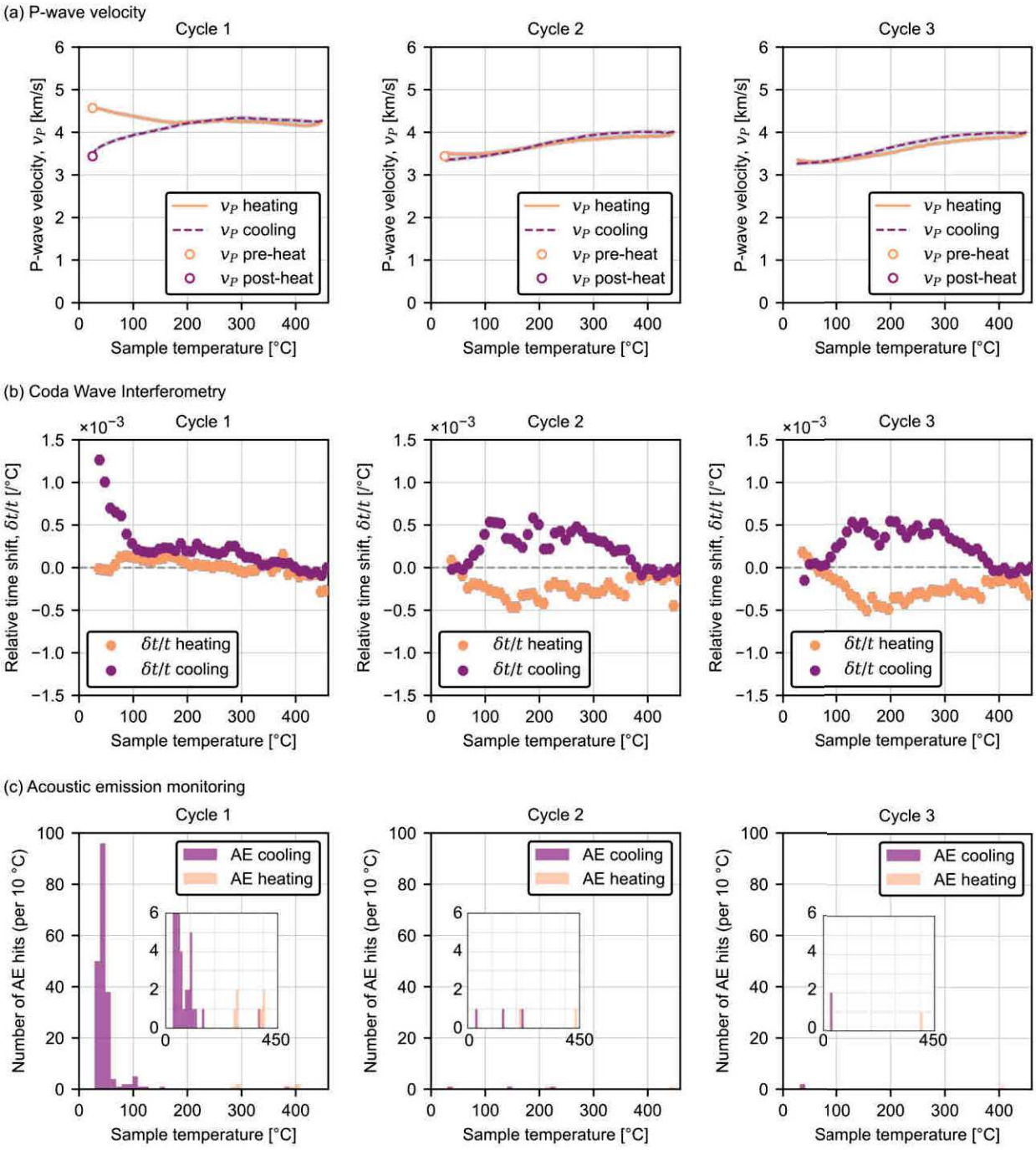

Figure 5.7: Comparison between (a) direct P-wave velocity (v_P), (b) coda wave interferometry (CWI) measurements, and (c) acoustic emission (AE) monitoring performed on samples of Rubble Creek Basalt when heated to 450 °C and cooled over three cycles. (a) P-wave velocity: symbols represent v_P measurements made at room temperature before and after heating; lines represent v_P against sample temperature during heating (solid) and cooling (dashed), calculated from the shift in P-wave arrival time with temperature and the initial v_P of the intact rock, measured prior to heating. (b) CWI: the relative time shift per °C (averaged over 10 °C intervals) against sample temperature. (c) AE monitoring: bars shows the number of AE hits per 10 °C against sample temperature.

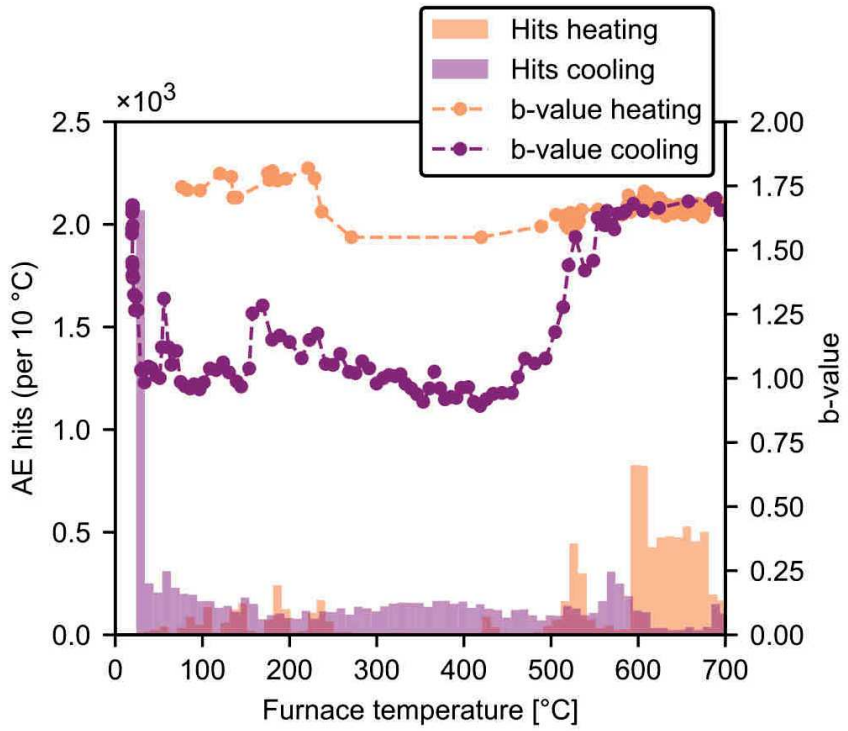

Figure 5.8: The number of acoustic emission (AE) hits and analogue seismic b-value against furnace temperature in bins of 10 °C during heating and cooling of samples of Rubble Creek Basalt to a maximum temperature of 700 °C. The b-values were calculated using the Aki (1965) maximum likelihood estimate.

v_P and a sharp increase in the relative time shift (Figure 5.7a), which were accompanied by the onset of AE. v_P is permanently decreased from 4.57 km/s prior to heating, to 3.38 km/s upon cooling.

Figure 5.8 shows the number of AE hits per 10 °C, during heating of another sample of Rubble Creek Basalt to a maximum temperature of 700 °C. The analogue seismic b-value was calculated using the Aki (1965) maximum likelihood estimate, in windows of 200 hits, at 100 hit intervals. Few AE were detected up to 500 °C, and AE activity was seen to increase between 500 and 550 °C, and between 600 and 700 °C (Figure 5.8). The analogue seismic b-value, initially around 1.75, decreased to roughly 1.6 at 250 °C. The subsequent increase in b-value at 500 °C to 1.7 coincided with the increase in AE. The increased AE rate and b-value suggests that some thermal microcracking occurred between 500 °C and 700 °C.

During cooling, the b-value saw a significant decrease from around 1.6 at 550 °C, to 0.9 at 450 °C (Figure 5.8). The decrease in b-value results from an increase in the number of higher amplitude AE hits, and is indicative of thermal microcracking, which is supported by the increase in AE activity at these temperatures. The b-value then re-

mains between 0.9 and 1.25 throughout cooling, until the sample temperature approaches room temperature, where the b-value increases sharply to 1.7, accompanied by a marked increase in the AE activity (Figure 5.8).

Measurements made at room temperature before and after heating to 700 °C showed v_P of the Rubble Creek Basalt sample to decrease from 4.45 km/s to 2.86 km/s, indicating significant thermal microcracking had occurred.

THERMAL CYCLING OF LA LUMBRE ANDESITE Figure 5.9 shows the measurements of v_P, the number of AE hits per 10 °C, and the CWI relative time shift with furnace temperature during three heating and cooling cycles of La Lumbre Andesite to a maximum temperature of 450 °C. During the first cycle, v_P initially increased with temperature, from 2.12 km/s, to 2.41 km/s at 250 °C (Figure 5.9a).

Betwee 250 and 450 °C, v_P was near constant during heating, reaching 2.47 km/s at 450 °C. The CWI relative time shift was also constant and low in amplitude between 250 and 450 °C (Figure 5.4b), showing little apparent change in velocity at these temperatures. The halt in the velocity increase coincided with the onset of AE at 250 °C (Figure 5.4c).

Cycles two and three showed a quasi-reversible increase of v_P with temperature of around 0.6–0.7 km/s, and a decrease in the number of detected AE hits. CWI measurements also showed very similar behaviour between cycles two and three, with generally no further permanent changes in microstructure. The decrease in velocity during cooling of cycles two and three is similar in amplitude to during the first cycle.

It is noted that at the end of cycle three, the AE activity increased, and an apparent decrease in velocity was observed, indicating damage to the sample. This could be attributed to thermal microcracking, but may be due to the applied load of 0.3 MPa on the sample. The observed net decrease in v_P was confirmed by measurements using a separate dedicated apparatus (see circle in Figure 5.9).

5.3.2 v_P, v_S and v_P/v_S

WAVE VELOCITIES OF ETNA BASALT The CWI relative time shift observed for the Etna Basalt was mostly positive during heating, and negative during cooling (Figure 5.4b), corresponding to an apparent increase in velocity with temperature. Assuming that velocity changes in the sample are isotropic and homogeneous, then the relative time shift in the arrival times of scattered waves may be equated to a change in the velocity of the rock. As for the Westerly Granite in the previous chapter (Section 4.1), the assumption was made here that apparent changes in CWI velocity are equal to changes in v_S. v_S,

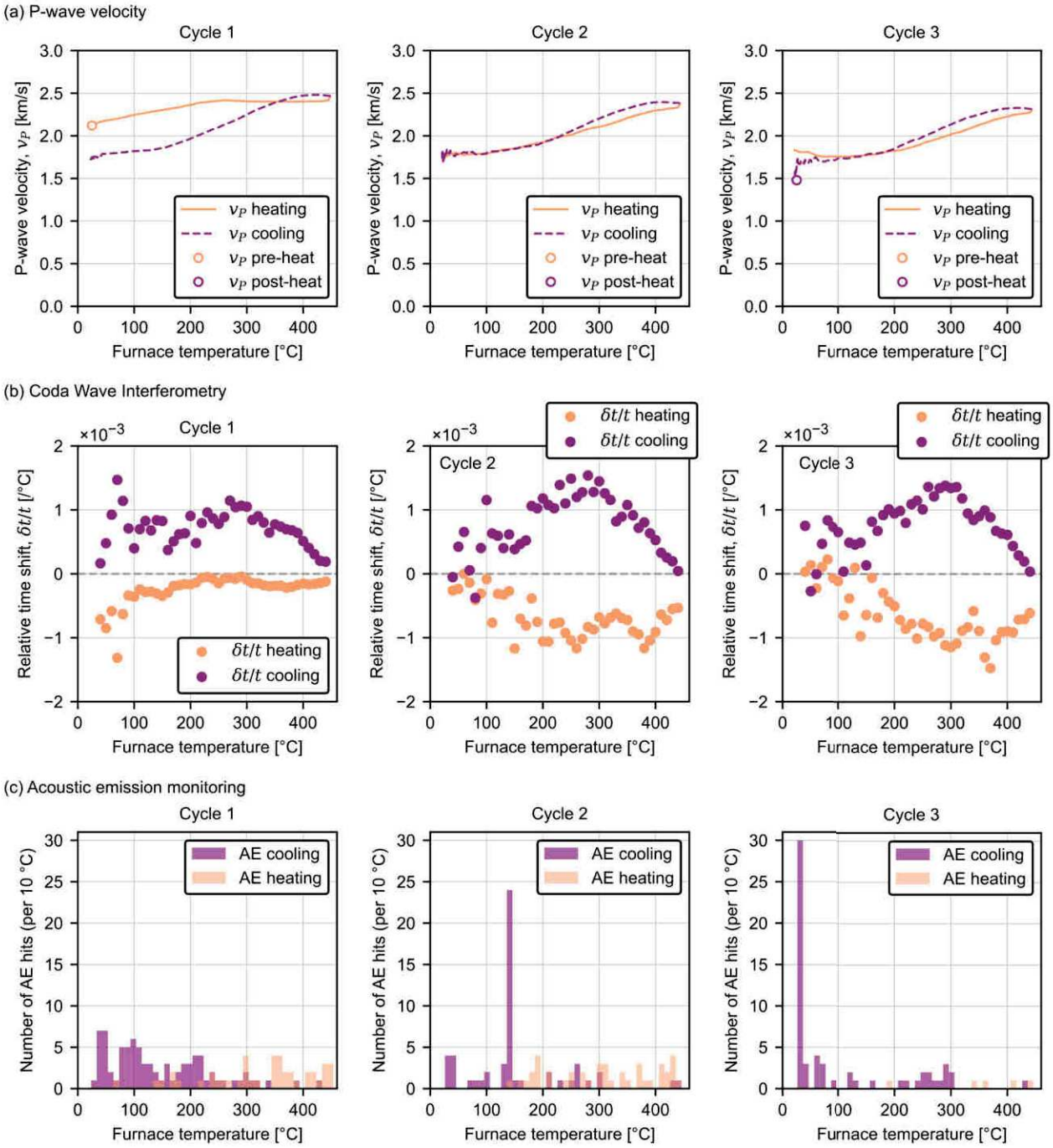

Figure 5.9: Comparison between (a) direct P-wave velocity (v_P), (b) coda wave interferometry (CWI) measurements, and (c) acoustic emissions (AE), made on samples of andesite from Volcàn de Colima, Mexico, when heated to 450 °C and cooled over three cycles. (a) P-wave velocity: symbols represent v_P measurements made at room temperature before and after heating; lines represent v_P against furnace temperature during heating (solid) and cooling (dashed), calculated from the shift in P-wave wave arrival time with temperature and the initial v_P of the intact rock, measured prior to heating. (b) CWI: the relative time shift per °C (averaged over 10 °C intervals) against furnace temperature. (c) AE monitoring: bars shows the number of AE hits per 10 °C against furnace temperature.

shown in (Figure 5.10) was calculated by multiplying the CWI relative velocity change by the static measurement of v_S made at room temperature prior to heating (see Chapter 2 for methods).

For the Etna Basalt, During the first cycle, v_S was seen to increase with temperature, from 2.30 km/s to 2.37 km/s, which was less than the increase in v_P (Figure 5.10) during cycle one. The v_P/v_S ratio therefore increased with temperature, by 9 %, from 1.49 to 1.59 (Figure 5.10).

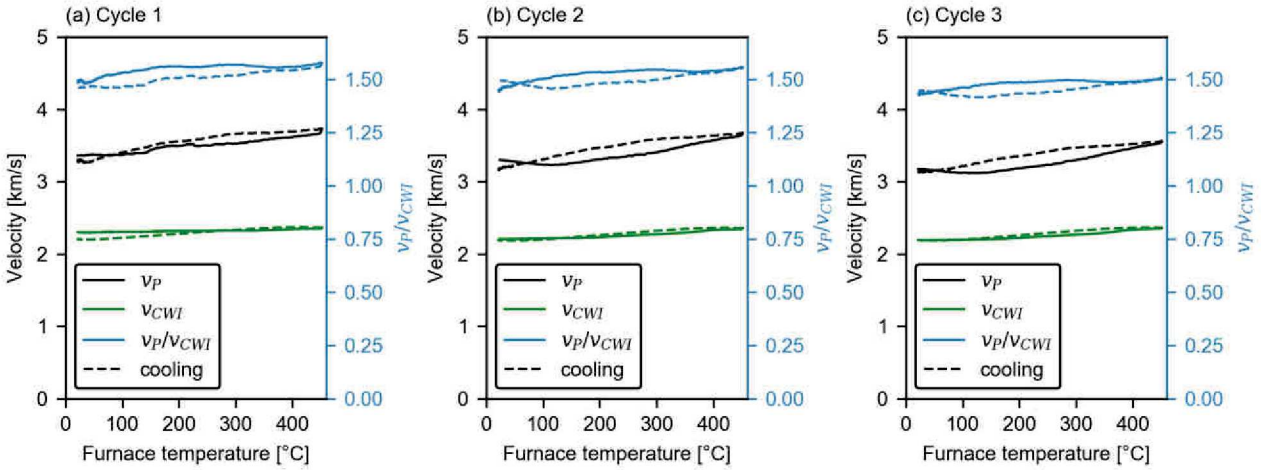

Figure 5.10: The wave velocity of Etna Basalt against furnace temperature during three heating and cooling cycles to a maximum temperature of 450 °C. Curves represent v_P (black), the CWI pseudo S-wave velocity, v_{CWI}, (green), and their ratio (blue). v_P and v_{CWI} are calculated respectively from the time shift of the P-wave first arrivals and the CWI relative time shift, scaled to the static v_P and v_S measurements of the unheated basalt. Solid lines indicate heating, and dashed lines indicate cooling.

WAVE VELOCITIES OF RUBBLE CREEK BASALT Figure 5.11 shows v_S, v_P, and their ratio against sample temperature. During the first cycle, v_S is near constant during heating, at around 2.58 km/s. During cooling, v_S decreases from around 250 °C to 2.32 km/s at room temperature, due to thermal microcracking (Figure 5.11). The v_P/v_S ratio showed a slight decrease with temperature during the first heating cycle, from 1.77 to 1.66 (Figure 5.10). During cooling, the ratio decreases further, to 1.51 at room temperature. During the second cycle for the Rubble Creek Basalt, v_S increased from 2.32 to 2.59 km/s at 450 °C, and the v_P/v_S ratio increased from 1.5 to 1.55.

WAVE VELOCITIES OF LA LUMBRE ANDESITE For the La Lumbre Andesite, due to the high attenuation and scattering of waves within the porous rock, the S-wave arrival time prior to heating could not be established with confidence, and hence the initial value of v_S at room temperature could not be calculated. However, the CWI method did

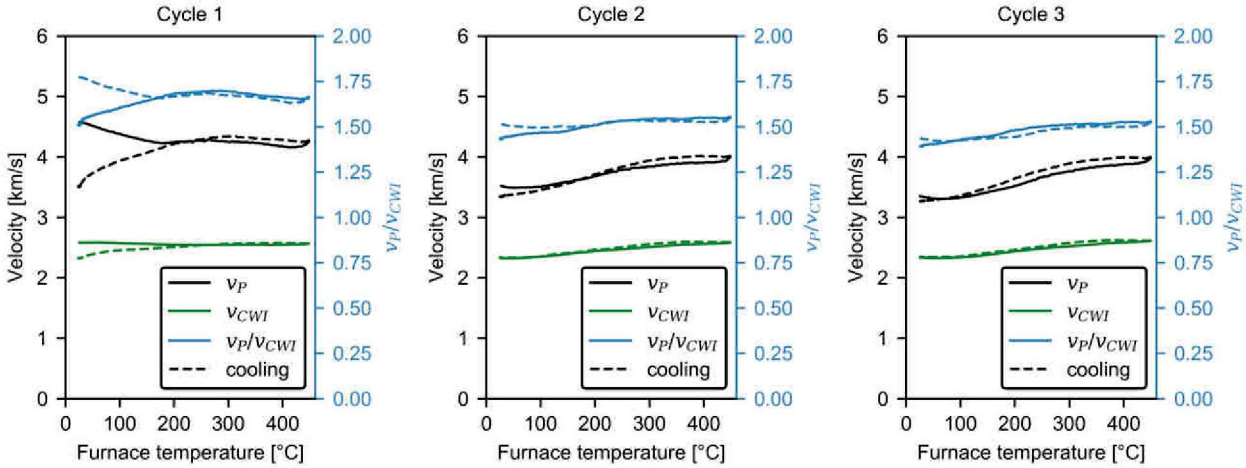

Figure 5.11: The wave velocity of Rubble Creek Basalt against sample temperature during three heating and cooling cycles to a maximum temperature of 450 °C. Curves represent v_P (black solid), the CWI pseudo S-wave velocity, v_{CWI}, (green), and their ratio (blue). v_P and v_{CWI} are calculated respectively from the time shift of the P-wave first arrivals and the CWI relative time shift (Equation 2.2), scaled to the static v_P and v_S measurements of the unheated basalt. Solid lines indicate heating, and dashed lines indicate cooling.

provide quantified relative changes in v_S. Figure 5.12 shows the relative changes in v_P, normalised to the initial velocity prior to heating, and the CWI relative velocity change (with respect to the first value, see Chapter 2 for details). Both v_P and the CWI relative velocity change showed a similar trend with heating and cooling for the La Lumbre Andesite, although the increase in v_P during heating of the first cycle was slightly greater than during cycles two and three.

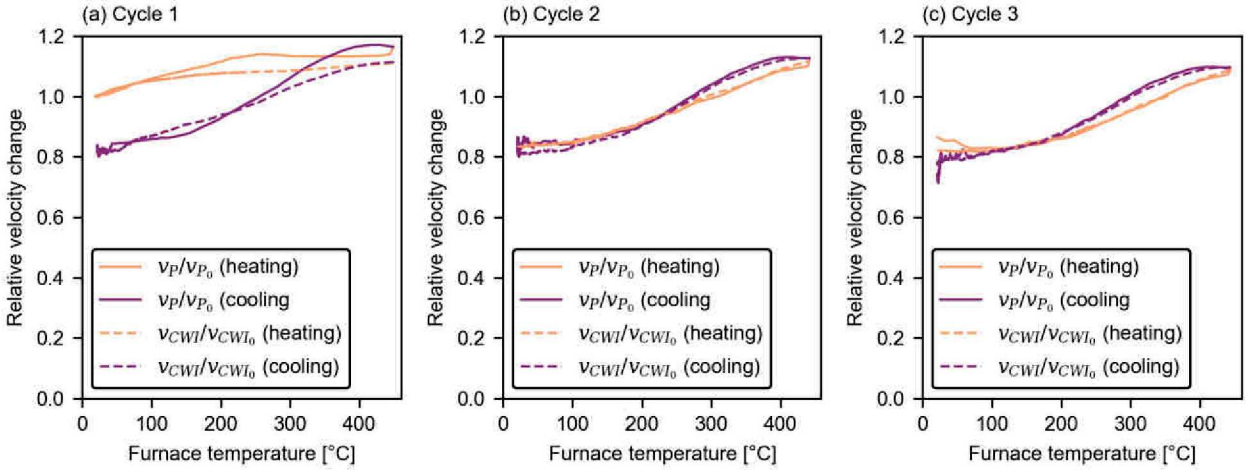

Figure 5.12: The relative wave velocities of La Lumbre Andesite, Volcàn de Colima, Mexico, against furnace temperature during three heating and cooling cycles (a–c) to a maximum temperature of 450 °C. Curves represent v_P (solid) normalised to the initial value prior to heating, and the relative change in the velocity calculated by Coda Wave Interferometry (v_{CWI}; dashed). The relative change in v_{CWI} is shown as the S-wave arrival time could not be picked to calculate the initial v_S (see text for details).

5.3.3 *Properties of the thermally-stressed Rubble Creek Basalt*

The Rubble Creek Basalt has a similar porosity to the granites studied previously (~0.3–1.5 %), and its porphyritic texture (a completely-crystallised groundmass containing phenocrysts) provides the most interesting comparison with the granites (Chapter 4).

To examine the influence of thermal stressing on the rock properties of the Rubble Creek Basalt, as for the granites (Chapter 4), a suite of variably thermally-stressed samples were prepared by heating to temperatures ranging from 100 to 900 °C and cooling, and measurements of their physical, mechanical, transport, and thermal properties were made. Two additional samples were heated to 300 and 700 °C, and "shock"-cooled through immersion in water. Presented below are measurements of the microcrack lengths and densities, and the physical, transport, thermal and mechanical properties of the heated samples, all performed at room temperature.

MICROCRACK DENSITY MICROANALYSIS Following the methodology presented in Chapter 3 (Griffiths et al., 2017a), the mean crack length ($2c$), the number of cracks per unit area (N_A), the 2D crack density ($\gamma = N_A c^2$; Walsh (1965)), and the surface area per unit volume (S_V; Underwood (1967)) were calculated from optical micrographs of thin sections of Rubble Creek Basalt. Un-heated samples, and samples heated to 300 and 700 °C (both slow and shock-cooled) were

analysed. Mean values of crack characteristics across each thin section are shown with thermal stressing temperature in Figure 5.13.

Figure 5.14 shows the distribution of the number of intersections of microcracks within the Rubble Creek Basalt thin sections with horizontal (P_I) and vertical, (P_{II}) test lines, and their sum (S_V) (see Chapter 3 for details). There is no clear trend in the spatial distribution of S_V, and P_I and P_{II} are similar for each thin section: there appears to be no spatial preference for thermal microcracking or preferential microcrack orientation within any of the thin sections.

The microcrack surface density (S_V) increased with thermal stressing temperature Figure 5.13, from 3.1/mm (unheated) to 9.6/mm (700 °C). The number of microcracks per unit area (N_A) also increased with thermal stressing temperature, from 25.4/mm^2 (unheated) to 115.7/mm^2 (700 °C). The mean microcrack length was seen to decrease with increasing thermal stressing temperature, from 0.10 mm (unheated) to 0.063 mm (slow-cooled) and 0.067 (shock-cooled) 700 °C samples. The decrease in the calculated microcrack length is partly due to the microcrack analysis procedure (Chapter 3), which splits intersecting microcracks at their junction points. Generally, γ increases with thermal stressing temperature, except for the 300 °C slow-cooled sample, which had the highest crack density (Figure 5.13c). This anomaly is due to the sensitivity of γ to the crack length, which was higher for this sample.

PHYSICAL AND TRANSPORT PROPERTIES Figure 5.15 reports the measurements of the connected porosity, v_P, and permeability of the thermally-stressed samples of the Rubble Creek Basalt. Measurements show: a porosity increase from 1.06 % (unheated) to 1.27 % at 800 °C and 1.19 % at 900 °C (Figure 5.15a); a permeability increase from 4.40×10^{-19} m^2 (100 °C) to 5.46×10^{-17} m^2 (900 °C) (Figure 5.15c); and a decrease in v_P from 4.45 km/s (unheated) to 2.54 km/s at 800 °C and 2.57 km/s at 900°C (Figure 5.15b). Whilst thermal microcracks affect the velocity and permeability, they do not significantly affect the porosity.

THERMAL PROPERTIES Figure 5.16 shows the thermal diffusivity, the thermal conductivity, and the specific heat of the heated Rubble Creek Basalt samples against thermal stressing temperature.

The thermal diffusivity shows little variation with thermal stressing temperature, remaining at around 0.7×10^{-6} m/s^2. The thermal conductivity shows a slight overall decrease with temperature, from 1.47 W/mK (unheated) to 1.37 W/mK (900 °C). The specific heat of the basalt remains at around 2.1 MJ K/m^3 regardless of heating temperature.

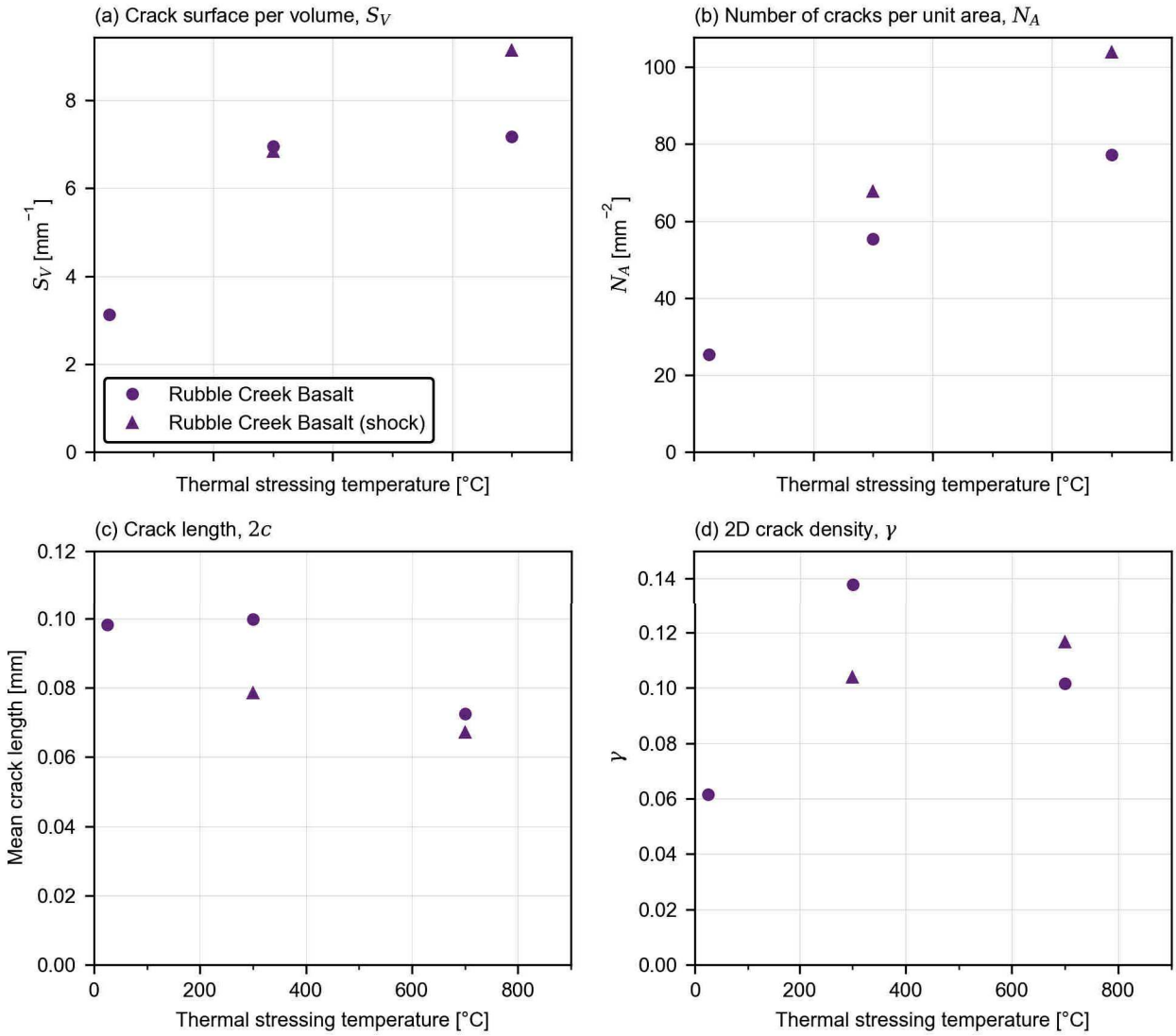

Figure 5.13: (a) Calculated crack surface area per volume (S_V; (Underwood, 1967)), (b) number of cracks per unit area (N_A) (c) mean crack length ($2c$) and (d) crack density (γ) against maximum heating temperature for Rubble Creek Basalt intact samples, and samples heated to 300 °C and 700 °C (both cooled at 1 °C (circles) and "shock"-cooled by quenching (triangles).

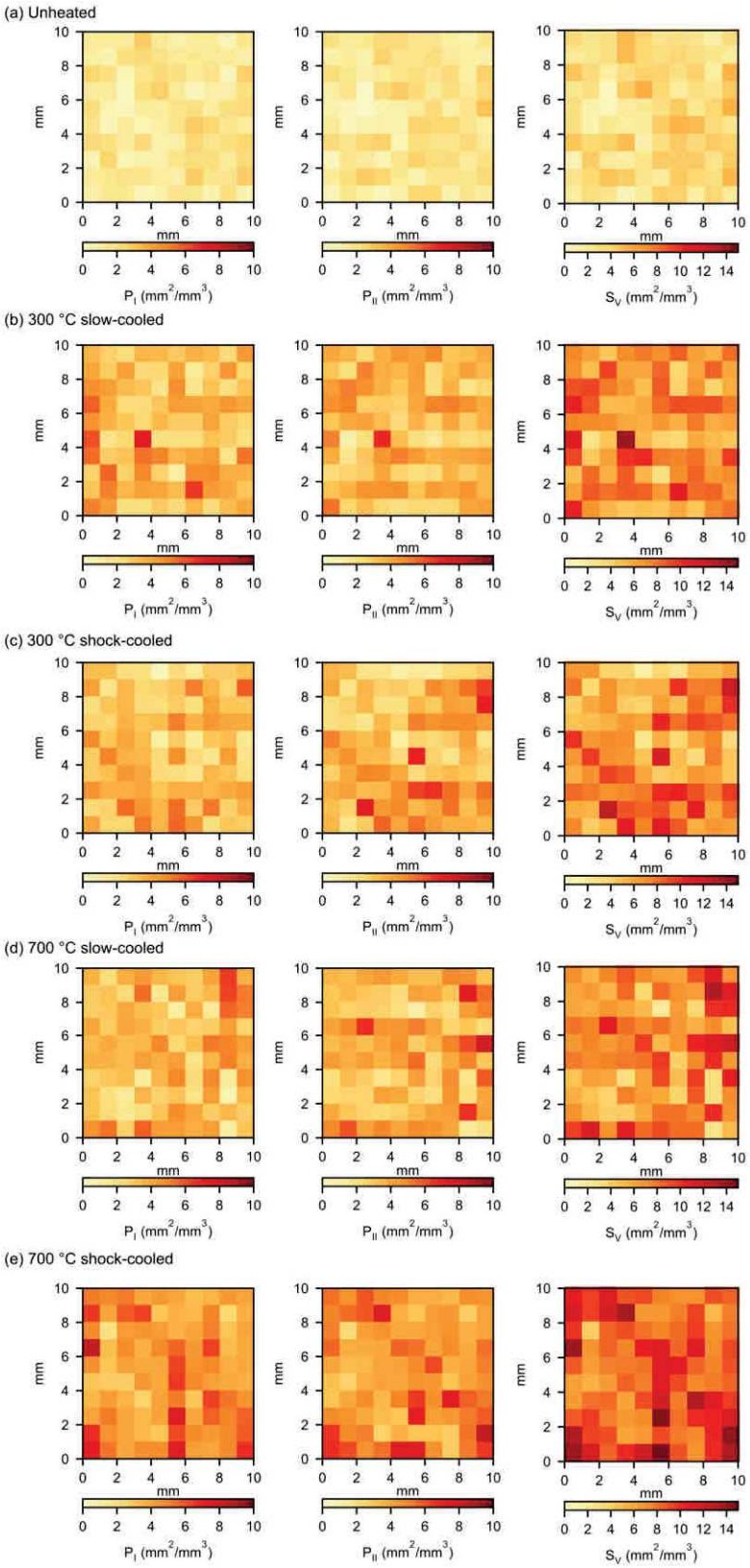

Figure 5.14: The number of intersections of microcracks with the horizontal (P_I) and vertical (P_{II}) test lines and their sum, the crack surface area per volume, S_V (Underwood, 1967) for thin sections of Rubble Creek Basalt samples heated to 300 °C and 700 °C (both cooled at 1 °C and shock-cooled by quenching).

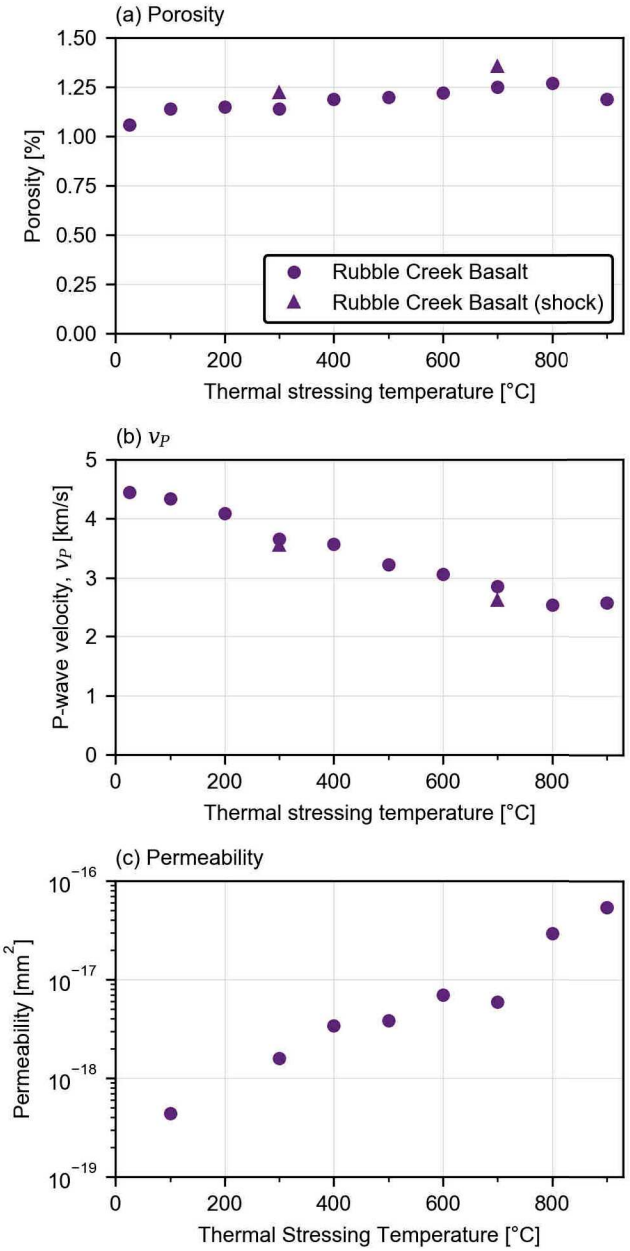

Figure 5.15: (a) Porosity, (b), P-wave velocity (v_P), and (c) permeability. Circles represent the samples cooled at 1 °C/min, and triangles represent the samples shock-cooled by quenching in water.

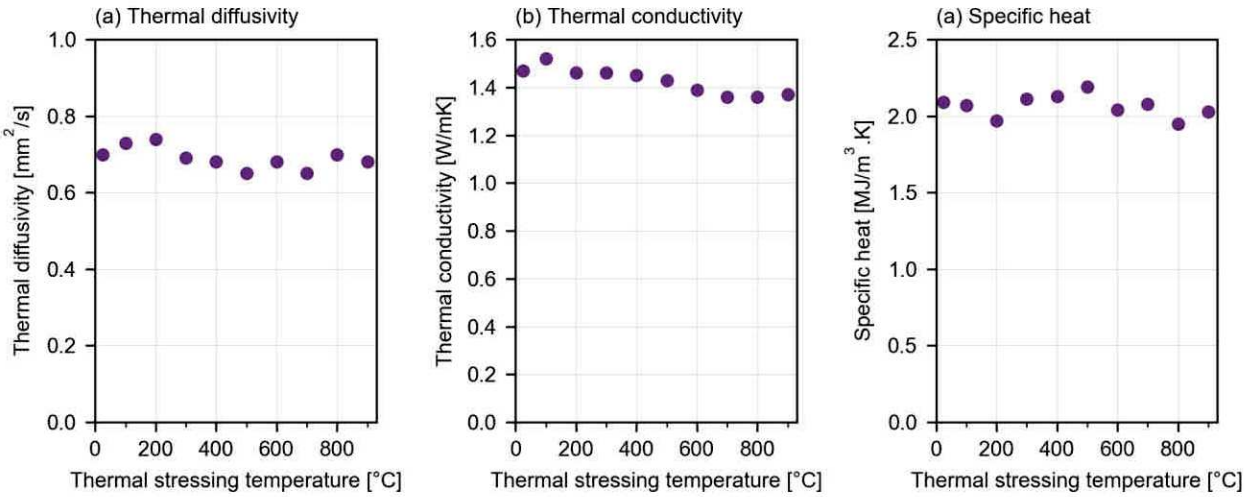

Figure 5.16: (a) Thermal diffusivity, (b) conductivity and (c) specific heat of thermally-stressed samples of Rubble Creek Basalt against thermal stressing temperature (cooled at 1 °C/min). Measurements were made using a Hot Disk TPS 500 Thermal Constants Analyser.

MECHANICAL PROPERTIES Figure 5.17 shows the uniaxial stress-strain curves of the uniaxial tests performed on the unheated, 300 °C, 700 °C (slow and shock- cooled) samples. The curves are similar for all samples, with the exception of the shock-cooled 700 °C sample, for which the initial non-linear section is longer. This non-linear part of the stress-strain curve is associated with microcrack closure (Walsh, 1965). As this sample has a higher porosity than the slow-cooled sample (Figure 5.15), but a similar crack density (Figure 5.13), it is suggested that higher aspect ratio microcracks may be present in the shock-cooled sample. The stress required to close higher aspect ratio microcracks is greater, roughly equal to the aspect ratio multiplied by the Young's modulus (Walsh, 1965).

The peak stresses (UCS) of the stress-strain curves (Figure 4.18) are shown in Figure 4.19. The UCS of the Rubble Creek Basalt shows no clear evolution with thermal stressing temperature, or microcrack density (Figure 5.13).

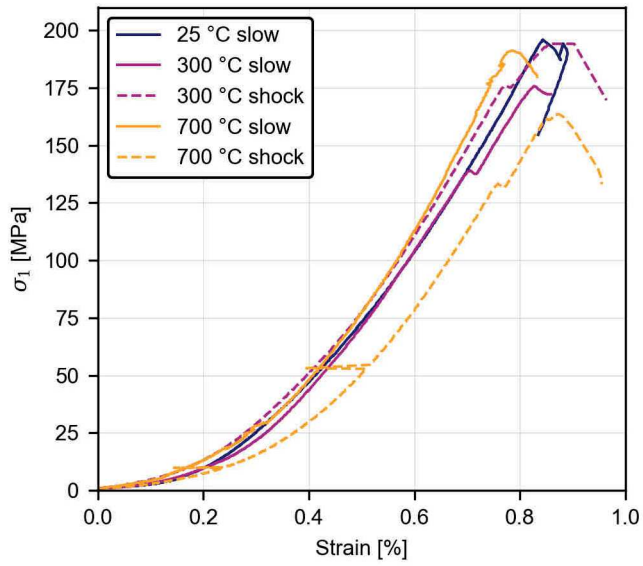

Figure 5.17: Uniaxial stress against axial strain measured during uniaxial tests on non-heated, 300 °C and 700 °C (cooled at 1 °C/min and shock-cooled) samples of Rubble Creek Basalt.

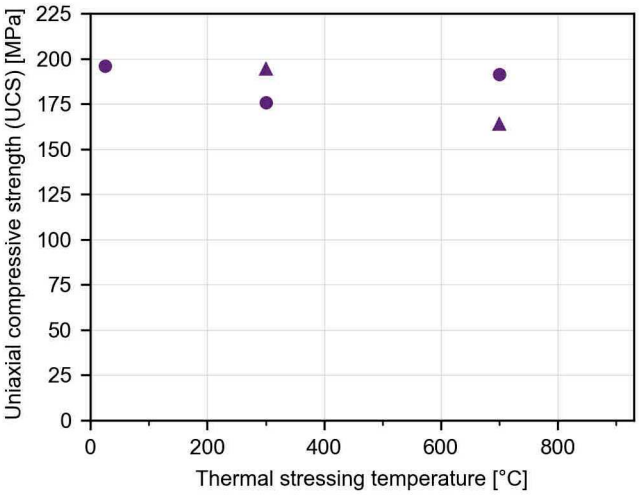

Figure 5.18: Uniaxial Compressive Strength (UCS) of Rubble Creek Basalt against maximum heating temperature (25–900 °C). Circles represent the samples cooled at 1 °C/min, and triangles represent the samples shock-cooled by quenching.

5.4 DISCUSSION

The three volcanic rocks were chosen to have different microstructures: the Etna Basalt had a porosity of 4 %; the Rubble Creek Basalt had a lower porosity of 1 %; and the andesite had a much higher porosity of 23 %. The three rocks varied in terms of microstructure,

both basalts were completely crystallised (unlike the andesite), the Etna Basalt contained small pores, the Rubble Creek Basalt contained no pores, and the La Lumbre Andesite contained large pores.

5.4.1 *Thermal microcracking*

5.4.1.1 *Thermal microcracking during heating*

Figure 5.19 shows the relative changes in v_P of the Etna Basalt, the Rubble Creek Basalt, and the La Lumbre Andesite with furnace temperature during three heating and cooling cycles to 450 °C. v_P has been normalised to the value at the beginning of each cycle. During the first cycle, the evolution of v_P with temperature was different for each rock (Figure 5.19). During heating: v_P of the Etna Basalt increased throughout; v_P of the La Lumbre Andesite increased up to 250 °C, and then remained constant up to 450 °C; and the v_P of the Rubble Creek basalt decreased throughout.

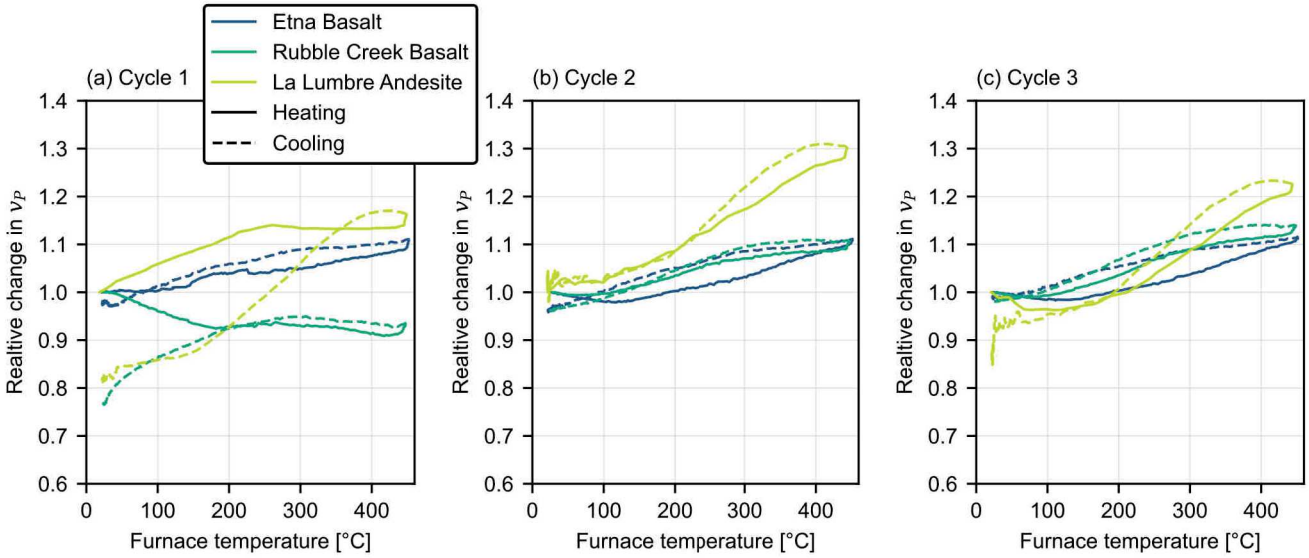

Figure 5.19: Relative change in P-wave velocity (v_P)—normalised to the velocity at the beginning of each cycle—against sample temperature during three heating (solid lines) and cooling (dashed lines) cycles (a–c) of samples of basalt from Mt. Etna, Italy (~4 % porosity), basalt from Rubble Creek, Canada (~1 % porosity), and andesite from Volcàn de Colima (~23 % porosity) to a maximum temperature of 450 °C.

Combined AE monitoring and velocity measurement showed no thermal microcracking to occur within the Rubble Creek Basalt during heating to 450 °C (no AE was detected), and little within the Etna Basalt (the velocity increased) (Figure 5.5 and Figure 5.7)

Here, the lack of thermal microcracking in the Etna Basalt and Rubble Creek Basalt during heating to 450 °C indicates that the ther-

mal expansion mismatch within the rock is insufficient to generate the stresses required for microcracking. This may be due to the pre-existing microcracks in the Etna Basalt (Figure 5.1) and Rubble Creek Basalt (Figure 5.2), accommodating the thermal strain without further microcracking (note that no stress relaxation through viscous deformation is expected here).

Additional AE monitoring tests were performed on the Etna Basalt and Rubble Creek Basalt during heating to 700 °C and cooling (velocity measurements could not be performed above 450 °C due to the limitations of the acoustic sensors). When the Etna Basalt was heated to 700 °C however, the increase in b-value and the rate of AE between 500 and 600 °C, and between 650 and 700 °C are indicative of thermal microcracking (Figure 5.5). When the Rubble Creek Basalt was heated to 700 °C some thermal microcracking was observed between 500 and 700 °C, through fluctuations in b-value coinciding with increased AE rate (Figure 5.8). Results show that at higher temperatures the thermal stresses surpassed the threshold for microcracking in the Etna and Rubble Creek Basalts.

The plateau in velocity of the La Lumbre Andesite during heating, observed in both the v_P and CWI measurements, and the onset of AE show that thermal microcracking occurred during heating from 250 to 450 °C (Figure 5.9). During cooling, however, v_P decreased throughout, from 2.47 km/s at 450 °C to 1.74 km/s at room temperature, which resulted in a permanent velocity decrease of 0.38 km/s due to thermal microcracking during the first cycle.

It is noted that for basalts containing zeolites, their velocity has been seen to decrease significantly when heated to beyond 350 °C (Kern, 1982), due to the breakdown of zeolites due to dehydration and an increase in crack porosity. Such behaviour was not observed for the rocks studied here, however, as the materials do not contain any zeolites (or chlorites, or clays, which also contain structurally-bound water (Kern, 1982)).

5.4.1.2 *Thermal microcracking during cooling*

Following cooling from 450 °C, an overall decrease in v_P was measured for all samples (Figure 5.19), and the net decrease in velocity observed in the Rubble Creek Basalt and the La Lumbre Andesite following the first cycle are attributed here to thermal microcracking (Table 5.1). For the Etna Basalt, no microcracking occurred during cooling, as the velocity decrease during cooling showed little hysteresis.

During cooling, the v_P of the Rubble Creek Basalt increased slightly between 450 °C and 250 °C, and then rapidly decreased between 250 °C and room temperature, the velocity decrease coinciding with an increase in AE activity (Figure 5.7). These results show that for the Rubble Creek Basalt, thermal microcracking occurred during cooling

of cycle one, between around 250 °C and room temperature. When the Rubble Creek Basalt was heated to 700 °C and cooled, the large decrease in b-value during cooling, with the increased AE rate throughout, suggest that thermal microcracking occurred predominantly during cooling (Figure 5.8). The increase in AE rate and b-value towards the end of cooling suggest that many small thermal microcracks were formed. Following heating to 700 °C and cooling, v_P of the Rubble Creek Basalt decreased by 64 % due to thermal microcracking, similar to the 63 % decrease in v_P measured by Vinciguerra et al. (2005), when they heated Seljadur Basalt (initial porosity of 4 %) to 900 °C. Browning et al. (2016) also observed AE during cooling when they performed AE monitoring during the heating and cooling of samples of dacite (Nea Kameni, Santorini, Greece) and a basalt (Seljadur, Iceland) to a peak temperature of 1100 °C, which they attributed to thermal microcracking. Combining AE monitoring and velocity measurements, thermal microcracking during cooling could be confirmed for the Rubble Creek Basalt.

For the Rubble Creek Basalt, thermal microcracking was observed during cooling, but not during heating. One explanation is that the crystal boundaries are weaker in tension than in compression, so that the stress criteria for failure are more easily fulfilled during cooling (contraction and pulling apart of crystals) than during heating (expansion and pushing together of crystals). Room temperature measurements of v_P of the Rubble Creek Basalt showed a decrease with thermal stressing temperature from 100 °C (Figure 5.15). The low AE activity during heating up to 100 °C (Figure 5.8) suggests that even at lower temperatures, thermal microcracking occurs during the cooling phase.

For the La Lumbre Andesite, the velocity decrease during cooling followed a similar trend during all cycles, including cycles two and three where no permanent velocity reduction was observed, suggesting that little thermal microcracking occurred during cooling of the first cycle.

Here, it was essential to perform AE monitoring during cooling in volcanic rock, as between the different rocks, thermal microcracking occurred throughout the entire thermal stressing cycle. A summary of the temperature conditions for thermal microcracking during cycle one for the Etna Basalt (negligible microcracking), the Rubble Creek Basalt (during cooling), and the La Lumbre Andesite (during heating) is shown in Table 5.1.

Browning et al. (2016) observed AE mostly during the cooling phase of thermal cycling to 1100 °C of: Seljadur Basalt, of initial porosity ~4 % and v_P of 5.52 km/s; and Nea Kameni Dacite, of initial porosity ~10 % and v_P of 5.29 km/s. Both of these rocks contain a crystallised groundmass. Assuming that the AE during cooling observed by Browning et al. (2016) was due to microcracking, all rocks that have

Rock	Description	Porosity	v_P	Microcracking during heating	Microcracking during cooling
Etna Basalt	Microcracks Crystallised groundmass Small pores	~4%	3.36 km/s	-	-
Rubble Creek Basalt	Microcracks Crystallised groundmass No pores	~1%	4.57 km/s	-	250–450 °C
La Lumbre Andesite	Microcracks Glass Large pores	~23%	2.12 km/s	250–450 °C	-

Table 5.1: The temperature conditions for thermal microcracking during cycle one of heating to 450 °C and cooling of Etna Basalt, Rubble Creek Basalt, and La Lumbre Andesite.

been observed to microcrack during cooling, here (Table 5.1) and in Browning et al. (2016), contained a crystallised groundmass.

The high initial v_P of the Seljadur Basalt and Nea Kameni Dacite (Browning et al., 2016) are indicative of a microcrack density lower than for the Rubble Creek Basalt, and significantly lower than for the Etna Basalt (Table 5.1). Whilst the Etna Basalt also has a crystallised groundmass, it did not undergo microcracking during cooling due to its high initial crack density and a Kaiser memory effect (Vinciguerra et al., 2005).

For the La Lumbre Andesite, however, microcracking was observed during heating (Table 5.1, Figure 5.9). This could be due to the many large pores within the La Lumbre Andesite, which weaken the material significantly (as predicted by the Sammis and Ashby (1986) model for brittle failure of porous material), thus making it more susceptible to thermal stresses. During cooling, the microcrack density of the La Lumbre Andesite was high, owing to both the initial microcracks, and those formed during heating. As for the Etna Basalt (Table 5.1), little thermal microcracking was observed during cooling owing to a Kaiser stress-memory effect. Whilst Browning et al. (2016) observed most AE during the cooling of both the Seljadur Basalt and Nea Kameni Dacite, during heating, AE activity was higher for the higher porosity Nea Kameni Dacite. This suggests that porosity plays an important role for thermal microcracking during heating.

It can be concluded that thermal microcracking may occur during cooling within low crack density volcanic rock containing a crystallised groundmass, and during heating within high porosity volcanic rock.

5.4.2 *Kaiser effect*

CYCLE ONE During cycle one of heating to 450 °C and cooling, changes in the v_P of Etna Basalt with temperature were quasi-reversible. This concurs with measurements made by Vinciguerra et al. (2005), who observed no significant change in the wave velocity of basalt from Mt. Etna measured at room temperature following heating to 300, 600, and 900 °C. They attributed the lack of a permanent velocity change to the high initial crack density in the basalt and a Kaiser memory effect (Kaiser, 1953)—whereby stresses in the rock must surpass those previously experienced to induce further damage. Heap et al. (2009a) also observed a stress-memory effect when they measured the elastic moduli of basalt from Mt. Etna both before and following heating to 900 °C at room pressure, seeing no change in Young's modulus or Poisson's ratio due to heating and cooling.

Here, however, when the Etna Basalt was heated to 700 °C and cooled (Figure 5.5), v_P was permanently decreased by 12 %. A decrease in velocity was not observed by Vinciguerra et al. (2005) when they heated Etna basalt to 600 or 900 °C.

Vinciguerra et al. (2005) performed AE monitoring on Etna Basalt during heating to 600 °C, and Figure 5.20 shows the cumulative number of AE hits they detected, alongside AE data from this study during the heating of Etna Basalt to 700 °C. The AE detected by Vinciguerra et al. (2005), in absence of any significant microcrack damage, was explained as being due to the elastic opening of cracks during heating. This may also be the case here when Etna Basalt was heated to 450 °C and cooled, but instead the velocity measurements indicate that that during heating cracks close rather than open. This does not explain, however, why more AE were detected during cooling than during heating, which remains unclear. The onset of AE observed here at around 110 °C during heating of the Etna Basalt to 700 °C (Figure 5.20) differs to the immediate onset of AE with heating observed by Vinciguerra et al. (2005). This could be due to friction between the waveguide and their sample as the contact pressure was not servo-controlled.

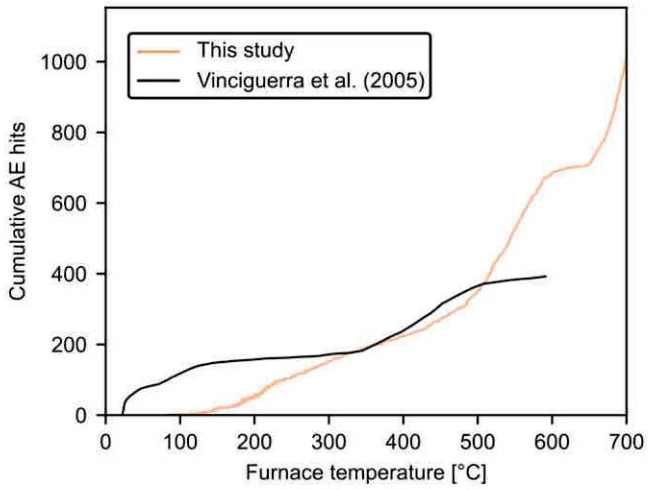

Figure 5.20: Cumulative AE hits during heating of Etna Basalt to 700 °C (this study), and data from Vinciguerra et al. (2005) during heating to 600 °C.

REPEATED CYCLES AE monitoring of volcanic rock has rarely been performed during repeated heating and cooling, despite their relevance for volcanic environments (Heap et al., 2017). Here, during cycles two and three, the velocities of all rocks were seen to change quasi-reversibly with temperature (Figure 5.19), indicating little further thermal microcracking occurred during the repeated cycles.

Whereas the Rubble Creek Basalt saw significant thermal microcracking during the cooling phase of the first cycle, and the La Lumbre Andesite microcracked during heating, the thermal stresses during cycles two and three were insufficient to cause significant thermal microcracking within either rock. This is characteristic of a Kaiser memory effect, and also shows that the Etna Basalt must have already experienced thermal stresses greater than those applied during these experiments.

5.4.3 *Crack closure during heating and velocity*

The increase in velocity with temperature is attributed to the closure of both pre-existing microcracks (during the first cycle for the Etna Basalt, and La Lumbre Andesite; Figure 5.19a), and/or newly-formed thermal microcracks (second and third cycles for the Rubble Creek basalt and La Lumbre andesite; Figure 5.19b, c). The velocity increase during heating was unexpected, and contrasts with measurements of velocity on the granites (Chapter 4), which decreased during heating in all cases. One exception is the study by Scheu et al. (2006), in which dacite collected from the Mt. Unzen volcano, Japan, was heated to 600 °C under 100 MPa confining pressure. The authors found both v_P and v_S to increase with temperature (from 5.11–5.48 km/s at room

temperature to 5.51–5.73 km/s at 600 °C). Explanations Scheu et al. (2006) propose for this behaviour are: the closure of pore space due to the thermal expansion of the rock matrix; crack closure through relaxation at high temperatures; and/or the presence of glass within the groundmass (Hughes and Maurette, 1957), the velocity of silica has been shown to increase with temperature by around 0.55 % per 100 °C (Ide, 1937).

As the wave velocities of all three rocks increased from the start of heating during cycles two and three, stress relaxation at these low temperatures is not expected. The Etna Basalt and the Rubble Creek Basalt contain no glass, and therefore the increase in v_P is most likely due to the closure of microcracks during heating as the groundmass expands, filling the void space (analogue to microcrack closure under confining pressure (Walsh, 1965)). The crack closure leads to an effective decrease in the crack density, which increases the wave velocity (O'Connell and Budiansky, 1974).

The La Lumbre Andesite does however contain some glass (Heap et al. (2017) found 13.5 % glass in samples of a similar andesitic block, collected adjacent to the La Lumbre Andesite discussed in this thesis). However, the increase in the v_P of glass at 450 °C is far lower than the ~30 % increase in v_P observed for the La Lumbre Andesite at 450 °C (Figure 5.12). For the La Lumbre Andesite, the significant velocity increase with heating is expected to be mostly due to crack closure.

It appears that in volcanic rock, the increase in velocity due to crack closure with heating competes with the intrinsic velocity of the rock matrix. To examine the influence of temperature on the matrix velocity of rock, Kern (1982) measured v_P and v_S of samples of various rocks under a high confining pressure of 600 MPa to 600 °C. Confinement was applied with the aim of closing all microcracks, to negate their influence on velocity changes, and the results showed that in the absence of microcracks, the wave velocity of basalt decreases with temperature. Here it appears that during the heating of volcanic rock, the velocity increase due to crack closure competes with the decrease in velocity of the rock matrix. During the first cycle, the velocity of the Etna Basalt was seen to increase with temperature due to crack closure, however, this was not the case for less porous Rubble Creek Basalt between 25 and 200 °C. In the case of the Rubble Creek Basalt, the decrease in wave velocity with increasing temperature during the first heating cycle suggests that any closure of the pre-existing microcracks was insufficient to counter the decreasing velocity of the rock matrix.

During the second and third heating cycles, the relative increase in v_P with heating of La Lumbre andesite was roughly twice that of the Etna and Rubble Creek basalts (Figure 5.19b and c). The La Lumbre Andesite had the lowest initial v_P, owing in part to its many large vesicles (Figure 5.3), which suggests that greater relative changes in

velocity due to microcrack closure/opening may be expected in rock that contains pores and microcracks (induced or otherwise).

Crack closure during heating of cycles two and three led to an increase in v_P/v_S by 9 % for the Etna Basalt (Figure 5.10), and by 3–4 % for the Rubble Creek Basalt (Figure 5.11). An increase in v_P/v_S with temperature could be attributed to the strong decrease in crack aspect ratio with the compliance of cracks or an effective decrease in crack density as cracks close. The v_P/v_S ratio for the La Lumbre Andesite was near constant, as the relative increase in v_P and v_S with temperature were near identical (Figure 5.12).

5.4.4 *Implications for volcanic and geothermal environments*

5.4.4.1 *Implications for volcanic environments*

Temporal changes in seismic velocity within volcanoes are used to infer changes in their structure, e.g. at: Mt. Etna (De Luca et al., 1997; Laigle et al., 2000; Patane et al., 2002); Mt. Erebus volcano, Antarctica (Grêt, 2005); Merapi volcano, Indonesia, (Sens-Schönfelder and Wegler, 2006). At Mt. Etna, for example, 3D velocity models have been inferred from seismic monitoring, to better understand the structure of the volcano (De Luca et al., 1997; Laigle et al., 2000; Patane et al., 2002; Villaseñor et al., 1998). See Figure 1.5 for a case study at Mt. Etna (Patane et al., 2002). At Volcàn de Colima (from which the La Lumbre Andesite originates), Lamb et al. (2017) used CWI of ambient seismic noise to observe an apparent decrease in wave velocity of 0.2 % prior to eruption. The velocity decrease was anticipated as being due to fracture formation within the volcano as magma rose. It is argued that the significant velocity changes with temperature observed here (Figure 5.19) may rival changes in velocity due to mechanical deformation in volcanic environments.

The v_P/v_S ratio is known to increase with temperature, especially as temperature approaches the solidus (Sanders et al., 1995) and, as such, high v_P/v_S ratios may be interpreted as intrusive bodies (De Luca et al., 1997). Here, the wave velocities and the v_P/v_S ratio of the Etna Basalt and Rubble Creek Basalt increased with temperatures of up to 450 °C (Figure 5.10) due to microcrack closure. These new data are especially important as most available measurements of wave velocity were made at room temperature. These results show that observed changes in v_P/v_S within volcanoes may have a significant temperature component in absence of partial melting, which may provide information for prior seismic models and further insight for seismic model interpretation. It should be noted that the samples here were dry. The v_P/v_S ratio is known to increase with fluid saturation (O'Connell and Budiansky, 1974), and therefore prior knowledge of the in-situ conditions (e.g. temperature, fluid saturation) is useful to better interpret seismic models.

Thermal microcracking, observed during cycle one in the Rubble Creek Basalt during cooling, and in the La Lumbre Andesite during heating, also strongly influences v_P and v_S (Figure 5.7 and Figure 5.9). Where velocity models are used to infer changes in the structure of volcanoes, thermal cracking due to changes in temperature may also play a role. For the Rubble Creek Basalt and the La Lumbre Andesite, the change in behaviour between the first and the repeated cycles also highlight the importance of thermal history on velocity changes with temperature.

A number of studies have shown the elastic velocities of basalt from Mt. Etna to increase with confining pressure. Vinciguerra et al. (2005) measured v_P and v_S under confining pressures of up to 80 MPa. They found v_P to increase from 3.19 km/s to 4.69 km/s, and v_S from 2.05 km/s to 2.64 km/s at 80 MPa in one of their samples. Stanchits et al. (2006) found a similar increase in v_P and v_S of basalt from Mt. Etna during hydrostatic loading; for example v_P was increased by 50 % at 120 MPa. An increase in v_P and v_S with hydrostatic pressure was observed by Fortin et al. (2011), from 3.1 km/s at room pressure, to 5.5 km/s at 190 MPa. The increase in velocity due to the closing of low aspect ratio cracks under pressure is of the same order of magnitude as those observed here, due to an increase in temperature (Figure 5.10).

Even at depth, temperature may still affect wave velocity through crack closure. In the experiments by Fortin et al. (2011), Stanchits et al. (2006), and Vinciguerra et al. (2005), the wave velocities of basalt from Mt. Etna were shown to continually increase with confinement, up to the maximum confining pressures (190 MPa in the study by Fortin et al. (2011)), indicating that some high aspect ratio microcracks remained open. Scheu et al. (2006) measured an increase in the v_P of a dacite from the Mt. Unzen volcano, Japan, from 5.11–5.48 km/s to 5.51–5.73 km/s when heated to 600 °C under 100 MPa confining pressure, indicating that a velocity increase with temperature, as observed here, can also be expected at depth.

Taken together, the permeability measurements made at room temperature on the Rubble Creek Basalt, and the in-situ velocity measurements suggest that the permeability of the Rubble Creek Basalt (and potentially the Etna Basalt and La Lumbre Andesite) may decrease with increasing temperature, as microcracks close (as hypothesised by Gaunt et al. (2016)). In the case of a magma-filled conduit, the permeability in and around the conduit influences the dynamics of volcanic eruption (e.g., Eichelberger et al. (1986), Farquharson et al. (2017), Gaunt et al. (2016), Kushnir et al. (2017b), and Melnik et al. (2005)). Kushnir et al. (2017a) observed a decrease in the permeability above the glass transition due to relaxation and crack closure, and Gaunt et al. (2016) measured a decrease in the permeability of a dacite by more than 4 orders of magnitude when heated to 800

°C, which was suggested to be caused by crack closure. Here, crack closure was also observed with increasing temperatures—at temperatures well below the glass transition and in volcanic rock containing no glass—suggesting that temperature may have a significant influence on fluid flow around the conduit.

Where the physical properties of volcanic rock have previously shown little permanent change following thermal stressing (e.g. Heap et al. (2014a), Kendrick et al. (2013), and Schaefer et al. (2015)), indicating that the rock was already highly microcracked, the pre-existing microcracks may still influence rock properties at elevated temperatures as they close. For example the strength of volcanic rock has been shown to increase with temperature: Heap et al. (2017) showed the strength of andesite to increase with temperature below the temperature of the glass transition; Meredith and Atkinson (1985) measured an increase in the fracture toughness of a gabbro with increasing temperature; and Duclos and Paquet (1991) showed the compressive strength of basalt to increase from ~340 MPa at ambient-temperature to ~450 MPa at 650 °C.

A Kaiser (thermal) stress-memory effect was observed during multiple thermal stressing cycles of the volcanic rock samples, resulting in little further thermal microcracking during repeated cycles. A Kaiser effect has previously been observed at the volcano scale (Krafla volcano, Iceland) by Heimisson et al. (2015), who observed cyclic inflation and deflation at the surface due to magma flow within the volcano, and which only resulted in seismicity once the maximum inflation of the previous cycles was surpassed. This suggests that cyclic thermal stressing associated with the movement of magma may also produce a Kaiser effect on a larger scale, whereby thermal stressing of the surrounding rock mass may only result in cracking once the rock reaches temperatures greater (or lower) than those already experienced.

5.4.4.2 *Implications for geothermal reservoirs*

At geothermal sites, as for volcanoes, the monitoring of changes in wave velocity provides valuable information on changes in the reservoir. Many geothermal reservoirs are hosted in volcanic rocks (Grant et al., 2013), and therefore results here show the conclusions drawn from velocity models may depend on rock type and the thermal history of the rock. For example, the Awibengkok geothermal system in Indonesia is hosted in fractured andesite and rhyodacite, which has a mean porosity of around 10.6 %, and temperatures within the reservoir range from 240 to 312 °C (Stimac et al., 2008). As the porous La Lumbre Andesite saw the largest relative changes in wave velocity with temperature, it is expected that significant relative changes in velocity with temperature may be observed within the Awibengkok reservoir.

The Rubble Creek Basalt was observed to microcrack during cooling, which may occur at geothermal reservoirs where cool water is injected. Cooling-induced thermal stresses can have negative consequences around an injection well, where the combined thermal and mechanical stresses can cause rock instability and borehole breakouts (Bérard and Cornet, 2003; De Simone et al., 2013). The La Lumbre Andesite exhibited microcracking during heating, which may have implications for high temperature geothermal reservoirs, where hot geothermal fluids are extracted, and may cause thermal microcracking of rock during their ascent.

Whilst thermal microcracks affected the velocity and permeability of thermally-stressed samples of Rubble Creek Basalt, they did not significantly affect the porosity. This is likely due to the low aperture of thermal microcracks cracks within the Rubble Creek Basalt (seen in Figure 5.2), whereby an increase in crack density influences the v_P (Guéguen and Schubnel, 2003) and permeability (Guéguen and Dienes, 1989), but does not cause a large increase in porosity. The thermal diffusivity of the Rubble Creek Basalt was also not strongly affected by thermal stressing, which is likely due to the low increase in microcrack porosity with heating (Figure 5.15a), which has a first-order control on the heat diffusion within rock (Zimmerman, 1989). The low aperture microcracks within the Rubble Creek Basalt also did not influence the rock strength (Figure 5.18), which appears to be controlled by pre-existing flaws within the rock. This was supported by the micrograph analysis, which showed the initial mean microcrack length within the Rubble Creek basalt to be around 0.1 mm, compared to 0.06 mm when heated to 700 °C and cooled (Figure 5.13), suggesting that the newly formed thermal microcracks were shorter than the longer pre-existing microcracks which dictate the strength of the sample.

Figure 5.21 shows a simple 1D heat diffusion model which considers heat flow between a geothermal well at 25 °C and the reservoir rock at 300 °C. The temperature of within the reservoir T, at time t, and at a distance x from the well is given by Equation 5.1, where T_{well} is the temperature of the well (20 °C here), T_i is the initial temperature of the reservoir (300 °C), and D is the thermal diffusivity of the reservoir.

$$T_(x,t) = T_{\text{well}} + (T_i - T_{\text{well}})\text{erf}\left(\frac{x}{\sqrt{4Dt}}\right) \tag{5.1}$$

The diffusivity (D) was taken to be that of Rubble Creek Basalt $0.7 \times 10^{-6}\,\text{m/s}^2$ for the range of 25–300 °C (Figure 5.16). The decrease in temperature penetrates further into the reservoir over time, which for the thermal stimulation of a geothermal well can be several days (Grant et al., 2013). As the reservoir cools, an increase in permeability is expected as the Rubble Creek Basalt cools (see AE during cooling in Figure 5.7 and measurements of physical properties in Fig-

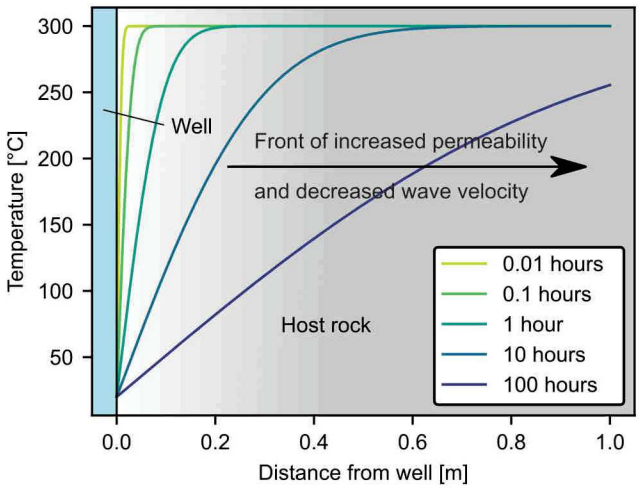

Figure 5.21: A simple 1D heat diffusion model of heat transfer from a geothermal well at 20 °C into the reservoir rock at 300 °C. The thermal diffusivity of the reservoir is that of Rubble Creek Basalt between 25 and 300 °C, 0.7×10^{-6} m/s^2 (Figure 5.16). As the temperature decreases further into the reservoir rock, thermal microcracking causes an increase in permeability and a decrease in wave velocity.

ure 5.15). Note that permeability enhancement due to microcracking would have a coupled effect with the temperature change, as thermal microcracking facilitates fluid flow further into the rock, accelerating cooling away from the well. The thermal diffusion model is relevant for the permeability evolution of the Rubble Creek Basalt, as measurements of physical properties (Figure 5.15 and microcrack densities (Figure 5.13) of the shock-cooled samples showed direct contact with cold water to have little added effect on the extent of thermal microcracking. It is understood, however, that fluid flow within many geothermal reservoirs is controlled by larger fractures, and not thermal microcracks. However, as thermal stimulation of geothermal wells enhance the permeability around the well due to the thermal contraction of the rock and the propagation of fractures (Grant, 2013; Jeanne et al., 2017; Kitao et al., 1995), thermal stresses due to cooling are expected to increase away from the well as fluid circulation is facilitated.

As a Kaiser stress-memory effect was observed when heating and cooling the volcanic rocks, it could be concluded that the permeability enhancement around geothermal wells due to thermal stimulation might not be repeatable. However, the circulation of high salinity geothermal fluids can cause significant mineral deposition within fractures (Batzle and Simmons, 1976), which can decrease permeability at geothermal wells (see Section C.1 and Griffiths et al. (2016)) and increase rock strength (Wyering et al., 2014). Therefore, thermal

stimulation can be used to clean out the mineral deposits (Siratovich et al., 2011), and cyclic thermal stressing could potentially re-fracture the newly strengthened rock (Engelder, 1987; Karner et al., 1997).

5.5 CONCLUSION

- Three volcanic rocks of different microstructures were selected: a basalt from Mt. Etna, Italy (~4 % porosity); a lower porosity (~1 %) basalt from "Rubble Creek", Canada; and a higher porosity (~23 %) andesite ("La Lumbre") from Volcàn de Colima, Mexico.
- AE monitoring and measurements of changes in wave velocity, using both P-wave direct travel time and Coda Wave Interferometry (CWI) techniques, were performed during three heating and cooling cycles to a maximum temperature of 450 °C.
- Changes in wave velocity during the first cycle were strongly dependant on rock type and microcrack content:
  - The Etna Basalt saw a reversible increase in velocity with increasing temperature, due to the closure of pre-existing microcracks;
  - The velocity of the Rubble Creek Basalt instead decreased during heating, controlled by the velocity decrease of its constituents. During cooling, significant thermal microcracking caused the velocity to decrease sharply;
  - The velocity of the La Lumbre Andesite increased during heating due to closure of pre-existing microcracks, until the increase was halted by thermal microcracking at around 250 °C. During cooling the velocity decreased.
- Table 5.2 shows the thermal conditions required for thermal microcracking within the volcanic rocks studied here, and within the Seljadur Basalt and Nea Kameni Dacite heated to 1100 °C and cooled by Browning et al. (2016) at a rate of 1 °C/min. The pore size results from observation of micrographs of thin sections (in Section 5.2 and Browning et al. (2016)).

  It is concluded that thermal microcracking may occur: during cooling within low crack density (high v_P) volcanic rock containing a crystallised groundmass (Rubble Creek Basalt, Seljadur Basalt, Nea Kameni Dacite); during heating within high porosity volcanic rock (La Lumbre Andesite, Nea Kameni Dacite); and during neither heating nor cooling in high crack density (low v_P) volcanic rock (Etna Basalt).

Rock	Description	Porosity	v_P	Microcracking during heating	Microcracking during cooling
Etna Basalt	Crystallised groundmass Small pores (< 0.1 mm)	~4%	3.36 km/s	No	No
Rubble Creek Basalt	Crystallised groundmass No pores	~1%	4.57 km/s	No	Yes
La Lumbre Andesite	Glass Large pores (~0.1–1 mm)	~23%	2.12 km/s	Yes	No
Seljadur Basalt Browning et al. (2016)	Crystallised groundmass Few pores	~4 %	5.52 km/s	42 AE hits	6166 AE hits
Nea Kameni Dacite Browning et al. (2016)	Crystallised groundmass Large pores (~0.1–1 mm)	~10 %	5.29 km/s	1310 AE hits	8573 AE hits

Table 5.2: The temperature conditions for thermal microcracking during cycle one of heating to 450 °C and cooling of Etna Basalt, Rubble Creek Basalt, and La Lumbre Andesite, and thermal cycling to 1100 °C of Seljadur Basalt and Nea Kameni Dacite (from Browning et al. (2016)).

- During the second and third heating/cooling cycles, all rocks saw a reversible increase in velocity with increasing temperature, due to the closing of new and old microcracks.
- CWI was used to infer changes in S-wave velocity (v_S) and calculate the v_P/v_S ratio in the Etna and Rubble Creek basalts. Whilst S-wave arrival times were too unclear to calculate v_S of the La Lumbre Andesite, CWI measurements gave an indication of the relative changes in v_S with temperature.
- v_P, v_S, and their ratio were shown to significantly increase with temperature, which has strong implications for the seismic monitoring of volcanoes, and geothermal reservoirs hosted in volcanic rock.
- Measurements on heated samples of Rubble Creek Basalt showed that thermal microcracks significantly increase the permeability of the rock, and suggest that permeability may also be decreased at elevated temperatures due to crack closure, influencing fluid flow within geothermal and volcanic systems.

6

THERMAL MICROCRACKING UNDER LOAD

This chapter presents the results of a pilot study of the influence of differential stress on thermal microcracking, and the influence of thermal microcracks formed under differential stresses on rock properties. In the previous chapters, thermal stressing experiments have been performed on rock samples under ambient pressure conditions, or under uniaxial stresses of 1 MPa or less, applied to ensure coupling between samples and acoustic sensors. Thus far, through microscopic analysis, no heterogeneity in the microcrack distribution nor preferential orientation of microcracks has been observed (see Section 4.2.2.3 for Garibaldi Grey Granite and Lanhélin Granite, and Section 5.3.3 for Rubble Creek Basalt). It has been assumed that the influence of uniaxial stresses of less than 1 MPa during heating and cooling on thermal microcracking are negligible, and that any small difference in the measurements of physical properties were due to sample variability.

In nature, rock is often simultaneously subject to significant thermal and mechanical stresses, in environments including geothermal reservoirs or volcanoes. For example, the superposition of thermal stresses and mechanical stresses around boreholes at geothermal sites increases the occurrence of breakouts (Bérard and Cornet, 2003).

Confining pressure has been shown to control the onset and the extent of thermal microcracking in rock. Wong and Brace (1979) measured the thermal expansion of several rocks during heating to 36 °C under varying hydrostatic pressures. For example, the thermal expansion during heating of a quartzite sample (from Cheshire, England) under 100 MPa confinement was greater than the contraction during cooling, resulting in a permanent increase in volume due to thermal microcracking. This strain hysteresis, however, was not observed when the rock was heated and cooled under pressures of 300 and 500 MPa; in these cases thermal microcracking was suppressed. Kern (1978) measured the volumetric strain of a granite during heating to temperatures of over 700 °C, under confining pressures of 10, 40 and 60 MPa, finding that the amplitude of thermal expansion with temperature decreased with confinement. Further, Kern (1979) measured P-wave (v_P) and S-wave (v_S) velocities of granite during heating to 770 °C under confining pressures ranging from 50 to 250 MPa, observing a decrease in wave velocity across the quartz α/β transition, the temperature of which increased with confining pressure—from 620 to 700 °C under 50 and 250 MPa, respectively. A similar shift in

the α/β transition was observed by Molen (1981), by 60–70 °C per 100 MPa.

The preferred orientation of mineral constituents and the orientation of microcracks affect the directionality of wave velocity (Kern, 1982). Kern (1982) measured the P-wave anisotropy of a series of crustal and mantle rocks of initial v_P anisotropies of between 5 to 20 % during heating to 700 °C under 600 MPa confining pressure. Kern (1982) found that the velocity anisotropy remained near constant (except for serpentinite, for which it increased by around 5 % between 500 and 700 °C), however, at room temperature, the anisotropy decreased by up to 5-10 % in all rocks when subject to confining pressures of up to 500 - 600 MPa, due to the closure of microcracks. These results showed that under high confining pressures and temperatures, the orientation of minerals, rather than microcracks, is the controlling factor of v_P anisotropy.

All the aforementioned experiments were performed under hydrostatic loading conditions. The influence of differential stresses on thermal microcracking, however, is less well known. During triaxial mechanical cracks grow towards the direction of principal stress (Ashby and Sammis, 1990), increasing permeability anisotropy (Farquharson et al., 2017; Mitchell and Faulkner, 2008; Oda et al., 2002; Souley et al., 2001; Zoback and Byerlee, 1975) and velocity anisotropy (Ayling et al., 1995; Guéguen and Schubnel, 2003; Stanchits et al., 2006; Yukutake, 1989). It may, therefore, be suggested that the superposition of differential stress, and isotropic thermal stresses may result in an preferential direction for thermal microcrack growth, even within an initially isotropic rock.

Here, the isotropic Westerly Granite (Lockner, 1998) and Rubble Creek Basalt (Figure 5.2) were selected, both rocks which contain microcracks of no preferential orientation (see Section 5.3.3 for stereological data on Rubble Creek Basalt, and Fredrich and Wong (1986) for Westerly Granite). Samples were heated and cooled to peak temperatures of 400 and 700 °C for the granite and 400 °C for the basalt. During heating and cooling, the samples were under constant uniaxial stresses ranging from 1–10 MPa for the granite, and 1–30 MPa for the basalt. Measurements of porosity, v_P, and permeability were made on the heated samples, to assess microcrack damage and orientation.

6.1 METHODS

Westerly Granite (Chapter 4) and Rubble Creek Basalt (Chapter 5) were selected for this study. Backscattered Scanning Electron Microscopy (SEM) micrographs of the granite and the basalt are shown in Figure 6.1 (note the difference in scale between the two images). Cylin-

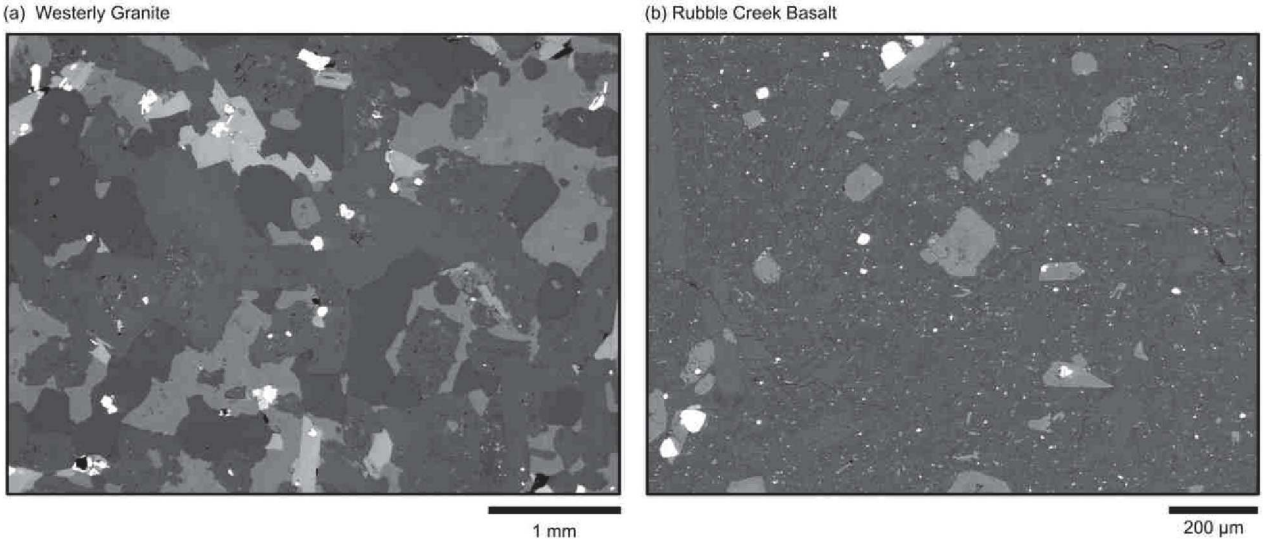

Figure 6.1: Backscattered scanning electron microscope (SEM) micrographs of (a) Westerly Granite and (b) Rubble Creek Basalt. Note the difference in scale between the two images.

drical samples of both rocks were prepared and dried in-vacuo prior to experimentation (Chapter 2).

Samples of each rock were heated within the experimental setup presented in Section 2.1, under uniaxial stresses of 1, 2.5, 5 and 10 MPa for the Westerly Granite heated to 700 °C, and under 1 and 10 MPa for the granite heated to 700 °C (see Table 6.1 for the thermal and mechanical stressing conditions). The basalt samples were heated to 400 °C under uniaxial stresses of 1, 10 and 30 MPa. All samples were heated and cooled at the same rate of 1 °C/min as for the experiments described elsewhere. To quantify changes in the influence of thermal microcracks on rock properties formed under load, measurements of v_P and permeability were made prior to, and following experiments (Chapter 2).

6.2 RESULTS AND DISCUSSION

6.2.1 *AE monitoring*

To compare AE between experiments performed under different uniaxial loads (and varied coupling with the sample) it is necessary to quantify the effect of uniaxial load on the AE amplitudes. For this, the AE amplitudes resulting from a Hsu-Nielson source (lead break) on the surface of samples of Westerly Granite and Rubble Creek Basalt were measured (Figure 6.2). The Westerly Granite sample was under uniaxial stresses of 1, 2.5, 5 and 10 MPa, and the basalt sample and 1 and 10 MPa for the Rubble Creek Basalt. The lead-break was repeated five times for each sample and uniaxial load. The AE amplitude in-

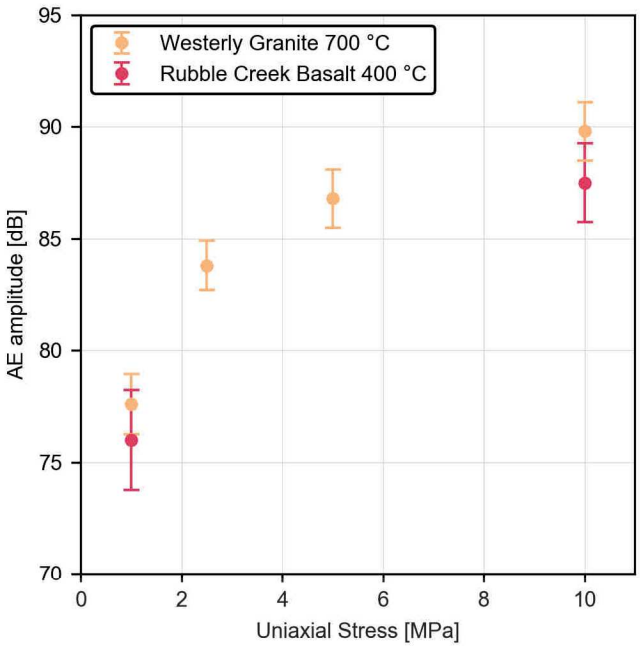

Figure 6.2: AE amplitudes from Hsu-Nielson source (lead break) on sample surface of Westerly Granite and Rubble Creek Basalt samples under uniaxial stresses of 1, 2.5, 5 and 10 MPa for the granite, and 1 and 10 MPa for the Rubble Creek Basalt. Error bars show the standard deviation of 5 recorded AE hits per sample and load.

creases with load, as the coupling between the samples and the sensor increases. The AE amplitudes recorded from a source at the surface of the basalt samples are, on average, lower than for the granite samples, although the difference is within the standard deviation.

The number of ring-down counts and the duration of the detected AE was seen to increase slightly with uniaxial load, likely owing to the increase in the detection threshold due to the increased coupling with the sample (as explained in the Chapter 2). Their average frequency (the AE ring-down count divided by the duration), showed no clear trend, and all values were within their standard deviation. Hence, the effect of an increase in load appears to be principally an increase in amplitude of the signal rather than its characteristics. This highlights the importance of applying servo-controlled load during experiments, to ensure that coupling with the sample is constant.

The AE rate detected during heating and cooling of Westerly Granite to a maximum temperature of 700 °C under 1, 2.5, 5 and 10 MPa are shown in Figure 6.3. The AE hit rate with temperature follows a similar trend for all uniaxial stresses (Figure 6.3), but is higher when the load is higher. The mean AE amplitudes during heating and cooling were 44.8, 47.7, 48.5, and 49.7 dB under loads of 1, 2.5, 5 and 10 MPa respectively.

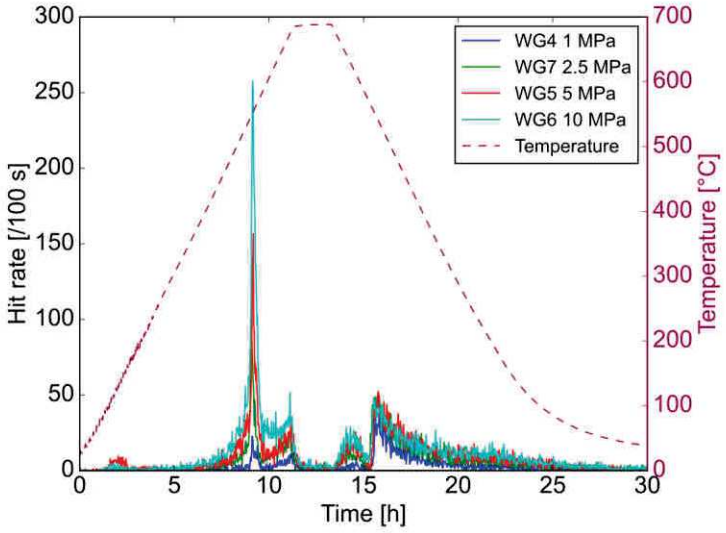

Figure 6.3: Cumulative AE hits and furnace temperature against time during heating of Westerly Granite samples to 700 °C and cooling, under uniaxial stresses of 1, 2.5, 5 and 10 MPa.

As for the lead break tests (Figure 6.2), the amplitude of AE hits increase under increasing load, and therefore the increased AE rate under higher loads may be due to the increased coupling with load and an effective decrease of the AE detection threshold. It is therefore difficult to compare the results of each test, and is the main reason for which, previously, samples subject to the same thermal stressing conditions were also subject to the same uniaxial stress. Unfortunately, AE data acquired during tests on the Rubble Creek Basalt are not shown here, as noise was an issue at higher loads, and the AE data for some tests were therefore incomplete.

6.2.2 *Physical and transport properties*

Figure 6.4 shows the connected porosity, P-wave velocity, and permeability of all thermally-stressed samples of Westerly Granite and Rubble Creek Basalt. These data are also reported in Table 6.1, as are values of porosity and v_P prior to heating when available. The permeabilities of the unheated samples were too low ($< 10^{-21}$) to be measured by the bench-top permeameter used here.

The porosities of the Westerly Granite samples heated to 700 °C are in the range of 2.5-3.0 %, higher than the initial value of 1.0 %, and show no clear trend with uniaxial stress (Figure 6.4a and 6.1). The slight increase in porosity between the Westerly granite samples heated to 400 °C under 1 and 10 MPa is within the variability of the samples. For Westerly Granite samples heated to both 400 and 700 °C, v_P appears to show a general increase with uniaxial stress (Figure 6.4b), which is outside of the error of the measurement and sam-

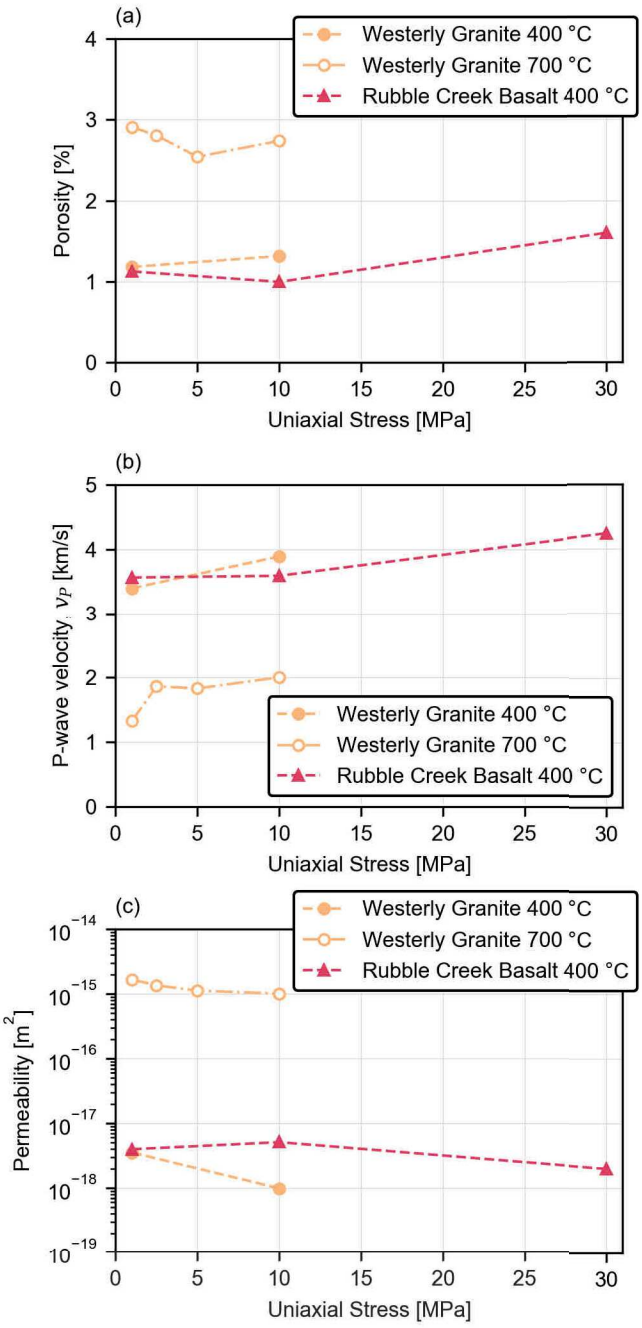

Figure 6.4: (a) Porosity, (b) P-wave velocity, and (c) permeability of Westerly Granite and Rubble Creek Basalt heated under uniaxial load to 400 and 700 °C under load against uniaxial stress. Dashed lines simply join data points of samples heated to the same peak temperature.

Rock	Temperature [°C]	Uniaxial stress [MPa]	Initial porosity [%]	Initial v_P [km/s]	Porosity [%]	v_P [km/s]	Permeability [m^2]
Westerly Granite	700	1	1.01	4.89	2.91	1.32	1.66×10^{-15} m^2
	700	2.5	1.05	4.91	2.81	1.86	1.35×10^{-15} m^2
	700	5	1	4.92	2.54	1.83	1.12×10^{-15} m^2
	700	10	1.05	4.9	2.74	2.00	1.01×10^{-15} m^2
	400	1	0.95	4.9	1.18	3.4	3.54×10^{-18} m^2
	400	10	0.93	4.86	1.31	3.89	9.86×10^{-19} m^2
Rubble Creek Basalt	400	1	-	4.5	1.12	3.57	3.97×10^{-18} m^2
	400	10	-	4.57	1.00	3.59	5.11×10^{-18} m^2
	400	30	-	4.62	1.6	4.24	1.98×10^{-18} m^2

Table 6.1: Physical properties of samples of Westerly Granite and Rubble Creek Basalt, before and after heating and cooling under uniaxial load.

ple variability (see initial values in 6.1), assuming that sample variability within thermally-stressed samples is negligible. Finally, the permeability of the Westerly Granite heated to both 400 °C and 700 °C decreases with uniaxial stress (Figure 6.4c): from 1.66×10^{-15} m^2 (1 MPa) to 1.01×10^{-15} m^2 (10 MPa) in the 400 °C samples, and from 3.54×10^{-18} m^2 (1 MPa) to 9.86×10^{-19} m^2 (10 MPa). The decrease in permeability indicates a decrease in the number or efficiency of pathways for fluid flow in the direction of the uniaxial stress. Although, the connected porosity shows no real variation with uniaxial stress (Figure 6.4a). Assuming the crack porosity is unchanged, the increase in v_P along the sample axis and stress direction with increasing stress might suggest a preferential alignment of microcracks with the same axial direction (Crampin, 1981). However, this alone does not explain the decrease in permeability, which expected to increase when cracks are aligned with the sample axis (assuming they are connected).

For the Rubble Creek Basalt, the porosity is very similar following heating to 400 °C under both 1 MPa and 10 MPa uniaxial stresses: 1.00 % and 1.12 %, respectively (Figure 6.4a). The sample heated to 400 °C under 30 MPa uniaxial stress has a significantly greater porosity of 1.6 %. The values of v_P and permeability of the two Rubble Creek Basalt samples heated under 1 and 10 MPa are also very similar, and v_P and permeability of the 30 MPa sample are respectively higher and lower (Figure 6.4). As for the Westerly Granite, the increase in v_P of the Rubble Creek Basalt with uniaxial stress (from 4.5 to 4.62 km/s), is accompanied by a decrease in permeability (from 3.97×10^{-18} m^2 to 1.98×10^{-18} m^2). The increase in connected porosity increases suggests that more (or wider) microcracks formed, and the increase in v_P suggests that these new microcracks are preferentially oriented in the stress direction (Crampin, 1981). However, the decrease in permeability indicates that they are not well connected, or favourable for

fluid flow. It should be noted that sample variability cannot be ruled out here as a cause of the difference in the measurements of physical properties.

Thermal microcracks in rock form firstly by separation of grain boundaries (Kranz, 1983), also observed in Westerly Granite by Fredrich and Wong (1986). The grain boundaries provide surfaces for fracture which, in an isotropic rock such as Westerly Granite (Lockner, 1998), are oriented equally in all directions (Figure 6.1a). The maximum uniaxial stresses of 10 MPa may therefore be insufficient to provide the necessary stress conditions for strongly anisotropic thermal microcracking in such a material. Indeed, 10 MPa is low compared to the uniaxial stress at the onset of dilatancy–around 120 MPa (Zoback and Byerlee, 1975) in Westerly Granite. The Rubble Creek Basalt however, contains fractures which are far longer than the grain size of the groundmass through which they traverse (Figure 6.1b). For this reason, the influence of grain boundaries on the orientation of thermal microcracks in the Rubble Creek Basalt may be weaker than for the Westerly Granite. Uniaxial stresses of less than 10 MPa appear to make no difference on thermal microcracking in the Rubble Creek Basalt. However, during heating and cooling under 30 MPa uniaxial stresses, there does appear to be a change in the microstructure of the basalt, where an increase in crack porosity is concurrent with a decrease in v_P and permeability.

To assess the stress experienced at the grain scale due to thermal expansion. Edwards (1951) considered an isotropic inclusion within a matrix, and gave the internal stress σ resulting from an increase in temperature as a function of the Young's modulus E, the thermal expansion difference between the inclusion and the matrix $\Delta\alpha$, and the temperature change ΔT (Equation 6.1).

$$\sigma \approx E\Delta\alpha\Delta T \tag{6.1}$$

Taking the Westerly Granite as an example: the value of $\Delta\alpha = 5.5 \times 10^{-6}$ /°C (Fredrich and Wong, 1986) for a quartz grain in Westerly Granite, and the Young's modulus $E = 56$ GPa of Westerly Granite (Johnson et al., 1978). The internal stress is around 116 MPa at 400 °C, and 208 MPa at 700 °C (discounting the additional thermal expansion of quartz at the α/β transition at 573 °C (Glover et al., 1995)). This means that the internal stresses within the Westerly Granite due to an applied uniaxial stress of 10 MPa (which is well below the 120 MPa at the onset of dilatancy (Zoback and Byerlee, 1975)) may be dwarfed by the thermal stresses at such temperatures. It may be necessary to select experimental conditions which close the gap between the amplitudes of thermal and mechanical stresses (i.e. increase the uniaxial load and/or decrease temperature), to better observe their interaction through measurements at the sample scale. It is suggested that a significant increase in load, and heating to a peak temperature com-

fortably above that of the onset of thermal microcracking for these rocks (e.g. 100–200 °C), would be the optimal conditions to observe a contrast between the extent and orientation of thermal microcracking

The methods used here to quantify the anisotropy of microcracking—comparison between measurements of v_P and permeability along the sample length—rely strongly on the consistency of thermal microcracking in terms of microcrack density under identical temperature conditions. For this reason, it was important to core samples of each rock from a same block and in the same direction, even if both rocks appear isotropic through microscopic observation. Further study should first include quantitative analysis of the microstructure of the thermally-stressed samples, to determine the crack densities (as in Chapter 3) and their orientations. Additional experiments, both under the same conditions to assess their repeatability, and under greater uniaxial stresses, would help to draw more firm conclusions on the influence of differential stress on thermal microcracking.

6.3 CONCLUSION

- This brief chapter presents a preliminary study on the influence of uniaxial stress on thermal microcracking in rock. The aim was to assess the influence of differential stress on the creation of thermal microcracks, and understand whether or not such stresses influence their direction of growth.
- Samples of Westerly Granite and Rubble Creek Basalt were heated and cooled under varying uniaxial loads (up to 10 MPa for the granite, and 30 MPa for the Rubble Creek Basalt), to temperatures of 400 and 700 °C for the granite and 400 °C for the basalt.
- Measurements of porosity, v_P, and permeability were employed to assess the quantity and preferential orientation of microcracks, and generally were little affected by the applied stress. In both rocks the connected porosity following heating and cooling is either the same (for Westerly Granite samples and Basalt samples heated under 10 MPa uniaxial stress or below), or increased (Rubble Creek Basalt heated under 30 MPa uniaxial stress). For the Westerly Granite, there appears to be a simultaneous decrease in permeability and increase in v_P between samples heated under increasing uniaxial stresses, as is the case for the Rubble Creek Basalt when heated to 400 °C under 30 MPa uniaxial stress.
- Considering the porosity is the same or greater with increasing uniaxial load, the increased velocity when heated under increased uniaxial loads indicate a potential preferential alignment of microcracks in the stress direction. The decrease in permeability with increasing uniaxial stress would suggest that

these aligned cracks are less well-connected. It is also possible, however, that differences in permeability and velocity could also be due to sample variability, for both the Rubble Creek Basalt and the Westerly Granite.

- Further study should include experiments during which samples are heated under increased uniaxial loads to lower peak temperatures, and quantitative microstructural observations of the microcrack network would aid in the interpretation of measurements of physical and transport properties.

7

CONCLUSIONS AND PERSPECTIVES

7.1 CONCLUSIONS

7.1.1 *A new apparatus for monitoring thermal microcracking*

AE MONITORING A major part of this project was the design and conception of a new experimental apparatus tailored specifically for Acoustic Emission (AE) monitoring of rock samples at high temperature. Chapter 2 details the design choices made to improve upon pre-existing apparatus described in the literature, and some examples are given below:

- A constant coupling between the sample and the piston was crucial for the reproducibility of measurements, and the comparison of results. This was ensured by a servo-controlled uniaxial press, with a continuous steel piston acting as a waveguide and applying a constant load on the sample.
- The AE transducer was kept cool by an air-cooling system, to avoid any changes in its electro-elastic response, and thus in the detection threshold of the AE system.
- The position of the AE transducer strongly influenced the signal quality and the AE detection threshold, which was found to be optimal when the AE transducer was embedded within the piston/waveguide, facing towards the sample.

VELOCITY MEASUREMENTS The next stage of development for the experimental apparatus was to provide the capability to perform velocity measurements at elevated temperatures (Chapter 2). For this, acoustic transducers with a high operating temperature (~500 °C) were used. They were placed in direct contact with either ends of a rock sample, and thus waves could be sent and received across the sample during heating and cooling. The recorded waveforms were first used to calculate the P-wave velocity (v_P) from changes in travel time during experiments. Subsequently, Coda Wave Interferometry (CWI; Snieder (2002)) was performed on the same waveform data, to infer changes in velocity and microstructure. The CWI apparent velocity changes were also used to provide insight into changes in the S-wave velocity (v_S).

Grêt (2004) demonstrated the use of CWI to observe changes in the microstructure of different rocks due to changes in fluid saturation, mechanical deformation and, in granite, temperature changes of up to

90 °C. Here, for the peak temperatures of 450 °C the method required some slight modifications:

- To calculate the relative time shift between waveforms, the stretching method (Larose and Hall, 2009; Sens-Schönfelder and Wegler, 2006) was preferred to the windowed cross-correlation method (Snieder, 2002), as time shifts were sometimes greater than half a wavelength.
- As the microstructure changed, correlation between the received waveforms and the initial reference waveform decreased. For this reason a fixed reference waveform could not be used. Instead, the relative time shift was calculated between consecutive waveforms (at 10 second intervals).
- Inherent biases of the experimental apparatus (the response of the piezo-transducers, changes in scattering properties of the steel transducer casings) were observed when operating at high temperatures. To correct for these, calibration tests were performed on a sample of fused quartz, for which the velocity change and thermal expansion was considered negligible.
- CWI was used to provide insight into changes in the S-wave velocity (v_S), using the same data used for the calculation of v_P.

7.1.2 *From microstructure to the sample scale*

Thermal microcracks influence the mechanical properties of the rock (for example, Homand-Etienne and Houpert (1989)), and micromechanical models exist to predict rock behaviour at the sample scale from quantitative microscale characterisation. The aim of Chapter 3 was to assess the influence of thermal microcrack damage on the mechanical properties of the rock samples. For this a large dataset was needed, comprising of mechanical data on rock containing variable and known amounts of microcrack damage. However, the large number of samples required an automated, robust and repeatable procedure for microcrack characterisation.

Chapter 3 presented a numerical tool for processing and analysing optical micrographs of thin sections of rock, to allow subsequent quantification of thermal microcrack length and spatial density. Optical micrographs were chosen here as they are more readily available and easily made in large numbers than Scanning Electron Microscopy (SEM) micrographs, which have also previously been used to observe microcracks (Arena et al., 2014; Brace et al., 1972; Delle Piane et al., 2015; Fredrich and Wong, 1986). It should be noted that the presented procedure for micrograph analysis may also be applied to the SEM micrographs which have advantages in terms of image resolution and sensitivity to density.

The method was applied to optical micrographs of thin sections of 11 variably thermally-damaged samples of a fine-grained granite, and the results were found to agree with manual measurements made using the stereological techniques of Underwood (1967). The resulting microcrack characteristics were then used to constrain micromechanical models for rock strength and stiffness, and compared with laboratory measurements. Results of the modelling of rock strength using the Ashby and Sammis (1990) wing crack model coincided with measurements on granite samples heated to temperatures of up to 600 °C. However, above this temperature, the calculated crack densities varied little, and could not explain the further measured decrease in strength. This was due to the widening of microcracks, unaccounted for by the measurement of microcrack damage and the wing crack model. Above the α/β transition of quartz, few new cracks form, but the "loosening" of grains due to the thermal expansion mismatch continues Johnson et al. (1978).

Crack densities inferred from the David et al. (2012) extension of the Walsh (1965) model for the compressibility of cracked rock followed a similar trend to the measured crack densities. Fitting the model to the experimental data also gave the crack aspect ratio, which increased with crack density and was in the range of $2.4 \times 10{-}4$ (unheated Garibaldi Grey Granite) to 5×10^{-4} (heated to 900 °C).

The micrograph analysis algorithm was used in Chapter 4 and Chapter 5 to calculate the crack length and density in thermally-stressed samples of three rocks, the Garibaldi Grey Granite, the coarser grained Lanhélin Granite, and the Rubble Creek Basalt. The calculated crack densities, combined with measurements of physical properties showed that thermal microcracks are wider in rock containing larger crystals, which has a profound affect on rock behaviour.

7.1.3 *The influence of thermal stress*

For the experiments where samples were heated to 450 °C and cooled, AE and velocity monitoring during the first and repeated cycles provided a baseline for comparison of results. By comparing the velocity changes between cycles, it was possible to distinguish non-permanent from permanent velocity changes; the latter indicating thermal microcracking. Measurements of v_P made at room temperature using a separate apparatus (Chapter 2) served as validation of the net v_P change observed over each cycle.

In the AE monitoring experiments at temperatures of up to 700 °C, the analysis of the AE amplitude distribution with temperature allowed the different phases of microcracking (for example, at the onset of microcracking and at the α/β transition of quartz) to be identified.

In all experiments, AE was also monitored during cooling, which has previously received little attention, yet AE was found to be present

in nearly all the thermal stressing experiments, on both the granites and the volcanic rocks. Repeated thermal cycling experiments have also rarely been performed, and are relevant for geothermal reservoirs and volcanoes (Heap et al., 2013b).

7.1.3.1 *The occurrence of thermal microcracking*

Three granites were selected for study in Chapter 4:

- Westerly Granite from Rhode Island, USA, 0.98 % porosity, mean grain size (diameter) ~0.75 mm;
- Garibaldi Grey Granite from British Columbia, Canada, 0.93 % porosity and grain size of ~1 mm;
- Lanhélin Granite from Brittany, France, 0.35 % porosity and grain size of ~2 mm.

Three volcanic rocks were selected for study in Chapter 5:

- A basalt from Mt. Etna, Italy, ~4 % porosity;
- A low porosity basalt ("Rubble Creek") from British Columbia, Canada, 1 % porosity ;
- A vesicular andesite ("La Lumbre") from Volcàn de Colima, Mexico, ~23 % porosity.

When thermally cycled to 450 °C, the granite samples were seen to microcrack during heating, with the onset of thermal microcracking observed at around 80 °C in the Westerly Granite, 65 °C in the Lanhélin Granite, and 100 °C in the Garibaldi Grey Granite. In granite, during slow heating, the thermal expansion mismatch between grains is known to be the cause of thermal microcracking (Kranz, 1983). The Lanhélin Granite had the lowest initial porosity of the three granites, which would explain why it underwent extensive thermal microcracking at lower temperatures, as there was less crack porosity within which to accommodate the thermal expansion mismatch. The influence of crack porosity alone, however, does not explain the difference in AE activity observed between the Westerly and Garibaldi Grey granites.

The the Rubble Creek Basalt and the Etna Basalt were heated to 450 °C for the first time, little microcracking was observed. In the basalts, the thermal expansion of the rock matrix did not cause a sufficient build-up of stresses to induce microcracking. The La Lumbre Andesite, however, cracked when heated to above 250 °C, which is suggested to be due to its weaker structure, owing to its many large pores.

When the granites were heated to 700 °C, AE amplitudes were shown to be greater with increasing grainsize, indicative of the extension of larger microcracks (Evans, 1978a) within the coarser grained

rock. Specifically in the Lanhélin Granite, the b-value indicated that many small cracking events occurred at the onset of heating, with larger cracking events throughout the rest of heating. As it was not possible to make velocity measurements during the 700 °C experiments, it was unclear to what extent thermal microcracking may have occurred during cooling. The constant b-value during cooling of the Lanhélin and Garibaldi Grey Granites indicated that little microcrack propagation occurred. However, for the Westerly Granite, changes in b-value during cooling across the quartz α/β transition (~573 °C, Glover et al. (1995)), were indicative of thermal microcracking.

During cooling from 450 °C, microcrack behaviour between the different rock types varied. Firstly, the granites all saw an increase in velocity during cooling, which was due to a reduction in microcrack aperture, as grains contracted. The velocity increase during cooling was however less than the decrease during heating, resulting in a significant permanent velocity reduction due to the thermal microcracks formed during heating. It was found that the Etna basalt and La Lumbre Andesite also exhibited little microcracking as they cooled from 450 °C.

The Rubble Creek Basalt, however, exhibited quite different behaviour, as thermal microcracking was shown to occur during cooling, from temperatures of around 250 °C. The cause of thermal microcracking within the basalt is suggested to be due to the contraction of the rock matrix, which created stresses that surpassed the tensile strength of the groundmass. Thermal microcracking in the Rubble Creek Basalt was also observed when cooled from 700 °C, using the rate of AE and analysis of their amplitude distribution. When Browning et al. (2016) observed AE during the cooling of an Icelandic basalt from 1100 °C, they attributed it to thermal microcracking. Here, through measurements of wave velocity and the analysis of AE rate and amplitude, it could be confirmed that thermal microcracking occurred within the Rubble Creek Basalt during cooling.

Through comparison of data presented here with that of Browning et al., 2016 (see Figure 1.3 of Chapter 1), it is concluded that, for volcanic rock, thermal microcracking may occur: during cooling within low crack density (high v_P) volcanic rock containing a crystallised groundmass (Rubble Creek Basalt (this study), and Seljadur Basalt and Nea Kameni Dacite (Browning et al., 2016)); during heating within high porosity volcanic rock (La Lumbre Andesite (this study) and Nea Kameni Dacite (Browning et al., 2016)); and during neither heating nor cooling in high crack density (low v_P) volcanic rock (Etna Basalt, this study).

It should be noted that here, however, AE during cooling did not always coincide with thermal microcracking, and velocity measurements were required to differentiate between AE due to microcracking, and AE (potentially) due to frictional events. In the granites, un-

like the Rubble Creek Basalt, it was suggested that the increase in AE detected during cooling of cycle one was due mainly to frictional sliding rather than microcracking. During the repeated cyclic heating of the granites, AE were detected during the cooling phase of each cycle, regardless of whether any new microcracking had occurred. It is still unclear, however, why the AE activity was less during heating than during cooling.

The fact that microcracking occurs in the granites during heating and not cooling has an important implication: measurements of crack density within the granites post-cooling apply also to the granite at the peak temperature, before cooling. However, in the Rubble Creek Basalt, thermal microcracking occurred during cooling, hence measurements of crack density once cooled are not representative of the rock at 450 °C during cycle one. Particular care is required when considering the microcrack population within volcanic rock at elevated temperatures from observations made at room temperature.

7.1.3.2 *Reversible and irreversible velocity change with temperature*

THE FIRST CYCLE Thermal microcracking during heating of the granites to 450 °C resulted in a significant drop in v_P and a negative apparent relative velocity change calculated by CWI. For example v_P was decreased by around 50 % in the Westerly and Lanhélin Granites, and 30 % in the Garibaldi Grey Granite at 450 °C. For the Garibaldi Grey Granite, both the relative decrease in velocity and AE activity during heating were less than in the other two granites, indicating less thermal microcracking to have occurred.

The influence of temperature on the wave velocity of Etna Basalt contrasted with measurements on the granites. v_P of the Etna Basalt increased near linearly with temperature, by more than 10 % at 450 °C, and CWI also showed an apparent increase in velocity during heating. The increase in velocity was linked to the closure of pre-existing microcracks with expansion of the rock matrix, analogue to the influence of confining pressure on crack aperture. Similar behaviour was observed in the La Lumbre Andesite during heating between room temperature and 250 °C, which saw an even greater relative increase in velocity than for the Etna Basalt. The greater relative change in velocity is in part due to the lower initial velocity of the andesite. However, from 250 °C, the increase in velocity was arrested by thermal microcracking, and the velocity remained near constant throughout the rest of the heating phase. The behaviour of the Rubble Creek Basalt was different again, where the velocity decreased during heating. The velocity of the Rubble Creek Basalt during heating of cycle one is controlled by the velocity change intrinsic to the rock matrix, which decreases with increasing temperature (Kern, 1982). The low initial microcrack porosity of the Rubble Creek Basalt seemed to limit the influence of microcrack closure on velocity as it was first heated.

During cooling, the wave velocity of all granite samples increased, due to a reduction in microcrack aperture, as grains contracted. The velocity increase during cooling was however less than the decrease during heating, resulting in a significant permanent velocity reduction on account of the thermal microcracks formed during heating.

During cooling, the wave velocity of all volcanic rock samples decreased. The velocity decrease in the Etna Basalt during cooling resulted in little permanent change overall, which signified firstly that little thermal microcracking occurred during heating and cooling, and secondly that the closure of thermal microcracks with temperature was non-permanent. As (Vinciguerra et al., 2005) previously measured no permanent change in the v_P and v_S of basalt from Mt. Etna when heated to 900 °C and cooled, it is of value to know that the wave velocities of basalt at Mt. Etna may still vary with temperature. The wave velocity of the La Lumbre Andesite showed a large decrease during cooling, for example, v_P decreased by more than 30 % of the initial value, resulting in a net reduction in v_P of 18 % during cycle one. It is suggested that the significant velocity decrease during cooling is due to the opening of both the pre-existing, and new microcracks induced during heating. The velocity of the Rubble Creek Basalt decreased significantly during cooling between 250 °C and room temperature due to the extensive thermal microcracking, resulting in a large permanent decrease in v_P of 23 %.

REPEATED CYCLES Generally, the Kaiser (thermal) stress-memory effect was obeyed, as repeated thermal cycling did not induce significant further thermal microcrack damage, and therefore variations in velocity with temperature were quasi-reversible.

In the granites, During repeated heating and cooling cycles, wave velocities were observed to decrease with increasing temperature by 10–20 % at 450 °C, showing that even in absence of thermal microcracking, velocity changes may be significant with changes in temperature. These results suggested that in the granite, cracks reversibly opened during heating and closed during cooling.

During the second and third heating/cooling cycles, all volcanic rocks saw a reversible increase in wave velocity with temperature, where microcracks instead closed with increasing temperature. The v_P of the La Lumbre Andesite increased by almost 30 % at 450 °C, compared to 10–15 % in the basalts. This suggests that larger relative changes in wave velocity might be expected in high porosity rock.

During the repeated cycles, microcracks within the granite opened during heating, and microcracks within the volcanic rocks closed. It is suggested that this difference in behaviour is due to the:

- Microcrack geometry: In granites, many cracks follow grain boundaries (Fredrich and Wong, 1986; Simmons and Richter, 1976). The thermal expansion mismatch of neighbouring crystals forces

them apart, effectively loosening the rock matrix (Homand-Etienne and Troalen, 1984). Thermal microcracks were observed to be more curved in the granite than in the volcanic rocks, so that any misalignment of grains has the effect of opening cracks further as they expand and push each other apart at their points of contact. In the volcanic rock, cracks were observed to be generally straighter, and no misalignment was visible.

- Crack length vs. grain size: In all rocks, the crack lengths were on the order of 0.1 mm. In granites, the lengths of microcracks are less than the grain size, as microcracks must traverse grain boundaries as they propagate. This is not the case for volcanic rocks containing glass or a crystallised groundmass. Therefore, at the scale of the microcracks within the glass/groundmass, the rocks is homogeneous and isotropic in terms of thermo-elastic moduli. This means that thermal expansion is also generally isotropic at the microcrack scale, which may facilitate crack closure.

In rock, during heating and cooling, there is a competing influence of the formation of microcracks, microcrack opening/closure, and the velocity intrinsic to the rock matrix for control of the overall velocity change. The contributions of each depend strongly on rock type and microstructure. The velocity changes observed with temperature may be significant, and have implications for the seismic monitoring and modelling of volcanoes, and geothermal reservoirs hosted in both granitic and volcanic rock.

7.1.4 *Thermal microcracking under heightened stress conditions*

THERMAL SHOCK-COOLING Samples of Garibaldi Grey Granite, Lanhélin Granite, and Rubble Creek Basalt were shock-cooled by immersion in water following heating to temperatures of 300 and 700 °C, to examine the influence of high thermal gradients on thermal microcrack formation (Chapter 4 and Chapter 5). For both the Lanhélin and Garibaldi Grey granites, microcrack density and porosity within the thermally shock-cooled samples were greater in comparison with samples heated to the same temperatures and slow-cooled (at 1 °C/min), particularly when shock-cooled from 700 °C. For the Rubble Creek Basalt, however, the increased thermal gradient during shock-cooling had little effect on the extent of microcracking. This suggests that for granite, high thermal gradients may contribute to increased thermal microcracking, which is relevant, for example, for the performance and stability of injection wells at geothermal reservoirs. The coarser-grained Lanhélin Granite was the most sensitive to shock-cooling, which is suggested to be due to the higher thermal

gradient across individual grains, and fewer grain boundaries over which the sudden thermal strain could be accommodated.

UNDER MECHANICAL STRESS Chapter 6 presents a pilot study to examine the extent and orientation of thermal microcracks formed under axial stress. Previously, the influence of confining pressure on thermal microcrack formation has been studied (e.g. Wang et al. (1989)), yet the influence of differential stresses is less well-known. For this, samples of Westerly Granite and Rubble Creek Basalt were heated under varying axial stresses (up to 10 MPa for the Westerly Granite, and 30 MPa for the Rubble Creek Basalt) during heating and cooling (to 400 and 700 °C for the Westerly Granite, and 400 °C for the Rubble Creek Basalt), to examine whether the influence of thermal microcracks on rock properties changes when they are formed under axial load. However, results showed that the applied axial stresses had little effect on the influence of the induced thermal microcracks on the permeability and v_P of the Westerly Granite and Rubble Creek Basalt. This suggests that the applied stresses were too low to influence thermal microcrack formation. Continuation of this work would involve performing similar experiments under higher uniaxial stressed, for example beyond the onset of dilatancy for these rocks, to see if and how thermal microcracks are influenced by increased applied stress. Modifications to the lower piston and load platen of the experimental apparatus are planned to allow experiments to be carried out under such axial loads.

7.1.5 *Consequences of thermal microcracking on the physical properties of rock*

Measurements at room temperature made on thermally stressed samples (heated to temperatures ranging from 100–900 °C) of Garibaldi Grey Granite and Lanhélin Granite showed an increase in crack density, porosity, and permeability, and decrease in v_P, thermal diffusivity and UCS with thermal stressing temperature. The coarser-grained, and least initially microcracked Lanhélin Granite was the most sensitive to thermal stressing, and underwent the greatest changes in physical properties with thermal stressing, owing in part to the larger microcrack aperture. These measurements also indicate that rock properties may vary with temperature, as microcracks propagate and widen during heating.

Measurements at room temperature on samples of Rubble Creek Basalt heated to temperatures of 100 to 900 °C showed that thermal microcracks significantly increased the permeability of the rock, and suggest that permeability may also be decreased at elevated temperatures due to crack closure. This is important for geothermal reservoirs, where permeability influences large scale convection within the reser-

voir (Magnenet et al., 2014), for connectivity between the injection well and the reservoir (Grant, 2013), and is a key factor for hydrofracturing around the well (Legarth et al., 2005). The potential for changes in permeability with temperature is also significant for volcanoes, where rock permeability influences the eruptive behaviour (e.g., Eichelberger et al. (1986), Farquharson et al. (2017), Melnik et al. (2005), and Sparks et al. (1997)).

The measured thermal diffusivity and conductivity decreased with increasing microcrack density and increasing microcrack aperture. The fine cracks within the Rubble Creek Basalt had less effect on the thermal properties than the wider cracks within the granites, which themselves were wider in the coarser grained material. It is expected that in the granite of the Soultz-sous-Forêts geothermal reservoir, in which grains may be more than 10 cm in diameter, that microcracking will greatly influence the thermal properties. Therefore rock type influences the coupling between heat flow and the thermal properties of rock. This is of particular interest for the behaviour and modelling of the heat flow within geothermal reservoirs, for which such coupled processes are paramount (Grant, 2013; Kohl et al., 1995).

7.2 PERSPECTIVES

COMBINED THERMAL AND MECHANICAL STRESS This thesis focused on the influence of temperature on rock microstructure under ambient pressure conditions. With a better understanding of microcrack behaviour in the absence of confining pressure, the next step would be monitor their formation under more representative pressure conditions of volcanoes and geothermal reservoirs. For example, at the Soultz-sous-Forêts site in Alsace, France, wells may be 5 km deep, and the increase in the vertical stress component with depth is around 25.6 MPa per km, and the horizontal components are of a similar amplitude (Cornet and Bérard, 2003; Genter et al., 2010; Valley and Evans, 2007). Wang et al. (1989) found that in Westerly Granite, the onset of microcracking occurred at 90 °C under 7 MPa confining pressure, and 135 °C under 55 MPa. It would be of interest to reproduce the reservoir conditions for deep geothermal reservoirs, to see if thermal microcracking is suppressed in the same way in different rock types and to what extent, and what happens to the rock during cooling.

LOW TEMPERATURE THERMAL STRESSES Here, experiments were performed where rock samples were heated to temperatures ranging from 100 °C to 900 °C. Solar-induced thermal stresses are sufficient to cause microcracking At lower temperatures within exposed rocks at the Earth's surface. (Eppes et al., 2016) placed a highly instrumented boulder of granite in open sun during a year, whilst performing con-

tinuous AE monitoring and measurements of the temperature and strain at the boulder surface. They found that AE occurred at certain moments of the day (Figure 7.1), which they attributed solar-induced thermal microcracking. They also modelled the stress within the boulder due to heating at its surface, and found that the time of maximum tensile strength within the boulder coincided with the hours of maximum detected AE (Figure 7.1).

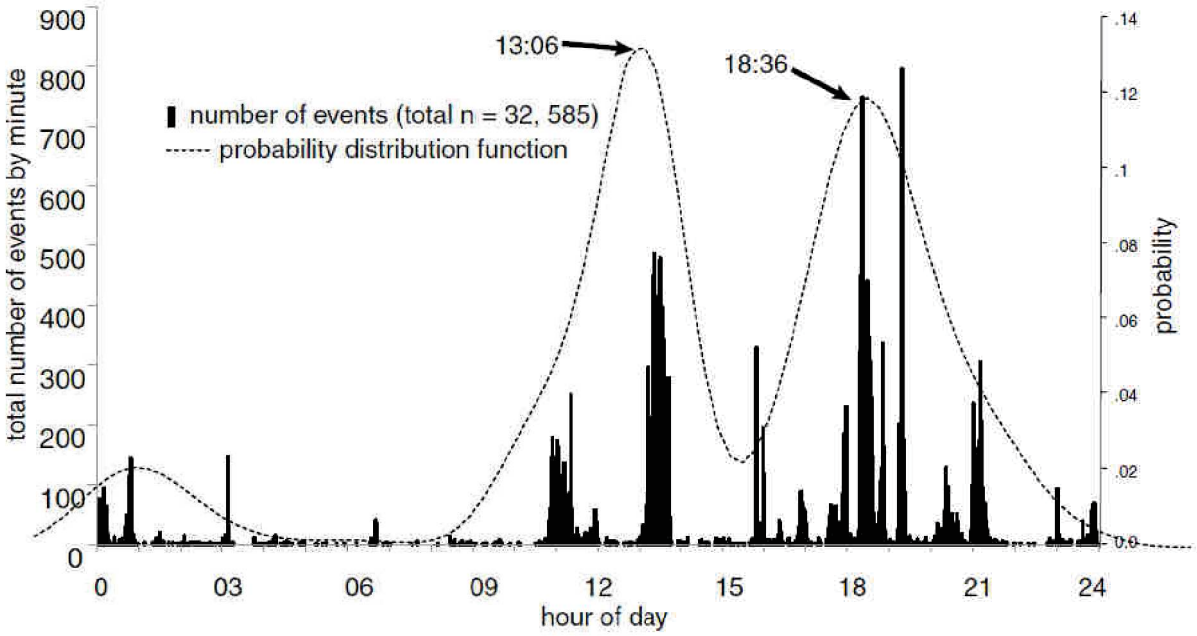

Figure 7.1: The total number of AE events that occurred during each minute of the day for the entire period of record (32,585 total events over 11 months). The dashed line is the calculated probability density function for the histogram. (from Eppes et al. (2016)).

To compliment the field measurements and modelling, the field conditions could be reproduced on granite samples in the laboratory, during longer duration, lower temperature thermal cycling experiments. As humidity seemed to be an important factor for thermal microcracking at the Earth's surface (Eppes et al., 2016), experiments could be performed on samples which have been variably saturated with water.

SIMULATION OF WAVE SCATTERING WITHIN MICROCRACKED ROCK

Here, Coda Wave Interferometry was used to infer changes in the rock microstructure during heating and cooling, from changes in the arrival times of elastic waves that have been reflected by boundaries or scattered by heterogeneities within the sample. These time delays were interpreted in terms of an apparent velocity change (which was evaluated to be the most significant), although time delays may also be due to the displacement of scattering and reflection points, and

the displacement of the source (Snieder (2006)). Further study is required to better understand the contributions of the different possible changes within the rock microstructure due to temperature change (e.g. deformation, the opening and closing of cracks, velocity changes of the rock matrix) to the apparent relative velocity change observed by CWI.

Ongoing research work by J. Azzola, a PhD student at Université de Strasbourg, focuses on the numerical simulation of wave scattering within rock, for analysis by Coda Wave Inteferometry (CWI). The procedure, illustrated in Figure 7.2, uses a 2D finite Element approach (Code_ASTER) to calculate the elastic deformation of the medium with temperature, and the propagation of seismic waves is modelled using a spectral element approach (SPECFEM2D).

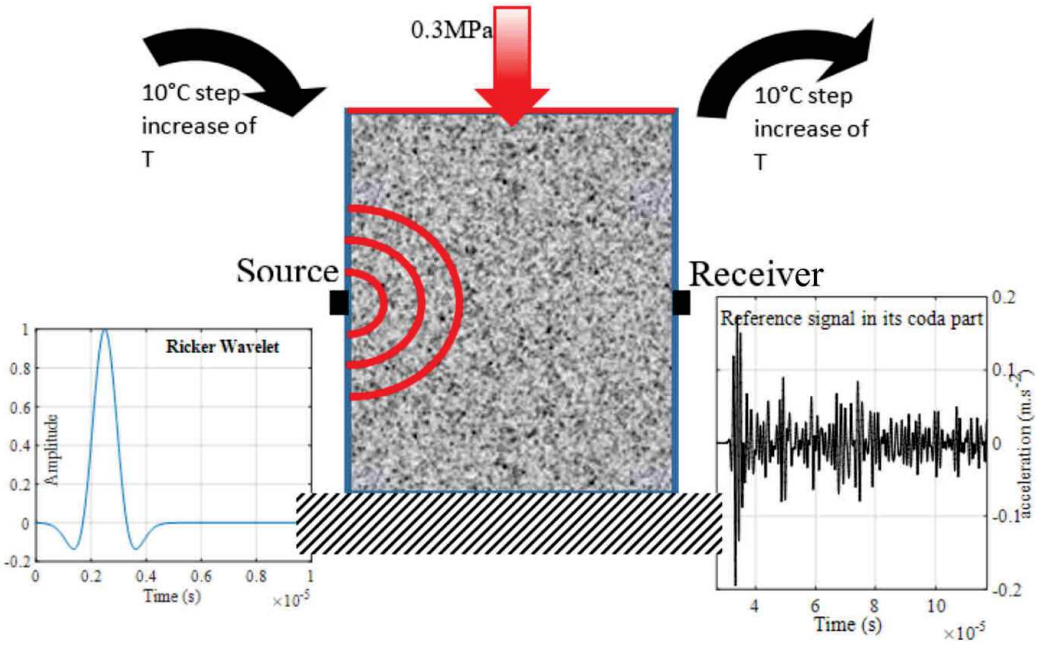

Figure 7.2: Current research by J. Azzola at Université de Strasbourg on the numerical simulation of wave scattering within rock, for analysis by Coda Wave Inteferometry (CWI) following changes in temperature. (from Azzola et al. (*in preparation*)).

The geometrical effect of the thermal expansion on the apparent wave velocity of a numerical Westerly Granite analogue (Figure 7.2) has been established. Future work will involve taking in to account changes in velocity with temperature and the addition and removal of scattering points, which may reproduce the high amplitude apparent velocity changes observed here (Chapter 4 and Chapter 5).

A

IMAGE ANALYSIS METHODOLOGY

This is the annexe to Chapter 3. To automatically calculate the 2D microcrack length and number of microcracks per unit area (number density), micrographs first need to be processed to obtain a binary image of the microcracks. We chose to use optical microscopy over SEM as it is cheaper and quicker to produce many images. However, unlike SEM, some grains or crystals may appear a similar dark colour to microcracks. Moreover, as microcracks must be distinguished from pores, any automated procedure to map microcracks cannot rely on grayscale alone. The method we present here takes advantage of the difference in aspect ratio between microcracks and pores/grains/crystals. The processing can be broken down into four main steps:

1. Filtering the microscope image to accentuate thin objects;
2. The segmentation step, separating the microcracks from the image background to create a binary image;
3. Iterative thinning or "skeletonisation" of the microcracks to form objects that are a single pixel in thickness;
4. Splitting of highly curved microcracks into multiple, straighter microcracks.

The script for the image processing is written in Python and uses Scipy's ndimage package, which contains various functions for multidimensional image processing, the scikit-image package61, and finally the Mahotas image processing package. Throughout, we work with 8-bit grayscale images; 2D integer arrays containing values ranging from 0 (black) to 255 (white). The script is available on demand from the corresponding author.

A.1 FILTERING

Microcracks are low aspect ratio features (Simmons and Richter, 1976). To obtain an image containing only microcracks, we must first separate them from the higher aspect ratio pores and grains/crystals. The original grayscale micrograph (Figure A.1a) is subject to a median filter that diminishes the thin microcracks whilst preserving larger objects such as pores and minerals (Figure A.1b). The median filter involves a moving window (here 15 x 15 pixels) that replaces the value of each pixel with the median of the values surrounding it. The window size was chosen to be several times larger than the microcrack aperture. The advantage of the median filter is its efficiency

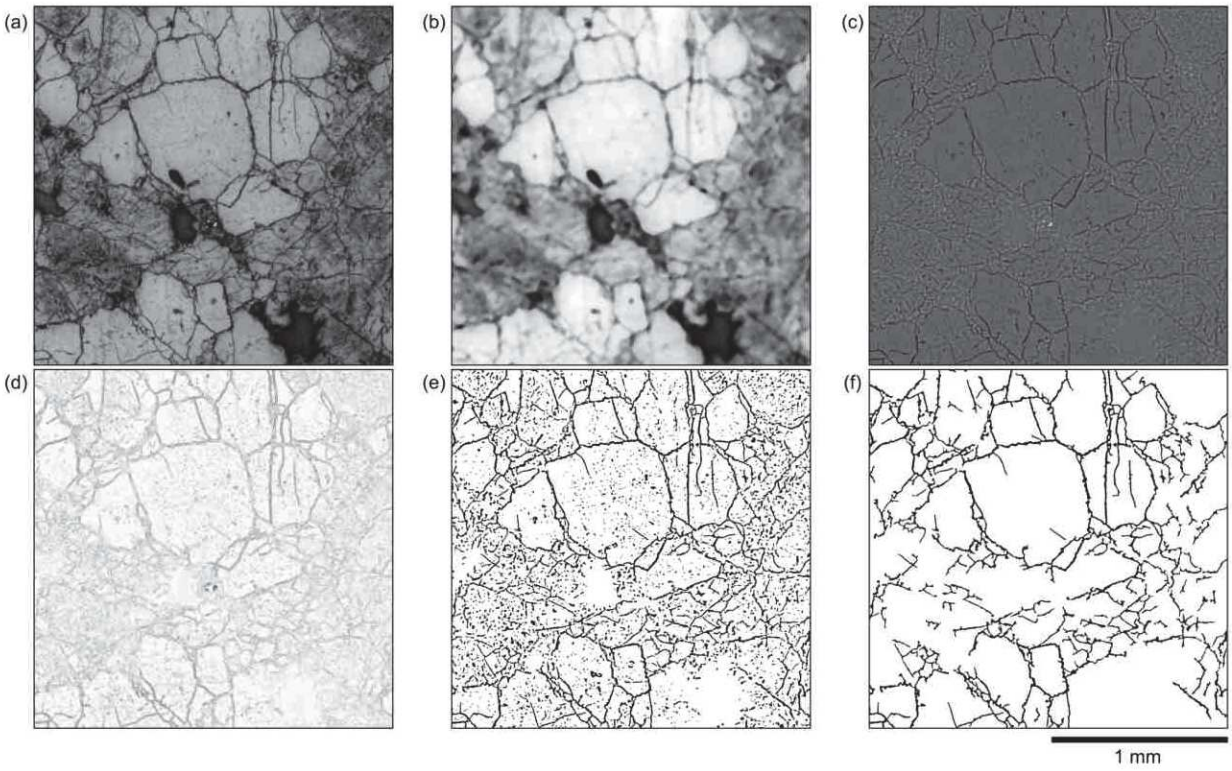

Figure A.1: Filtering and segmentation: (a) the original cropped 2 mm × 2 mm optical micrograph of a fine-grained granite sample heated to 600 °C, (b) the median filtered original, (c) the subtraction of (b) from (a), (d) the Sobel filtered gradient of (c), (d) the result of the watershed segmentation of (c) using (d), and (f) the binary segmented image with noise removed.

in preserving edges, unlike smoothing filters such as Gaussian blur or mean filters. Calculating the difference between these images results in a grayscale image containing only thin or small objects (Figure A.1c).

A.2 SEGMENTATION

To create a binary image of the microcracks, the employed segmentation method is the watershed algorithm (part of the scikit-image (Walt et al., 2014) image processing Python package), which treats the grayscale as topography, "flooding" the image to separate areas of similar elevation. The watershed algorithm requires two input images, a seed image and a gradient image. The seed image contains markers which label areas of Figure A.1c as microcracks, background or unknown, depending on their grayscale values. Here, dark areas (low grayscale value) are labelled as microcracks and light areas (high grayscale value) are the background. We calculate the mask from the median grayscale value of Figure A.1c, which provides the grayscale

value of the background. All areas of grayscale above the median minus 10 are labelled as background. All areas of grayscale less than 20 below the median are labelled as microcracks. Pixels with intermediate grayscales do not have a label. The gradient image of Figure A.1c is generated using Sobel filter and is shown in Figure A.1d. The Sobel filter calculates the discreet central difference gradient in grayscale at each pixel in both the horizontal and vertical directions and then sums their squares. The resulting grayscale image is dark where the gradient is steep and light in flatter areas (Figure A.1d). The watershed algorithm then extends the labelled regions, prioritising extension in the direction of low gradients. This process continues until the labelled areas meet and the entire image is segmented (Figure A.1e).

Next, noise is removed by locating and removing all small objects. The "label" and "find objects" functions of the Scipy Ndimage Python package provide an ensemble of rectangular arrays containing each object. The dimensions of these arrays are the exact height and width of the object in pixels. We then calculate the length of their diagonal and remove all of those that are smaller than a given value (here 80 µm or 40 pixels).

Following segmentation, some white pixels may be present inside the black cracks. The removal of the white pixels is achieved by "dilating" and "eroding" the image. Dilation is a morphological technique which involves visiting each pixel and setting it to black if there is a black pixel adjacent. Once all holes are filled, a consequent erosion of the image returns the black areas to their original thickness without reopening holes. Erosion works similar to dilation, setting each pixel to white if there is an adjacent white pixel.

A.3 THINNING AND PRUNING

Next we iteratively thin the cracks to a thickness of a single pixel, whilst conserving their length and connectivity, using the "thin" function of the Mahotas Python package (Coelho, 2013). The aim is to make it easier to calculate microcrack length, and to split branched microcrack networks into individual microcracks. Like erosion and dilation, thinning is another morphological technique that involves scanning the image for certain structural elements using a hit-or-miss transform before removing them. These structural elements are 3 × 3 pixel arrays that represent all the possible configurations for black pixels along the microcrack boundaries that could be set to white without compromising the continuity of the microcrack (excluding microcrack end points). Once these pixels have been located, they are set to white and the process begins again. This process is continued until further thinning has no effect and the image has been entirely skeletonized (Figure A.2a).

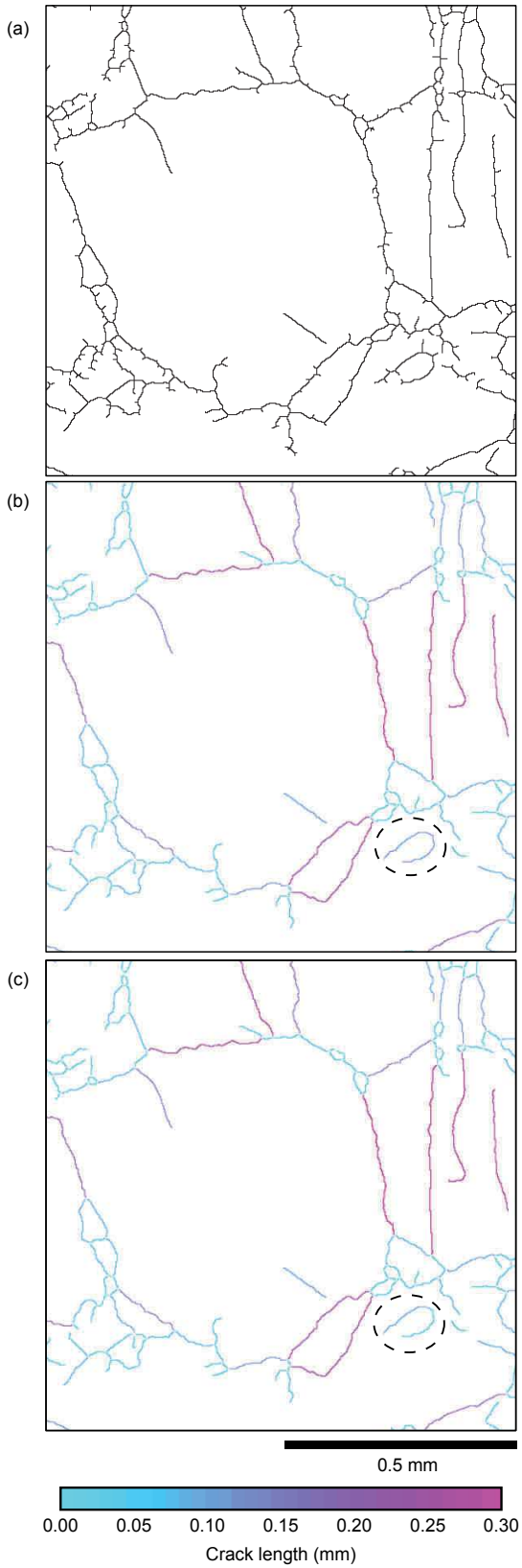

Figure A.2: a) The thinned version of the segmented image (1 x 1 mm zoom on centre of Figure A.2f), which exhibits short residual branches from the thinning algorithm. The microcracks are then pruned (b), and their original lengths are restored in (c) following the procedure presented in Figure A.3. The microcracks in (b) and (c) are coloured according to their approximated lengths, we see that highly a curved microcrack in (b) has been split into two shorter microcracks in (c) as demonstrated by Figure A.4.

Following the thinning procedure there are often short residual branches (Figure A.2a) that must be removed to prevent them from later contributing to the microcrack population. The method employed to prune these unwanted branches involves two steps. First, a hit-or-miss transform iteratively locates and removes all end points of the skeleton image. The number of iterations is set to 15, the same as the median filter window size. The resulting image is now assumed to contain only microcracks, although some may still retain more than two end points at this stage. To resolve this, the second step of pruning involves another hit-or-miss algorithm to locate and remove all intersection points (or branch points) in the image, separating branches into individual microcracks. As previous the end points are then iteratively removed until all microcracks have only two ends (Figure A.2b).

Whilst pruning removes the parasitic branches, it also shortens the main branches (Figure A.2a, b). To restore the length of the main branches, one could iteratively dilate the pruned image and intersect it with the unpruned original. The disadvantage of this approach is that residual branches near microcrack ends are also recovered. To avoid this, we propose a modification of this method, demonstrated in Figure A.3. First, we locate all microcracks in the pruned image and dilate their end points before intersecting them with the un-pruned microcrack (as described above).

Next, all branch points are located and removed, isolating the pixels of the growing parasitic branches that are removed once again by locating and removing all small objects (those composed of up to 2 pixels). The branch points are then redrawn and the procedure is repeated until there are no further changes to the skeleton image. This method allows for an almost complete recovery of the microcrack length lost during the first stage of pruning, without recovering any residual branches. The resulting image (Figure A.2c) contains microcracks that are each a single pixel in width and have exactly two end points. This geometry makes it easier to calculate their lengths and split up any highly curved microcracks into multiple straighter microcracks.

A.4 MICROCRACK LENGTH AND CURVATURE

The length of a microcrack can be approximated by the distance between its two end points (Figure A.4). This assumption is however only strictly true when the microcrack follows a straight line and is increasingly unsatisfactory as microcrack curvature increases. Before calculating the microcrack lengths, we scan the image for microcracks that have an overall curvature greater than a certain value and split them into two shorter microcracks, repeating the process until all microcracks fulfil this criterion. The curvature is quantified

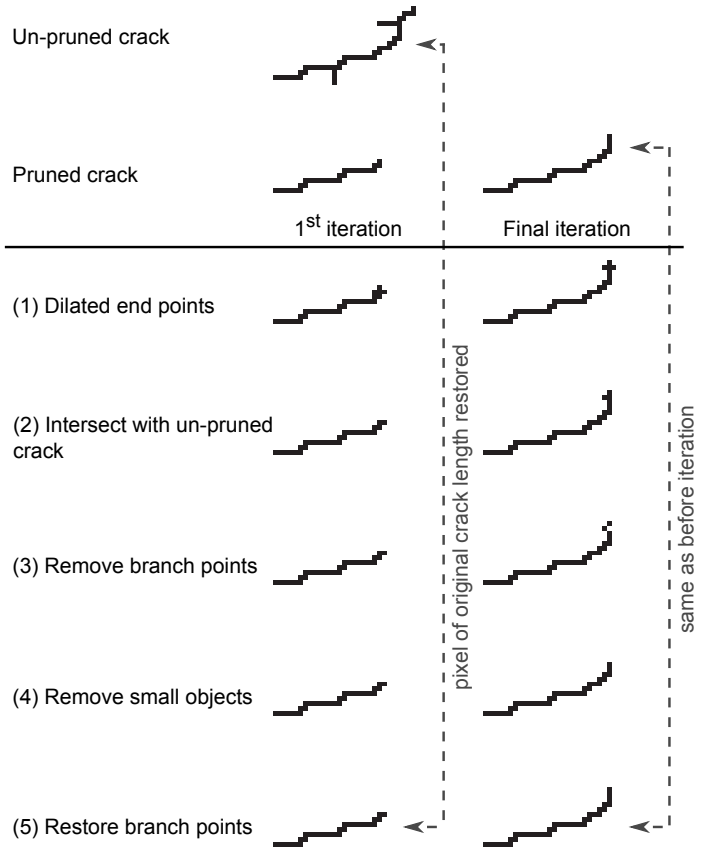

Figure A.3: An example showing the iterative procedure to restore the original microcrack length following the pruning of parasitic branches. The microcrack is iteratively dilated at its end points, whilst any pixels of the residual branches which may reappear are removed at each iteration. This algorithm ends once further iterations no longer affect the image, resulting in the restoration of the original microcrack length.

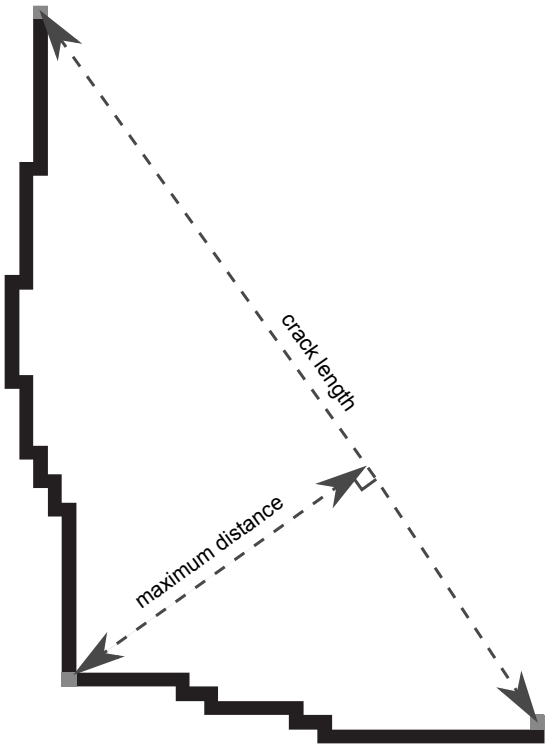

Figure A.4: The microcrack length is approximated by the distance between its two end points. If the farthest pixel of the microcrack is too far from this approximation (defined by the user), it is removed, splitting the microcrack into two shorter, straighter microcracks.

by the ratio of the maximum distance between the microcrack and the straight microcrack approximation, to the length of the straight microcrack approximation (Figure A.4). If this ratio is greater than a user-defined value, the farthest pixel from the approximated microcrack is removed thus separating the original curved microcrack in two. The microcracks in Figure A.2c have been split where the curvature was high. The maximum ratio used here corresponds to a microcrack made up of two straight lines of the same length, at an angle of 70 ° to each other.

B

P-WAVE VELOCITY AND CWI: WAVEFORM ANALYSIS CODE

The Matlab scripts below were used to process the waveform data issuing from the active acoustic monitoring experiments. Firstly, to calculate changes in P-wave travel time, and secondly to perform interferometry to calculate the relative time-shift between waveforms (See Chapter 2 for explanation of the method, and Chapter 4 for results). Comments within the scripts themselves contain an explanation of the code.

B.1 P-WAVE VELOCITY

Below is the Matlab function used to calculate the change in P-wave travel time between two waveforms by cross-correlation.

Listing B.1: Code for calculation of P-wave travel time shift.

```
function [DT,C]=dt_1st_arrival(data, iStart, iEnd, plotGraphs)
% nw: Number of points in the P-wave window to consider
% iRef: spacing in time between reference traces
% i0: set the 1st point of the seismogram for the P-wave
% plotGraphs = 'True' to show correlation function

if nargin < 4
   plotGraphs = 'False';
end

data = data(max(data') > 0, :); % Remove zero traces

% Set frequncy sampling
fs=2e6;

% Get the # of measurements
[e1,~]=size(data);
% Number of points in the P-wave window to consider

% Build a tapering window
nw = iEnd - iStart;
tw = tukeywin_coda(nw,0.1);

% Build the first trace for reference;
x0 = data(1,iStart:iEnd-1);
x0 = x0-mean(x0);
x0 = x0.*tw';
```

```
C(1:e1)=0;
DT(1:e1)=0;

for iTrace = 1:e1-1
    fprintf('Comparing trace %d of %d to trace %d\n', iTrace+1,
        e1, iTrace);
    % Process next trace
    x1 = data(iTrace+1,iStart:iEnd-1);
    x1 = x1-mean(x1);
    x1 = x1.*tw';
    [R,L]=xcorrel(x0,x1,nw);

    R(1:nw/2-10) = 0; R(nw/2 + 10:end) = 0;

    [Cmax,Imax]=max(R);
    dt=interpolate_poly_2nd_cc(L,R,Imax,fs);

    C(iTrace) = Cmax;
    DT(iTrace+1) = dt + DT(iTrace);

    if strcmp(plotGraphs, 'True')
        figure
        plot(x0); hold on; plot(x1);
        figure
        plot(L,R)
    end

    x0 = x1; % New trace becomes old one
    % Set new reference
%     if mod(itrace, iRef) == 0
%         x0 = x1; % Set new reference
%         dt0 = DT(itrace); % Keep cumulative velocity change
%     end
end

function dt=interpolate_poly_2nd_cc(L,R,Imax,fs)

% The purpose of this function is to compute the second order
    polynomial
% that fits the maximum of the correlation function and the two
    neighboring
% points. Then the sub-sample time delay is obtained from the
    maximum of
% the polynomial function. The form of the polynom is P(1)*L.^2+P
    (2).*L+P(3)

% Get the first coefficient
P(1) = (2*R(Imax) - R(Imax-1) - R(Imax+1))/(2*L(Imax)^2-L(Imax-1)
    ^2-L(Imax+1)^2);
% Get the second coefficient
P(2) = R(Imax+1) - R(Imax) - P(1)*(L(Imax+1)^2 - L(Imax)^2);
% Get the third coefficient
```

```
P(3) = R(Imax) - P(1)*L(Imax)^2 -P(2)*L(Imax);
% The position of the maximum is taken as the delay when the
    derivative of
% the polynomila is null (maximum of the function)
dt = (-P(2)/(2*P(1)))/fs;

function [Cxy,L]=xcorrel(x1,x2,ns)

% Here we suppose x1 and x2 have the same length (ns) and ns = 2^
    n where n
% is an integer

% Compute the cross-spectrum and go back in time domain to obtain
     the
% correlation function
Cxy=fftshift(ifft(fft(x1).*conj(fft(x2))));

% Compute the autospectra of signals 1 and 2
Cxx=ifft(fft(x1).*conj(fft(x1)));
Cyy=ifft(fft(x2).*conj(fft(x2)));
% Extract the auto-spectra at zero lag for normalization
A = sqrt(Cxx(1)*Cyy(1));

% Normalize the correlation function
Cxy = Cxy./A;

% Build the delay vector
L = 1:length(x1);
L = L - round(ns/2)-1;

function w=tukeywin_coda(n,r)

t = linspace(0,1,n)';
% Defines period of the taper as 1/2 period of a sine wave.
per = r/2;
tl = floor(per*(n-1))+1;
th = n-tl+1;
% Window is defined in three sections: taper, constant, taper
w = [ ((1+cos(pi/per*(t(1:tl) - per)))/2);  ones(th-tl-1,1); ((1+
    cos(pi/per*(t(th:end) - 1 + per)))/2)];
```

B.2 CWI

Below is the Matlab function used in the processing of CWI waveform data, to calculate the relative time shift between two waveforms using both the windowed cross-correlation (Snieder, 2002) and stretching techniques (Larose and Hall, 2009; Sens-Schönfelder and Wegler, 2006). This script is based on the original code by Olivier Lengliné, to which the function for the CWI "stretching" method (Larose and Hall, 2009; Sens-Schönfelder and Wegler, 2006) was added.

Two functions are proposed for the cross-correlation method, "Original" and "Fast". The "Original" function uses Fourier interpolation of waveforms, while the "Fast" function does not. Interpolation is not necessary where the sampling rate is high enough and the time-shifts low enough for a sufficient correlation between the compared waveforms.

Listing B.2: Code for calculation of CWI relative travel time.

```
function [A, A_corr, R] = coda_process_data(data, spacing, type)

% type gives choice between calculating time shift by cross
    correlation
% in windows along the waveform, or by stretching of waveform by
    fixed
% a certain factor and seeing which corresponds best to the
    following
% waveform
% a_k is the relative time shift between a_k and a_k+1
% A is the cumulative of a_k

[nMeasure,~] = size(data); % number of traces
traces = 1:abs(spacing):nMeasure; % Indexes of traces to compare
aMax = 0.002;
factors = 1 + linspace(-aMax, aMax, 1000);
length(factors)
A = zeros(length(traces),1); % relative velocity change
A_corr = zeros(length(traces),1); % relative velocity change

if strcmp(type, 'Stretch')
    R = zeros(length(traces), length(factors)); % mean of maxima
        of correlation function
end
if strcmp(type, 'Fast') || strcmp(type, 'Original')
    R = zeros(length(traces)); % mean of maxima of correlation
        function
end

if spacing >0 % Forward direction
    for k = 1:length(traces)-1
        % Compare consecutive traces
        fprintf('Comparing trace %d of %d to trace %d\n', traces(
            k), nMeasure, traces(k+1));
        % Compare trace to base, keeping a at reference trace
        if strcmp(type, 'Stretch')
            [a_k, R(k,:)]= coda_process_stretch(data(traces(k),:)
                , data(traces(k+1),:), factors);
        end
        if strcmp(type, 'Fast')
            [a_k, R(k)] = coda_process_fast(data(traces(k),:),
                data(traces(k+1),:));
        end
```

```
        if strcmp(type, 'Original')
            a_k = coda_process_original(data(traces(k),:), data(
                traces(k+1),:));
        end

        A(k+1) = A(k) + a_k; % cumulative dv/v
        A_corr(k+1) = (a_k + 1)*(A_corr(k) + 1) - 1; % cumulative
             dv/v0
    end
end


%% Coda process by cross correlation
function [a0, Rmax]=coda_process_fast(Trace1, Trace2, plotGraphs)
% Calculates a = - (t2 - t1)/t2

if nargin < 3
   plotGraphs = 'False';
end

%% Input parameters
Fs      = 2e6 ; % Sampling frequency
filt_f1 = 50e3 ; % Filter corner frequencies (lower bound)
filt_f2 = 850e3 ; %                           (higer bound)
Nms     = 50  ; % Number of dt measurements
nwin    =   128 ; % Window 1/2 width  (in samples)
HalfWidth = nwin/Fs ; % Window 1/2 width for DT measurements (in
    s)

%% Time and Freq.
Maxt    = length(Trace2)/Fs;    % Time vector length
t  = 0:1/Fs:Maxt-1/Fs;         % Time
[b,a]   = butter(4,[filt_f1,filt_f2]*2/Fs) ; % Parameter for the
    filter
t0 = (HalfWidth*Fs+1)/Fs;       % First time
tend = Maxt-(HalfWidth*Fs+1)/Fs;% Last time
MeasrTime = linspace(t0,tend,Nms); %  DT measurement center times
HWN = HalfWidth*Fs    ; % Taper window length (in samples)
T = tukeywin(2*HWN+1) ; % Tapering window (Here a Tukey window)
NTM    = length(MeasrTime) ; % Number for DT measurements

% Filter the two signals
Trace1_f = filtfilt(b,a,Trace1-mean(Trace1)); Trace1_f = Trace1_f
    ';
Trace2_f = filtfilt(b,a,Trace2-mean(Trace2)); Trace2_f = Trace2_f
    ';

if strcmp(plotGraphs,'True')

    plot(Trace1_f); hold on
    plot(Trace2_f)
end
```

```
a = zeros(1,length(MeasrTime));

%% Compute time-shifts at different times
for i=1:NTM
    tm=MeasrTime(i);                % Get the time of the
        measurement

    [~,itm] = min(abs(t-tm));       % Get index of the closest
        time
    MeasrTime(i) = t(itm);          % Use time of time sample

    Trace1_ft = Trace1_f(itm-HWN:itm+HWN).*T; %Taper the signal
        #1
    Trace2_ft = Trace2_f(itm-HWN:itm+HWN).*T; %Taper the signal
        #2

    % Compute the cross-correlation function
    [Ri,Li]=xcorr(Trace2_ft,Trace1_ft,'coeff'); % Similarity
        between Trace2_ft and
    % shifted Trace1_ft. The time vector is that of Trace2_ft
    [Rmax,I] = max(Ri); % Find index of max. of correlation
        function
    M = [[1, Li(I-1), Li(I-1)^2];
         [1, Li(I), Li(I)^2];
         [1, Li(I+1), Li(I+1)^2]];
    P = M\[Ri(I-1); Ri(I); Ri(I+1)]; % 2nd order polynomial
        coefficients
    Lmax = -P(2)/(2*P(3)); % Index of maximum
    a(i) = - Lmax/Fs; % Time of maximum
    % Uncomment these two lines if you want to display the
    % cross-correlation function

end

Rmax = mean(Rmax);
b = robustfit(MeasrTime, a);
a0 = b(2);

if strcmp(plotGraphs,'True');
    plot(MeasrTime);
    hold off
    plot(MeasrTime, a,'o')
    hold on
    plot(MeasrTime, b(2)*MeasrTime + b(1))
    pause
end


function [a0, R]=coda_process_stretch(Trace1, Trace2, factors)
%% Coda process by calulating shift
% Input parameters
```

```
Fs      = 2e6 ; % Sampling frequency
filt_f1 = 50e3 ; % Filter corner frequencies (lower bound)
filt_f2 = 850e3 ; %                          (higer bound)
Nms     = 50  ; % Number of dt measurements
nwin    =   128 ; % Window 1/2 width  (in samples)
HalfWidth = nwin/Fs ; % Window 1/2 width for DT measurements (in
    s)

% Time and Freq.
Maxt    = length(Trace2)/Fs;    % Time vector length
t  = 0:1/Fs:Maxt-1/Fs;         % Time
[b,a]   = butter(4,[filt_f1,filt_f2]*2/Fs) ; % Parameter for the
    filter
t0 = (HalfWidth*Fs+1)/Fs;       % First time
tend = Maxt-(HalfWidth*Fs+1)/Fs;% Last time
MeasrTime = linspace(t0,tend,Nms); %  DT measurement center times
HWN = HalfWidth*Fs    ; % Taper window length (in samples)
T = tukeywin(2*HWN+1) ; % Tapering window (Here a Tukey window)
NTM    = length(MeasrTime) ; % Number for DT measurements

% Filter the two signals
Trace1_f = filtfilt(b,a,Trace1-mean(Trace1)); Trace1_f = Trace1_f
    ';
Trace2_f = filtfilt(b,a,Trace2-mean(Trace2)); Trace2_f = Trace2_f
    ';

% figure
% plot(Trace1_f)
% hold on
% plot(Trace2_f)

R = zeros(1, length(factors));

%figure
%hold on
for i = 1:length(factors)
    Trace2_f_stretched = interp1(t, Trace2_f, t.*factors(i), '
        spline');
    [Ri,~]=xcorr(Trace2_f_stretched(1:end-10), Trace1_f(1:end-10)
        , 'coeff');
    R(i) = max(Ri);
    %plot(Trace2_f_stretched)
end
%plot(Trace1_f, 'k')
%plot(Trace2_f, '--k')

%figure
%plot(factors, R)
size(R)
[~, iMax] = max(R);
%Trace2_f_stretched = interp1(t, Trace2_f, t.*factors(iMax), '
    PCHIP');
```

```
% figure
% hold on
% plot(Trace1_f, 'b')
% plot(Trace2_f, 'g')
% plot(Trace2_f_stretched, '--g')

a0 = 1-factors(iMax)

% figure
% plot(abs(Trace1_fft))
% hold on
% plot(abs(Trace2_fft))


function [a0]=coda_process_original(Trace1,Trace2)
% Input parameters
Fs      = 2e6 ; % Sampling frequency
filt_f1 = 100e3 ; % Filter corner frequencies (lower bound)
filt_f2 = 850e3 ; %                            (higer bound)
Nms     = 100   ; % Number of dt measurements
nwin    =   128 ; % Window 1/2 width  (in samples)
HalfWidth = nwin/Fs ; % Window 1/2 width for DT measurements (in
    s)

% Time and Freq.
Maxt    = length(Trace1)/Fs;    % Time vector length
t    = 1/Fs:1/Fs:Maxt;          % Time
[b,a]   = butter(4,[filt_f1,filt_f2]*2/Fs) ; % Parameter for the
    filter
t0 = (HalfWidth*Fs+1)/Fs;       % Fist time
tend = Maxt-(HalfWidth*Fs+1)/Fs;% Last time
MeasrTime = linspace(t0,tend,Nms); %  DT measurement center times


HWN = HalfWidth*Fs    ; % Taper window length (in samples)
T = tukeywin(2*HWN+1) ; % Tapering window (Here a Tukey window)

% Number of points to keep around the 0 delay of the interpolate
    CC
% function
nmax=1e3;
% Number of points for interpolation of the CC function
ninterp=2^15;

NTM    = length(MeasrTime) ; % Number for DT measurements
X=zeros(NTM,2*nmax+1); % Matrix with all correlation functions

% Filter the two signals
Trace1_f = filtfilt(b,a,Trace1-mean(Trace1)); Trace1_f = Trace1_f
    ';
Trace2_f = filtfilt(b,a,Trace2-mean(Trace2)); Trace2_f = Trace2_f
    ';
```

```
nwin=2*nwin+1;
LAGS = -ninterp+1:ninterp-1;
LAGS = LAGS *  nwin / ninterp;
LAGS = LAGS(ninterp-nmax:ninterp+nmax);
LAGS = LAGS/Fs;

% Compute time-shifts at different times
for i=1:NTM
    tm=MeasrTime(i);               % Get the time of the
        measurement

    [~,itm] = min(abs(t-tm));      % Get the closest time

    Trace1_ft = Trace1_f(itm-HWN:itm+HWN).*T; %Taper the signal
        #1
    Trace2_ft = Trace2_f(itm-HWN:itm+HWN).*T; %Taper the signal
        #2

    % Fourier interpolation of the signal to get a better time
        delay
    % estimation
    Trace1_i = interpft(Trace1_ft,ninterp);
    Trace2_i = interpft(Trace2_ft,ninterp);

    % Compute the cross-correlation function
    [Ri,Li]=xcorr(Trace1_i,Trace2_i,'coeff');

    % Uncomment these two lines if you want to display the
    % cross-correlation function
    %plot(Li/ninterp*nwin,Ri,'r'); hold off
    %pause

    % Keep in a matrix the cross-correlation function at the
        current time
    % step
    X(i,:) = Ri(ninterp-nmax:ninterp+nmax);
end

% Estimate the dt/t from the matrix X. This will be obtained by a
     search
% grid on all possible values of a (slope)

% Get the interpolated sampling time interval
dt=LAGS(2)-LAGS(1);

% Make a vector with the number of measurements
x=1:NTM;
[e1,e2]=size(X);

% Initialize the RMS
K=0;
```

```
% Loop on all possible values of dt/t
for a = -2.5:5e-3:2.5

    % Get the values of the CC function for such a slope
    y=round(a*x+nmax+1);
    K_test=sum(X(sub2ind([e1 e2],x,y)));

    % Update the cost function if necessary
    if(K_test>K)
        a0 = a;
        K=K_test;
    end
end
% Put the result in the correct physical unit
a0=a0*dt/MeasrTime(end)*NTM;

%figure; imagesc(X)
```

C

OTHER PUBLISHED WORK

The following four contributions were published during the PhD:

- L. Griffiths, M. J. Heap, F. Wang, D. Daval, H. A. Gilg, P. Baud, J. Schmittbuhl, and A. Genter (2016). 'Geothermal implications for fracture-filling hydrothermal precipitation.' In: *Geothermics* 64, pp. 235–245. ISSN: 0375-6505. DOI: 10.1016/j.geothermics.2016.06.006;
- L. Griffiths, M. J. Heap, T. Xu, C.-f. Chen, and P. Baud (2017b). 'The influence of pore geometry and orientation on the strength and stiffness of porous rock.' In: *Journal of Structural Geology* 96, pp. 149–160. ISSN: 01918141. DOI: 10.1016/j.jsg.2017.02.006;
- L. Griffiths, M. J. Heap, P. Baud, and J. Schmittbuhl (2017a). 'Quantification of microcrack characteristics and implications for stiffness and strength of granite.' In: *International Journal of Rock Mechanics and Mining Sciences* 100, pp. 138–150. ISSN: 13651609. DOI: 10.1016/j.ijrmms.2017.10.013.
- L. Griffiths, O. Lengliné, M. J. Heap, P. Baud, and J. Schmittbuhl (2018). 'Thermal Cracking in Westerly Granite Monitored Using Direct Wave Velocity, Coda Wave Interferometry, and Acoustic Emissions.' In: *Journal of Geophysical Research: Solid Earth* 0.0. ISSN: 2169-9313. DOI: 10.1002/2017JB015191.

The two most recent contributions make up Section 4.1 in Chapter 4, and Chapter 3, and the two previous works are provided here for reference.

Geothermal implications for fracture-filling hydrothermal precipitation

L. Griffiths[1]*, M.J. Heap[1], F. Wang[1], D. Daval[2], H. A. Gilg[3], P. Baud[1], J. Schmittbuhl[1], A. Genter[4]

[1]Institut de Physique de Globe de Strasbourg, Université de Strasbourg/EOST, CNRS UMR 7516, France

[2]Laboratoire d'Hydrologie et de Géochimie de Strasbourg, Université de Strasbourg/EOST, CNRS UMR 7517, Strasbourg, France

[3]Lehrstuhl für Ingenieurgeologie, Technische Universität München, Arcisstr. 21, 80333, Munich, Germany

[4]ES-Géothermie, 3 Chemin du Gaz, Haguenau, 67500, France

* Corresponding author: Luke Griffiths *luke.griffiths@unistra.fr*

https://doi.org/10.1016/j.geothermics.2016.06.006

Abstract

In geothermal reservoirs, fluid circulation is greatly dependent on the geometry, density, and hydraulic properties of fractures. The Soultz-sous-Forêts geothermal site located in the Upper Rhine Graben in Alsace, France, consists of a granitic basement overlain by a 1.4 km-thick sedimentary succession. Core analysis and borehole wall imagery collected from reconnaissance well EPS1, drilled vertically to a depth of 2230 m, revealed an extensive fracture network throughout the granite and overlying sediments, including both open fractures and fractures sealed through mineral precipitation (primarily quartz, illite, chlorite, calcite, dolomite, barite, pyrite and galena). Here we present a combined experimental and modelling study that aims to provide insights into the permeability anisotropy in the Triassic Buntsandstein sandstone (1 - 1.4 km depth) and the impact of mineral precipitation. We targeted borehole samples that best represented the variability of fractures within the Buntsandstein. Forty cylindrical samples (40 mm in length and 20 mm in diameter) were prepared from the chosen borehole samples such that they contained sealed or partially-sealed fractures either parallel or perpendicular to their axis. We also prepared samples of the intact host rock. These samples were then subject to porosity and permeability measurements, and thin sections were made for Scanning Electron Microscopy (SEM) to characterise the nature of the fractures and the precipitated minerals. Permeability measurements of the Buntsandstein host rock yielded values ranging from 10^{-15} m^2 to less than 10^{-18} m^2. SEM and X-ray powder diffraction analyses suggest that prevalent pore-filling illitic clays can explain the low permeability of the sandstone host rock. Additionally, we found that the permeability of fractures depends on the nature of the filling and the extent of sealing, with barite providing the most effective precipitate. Taking into account the geothermal fluid composition at Soultz-sous-Forêts, we employ a kinetic model for the barite crystal growth rate with temperature to provide an estimate for the time scale over which open fractures can seal through barite precipitation (from months to days depending on temperature). The rate increases dramatically as the temperature of the geothermal brine decreases, highlighting the risk of mineral precipitation at geothermal sites, where fluid temperature fluctuates due to circulation through the reservoir rock and fluid mixing around the injection well. An improved knowledge of the time dependency of fracture permeability will provide insights into the permeability anisotropy in the Buntsandstein and may have repercussions for the geothermal exploitation and for the ongoing fluid flow modelling of the Soultz-sous-Forêts geothermal reservoir.

Keywords

Geothermal reservoir, Soultz-sous-Forêts, Buntsandstein, permeability, fracture sealing, barite.

1 Introduction

Fluid circulation in geothermal reservoirs is susceptible to the geometry and hydraulic properties of fractures (Grant and Bixley, 2011). The Soultz-sous-Forêts Enhanced Geothermal System (EGS) is located in the Upper Rhine Graben in Alsace, France, and consists of a granitic basement overlain by a 1.4 km-thick sedimentary succession (Kappelmeyer and Gerard, 1989; Baria et al., 1999). This is a site of significant geothermal potential due to the high thermal gradient in the first 1 km of the sedimentary cover (~100 °C/km) and the abundance of natural brines (Gérard et al., 2006; Genter et al., 2010). These brines have a high salinity, containing total dissolved solids of around 100 g/L and circulate over several kilometres, facilitating heat transfer (Sanjuan et al., 2010). Exploiting this natural heat source involves the use of deep wells and the fracture network in the granitic basement. The fracture network in the granite has been extensively studied (Surma and Géraud, 2003; Dezayes et al., 2010; Sausse et al., 2010; Genter and Traineau, 1996; Ledésert et al., 1993) as it is the target for two EGS heat exchangers at 3.5 and 5 km depth (Genter et al., 2010). In the Buntsandstein sandstone (1–1.4 km depth) and the granite below, the temperature gradient is lower (~30 °C/km and ~5 °C/km, respectively) than in the above sediments and has been linked to fluid convection (Pribnow and Clauser, 2000; Vidal et al., 2015). Numerical modelling of this hydrothermal convection at Soultz-sous-Forêts finds that the Buntsandstein, as well as the granite, plays an important role in controlling regional fluid flow (Guillou-Frottier et al., 2013; Magnenet et al., 2014).

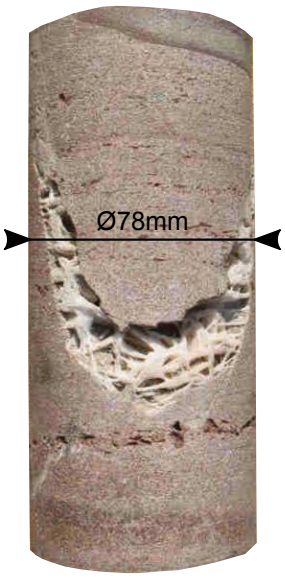

Figure 1: *Photo of a fractured Buntsandstein core sample from exploration well EPS1 at 1374 m depth. The rock contains a large fracture of roughly 1 cm in width, filled with precipitated barite crystals.*

Core analysis and borehole wall imagery collected from reconnaissance well EPS1 (Soultz-sous-Forêts), drilled vertically to a depth of 2230 m, reveal the geometry of an extensive fracture network throughout the granite and overlying sediments. This includes both open fractures and fractures filled through mineral precipitation (primarily quartz, barite, calcite, and galena; Vernoux et al., 1995). EPS1 was continuously cored from 930 m to 2227 m measured depth and the granitic basement was reached at 1417 m (throughout this paper, all reported depths are measured depths). In the Buntsandstein (1000–1417 m depth in EPS1), core analysis gave an average fracture density of 0.83/m (Genter et al., 1997). These fractures are for the most part sub-vertical, and generally have a width of 0.1 – 3 mm. Their average width is about 2 mm however some rare fractures can be up to 5 cm wide (Vernoux et al., 1995). Figure 1 is an example of the EPS1 Buntsandstein core containing a large fracture, roughly 1 cm in width, filled with precipitated barite ($BaSO_4$). In terms of their spatial distribution, the fractures have a preferred orientation; the two major fracture sets strike N005°

and N170°, dipping 70°W and 70°E respectively (Genter et al., 1997).

Some of these fracture zones within the Buntsandstein have been shown to be permeable, through analysis of Soultz-sous-Forêts mud and well logging data (Vidal et al., 2015). In the same study, the presence of secondary precipitated minerals within the fracture zones and an associated reduction in permeability is also discussed. Indeed, the importance of fracture sealing in a geothermal context has been highlighted by recent study by McNamara et al. (2016), who identify calcite sealing mechanisms in the Kawerau Geothermal Field, New Zealand. Fracture sealing is already known to occur in volcanic systems, which are highly dynamic with regards to temperature and fluid flow, and where mineral precipitation is expected to contribute to a decrease in permeability and create a barrier for fluids (Ball et al., 2015).

The above studies highlight the importance of the fractured Triassic Buntsandstein sandstone for regional fluid flow and temperature distribution, as well as the potential for mineral precipitation to influence fracture permeability. Hydraulic properties of the Buntsandstein host rock have been quantified through permeability measurements of the EPS1 core, including laboratory measurements (Sizun, 1995), and measurements using a TinyPerm II field permeameter (Haffen et al., 2013). Both studies find the permeability to vary with depth in the range of 10^{-16} – 5 x 10^{-13} m^2. However, due to the anticipated importance of fracture sealing on regional permeability and permeability anisotropy, we provide in this study new laboratory porosity and permeability measurements on Buntsandstein core samples with and without partially-sealed and sealed fractures. We then look specifically at barite precipitation, which is abundant in fractures in the core samples, and model the crystal growth rate with temperature, providing a time scale for sealing. Finally, we discuss the geothermal implications for permeability anisotropy and its time dependency due to mineral precipitation.

2 Core description

For our study, we targeted borehole core from exploration well EPS1 well that best represents the variability of preserved fractures within the Buntsandstein (Figure 2). Core was selected from sections where the fracture density is noticeably greater, in the Upper Buntsandstein (1038 m depth), the Middle Buntsandstein (1083 m, 1089 m, and 1092 m depth), and the Lower Buntsandstein (1379 m depth). Heterogeneity in grain size and cementation is macroscopically visible between the selected samples (Figure 2). Bands of coarse grains (5-15 mm in width) are visible within the samples from 1083 m, 1089 m, and 1092 m depth. The sample from 1038 m depth shows less grain size heterogeneity. This is also the case at 1379 m depth where the core contains a red and green alternating coloration but a homogeneous grain size.

These core samples include sub-vertical fractures containing mineral precipitates. The fracture width ranges from 0.5 mm to 2 mm. These are representative of the preserved fractures in the EPS1 core (Vernoux et al., 1995) however, as mentioned above, some larger fractures are also present (Figure 1). Slip along fractures can be observed, particularly in the case of the 1038 m, 1089 m, and 1379 m core samples where there is 5 – 10 mm of misalignment in bedding (Figure 2). We see no misalignment inside the fracture filling at this scale.

3 Microstructural observations and host rock mineralogy

Thin sections were prepared from offcuts of the Buntsandstein containing the sealed fractures, one for each of the 5 depths of investigation. These were subject to scanning electron microscopy (SEM) to characterise the host rock (Figure 3) and the fractures (Figure 4).

3.1 Host rock

The host rock of the 1038 m depth sample (Figure 3a) contains quartz and feldspar grains of around 0.5 mm in diameter and the feldspar is etched in some cases. At 1083 m depth (Figure 3b), grains are finer, 0.1 - 0.2 mm in diameter. The thin section of the rock from 1089 m (Figure 3c) contains bands of different grain sizes.

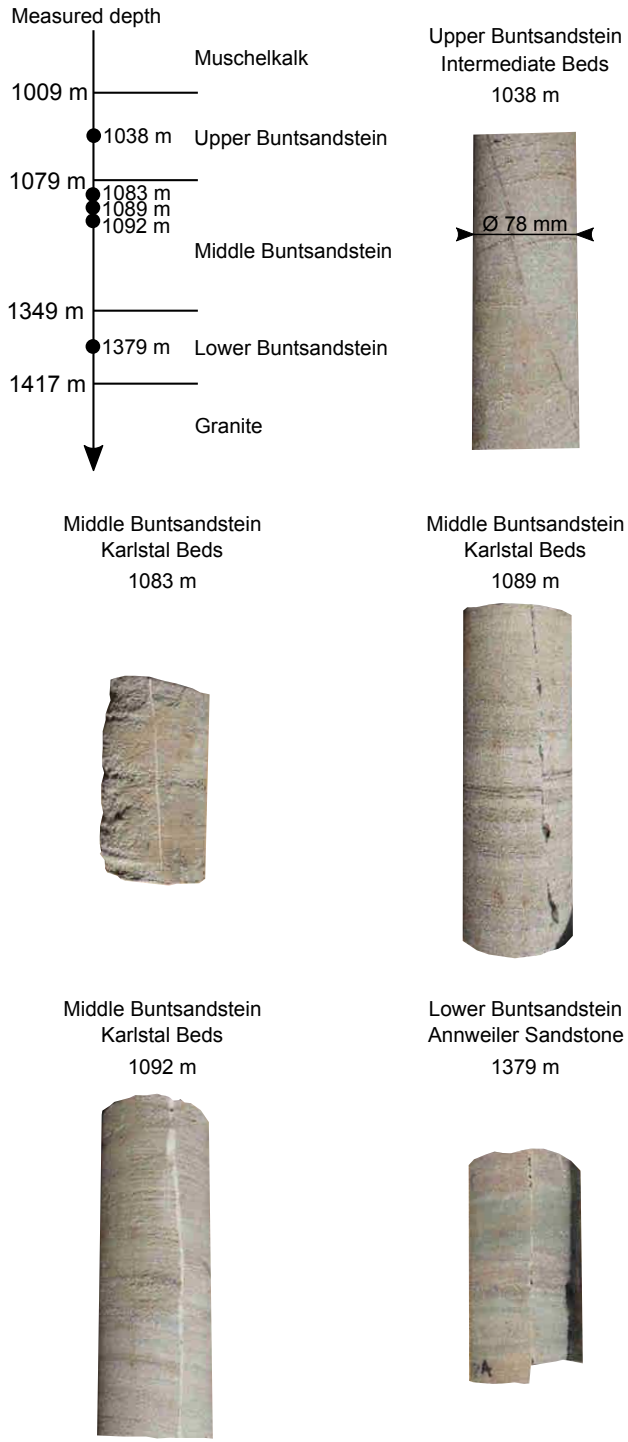

Figure 2: *Stratigraphy of and adjacent to the Buntsandstein, complete with the depths of the Formations (Muschelkalk, Upper, Middle, and Lower Buntsandstein, and the granite) and the depths of sampled cores from EPS1 (measured depths of 1038 m, 1083 m, 1089 m, 1092 m, and 1379 m). Photographs of the retrieved cores are also shown, which all contain sub-vertical sealed fractures with widths in the millimetre scale.*

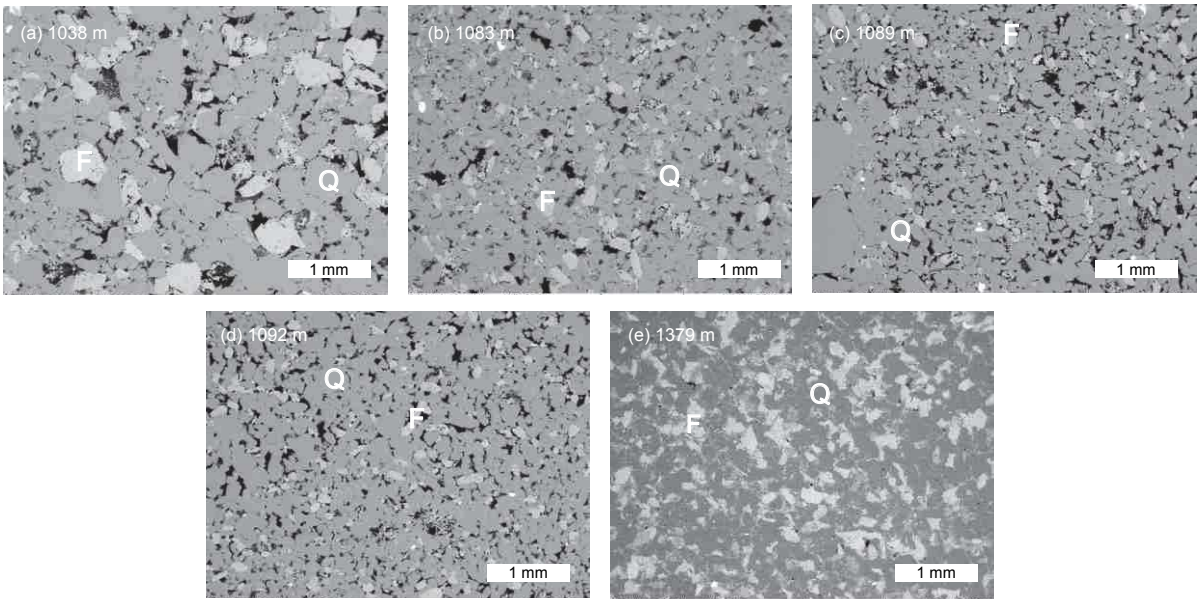

Figure 3: *SEM micrographs of thin sections of the intact rock from each core sample. These images show the intact host Buntsandstein at (a) 1038 m, (b) 1083 m, (c) 1089 m, (d) 1092 m, and (e) 1379 m depth. 'Q' and 'F' label the quartz and feldspar grains, respectively, and the porosity is black.*

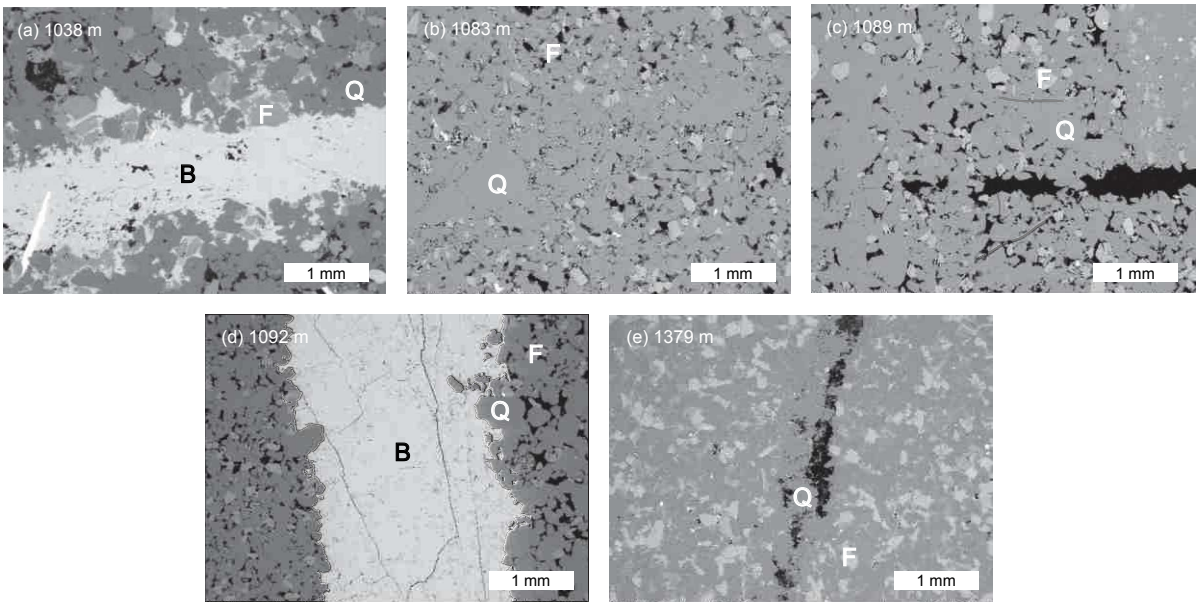

Figure 4: *SEM micrographs of thin sections from each core sample. SEM micrographs of thin sections of rock containing partially-sealed fractures. 'Q' and 'F' label the quartz and feldspar grains, respectively, and the porosity is black. (a) and (d) show thick fractures sealed by barite precipitation, labelled 'B'. At the bottom left of (a), is an elongated siderite crystal. The fractures in (b), (c) and (e) contain quartz and K-feldspar. Both (c) and (e) show only partial sealing.*

Fine grains of 0.1 – 0.2 mm in diameter occupy most of the image while quartz grains of ~1 mm in diameter can be seen in the lower left hand corner of the image. At 1092 m depth (Figure 3d), the grain size appears more homogeneous although there is still a band of larger grains and pores along the top half of the image. Finally, at 1379 m (Figure 3e) depth we see grains of 0.1 – 0.3 mm in diameter and a reduced pore space compared to the previous samples.

X-Ray Diffraction (XRD) techniques were used to determine the bulk rock mineral composition (Table 1) at each depth. Two 1083 m samples were analysed due to the heterogeneity of the core at this depth. The samples were gently disaggregated using an agate mortar, resulting in 10-15 g of powdered material. For bulk rock mineral quantification, an aliquot was ground together with 10 % ZnO as an internal standard for 8 minutes in 10 ml of isopropyl alcohol using a McCrone Micronising Mill with agate cylinder elements. The XRD analyses (2-70 ° 2θ) were performed on top-loaded powder mounts using a Philips PW 1800 X-ray diffractometer (Cu$K\theta$, graphite monochromator, 10 mm automatic divergence slit, step-scan 0.02 ° 2θ increments per second, counting time 1s per increment, 40 mA, 30 kV). The Rietveld program BGMNwin 1.8.6 was used for phase quantification. For clay mineralogical investigations, the sample was dispersed using an ultrasonic bath in deionized water. The < 2 μm fraction was separated by sedimentation in Atterberg cylinders. The oriented clay mineral aggregates were prepared by sedimentation and air-drying of the aqueous suspension on glass slides. XRD scans (2-30° 2θ) were performed on both an air-dried and a glycolated (24 hours in saturated glycol vapour at 80 °C) mount.

The Buntsandstein samples contain quartz, K-feldspars (orthoclase and microcline), and an $R3$ interstratified illite-smectite with less than 5 % expandable layers and possibly also discrete illite/mica. The 1379 m deep sample contains much more illitic material, (20 mass%) as compared to 1 - 3 mass% at shallower depths.

Table 1: *Results of the X-ray powder diffraction analyses of the host rock at each investigation depth. Two samples of the 1038 m core were analysed due to its strong heterogeneity.*

Measured depth (m)	Lithostratigraphy	Quartz (mass%)	Orthoclase (mass%)	Microcline (mass%)	Illite-Smectite (mass%)
1038	Upper Buntsandstein – Intermediate Beds	81	6	11	2
1083	Middle Buntsandstein – Karlstal Beds	91	3	5	1
1083	"	82	5	10	3
1089	"	87	5	6	2
1092	"	86	6	6	2
1379	Lower Buntsandstein – Annweiler Sandstone	63	5	12	20

3.2 Fractures

Figure 4 shows micrographs of the 5 thin sections containing sealed fractures. The fracture in the 1038 m depth sample (Figure 4a) is 1 mm wide and is sealed with barite crystals. The 1083 m sample contains a 1 mm thick band composed of large quartz grains (Figure 4b). The micrograph of the 1089 m core (Figure 4c) shows a partially sealed fracture containing quartz and K-feldspar. The 1092 m sample (Figure 4d) contains a large fracture (2 mm wide), completely sealed with barite. Finally, the 1379 m depth sample (Figure 4e) hosts a variably sealed fracture containing clay and quartz grains.

4 Laboratory experiments

4.1 Sample preparation and experimental methods

Forty cylindrical samples (nominally 40 mm in length and 20 mm in diameter) were prepared from the borehole core such that they contained sealed or partially-sealed fractures either parallel or perpendicular to their axis. These samples were cored either parallel or perpendicular to bedding (the orientations are given in Table 2). We also prepared samples of the intact host rock, containing no fractures. Examples of the prepared samples are shown in Figure 5. These samples were then subject to gas porosity measurements and gas permeability measurements. The connected porosity was calculated from the sample bulk volume measured using callipers and the rock matrix volume measured using a helium pycnometer (Micromeritics AccuPyc II 1340). Permeability measurements were made on jacketed samples using the steady state method, under a confining pressure of 1 MPa. Volumetric flow was measured using a gas flow meter for several pressure gradients across the sample. Two flow meters were used, one for high flow rates (i.e. high permeability samples) and one for low flow rates (i.e. low permeability samples). Darcy's law was used to calculate the permeability (applying the Klinkenberg or Forchheimer correction where necessary). The permeability range measurable with this setup is 10^{-18} – 10^{-11} m^2.

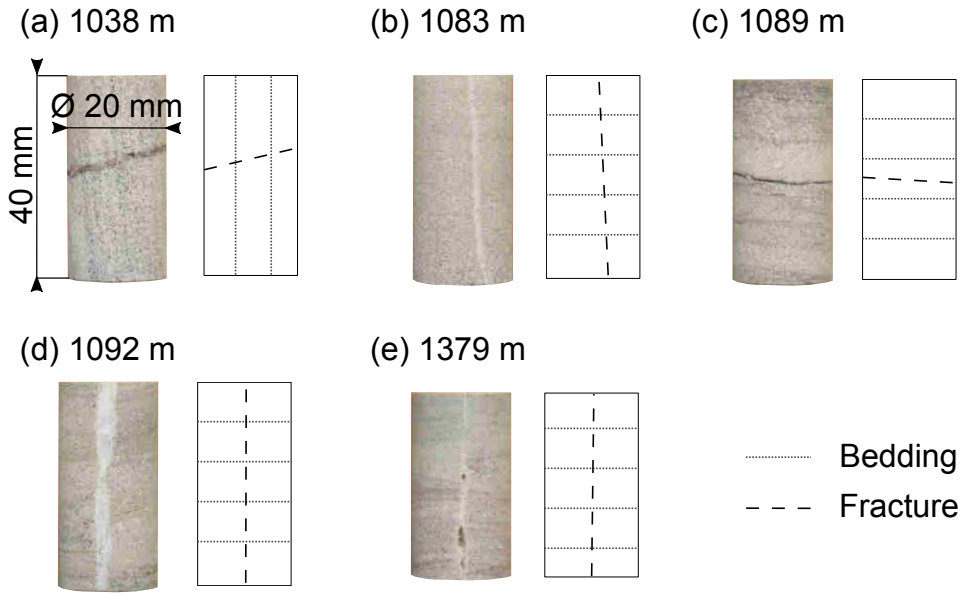

Figure 5: *Photographs of examples of the Buntsandstein samples from (a) 1038 m, (b) 1083 m, (c) 1089 m, (d) 1092 m, and (e) 1379 m depth. They contain fractures and bedding perpendicular or parallel to their axis, described by the drawing to their right. For a complete list of the 40 samples and their fracture and bedding orientations, see Table 2. These samples were subject to porosity and permeability measurements. Permeability was measured across their axes.*

4.2 Porosity and permeability of the intact rock samples

Connected porosity measurements of the intact Buntsandstein sandstone give values ranging from 2.9 % to 20.7 % (Table 2). These porosity measurements on the intact materials are shown in Figure 6a as a function of depth. The samples from 1028 m depth have a relatively consistent porosity, ranging from 8.2 % to 10.9 %. The same is true for the values at 1089 m, which range from 10.0 % to 13.2 % and at 1089 m, which are between 10.5 % and 13.2 %. At 1083 m depth, the porosity is much more variable, 9.9 % - 20.7 % which

reflects the high variability of the core sample (Figure 2). Finally, the 1379 m samples give very consistent values of around 3 % porosity.

Permeability measurements of the Buntsandstein host rock yielded values ranging from 9.2 x 10^{-18} to 6.9 x 10^{-15} m^2 (Table 2). The samples from 1379 m depth were too impermeable to be measured using our experimental setup (<10^{-18} m^2). Figure 6b is a synopsis plot containing all of the intact rock permeability data against depth, samples cored both parallel and perpendicular to bedding are presented. The permeability of the 1038 m core is less variable than the other samples (1083 – 1092 m depth), which span across several orders of magnitude.

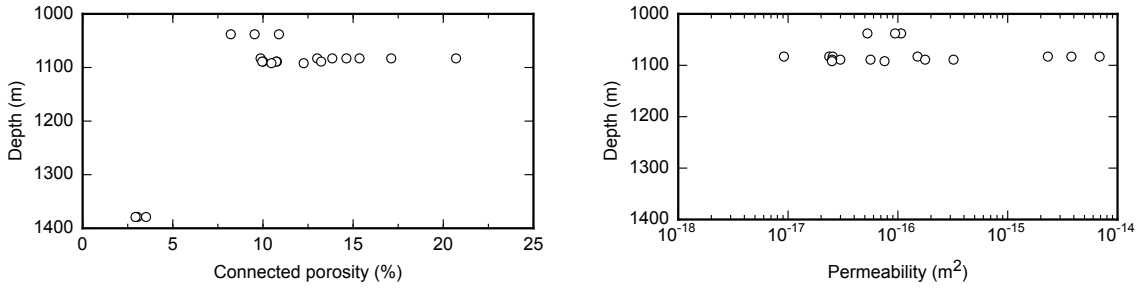

Figure 6: *(a) Porosity against depth for all of the intact samples (Table 2). At 1379 m depth, the variation of porosity between samples is very low. For the samples from shallower depths, however, the porosity is more variable, the 1038 m samples showing the smallest variation. (b) Permeability against depth for all of the intact, un-fractured samples from 1038 m, 1083 m, 1089 m, 1092 m depth (Table 2). Samples cored both parallel and perpendicular to bedding are represented. The 1379 m depth samples were too impermeable for our experimental setup (<10^{-18} m^2). The permeability values of the 1038 m depth samples show the least variation. The values at other depths vary across several orders of magnitude.*

4.3 Porosity and permeability of the fractured samples

Figure 7 shows the permeability against the porosity values (Table 2) at each core depth plotted on separate graphs. The directions of the bedding and the fracture with regards to the flow direction is shown via the symbol representing each data point as explained in the figure caption. Note that the scales are different to better show the data. A synopsis plot, containing all of the porosity-permeability data, is shown in Figure 8.

The porosity of samples extracted from 1038 m depth (Figure 7a) varies between 8.2 % and 10.9 % and the permeability is in the range of 10^{-17} - 10^{-16} m^2 for all samples, both show little variation, regardless of the presence and orientation of bedding and fractures.

In Figure 7b, at 1083 m depth, we see more variability in the porosity (9.9 – 20.7 %) and permeability (9.2 x 10^{-18} - 6.9 x 10^{-15} m^2). The permeability of the intact (fracture free) samples is around 2 orders of magnitude higher for samples cored parallel to the bedding. The permeability of these samples cored parallel to the bedding is however lower for those containing a sealed fracture perpendicular to the flow direction. The permeability of samples containing a sealed fracture parallel to flow are roughly the same permeability as the host rock.

The samples from 1089 m depth (Figufre 7c) show a lower variation in porosity (10.0 – 13.2 %) whereas the permeability can vary by more than an order of magnitude. Generally, the permeability parallel to the bedding is greater, as is the case at 1083 m depth. It is difficult to pick out a trend regarding the flow vs. fracture direction.

The porosity of the 1092 m samples ranges from 10.5 to 13.4 % and the permeability from 2.5 x 10^{-17} to 6.4 x 10^{-16} m^2 (Figure 7d). The permeability values are roughly an order of magnitude higher for samples containing a fracture (regardless of the fracture orientation).

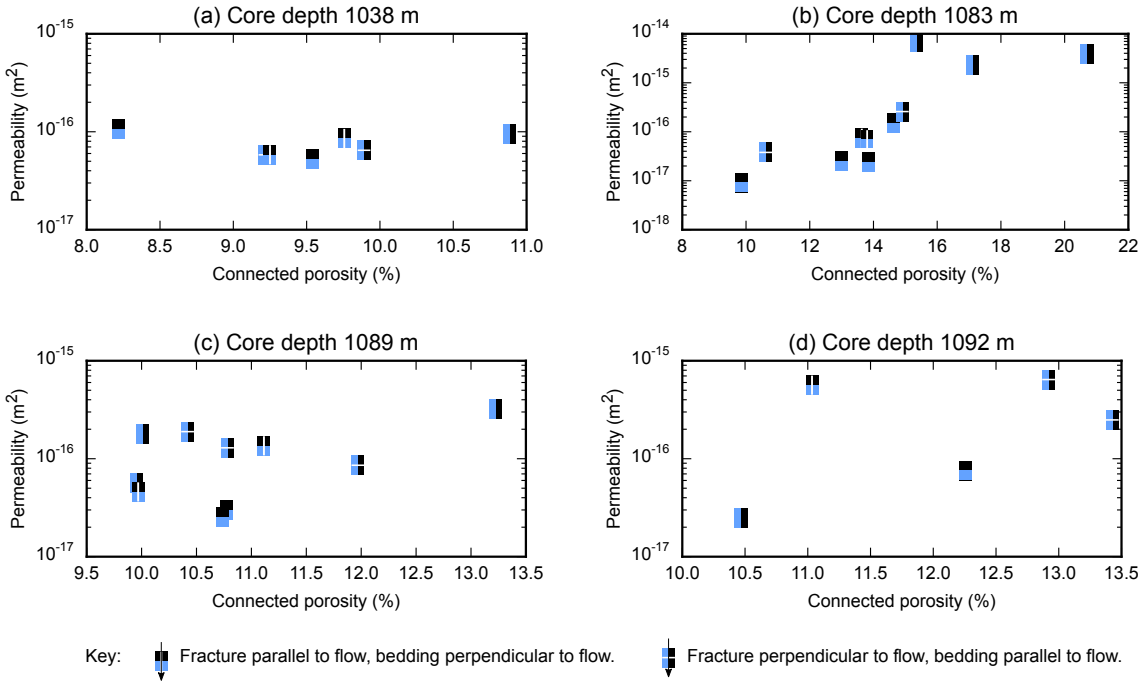

Figure 7: *Permeability against porosity for samples from (a) 1038 m, (b) 1083 m, (c) 1089 m, (d) 1092 m depth. The symbols show the orientation of the bedding and the fracture. Vertical white lines are fractures parallel to the sample axis i.e. the flow direction. Horizontal white lines are fractures perpendicular to flow. Similarly, two vertical blue and black stripes represent samples for which bedding is parallel to their axis and to fluid flow, two horizontal stripes represent bedding perpendicular to the flow direction.*

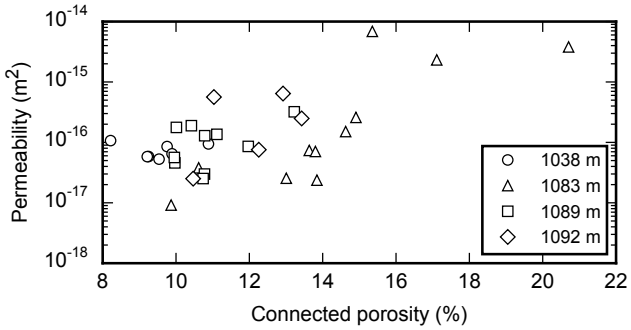

Figure 8: *Synopsis plot of permeability against porosity for all samples from 1038m, 1083 m, 1089 m, 1092 m depth (Table 2). No distinction is made regarding the fracture or bedding orientations. The permeability of the Annweiler sandstone samples from 1379 m depth was too low to be measured with the apparatus used in this study (<10^{-18} m^2).*

Table 2: *Porosity and permeability measurements of all 40 Buntsandstein samples. For the permeability tests, the fluid flow direction with regards to bedding and fracture orientation is given.*

Measured depth (m)	Lithostratigraphy	Connected porosity (%)	Permeability (m^2)	Bedding vs. flow direction	Fracture vs. flow direction	Approximate fracture aperture (mm)
1038	Upper Buntsandstein – Intermediate Beds	9.3	5.8×10^{-17}	perpendicular	parallel	1 - 2
1038	"	9.8	8.5×10^{-17}	perpendicular	parallel	1
1038	"	9.5	5.3×10^{-17}	perpendicular	intact	-
1038	"	8.2	1.1×10^{-16}	perpendicular	intact	-
1038	"	9.9	6.5×10^{-17}	parallel	perpendicular	1 - 2
1038	"	9.2	5.8×10^{-17}	parallel	perpendicular	1 - 2.5
1038	"	10.9	9.4×10^{-17}	parallel	intact	-
1083	Middle Buntsandstein – Karlstal Beds	9.9	9.2×10^{-18}	perpendicular	intact	-
1083	"	14.6	1.5×10^{-16}	perpendicular	intact	-
1083	"	17.1	2.3×10^{-15}	parallel	intact	-
1083	"	20.7	3.8×10^{-15}	parallel	intact	-
1083	"	13.8	2.4×10^{-17}	perpendicular	intact	-
1083	"	13.6	7.4×10^{-17}	perpendicular	parallel	1 - 2
1083	"	13.0	2.5×10^{-17}	perpendicular	intact	-
1083	"	13.8	7.1×10^{-17}	perpendicular	parallel	1 - 1.5
1083	"	15.4	6.9×10^{-15}	parallel	intact	-
1083	"	14.9	2.6×10^{-16}	parallel	perpendicular	1 - 2
1083	"	10.6	3.8×10^{-17}	parallel	perpendicular	1 - 2
1089	Middle Buntsandstein – Karlstal Beds	10.4	1.9×10^{-16}	parallel	perpendicular	0.5 - 1
1089	"	10.0	1.8×10^{-16}	parallel	intact	-
1089	"	10.0	4.6×10^{-17}	perpendicular	parallel	0.5 - 1
1089	"	11.1	1.4×10^{-16}	perpendicular	parallel	0.5 - 1.5
1089	"	10.8	3.0×10^{-17}	perpendicular	intact	-
1089	"	10.7	2.5×10^{-17}	perpendicular	intact	
1089	"	12.0	8.6×10^{-17}	parallel	perpendicular	0.5 - 1.5
1089	"	10.8	1.3×10^{-16}	parallel	perpendicular	0.5 - 1.5
1089	"	10.0	5.6×10^{-17}	parallel	intact	-
1089	"	13.2	3.2×10^{-16}	parallel	intact	-
1092	Middle Buntsandstein – Karlstal Beds	11.0	5.6×10^{-16}	perpendicular	parallel	2 - 4
1092	"	12.3	7.6×10^{-17}	perpendicular	intact	-
1092	"	13.4	2.5×10^{-16}	parallel	perpendicular	2 - 4.5
1092	"	10.5	2.5×10^{-17}	parallel	intact	-
1092	"	12.9	6.4×10^{-16}	parallel	perpendicular	0.5 - 1
1379	Lower Buntsandstein – Annweiler Sandstone	3.6	$< 10^{-18}$	perpendicular	parallel	0.5 - 1
1379	"	3.7	$< 10^{-18}$	perpendicular	parallel	0.5 - 2
1379	"	3.0	$< 10^{-18}$	perpendicular	intact	-
1379	"	2.9	$< 10^{-18}$	perpendicular	intact	-
1379	"	3.7	$< 10^{-18}$	parallel	perpendicular	0.5 - 1.5
1379	"	3.5	$< 10^{-18}$	parallel	intact	-

5 Discussion

5.1 Permeability of the Buntsandstein

Our permeability measurements yield values in the range of 9.2 x 10^{-18} – 6.9 x 10^{-15} m^2 (Table 2) for the measurable samples (i.e. all but the 1379 m depth core, which has a significantly lower permeability). We see a general trend of increasing permeability with porosity (Figure 8). Previous studies on porous sandstones with a connected porosity in the range of 4 % to 35 % reported permeability values in the range of 10^{-16} m^2 to 2 x 10^{-12} m^2 (Bourbié and Zinszner, 1985; David et al., 1994 ; Zhu and Wong, 1997; Vajdova et al., 2004; Baud et al., 2012). Considering the connected porosities of these samples, 8.2 – 20.7 %, this permeability range could therefore be considered low for sandstone. As mentioned above, the permeability of the samples from 1379 m depth was even not measureable using our apparatus (<10^{-18} m^2). A likely explanation for this is the prevalence of clay at all depths. SEM images, for example, show an abundance of pore-filling clays (examples shown in Figure 9). This is especially the case for the Annweiler sandstone at 1379 m depth, where the pore space is drastically diminished (Figure 9b) and clay is also visible in the fracture itself (Figure 4e) (see also Vernoux et al., 1995). This was subsequently confirmed by XRD results (Table 1) where Illite-smectite is omnipresent, notably at 1379 m depth where it occupies 20 mass% of the bulk rock. These clay minerals which appear to block the pore throats could explain the low permeability of our samples (Table 2, Figure 8). Furthermore, our permeability measurements were made using nitrogen gas as the permeant and due to the clay content in some samples, the water permeability could well be lower (Davy et al., 2007; Faulkner and Rutter, 2000; Tanikawa and Shimamoto, 2006; Tanikawa and Shimamoto, 2009). A previous study of the EPS1 Buntsandstein core measured permeability of the host rock with depth using a TinyPerm II field permeameter (which has a working range of 10^{-16} – 10^{-11} m^2) and gave values from 10^{-16} m^2 to 5 x 10^{-13} m^2 (Haffen et al., 2013). Our laboratory measurements of some samples of the Middle Buntsandstein host rock yield values within this range (Figure 6b), however all other samples were found to be less permeable, highlighting the limitations of the TinyPerm for certain units of the Buntsandstein.

We highlight that samples are 40 mm in length and 20 mm in diameter and cannot therefore take into account reservoir-scale heterogeneities such as meso and macro scale fractures. They do, on the other hand, contain fractures with apertures representative of those observed in well EPS1 (Table 2; Vernoux et al., 1995).

5.2 Permeability anisotropy of the Buntsandstein

For all samples, our XRD results show that the precipitated hydrothermal minerals seen in the fractures (Figures 2 and 4) are not present in the bulk rock (Table 1). This suggests that these fractures were once conduits for geothermal brines. However, through mineral precipitation, their permeability has likely decreased. As the fractures have a preferred orientation, striking N005° and N170° and dipping 70°W and 70°E respectively (Genter et al., 1997) the degree of permeability anisotropy within this unit may have therefore diminished over time if the sealed fractures exist on a reservoir length scale. The lack of precipitated hydrothermal minerals in the host rock of these materials suggest that the fluids utilise other channels through the fracture or switched to adjacent open or partially-sealed fractures. An extreme scenario would be where these large vertical fractures become completely sealed by precipitates and compartmentalise large scale fluid flow.

We observe an anisotropy due to bedding (see in particular Figures 7b and 7c) and that sealed or partially sealed fractures could serve to homogenise the permeability of certain layer within the Buntsandstein (Figure 10). For example, the high permeability parallel to bedding in the intact 1083 m depth Karlstal Beds samples (Figure 7b) is reduced to the lower permeability of the samples cored perpendicular to bedding in the presence of sealed fractures. These sealed fractures are effectively cancelling the anisotropy due to bedding.

Both at the core scale and in the SEM images, the extent of fracture sealing within the Buntsandstein unit is visibly variable. Indeed, (Vernoux et al., 1995), give a ratio of the free aperture per total fracture aperture of 0.2 for the entire population of fractures in the Buntsandstein. This is reflected in the permeability measurements (Figure 7), where partially sealed fractures may still act as conduits for flow (see also Neuville

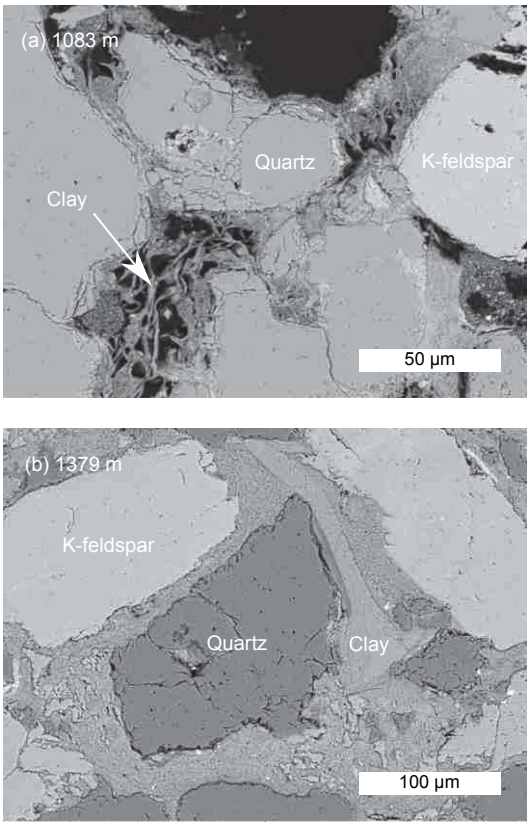

Figure 9: *SEM micrographs of thin sections of Buntsandstein EPS1 core samples from (a) 1083 m (Karlstal Beds) and (b) 1379 m depth (Annweiler sandstone). Pore-filling clays are visible in both images and in (b) they appear to occupy all the available pore space.*

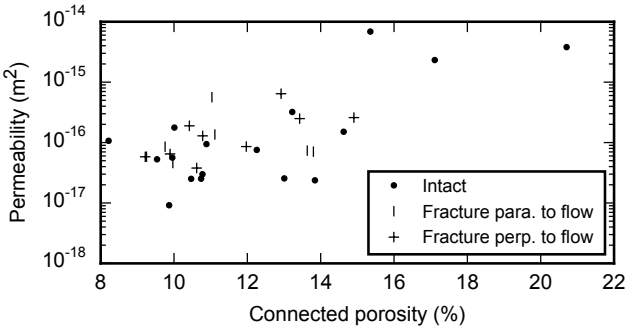

Figure 10: *Synopsis plot of permeability against porosity for all samples from 1038 m, 1083 m, 1089 m, 1092 m depth (Table 2). Data points are grouped according to the presence and orientation of fractures with regards to flow (parallel or perpendicular). The permeability of the Annweiler sandstone samples from 1379 m depth was too low to be measured with the apparatus used in this study (<10^{-18} m^2).*

et al., 2012a; Neuville et al., 2012b) Within our sample set, the extent of sealing seems to depend on the nature of the precipitate and barite precipitation seems to be the most efficient at sealing large fractures (e.g. Figure 1), as well as one of the most abundant in the core. For this reason, we chose to model the growth rate of barite crystals in a geothermal context to quantify the time required for fracture sealing.

5.3. A time scale for fracture sealing

Barite ($BaSO_4$) scaling is commonly observed in hydrocarbon reservoirs where highly concentrated brines are extracted from oil wells (Templeton, 1960). The same is true at the Soultz-sous-Forêts geothermal site, where it is abundant in the well core (Vernoux et al., 1995). Furthermore, barite is the most common precipitate in Soultz-sous-Forêts scaling and has been observed in pipes at the surface installations (Scheiber et al., 2013). Moreover, due to the extremely low solubility of barite, it requires mechanical removal (Christy and Putnis, 1993) which halts production and is both expensive and time consuming. Because of these risks, it is important to understand how quickly barite could precipitate in a geothermal context.

Strictly speaking, overall precipitation rate laws for any mineral should account for both the nucleation and growth steps (e.g. Fritz and Noguera, 2009). However, for most minerals, critical data that are required to model the nucleation step are currently missing (e.g. interfacial energy, see Fernandez-Martinez et al., 2013), such that studies aimed at modelling the precipitation rate of secondary phases often focus on the growth step, starting with an ad hoc precursor surface (see Daval et al., 2009 and references therein). A similar strategy was applied here, starting from nuclei with a size corresponding to that of a primitive cell of barite. Such a conservative choice ensures that barite precipitation rate is not artificially overestimated. The model for the crystal growth rate of barite relies on the rate equation (1), which gives the precipitation rate of barite R_T (mol/m^2/s) for a given temperature T. This is a second order rate law, characteristic of spiral growth (Christy and Putnis, 1993) and is a function of the rate constant k_T (mol/m^2/s), and Ω_T, which is the reaction quotient divided by the equilibrium constant for barite precipitation.

$$R_T = k_T(\Omega_T - 1)^2 \quad (1)$$

An Arrhenius law (2) relates the rate constant k_T to temperature. The pre-exponential factor k_0 (mol/m^2/s) and the activation energy E_a (J) were calculated using data from Christy and Putnis, 1993. R_m is the universal gas constant and T (K) is the temperature of the solution.

$$k_T = k_0 exp(-\tfrac{E_a}{R_m T}) \quad (2)$$

The values of Ω_T were calculated using the CHESS (Chemical Equilibrium of Species and Surfaces) program (Van der Lee and De Windt, 2002), which models the equilibrium state of complex aquatic systems. The chemical composition of the Soultz-sous-Forêts brine was the input for the CHESS model (Table 3, from Sanjuan et al., 2010). These data are the closest available (from well GPK1, 500 m away) to our Buntsandstein EPS1 core and are from a similar depth (1845 m). The chemical composition is sufficiently homogeneous to be assumed constant with depth (Sanjuan et al., 2010). We consider only the effect of temperature on barite precipitation, ignoring any variation in fluid composition. For hydrocarbon or geothermal reservoirs, the injection fluid (often seawater) can differ to the fluid in the reservoir. The fluid mixing of injected salty seawater, which has a high sulphate content, with in-situ barium rich hydro-geothermal fluid can encourage barite scaling (Sorbie and Mackay, 2000). In our case, sulphate concentrations are already high and therefore our model does not take fluid mixing into account.

Table 3: *Analytical fluid composition data from well GPK-1 (taken from Sanjuan et al., 2010).*

Well	GPK1-KD006
Depth (m)	1845
pH	5.02
Na (g/L)	28
K (g/L)	3.28
Ca (g/L)	7.3
Cl (g/L)	58.1
SO4 (mg/L)	220

Table 3: *Analytical fluid composition data from well GPK-1 (taken from Sanjuan et al., 2010).*

Well	GPK1-KD006
Ba (mg/L)	12.5

From the precipitation rate R_T at different temperatures (1), and assuming a spherical barite crystal, we can infer the radial growth rate (3). Here ρ and M are respectively the density and the molar mass of barite.

$$\left[\frac{\mathrm{dr}}{\mathrm{dt}}\right]_T = \frac{3MR_T}{\rho} \tag{1}$$

Figure 11 shows the modelled radial growth rate of a barite crystal against temperature. Up to 200 °C, the growth rate decreases dramatically with temperature. These results, which may seem intriguing because k_T is an intrinsic function of T, actually underline the critical role of the temperature dependence of barite solubility. They are further supported by a study by (Templeton, 1960), who finds an increase in the solubility of barite with temperature for solutions within the range of 25-95 °C. Above 200 °C, the trend inverses and we see an increase of the growth rate with temperature. We note that barite solubility has been shown to increase with pressure (Blount, 1977) so that the depressurisation of geothermal brines will also encourage precipitation.

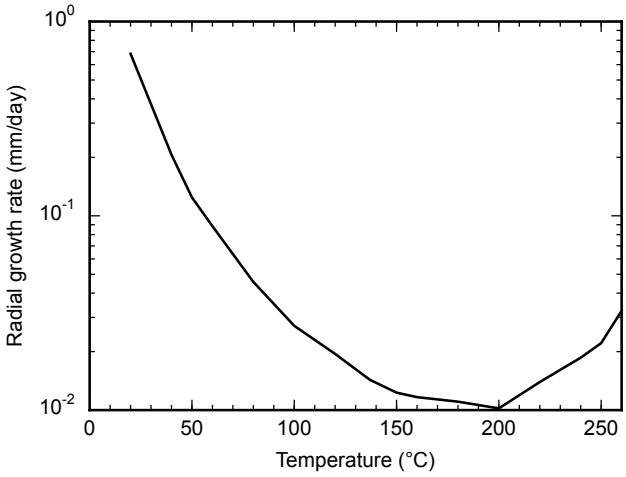

Figure 11: *The modelled barite crystal radial growth rate against temperature as calculated from Christy and Putnis, 1993. The growth rate is lowest at temperatures of around 200 °C, it then increases dramatically with decreasing temperature. The growth rate increases with temperature above 200 °C.*

5.3 Geothermal implications

As discussed above, the permeability of the host Buntsandstein is reduced due to pore-filling clays (Figure 9). When it comes to modelling fluid flow, the permeability of the Buntsandstein plays an important role at Soultz-sous-Forêts. Indeed, assigning low permeability values ($<10^{-14}$ m^2) to the Triassic sediments has been shown to inhibit the formation of fluid convection cells (Magnenet et al., 2014). Although some layers may be permeable ($>10^{-15}$ m^2), the presence of low permeability layers would suggest that for large scale convection to occur within the Buntsandstein as a whole, open or partially sealed fractures must be available to facilitate fluid flow.

The precipitation rate of barite increases dramatically with decreasing temperature (Figure 11). At the Soultz-sous-Forêts geothermal site, sulfate and sulphide scaling is particularly visible in the cold part of the surface installations where water is cooled from 160 °C to 60 °C, but scaling can even appear in the injection well (Scheiber et al., 2013). During production tests in November 2008 at Soultz-sous-Forêts, geothermal brine was extracted from the reservoir at around 155 °C and re-injected at 50 °C (Genter et al., 2009). The modelled crystal growth rate (Figure 11) would suggest that given the same composition, barite crystals will form 10 times faster from the cooler fluid (from 0.01 mm/day to 0.1 mm/day in radial growth). These calculated rates are consistent with observations at the surface installations where, in 2011, between cleaning the heat exchanger in March and opening it in September to sample scalings, a barite-celestine solid solution $(Ba,Sr)SO_4$ formed platelets of a few millimetres in thickness (Nitschke et al., 2014).

At Soultz-sous-Forêts, temperatures can reach 200 °C at 5 km depth (Genter et al., 2010) and if the saturated geothermal brine were to circulate upwards and cool, it would encourage a faster precipitation. This would be especially true if deep geothermal fluids were to reach 1 km depth, above which the thermal gradient is much higher than the 5 °C/km measured between 1.5 and 3.5 km depth. Within the Buntsandstein, the fluid temperature is around 130 °C and at this temperature, the model gives a radial growth rate of barite crystals to be around 1.5 x 10^{-2} mm/day. To better understand the typical radius of a barite crystal, we used polarised light microscopy to distinguish the crystal orientation of individual barite crystals in the thin section from 1092 m depth (Figure 4d). We found they each span roughly 1 mm across the fracture aperture, i.e. for the spherical model they have an equivalent radius of around 0.5 mm. In this case, at a radial growth rate of 1.5 x 10^{-2} mm/day, a 2 mm wide (the average fracture aperture of the Buntsandstein, Table 2; (Vernoux et al., 1995)) fracture could seal in around 1 month, well within the 20-50 year lifetime of a producing geothermal site. We note that this simple model does not take into account the spatial variablility of the precipitation rate due to the channeling of flow (Méheust and Schmittbuhl, 2001). Despite of these short sealing time scales, open and partially sealed fractures are still observed in the Buntsandstein, this could be explained by slip along fractures, keeping permeable pathways open.

Since fractures are influence fluid flow in the reservoir, as well as ensuring its hydraulic connection to the injection well, mineral precipitation could therefore have a large impact on geothermal production. The precipitation rate is a function of the temperature and composition of the injected fluids which could be manipulated if required. The addition of chemical precipitation inhibitors to the injection fluid is also an efficient, but expensive, solution (e.g. Scheiber et al., 2013).

6 Conclusion

Generally speaking, open fractures are thought to affect the permeability and permeability anisotropy of geothermal reservoirs. In particular, the Triassic Buntsandstein sandstone (1–1.4 km depth), an important unit for regional fluid flow at Soultz-sous-Forêts, exhibits a dense fracture network. Microstructural observations of selected Buntsandstein core samples show how these fractures are variably sealed by precipitated minerals and therefore their influence on fluid flow is less predictable. We quantified, through new porosity and permeability measurements, the hydraulic properties of the Buntsandstein. As a result of pore-filling clays, the values of permeability of the host rock were lower than we expected based on porosity and permeability data on similarly porous sandstones. We found that the presence of low permeability sealed fractures can homogenise the permeability anisotropy (for example due to bedding), although we highlight that at the reservoir scale, fluids may find new vertical pathways through remaining open or partially-sealed fractures. These results highlight the importance of mineral precipitation at a geothermal site, as well injectivity and regional fluid flow depend on a reliable network of permeable fractures. To look at the time scale for sealing, we specifically targeted the precipitation of barite, seen at Soultz-sous-Forêts and in many other hydro-geothermal contexts worldwide. Our model takes into account the Soultz-sous-Forêts geothermal fluid composition and gives the precipitation rate of barite as a function of temperature, showing it to decrease as the geothermal fluid cools. Between the temperatures at the extraction well (~150 °C) and the re-injection well (~50 °C), the modelled crystal growth rate increases by an order of magnitude. Within the Buntsandstein, at around 130 °C, the radial growth rate of barite crystals is predicted to be around 10^{-2} mm/day meaning that the permeability of

a geothermal reservoir around the injection well could vary greatly over the course of production.

7 Acknowledgements

The authors would like to thank GEIE Exploitation Minière de Chaleur for providing the Soultz core samples and relevant information; Bertrand Renaudié for sample preparation; Gilles Morvan for his SEM assistance; and Jamie Farquharson and Alex Kushnir for the development and maintenance of the permeameter. The authors acknowledge the support of the French Agence Nationale de la Recherche (ANR), under grant ANR-ANR-15-CE06-0014-01 (project CANTARE). This work has been published under the framework of LABEX grant ANR-11-LABX-0050_G-EAU-THERMIE-PROFONDE and therefore benefits from state funding managed by the Agence National de la Recherche (ANR) as part of the "Investissements d'avenir" program.

8 References

Ball, J.L., Stauffer, P.H., Calder, E.S., Valentine, G.A., 2015. The hydrothermal alteration of cooling lava domes. Bull. Volcanol. 77. doi:10.1007/s00445-015-0986-z

Baria, R., Baumgärtner, J., Gérard, A., Jung, R., Garnish, J., 1999. European HDR research programme at Soultz-sous-Forêts (France) 1987-1996. Geothermics 28, 655–669. doi:10.1016/s0375-6505(99)00036-x

Baud, P., Meredith, P., Townend, E., 2012. Permeability evolution during triaxial compaction of an anisotropic porous sandstone. J. Geophys. Res. Solid Earth 117, B05203. doi:10.1029/2012JB009176

Blount, C.W., 1977. Barite solubilities and thermodynamic quantities up to 300 degrees C and 1400 bars. Am. Mineral. 62, 942–957.

Bourbié, T., Zinszner, B., 1985. Hydraulic and acoustic properties as a function of porosity in Fontainebleau Sandstone. J. Geophys. Res. Solid Earth 90, 11524–11532. doi:10.1029/JB090iB13p11524

Christy, A.G., Putnis, A., 1993. The kinetics of barite dissolution and precipitation in water and sodium chloride brines at 44–85°C. Geochim. Cosmochim. Acta 57, 2161–2168. doi:10.1016/0016-7037(93)90557-D

Daval, D., Martinez, I., Corvisier, J., Findling, N., Goffé, B., Guyot, F., 2009. Carbonation of Ca-bearing silicates, the case of wollastonite: Experimental investigations and kinetic modeling. Chem. Geol., CO2 geological storage: Integrating geochemical, hydrodynamical, mechanical and biological processes from the pore to the reservoir scale 265, 63–78. doi:10.1016/j.chemgeo.2009.01.022

David, C., Wong, T.-F., Zhu, W., Zhang, J., 1994. Laboratory measurement of compaction-induced permeability change in porous rocks: Implications for the generation and maintenance of pore pressure excess in the crust. Pure Appl. Geophys. 143, 425–456. doi:10.1007/BF00874337

Davy, C.A., Skoczylas, F., Barnichon, J.-D., Lebon, P., 2007. Permeability of macro-cracked argillite under confinement: gas and water testing. Phys. Chem. Earth Parts ABC 32, 667–680.

Dezayes, C., Genter, A., Valley, B., 2010. Structure of the low permeable naturally fractured geothermal reservoir at Soultz. Comptes Rendus Geosci. 342, 517–530. doi:10.1016/j.crte.2009.10.002

Faulkner, D.R., Rutter, E.H., 2000. Comparisons of water and argon permeability in natural clay-bearing fault gouge under high pressure at 20 C. J Geophys Res 105, 415–16.

Fernandez-Martinez, A., Hu, Y., Lee, B., Jun, Y.-S., Waychunas, G.A., 2013. In Situ Determination of Interfacial Energies between Heterogeneously Nucleated CaCO3 and Quartz Substrates: Thermodynamics of CO2 Mineral Trapping. Environ. Sci. Technol. 47, 102–109. doi:10.1021/es3014826

Fritz, B., Noguera, C., 2009. Mineral Precipitation Kinetics. Rev. Mineral. Geochem. 70, 371–410. doi:10.2138/rmg.2009.70.8

Genter, A., Castaing, C., Dezayes, C., Tenzer, H., Traineau, H., Villemin, T., 1997. Comparative analysis of direct (core) and indirect (borehole imaging tools) collection of fracture data in the Hot Dry Rock Soultz reservoir (France). J. Geophys. Res. 102, 15419–15419. doi:10.1029/97JB00626

Genter, A., Evans, K., Cuenot, N., Fritsch, D., Sanjuan, B., 2010. Contribution of the exploration of deep crystalline fractured reservoir of Soultz to the knowledge of enhanced geothermal systems (EGS). Comptes Rendus Geosci., Vers l'exploitation des ressources géothermiques profondes des systèmes hydrothermaux convectifs en milieux naturellement fracturésOn the way to the exploitation of deep geothermal resources in naturally fractured environments 342, 502–516. doi:10.1016/j.crte.2010.01.006

Genter, A., Fritsch, D., Cuenot, N., Baumgärtner, J., Graff, J.-J., 2009. Overview of the current activities of the European EGS Soultz project: from exploration to electricity production, in: Proceedings, 34th Workshop on Geothermal Reservoir Engineering, Standford University, Stanford, California, USA. pp. 9–11.

Genter, A., Traineau, H., 1996. Analysis of macroscopic fractures in granite in the HDR geothermal well EPS-1, Soultz-sous-Forêts, France. J. Volcanol. Geotherm. Res. 72, 121–141. doi:10.1016/0377-0273(95)00070-4

Gérard, A., Genter, A., Kohl, T., Lutz, P., Rose, P., Rummel, F., 2006. The deep EGS (Enhanced Geothermal System) project at Soultz-sous-Forêts (Alsace, France). Geothermics 35, 473–483. doi:10.1016/j.geothermics.2006.12.001

Grant, M.A., Bixley, P.F., 2011. Geothermal reservoir engineering, 2nd ed. ed. Academic Press, Burlington, MA.

Guillou-Frottier, L., Carrè, C., Bourgine, B., Bouchot, V., Genter, A., 2013. Structure of hydrothermal convection in the Upper Rhine Graben as inferred from corrected temperature data and basin-scale numerical models. J. Volcanol. Geotherm. Res. 256, 29–49. doi:10.1016/j.jvolgeores.2013.02.008

Haffen, S., Geraud, Y., Diraison, M., Dezayes, C., 2013. Determination of fluid-flow zones in a geothermal sandstone reservoir using thermal conductivity and temperature logs. Geothermics 46, 32–41. doi:10.1016/j.geothermics.2012.11.001

Kappelmeyer, O., Gerard, A., 1989. The European geothermal project at Soultz-sous-Forêts, in: IB Ramberg and E. R. Neu-Mann, Eds., The European Geothermal Update: Proceedings of the Fourth International Seminar on the Results of EC Geothermal Energy Research and Demonstration. pp. 285–554.

Ledésert, B., Dubois, J., Genter, A., Meunier, A., 1993. Fractal analysis of fractures applied to Soultz-sous-Forets hot dry rock geothermal program. J. Volcanol. Geotherm. Res. 57, 1–17. doi:10.1016/0377-0273(93)90028-P

Magnenet, V., Fond, C., Genter, A., Schmittbuhl, J., 2014. Two-dimensional THM modelling of the large scale natural hydrothermal circulation at Soultz-sous-Forêts. Geotherm. Energy 2. doi:10.1186/s40517-014-0017-x

McNamara, D.D., Lister, A., Prior, D.J., 2016. Calcite sealing in a fractured geothermal reservoir: Insights from combined EBSD and chemistry mapping. J. Volcanol. Geotherm. Res. 323, 38–52. doi:10.1016/j.jvolgeores.2016.04.042

Méheust, Y., Schmittbuhl, J., 2001. Geometrical heterogeneities and permeability anisotropy of rough fractures. J. Geophys. Res. Solid Earth 106, 2089–2102. doi:10.1029/2000JB900306

Neuville, A., Toussaint, R., Schmittbuhl, J., 2012a. Fracture aperture reconstruction and determination of hydrological properties: a case study at Draix (French Alps). Hydrol. Process. 26, 2095–2105. doi:10.1002/hyp.7985

Neuville, A., Toussaint, R., Schmittbuhl, J., Koehn, D., Schwarz, J.-O., 2012b. Characterization of major discontinuities from borehole cores of the black consolidated marl formation of Draix (French Alps). Hydrol. Process. 26, 2085–2094. doi:10.1002/hyp.7984

Pribnow, D., Clauser, C., 2000. Heat and fluid flow at the Soultz hot dry rock system in the Rhine Graben, in: World Geothermal Congress, Kyushu-Tohoku, Japan. pp. 3835–3840.

Sanjuan, B., Millot, R., Dezayes, C., Brach, M., 2010. Main characteristics of the deep geothermal brine (5 km) at Soultz-sous-Forêts (France) determined using geochemical and tracer test data. Comptes Rendus Geosci. 342, 546–559. doi:10.1016/j.crte.2009.10.009

Sausse, J., Dezayes, C., Dorbath, L., Genter, A., Place, J., 2010. 3D model of fracture zones at Soultz-sous-Forêts based on geological data, image logs, induced microseismicity and vertical seismic profiles. Comptes Rendus Geosci., Vers l'exploitation des ressources géothermiques profondes des systèmes hydrothermaux convectifs en milieux naturellement fracturés. On the way to the exploitation of deep geothermal resources in naturally fractured environments 342, 531–545. doi:10.1016/j.crte.2010.01.011

Scheiber, J., Seibt, A., Birner, J., Genter, A., Moeckes, W., 2013. Application of a Scaling Inhibitor System at the Geothermal Power Plant in Soultz-sous-Forêts: Laboratory and On-Site Studies, in: Proceedings, European Geothermal Congress 2013.

Sizun, J.-P., 1995. Modification des structures de porosité de grès lors de transformations petrographiques dans la diagenèse et l'hydrothermalisme. Université Louis Pasteur, Strasbourg, France., Institut de Geologie Strasbourg.

Sorbie, K.S., Mackay, E.J., 2000. Mixing of injected, connate and aquifer brines in waterflooding and its relevance to oilfield scaling. J. Pet. Sci. Eng. 27, 85–106. doi:10.1016/S0920-4105(00)00050-4

Surma, F., Géraud, Y., 2003. Porosity and Thermal Conductivity of the Soultz-sous-Forêts Granite, in: Kümpel, H.-J. (Ed.), Thermo-Hydro-Mechanical Coupling in Fractured Rock, Pageoph Topical Volumes. Birkhäuser Basel, pp. 1125–1136.

Tanikawa, W., Shimamoto, T., 2009. Comparison of Klinkenberg-corrected gas permeability and water permeability in sedimentary rocks. Int. J. Rock Mech. Min. Sci. 46, 229–238.

Tanikawa, W., Shimamoto, T., 2006. Klinkenberg effect for gas permeability and its comparison to water permeability for porous sedimentary rocks. Hydrol. Earth Syst. Sci. Discuss. 3, 1315–1338.

Templeton, C.C., 1960. Solubility of Barium Sulfate in Sodium Chloride Solutions from 25° to 95° C. J. Chem. Eng. Data 5, 514–516. doi:10.1021/je60008a028

Vajdova, V., Baud, P., Wong, T., 2004. Permeability evolution during localized deformation in Bentheim sandstone. J. Geophys. Res. Solid Earth 109, B10406. doi:10.1029/2003JB002942

Van der Lee, J., De Windt, L., 2002. Chess tutorial and Cookbook (Updated for version 3.0). Eds ENSMP-CIG LHMRD0213.

Vernoux, J.F., Genter, A., Razin, P., Vinchon, C., BRGM, O., BRGM, N.-P. de C., 1995. Geological and petrophysical parameters of a deep fractured sandstone formation as applied to geothermal exploitation. BRGM Rep. 38622, 70.

Vidal, J., Genter, A., Schmittbuhl, J., 2015. How do permeable fractures in the Triassic sediments of Northern Alsace characterize the top of hydrothermal convective cells? Evidence from Soultz geothermal boreholes (France). Geotherm. Energy 3. doi:10.1186/s40517-015-0026-4

Zhu, W., Wong, T. -f., 1997. The transition from brittle faulting to cataclastic flow: Permeability evolution. J. Geophys. Res. 102, 3027–3027. doi:10.1029/96JB03282

The influence of pore geometry and orientation on the strength and stiffness of porous rock

Luke Griffiths[1], Michael J. Heap[1], Tao Xu[2], Chong-feng Chen[2], and Patrick Baud[1]

[1] *Institut de Physique de Globe de Strasbourg, Université de Strasbourg/EOST, CNRS UMR 7516, France.*

[2] *Center for Rock Instability and Seismicity Research, Northeastern University, Shenyang 110819, China.*

Corresponding authors: L. Griffiths (luke.griffiths@unistra.fr) and M. Heap (heap@unistra.fr)

https://doi.org/10.1016/j.jsg.2017.02.006

Abstract

The geometry of voids in porous rock fall between two end-members: very low aspect ratio (the ratio of the minor to the major axis) microcracks and perfectly spherical pores with an aspect ratio of unity. Although the effect of these end-member geometries on the mechanical behaviour of porous rock has received considerable attention, our understanding of the influence of voids with an intermediate aspect ratio is much less robust. Here we perform two-dimensional numerical simulations (Rock Failure Process Analysis, $RFPA_{2D}$) to better understand the influence of pore aspect ratio (from 0.2 to 1.0) and the angle between the pore major axis and the applied stress (from 0 to 90°) on the mechanical behaviour of porous rock under uniaxial compression. Our numerical simulations show that, for a fixed aspect ratio (0.5) the uniaxial compressive strength and Young's modulus of porous rock can be reduced by a factor of ~2.4 and ~1.3, respectively, as the angle between the major axis of the elliptical pores and the applied stress is rotated from 0 to 90°. The influence of pore aspect ratio on strength and Young's modulus depends on the pore angle. At low angles (~0-10°) an increase in aspect ratio reduces the strength and Young's modulus. At higher angles (~40-90°), however, strength and Young's modulus increase as aspect ratio is increased. At intermediate angles (~20-30°), strength and Young's modulus first increase and then decrease as pore aspect ratio approaches unity. These simulations also highlight that the influence of pore angle on compressive strength and Young's modulus decreases as the pore aspect ratio approaches unity. We find that the analytical solution for the stress concentration around a single elliptical pore, and its contribution to elasticity, are in excellent qualitative agreement with our numerical simulations. The results of our numerical modelling are also in agreement with recent experimental data for porous basalt, but fail to capture the strength anisotropy observed in experiments on sandstone. We conclude that the alignment of grains or platy minerals such as clays exerts a greater influence on strength anisotropy in porous sandstones than pore geometry. Finally, we show that the strength anisotropy that arises as a result of preferentially aligned elliptical pores is of a similar magnitude to that generated by bedding in porous sandstones and foliation in low-porosity metamorphic rocks The modelling presented herein shows that porous rocks containing elliptical pores can display a strength and stiffness anisotropy, with implications for the preservation and destruction of porosity and permeability, as well as the distribution of stress and strain within the Earth's crust.

Keywords: Aspect ratio; pore angle; porosity; Young's modulus; uniaxial compressive strength; numerical modelling

Highlights

- Rock strength and stiffness are reduced as pore angle is rotated from 0 to 90°.
- Influence of pore aspect ratio on strength and stiffness depends on the pore angle.
- Influence of pore angle on strength and stiffness decreases as the pore aspect ratio approaches unity.
- We compare strength anisotropy as a result of bedding, foliation, and pore geometry.

- Pore geometry and orientation emerges as an important metric for a range of geoscience disciplines.

1 Introduction

Most rocks contain porosity in the form of pores, microcracks, or a combination of the two. Porosity is known to exert a first-order control on the physical properties of rocks. For example, with increasing porosity, strength (e.g., Al-Harthi et al., 1999; Chang et al., 2006; Zhu et al., 2011; Baud et al., 2014; Schaefer et al., 2015) and Young's modulus (e.g., Chang et al., 2006) decrease and permeability increases (e.g., Bourbié and Zinszner, 1985; Farquharson et al., 2015). These studies have shown that porosity alone does not control the mechanical and hydraulical behaviour of rocks, highlighting an important role for the geometry of the void space (e.g., Chang et al., 2006; Farquharson et al., 2015). The aspect ratio (the ratio of the minor to major semi axis) of an elliptical void within a rock will fall between two end-members: microcracks that have a very low aspect ratio (10^{-3} – 10^{-5}, Simmons and Richter, 1976) and perfectly spherical pores with an aspect ratio of unity. Indeed, recent advances in X-ray micro-computed tomography (μCT) have shown that porous rocks contain a wide variety of pore shapes (e.g., Ji et al., 2012; Rozenbaum and Rolland du Roscat, 2014; Ji et al., 2015; Schmitt et al., 2016; Luquot et al., 2016; Bubeck et al., 2017).

Although two-dimensional micromechanical and numerical models exist to help understand the influence of uniformly aligned microcracks (e.g., Ashby and Sammis, 1990) and circular pores (e.g., Sammis and Ashby, 1986; Heap et al., 2014) on the mechanical behaviour of porous materials, including rocks, much less is known as to the influence of voids with an intermediate aspect ratio. A recent experimental study has shown, using uniaxial compressive strength tests, that basalt samples containing elliptical pores (aspect ratio ≈ 0.5) oriented with their major axis perpendicular to the loading direction were measurably weaker than those prepared to contain pores with their major axis parallel to loading (Bubeck et al., 2017). Although this study offers insight into the influence of non-spherical pores on mechanical behaviour, it remains challenging to isolate the influence of a specific parameter (e.g., pore aspect ratio, pore orientation with regards to the loading direction, and porosity) using natural samples, a consequence of their inherent variability. To circumvent natural variability, we use here a numerical modelling approach to isolate the role of select pore geometrical parameters (pore aspect ratio and pore orientation) on the compressive strength and Young's modulus of porous materials. We report on the results of numerical simulations, using the two-dimensional Rock Failure Process Analysis code ($RFPA_{2D}$; Tang, 1997), in which we uniaxially deform rectangular samples populated with elliptical pores. Samples were built to contain different porosities (from 0.02 to 0.2), pore aspect ratios (from 0.2 to 1.0), and angles between the pore major axis and the loading direction (from 0 to 90°). Finally, the results of the $RFPA_{2D}$ modelling are compared with two-dimensional analytical solutions for the stress concentration around a single elliptical pore (from Jaeger et al., 2009) the contribution of the elliptical pore to the Young's modulus (from Kachanov et al., 1994). We also compare our modelled results with new and previously published experimental data (basalt, sandstone, and limestone), and compare the strength anisotropy generated by the preferential alignment of elliptical pores, bedding in porous sandstones, and foliation in low-porosity metamorphic rocks.

2 Description of numerical simulations

The two-dimensional Rock Failure Process Analysis code ($RFPA_{2D}$) is a numerical model based on elastic damage mechanics (Tang, 1997). We used the model to uniaxially deform 400 × 200 pixel rectangular bitmap images that contained elliptical pores with a major axis of 20 pixels in length (Figure 1). Considering a resolution of 0.1 mm/pixel, the images are analogous to rectangular samples 40 mm in length and 20 mm in width containing elliptical pores with a major axis of 2 mm. These samples were generated using a MATLAB script. To generate a bitmap image, we first selected a fixed pore aspect ratio (the ratio of the minor to major semi axis) and a fixed pore angle, β, (the angle measured from the vertical long axis of the rectangle and the major axis of the elliptical pore in a clockwise manner). We then iteratively added pores to the

image in random locations until the target porosity was met. Pores were not allowed to overlap, although they could intersect the boundary of the image (Figure 1). Each 0.1 mm square element was assigned a Young's modulus (E) and a value of compressive ($\sigma_{\rm cr}$) and tensile ($\sigma_{\rm tr}$) strength. The pores were considered to have zero strength and Young's modulus, whilst the elements comprising the matrix were assigned values of strength and Young's modulus using a Weibull probability density function (Weibull, 1951; Wong et al., 2006):

$$x\left(u\right) = \frac{m}{u_0}\left(\frac{u}{u_0}\right)^{m-1}\exp\left[-\left(\frac{u}{u_0}\right)^{m}\right] \qquad (1)$$

where $x\left(u\right)$ is $\sigma_{\rm cr}\left(u\right)$, $\sigma_{\rm tr}\left(u\right)$, or $E\left(u\right)$, and u and u_0 are respectively the scale parameter of an individual element and the scale parameter of the average element (given in Table 1), respectively. We chose a matrix homogeneity factor m—the Weibull shape parameter—of 3 for all of our simulations. High values of m will yield more homogeneous samples (the property of a particular element will be closer to the chosen mean), and vice-versa (see Xu et al., 2012). Examples of the distribution (given by Equation 1) of Young's modulus (E) and uniaxial compressive strength ($\sigma_{\rm cr}$) are provided in Figure 2 (for a sample containing 80,000 elements, $m = 3$, and the matrix element properties given in Table 1). Our matrix element properties (Table 1) and homogeneity factor ($m = 3$) are the same as those used in the recent publications of Heap et al. (2014; 2015a; 2016). Although, for example, the mean uniaxial compressive strength on the microscale appears high (Table 1), the homogeneity factor ensures that the elements within the sample contain a wide range of values (Figure 2 shows that element compressive strength varies from ~100 to ~4500 MPa), similar to the microscale heterogeneities expected within a natural sample. Due to these microscale heterogeneities, the macroscopic strength is much less than the mean strength of an element on the microscale. Indeed, a sample containing zero porosity, using the mean microscale values in Table 1 and $m = 3$, has a uniaxial compressive strength of 553 MPa (Heap et al., 2014), a value similar to that of porosity-free borosilicate glass (Vasseur et al., 2013).

Table 1: *The mean physical and mechanical properties of the matrix elements (i.e., the 0.1 mm squares that form the sample) used in the Rock Failure Process Analysis code (RFPA$_{2D}$) numerical modelling. The value assigned to each element was determined using the Weibull probability function (Equation 1; see Figure 2). The matrix element properties are the same as those used in the recent publications of Heap et al. (2014; 2015a; 2016).*

Homogeneity index	3
Mean uniaxial compressive strength (MPa)	2300
Mean Young's modulus (GPa)	100
Poisson's ratio	0.25
Ratio of compressive to tensile strength	10
Frictional angle (°)	30

The rectangular samples were deformed uniaxially ($\sigma_1 > \sigma_2 = \sigma_3 = 0$) in compression in 0.002 mm increments parallel to their vertical long axes. Following the first displacement increment, the axial stress, σ, acting on each 0.1 mm element was calculated using a linear elastic constitutive law:

$$\sigma = E_0\left(1 - D\right)\varepsilon \qquad (2)$$

where D is the isotropic damage variable and ε is the axial strain. An element was considered damaged if one of two strength criteria were met, the maximum tensile strain criterion (Figure 3):

$$D = \begin{cases} 0 & \varepsilon_{t0} < \varepsilon < 0 \\ 1 - \frac{\sigma_{\rm tr}}{\varepsilon E_0} & \varepsilon_{\rm tu} \leq \varepsilon < \varepsilon_{t0} \\ 1 & \varepsilon_{\rm tu} < \varepsilon \end{cases} \qquad (3)$$

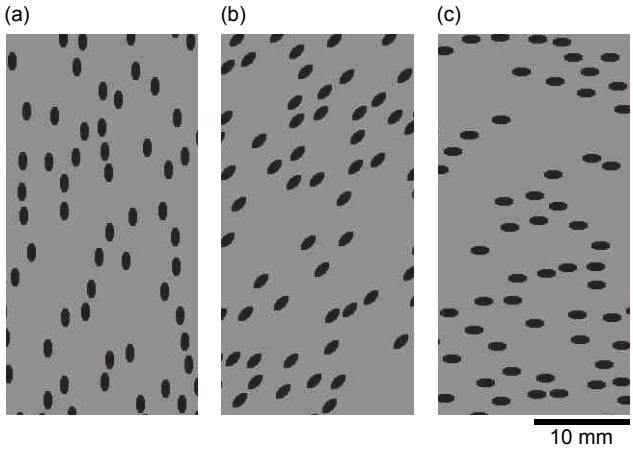

Figure 1: *Examples of randomly generated numerical samples containing a porosity of 0.1 and elliptical pores with an aspect ratio of 0.5. Samples are rectangular bitmap images (400 × 200 pixels; 40 × 20 mm) containing elliptical pores with a major axis of 20 pixels in length (i.e., 2 mm). The angles between the vertical long axis of the rectangular sample (i.e., the loading direction) and the major axis of the elliptical pore, β, are (a) 0°, (b) 45°, and (c) 90°.*

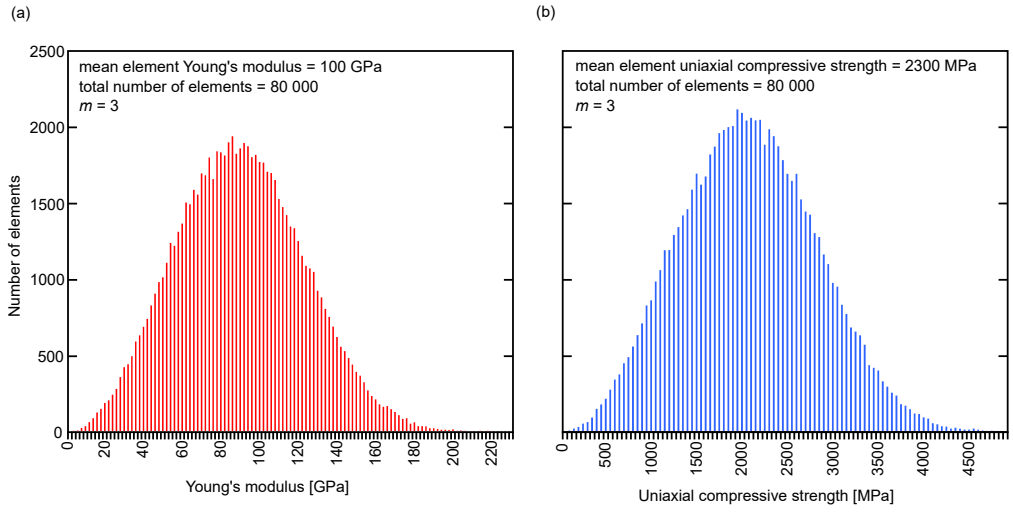

Figure 2: *Examples of the distribution of (a) Young's modulus and (b) uniaxial compressive strength for a sample with the mean element physical and mechanical properties given in Table 1 and a Weibull shape factor* m *= 3 (the homogeneity factor). The sample contains 80,000 elements.*

and the Mohr-Coulomb criterion (Figure 3):

$$D = \begin{cases} 0 & 0 < \varepsilon \ < \varepsilon_{c0} \\ 1 - \frac{\sigma_{cr}}{\varepsilon E_0} & \varepsilon_{c0} \leq \varepsilon \end{cases} \qquad (4)$$

Fig. 3 shows the axial stress against axial strain for an individual element, calculated from Eq. (3) using values of D from Eqs. (3) and (4). The ultimate tensile (extensional) strain of the element is given as $\varepsilon_{\mathrm{tu}}$ (Figure 3). Further, $\sigma_{\mathrm{tr}} = \ \lambda\sigma_{t0}$, where λ is the residual strength coefficient, and σ_{t0} is the uniaxial tensile strength at the elastic strain limit ε_{t0} (Figure 3). The residual uniaxial compressive strength σ_{cr} is defined as $\sigma_{\mathrm{cr}} = \ \lambda\sigma_{c0}$, where λ is the residual strength coefficient, and σ_{c0} is the uniaxial compressive strength at the elastic strain limit ε_{c0} (Figure 3). If an element was damaged, its Young's modulus was modified according to the elastic damage constitutive law (Lemaitre and Chaboche, 1994):

$$E = E_0 \, (1 - D) \qquad (5)$$

where E_0 is the Young's modulus of the damaged element. A Young's modulus of 1.0×10^{-5} GPa was assigned to any element for which $D = 1$ to prevent the system of equations from being ill-posed. If no elements were damaged following the displacement increment (i.e., Equations (3) and (4) were not satisfied), the sample was subjected to the next 0.002 mm displacement increment. If a number of elements were damaged, the stress acting on each element within the sample was recalculated using Equation (2). This process continued until only very few elements were damaged during the calculation step, at which point the sample was subjected to the next 0.002 mm displacement increment. The simulation was halted once the sample had succumbed to macroscopic failure (the formation of a throughgoing fracture). During the simulations, the elements within the modelled sample are fixed in the vertical direction, but can move freely in the horizontal direction (as is the case for uniaxial compressive strength experiments in the laboratory). A flow chart detailing the modelling procedure is given as Figure 4.

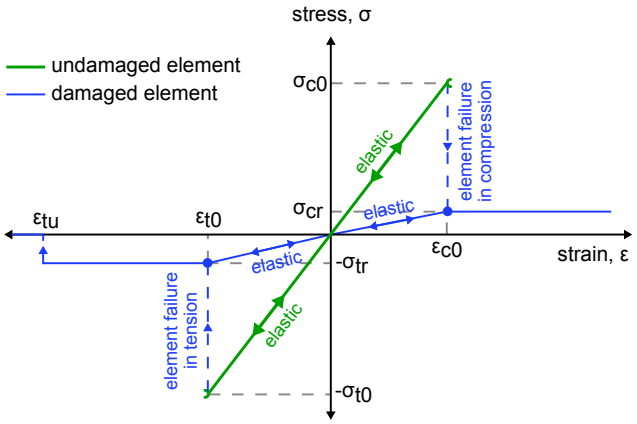

Figure 3: *A schematic axial stress-strain curve for an element under uniaxial compressive and tensile stress, as calculated from the elastic damage constitutive law (Eq. 2). The thick green line represents the axial stress-strain curve of the undamaged element in the elastic regime. The element may become damaged if it is deformed to a critical strain in tension or compression (see Eqs. (3) and (4)). The thinner blue line represents the axial stress-strain curve of the damaged element. (For interpretation of the references to colour in this figure, the reader is referred to the web version of this article.)*

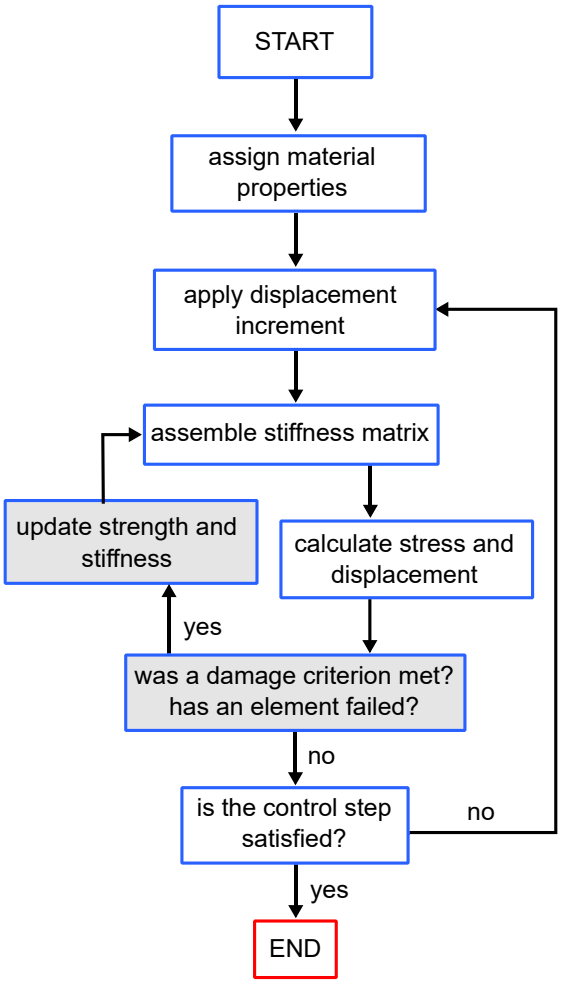

Figure 4: *A flow chart outlining the procedure for the Rock Failure Process Analysis ($RFPA_{2D}$) code numerical model.*

3 Results

3.1 Pore angle as a control on mechanical behaviour

To investigate the influence of the angle between the pore major axis and the applied stress, β, on the compressive strength and Young's modulus, we performed 24 simulations in which we varied the pore angle (β = 0-90°) but kept the porosity (0.1) and pore aspect ratio (0.5) constant (Figure 5). We performed at least two simulations for each sample configuration, the results of which differ slightly due to the random placement of pores within the generated sample (using our MATLAB script) and the fact that the elements are assigned their physical properties based on the Weibull probability density function shown in Equation (1). The simulations show that the uniaxial compressive strength and Young's modulus decrease from ~225 to ~100 MPa and from ~67 to ~50 GPa, respectively, as the angle between the pore major axis and the loading direction, β, increases from 0 to 90° (Figure 5).

To understand the influence of pore angle on the mechanical behaviour of samples containing different porosities, we performed an additional 24 simulations in which we varied the porosity (from 0.02 to 0.2) and pore angle (β = 0, 45, and 90°) for a fixed pore aspect ratio of 0.5 (Figure 6). We performed at least two simulations for each sample configuration. The relative reduction in strength as the pore angle is increased from 0 to 90° remains essentially constant at porosities between 0.02 and 0.2 (Figure 6a). However, our simulations show that the relative reduction in Young's modulus with increasing pore angle is greater when the porosity is higher (Figure 6b). For example, Young's modulus is only reduced from ~80 to ~74 GPa as pore angle, β, is increased from 0 to 90° at a porosity of 0.02, but is reduced from ~54 to 30 GPa at a porosity of 0.2 (Figure 6b).

3.2 Pore aspect ratio as a control on mechanical behaviour

To investigate the influence of the pore aspect ratio on compressive strength and Young's modulus, we performed over a hundred numerical simulations in which we varied the aspect ratio (from 0.2 to 1.0) and pore angle (β = 0-90°), but kept the porosity fixed at 0.1 (Figure 7). We performed at least two simulations for each sample configuration. Our simulations show that the influence of pore aspect ratio (from 0.2 to 1.0) on strength and Young's modulus depends on the pore angle. For low angles (β = 0-10°) an increase in aspect ratio results in reductions to strength and Young's modulus (Figure 7). For higher angles (β = 40-90°) between the pore major axis and the loading direction, strength and Young's modulus increase with increasing aspect ratio (Figure 7). At intermediate angles (β = 20-30°), strength and Young's modulus first increase and then decrease as pore aspect ratio is increased (Figure 7). Pore aspect ratio also controls the magnitude of the difference in compressive strength and Young's modulus as pore angle, β, increases. For example, strength decreases from ~225 to ~100 MPa (a decrease of about a factor of two) as the angle, β, increases from 0 to 90° for an aspect ratio of 0.5 (the results shown in Figure 5). However, for an aspect ratio of 0.2, strength decreases from ~350 to ~50 MPa (a decrease of a factor of seven) for the same increase in angle, β (Figure 7). The influence of pore angle, β, on compressive strength and Young's modulus decreases as the pore aspect ratio approaches unity (Figure 7).

4 Discussion

4.1 Comparison with analytical solutions for stress and strain around a single elliptical pore

Our numerical simulations show that the geometry and orientation of elliptical pores influences the strength and Young's modulus at the sample lengthscale (Figures 5, 6, and 7). In the following section, we aim to provide a qualitative explanation for these results using existing analytical solutions for the stress concentration around a single elliptical pore, and its contribution to elasticity. Since these solutions are for a single pore, they

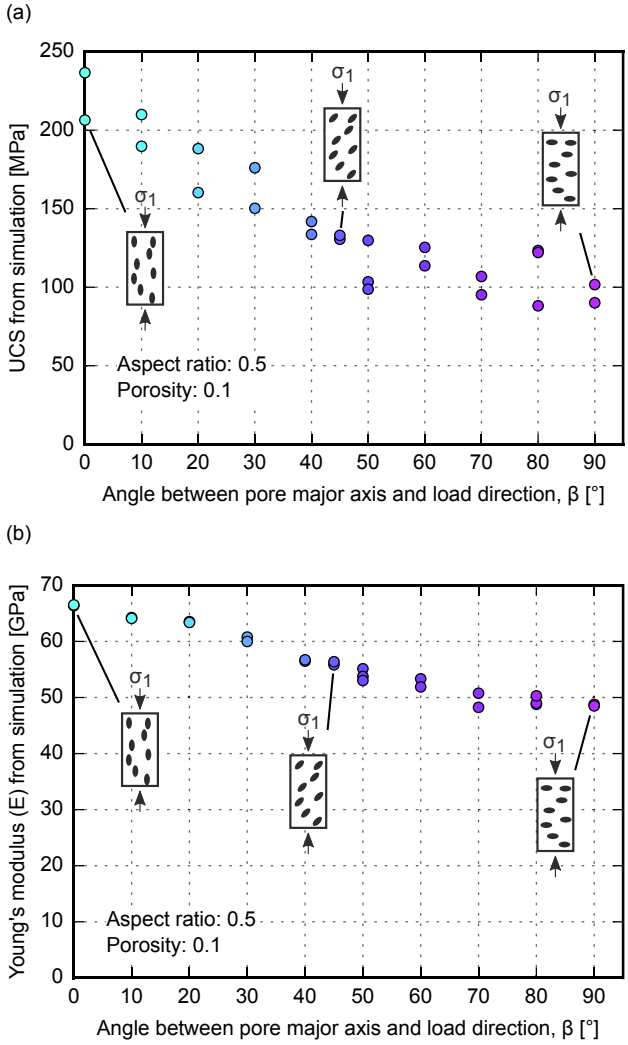

Figure 5: *The results of the Rock Failure Process Analysis ($RFPA_{2D}$) code numerical modelling for (a) UCS and (b) Young's modulus as a function of the angle between the vertical long axis of the rectangular sample (i.e., the loading direction) and the major axis of the elliptical pore, β. The 2D numerical samples have a porosity of 0.1 and contain pores 2 mm in length with an aspect ratio of 0.5. (For interpretation of the references to colour in this figure, the reader is referred to the web version of this article.)*

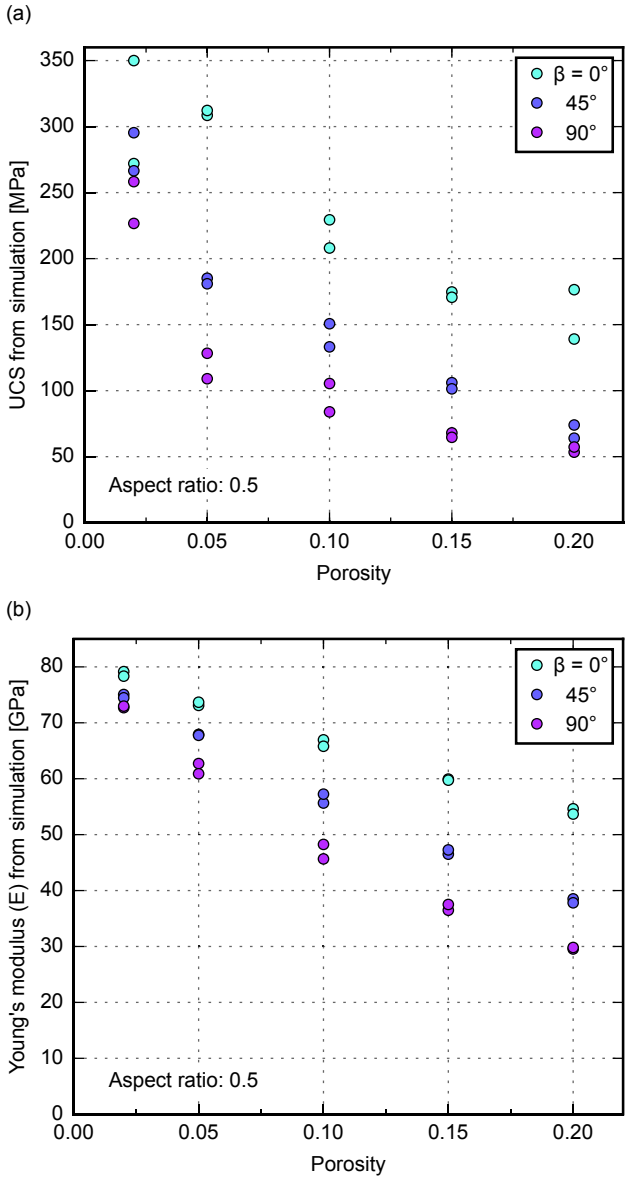

Figure 6: *The results of the Rock Failure Process Analysis ($RFPA_{2D}$) code numerical modelling for (a) UCS and (b) Young's modulus as a function of porosity for samples containing elliptical pores of 2 mm length and 0.5 aspect ratio, with major axes at angles of 0, 45, and 90° to the vertical long axis of the rectangular sample (i.e., the loading direction). (For interpretation of the references to colour in this figure, the reader is referred to the web version of this article.*

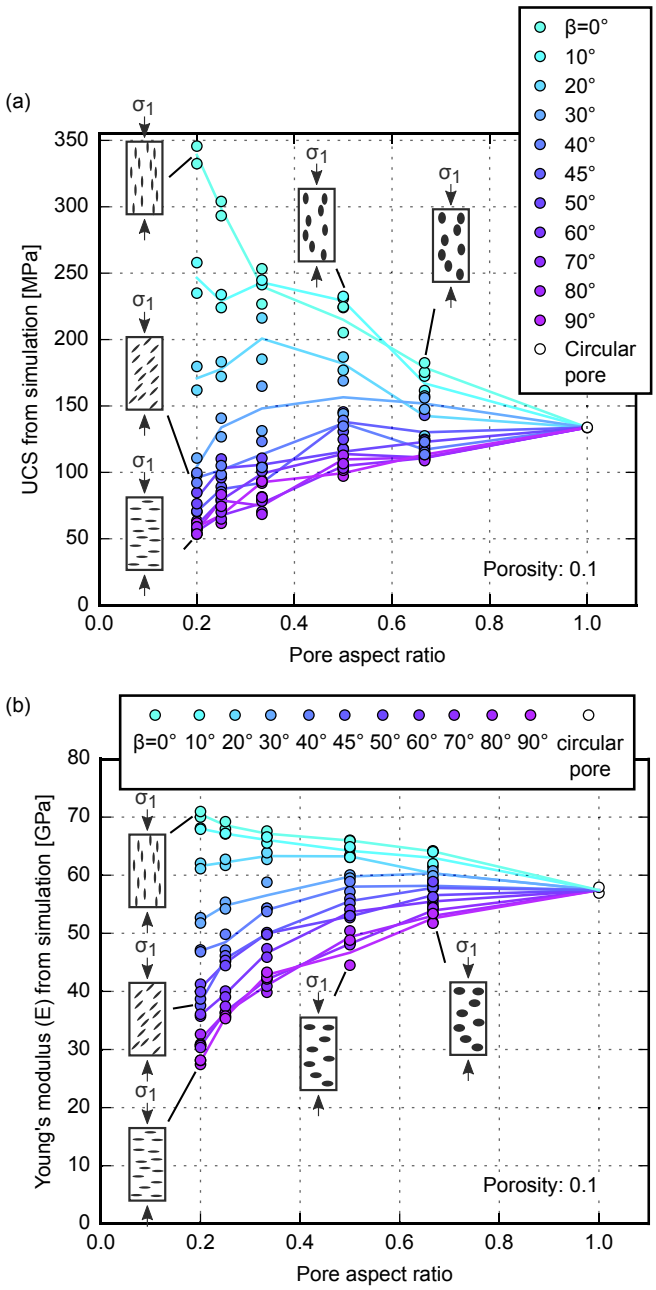

Figure 7: *The results of the Rock Failure Process Analysis ($RFPA_{2D}$) code numerical modelling for (a) UCS and (b) Young's modulus as a function of pore aspect ratio for samples containing a porosity of 0.1 and elliptical pores of 2 mm length with their major axes at angles of 0, 10, 20, 30, 40, 45, 50, 60, 70, 80, and 90° to the vertical long axis of the rectangular sample (i.e., the loading direction), β. Lines on the graphs connect the mean value of UCS and Young's modulus for each pore angle. (For interpretation of the references to colour in this figure, the reader is referred to the web version of this article.*

do not account for pore interaction. Pore interaction may become non-negligible when pores are separated by less than the length of a pore major axis (Rice, 1997; Tsukrov and Kachanov, 1997), which is likely the case for some of our high-porosity numerical samples.

4.1.1 Analytical solution for the stress along the pore boundary

The analytical solution for the tangential, or hoop stress, along the boundary of a two-dimensional elliptical void in an infinite medium, under an applied ("far-field") uniaxial stress σ_1, is given by Equation (6) (Jaeger et al., 2009). The hoop stress is a function of σ_1, the lengths of the major and minor semi-axes of the ellipse, here a and b respectively, the angle of the major axis with regards to the loading direction, β, and the location along the ellipsis boundary given by the angle, η, in elliptical coordinates:

$$\tau_{\nu\nu} = \sigma_1 \frac{2ab - \left(a^2 - b^2\right)\cos\left(2\beta\right) - \left(a+b\right)^2 cos(2\left(\beta - \eta\right))}{a^2 + b^2 - \left(a^2 - b^2\right)\cos\left(2\eta\right)} \qquad (6)$$

For a given applied stress (σ_1), pore aspect ratio, and angle from the pore major axis to the loading direction (β), the hoop stress has a maximum along the pore boundary, which we note $\tau_{\nu\nu\max}$. Figure 8a shows the applied stress, σ_1, required to generate a hoop stress of 1 MPa as the angle between the major axis and the loading direction, β, is increased from 0 to 90°. The applied stress required to generate a hoop stress of 1 MPa is higher when the pore angle, β, is lower (Figure 8a). Therefore, pores oriented so that their major axes are perpendicular to the direction of a given applied stress will intensify the stress to a greater extent than pores oriented parallel to that stress. This is in accord with the results from our numerical simulations: the strongest samples contain pores with their major axes oriented parallel to the loading direction, and the weakest samples contain pores oriented perpendicular to loading (Figure 5a).

Figure 8b shows the values of applied stress, σ_1, required for a maximum hoop stress $\tau_{\nu\nu\max}$ of 1 MPa for a single pore of varying aspect ratio (0.2 to 1) and angle to the loading direction (β = 0 to 90°). For the end-member scenario of circular pores (aspect ratio of unity), the applied stress required to maintain the hoop stress at 1 MPa is constant with pore angle, β, because the geometry is invariant by rotation. However, we observe a complex relationship between the applied stress and hoop stress with pore angle, β, and aspect ratio for an elliptical pore. At low pore angles (i.e., pores parallel or sub-parallel to the applied stress; β = 0-10°), an increase in pore aspect ratio decreases the value of the applied stress needed to maintain the hoop stress. However, at greater pore angles (pores perpendicular or sub-perpendicular to the applied stress; β = 40-90°) an increase in aspect ratio increases the applied stress required to maintain the hoop stress (Figure 8b). At intermediate angles (β = 20-30°), the applied stress required to maintain the hoop stress first increases and then decreases as pore aspect ratio increases (Figure 8b). We also note that the influence of pore angle, β, on strength decreases as the pore aspect ratio approaches unity (Figure 8b).

The evolution of the stress intensification with pore angle and aspect ratio (Figure 8) is in excellent qualitative agreement with the evolution of strength in the numerical samples (Figures 5a and 7a). The analytical solutions (Figure 8) therefore suggest that the magnitude of the stress calculated on the boundary of a single elliptical pore is directly related to the macroscopic strength of a sample containing multiple pores of equivalent geometry (Figures 5a and 7a).

4.1.2 Analytical solution for pore elasticity

The Young's modulus of a two-dimensional elliptical void, oriented so that its major axis is parallel ($\beta = 0°$) (Equation (7)) or perpendicular ($\beta = 90°$) (Equation (8)) to the applied ("far-field") stress can be calculated from its strain response under uniaxial loading (Kachanov et al., 1994). The Young's modulus of the pore oriented with its major axis parallel and perpendicular to the loading direction is a function of a and b, the lengths of the major and minor semi-axes of the pore, and E_0, the Young's modulus of the rock matrix:

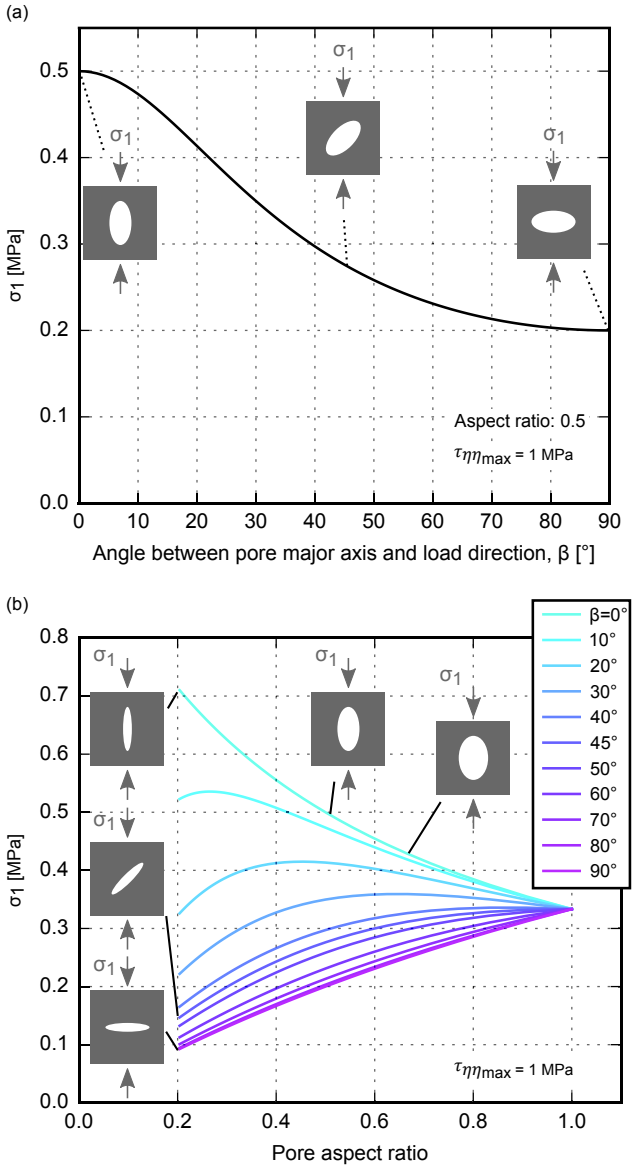

Figure 8: *(a) The applied ("far-field") stress required for a maximum hoop stress of 1 MPa along the boundary of a 2D elliptical pore of aspect ratio 0.5, as a function of the angle between the major axis of the elliptical pore and the uniaxial loading direction (β = 0-90°) (calculated using Equation (6)). (b) The applied ("far-field") stress required for a maximum hoop stress of 1 MPa along the boundary of a 2D elliptical pore as a function of aspect ratio (ranging from 0.2 to 1), for angles of 0, 10, 20, 30, 40, 45, 50, 60, 70, 80, and 90° between the pore major axis and the uniaxial loading direction, β (calculated using Equation (6)). (For interpretation of the references to colour in this figure, the reader is referred to the web version of this article.)*

$$E_{||} = E_0 \frac{a}{a+2b} \qquad (7)$$

$$E_{\perp} = E_0 \frac{b}{2a+b} \qquad (8)$$

Figure 9 shows the ratio of the pore and the rock matrix Young's moduli against pore aspect ratio (ranging from 0.2 to 1), for pores oriented with their major axes at 0 and 90° to the direction of the applied stress. For a given E_0, the Young's modulus of the pore oriented with its major axis parallel to the applied stress (β = 0°) decreases with increasing pore aspect ratio (Figure 9). By contrast, the Young's modulus of the pore in the perpendicular direction (β = 90°) increases with increasing pore aspect ratio (Figure 9). The same trend is observed in our numerical simulations (Figure 7b).

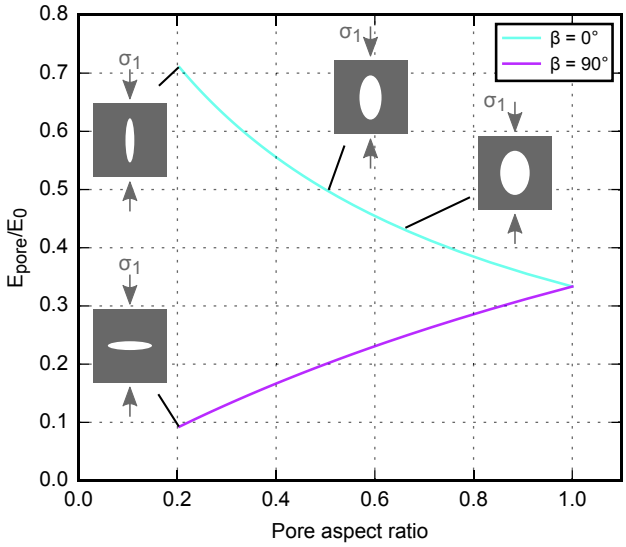

Figure 9: *The ratio of the Young's modulus of a 2D elliptical pore and the Young's modulus of the rock matrix as a function of pore aspect ratio (ranging from 0.2 to 1), for pores with their major axes oriented at 0 and 90° to the applied ("far-field") stress, β (calculated using Equations (7) and (8)). (For interpretation of the references to colour in this figure, the reader is referred to the web version of this article.)*

Furthermore, Kachanov et al. (1994) show that in the presence of multiple pores, even when randomly oriented, the porosity alone is not enough to determine the bulk elastic properties; the pore aspect ratio is required. This is reflected in the results of our two-dimensional numerical simulations, where variations in pore aspect ratio (Figure 7b) may in certain cases have a greater influence on the Young's modulus than the porosity (Figure 6b).

4.2 Comparison with experimental data

4.2.1 Comparison with porous basalt data

We consider the numerical modelling presented herein to be particularly relevant for extrusive volcanic rocks (the pores are more likely to approximate an ellipse in extrusive volcanic rocks than in clastic materials, for which the pores are the interstitial voids between grains or fragments). The pores preserved in volcanic rocks are the frozen relicts of bubbles in magma, the shape and orientation of which can be modified by a number of volcanic processes (Shea et al., 2010). For example, magmas can experience significant strains

during their ascent in the volcanic conduit, a process that can stretch and elongate bubbles (Arbaret et al., 2007; Okumura et al., 2010; Shields et al., 2014; Kushnir et al., 2016). In extreme cases, such shearing can form tube pumice, a rock that contains pores with a very low aspect ratio (Marti et al., 1999; Wright et al., 2006; Dingwell et al., 2016). Pore shape anisotropy preserved in volcanic rocks can also be the result of, for example, rheomorphic flow (Andrews and Branney, 2011) or viscous compaction (Quane et al., 2009; Heap et al., 2017).

We will now compare the strengths and Young's moduli from our numerical simulations with recently published experimental data on porous basalts (Bubeck et al., 2017). The mean pore aspect ratio for the basalts of Bubeck et al. (2017) was determined to be 0.32-0.54, and we plot these data together with our simulated output for a pore aspect ratio of 0.5 in Figure 10. Although the absolute values of compressive strength and Young's modulus for the basalt are considerably lower than for our numerical samples (since the strengths and Young's moduli of our samples depends on the pre-selected element parameters in Table 1) we see that, similar to our simulations, the basalt is weaker when the applied stress is at 90° to the preferred orientation of the pore major axes than at 0° (Figure 10). The anisotropy of the strength and Young's modulus can be expressed by the ratio of the mean value for an angle of 0° over the mean value for 90°. Anisotropy values for strength and Young's modulus for our numerical simulations and the experiments of Bubeck et al. (2017) are given in Table 2. The Young's modulus anisotropy factor for the basalt (average porosity = 0.165) experiments is 1.7 (Table 2). This value lies between those calculated for the simulated deformation 0.15 and 0.2 porosity samples: 1.6 and 1.8, respectively (Table 2). The strength anisotropy factor is however lower for the experimental data than for our simulations (Table 2). The experiments yield a strength anisotropy factor of 2.0, while the simulations for porosities of 0.15 and 0.2 provide values of 2.6 and 2.9, respectively (Table 2). We interpret this discrepancy as a result of the pore geometry variability (radius, shape, orientation) in the natural samples. For example, the pore size is variable (the basal zone basalts contain pores with volumes $<<5$ mm^3 and >5 mm^3)—a factor that affects the stress intensification at the tip of a pore-emanating microcrack (Sammis and Ashby, 1986)—and the major axes of the pores will not all be parallel. By contrast, all the pores in the numerical simulations have an identical geometry and orientation. Nevertheless, we find that our numerical simulations are in good overall agreement with the porous basalt data of Bubeck et al. (2017).

Table 2: *Unconfined compressive strength (UCS) and Young's modulus (*E*) anisotropy factors for the numerical simulations (this study) and the experimental data for basalt from Bubeck et al. (2017). Anisotropy factors were calculated using the mean values of UCS and Young's modulus.*

	Porosity	UCS anisotropy factor	E Anisotropy factor
Numerical, this study	0.02	1.3	1.1
	0.05	2.6	1.2
	0.1	2.3	1.4
	0.15	2.6	1.6
	0.2	2.9	1.8
Experimental (basalt), Bubeck et al. (2017)	0.165 (mean)	2.0	1.7

4.2.2 Comparison with sandstone and limestone data

The pores of a clastic rock such as sandstone are the interstitial voids between grains and, as a result, an ellipse may not best represent their shape. Nevertheless, we consider it interesting to compare our modelled results with data for sandstone, since the pores within sandstone are commonly preferentially oriented with their major axis parallel to bedding (i.e., they are likely to exhibit a pore shape anisotropy). Indeed, anisotropy of

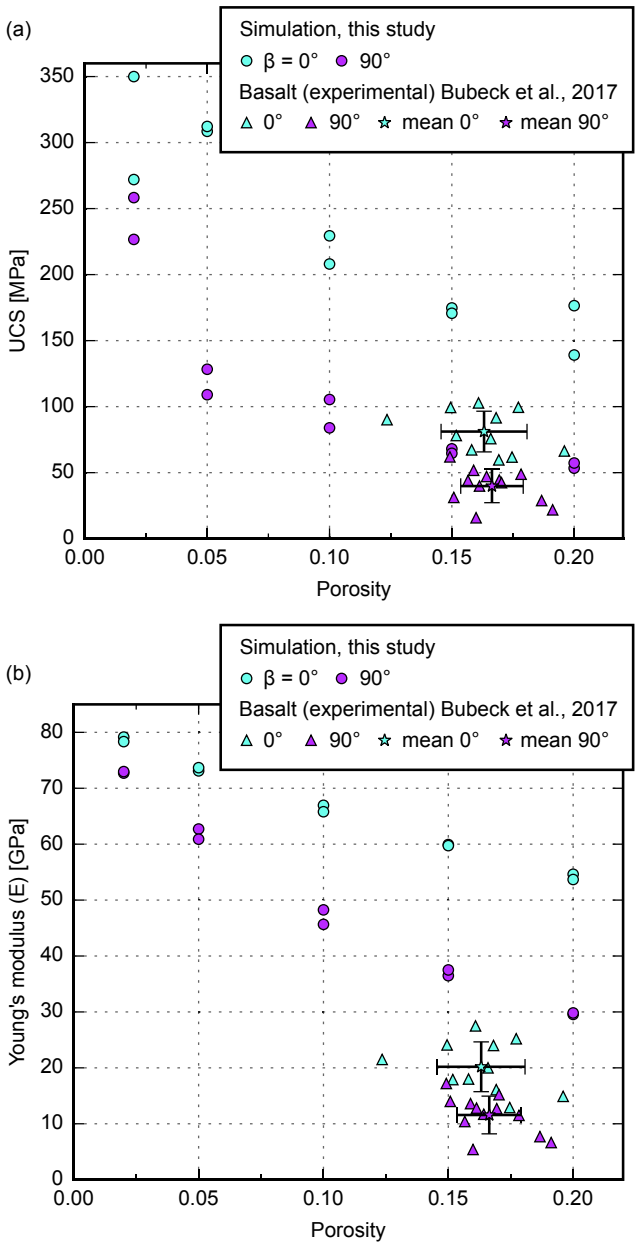

Figure 10: *(a) UCS and (b) Young's modulus as a function of porosity from our numerical simulations, plotted alongside data from a recent experimental study on basalt of Bubeck et al. (2017). The numerical samples contain pores with an aspect ratio of 0.5 that are oriented so that their major axis is at an angle of 0 or 90° to the vertical long axis of the rectangular sample (i.e., the loading direction), β. The basalt samples have a mean aspect ratio in the range of 0.32-0.54 (Bubeck et al., 2017). The experimental data shown here are for basalt samples prepared so that their pore major axis is orientated at an angle of 0 or 90° to the sample axis (i.e., the loading direction). For the Bubeck et al. (2017) data, we also plot the mean values for each pore orientation with the standard deviation. (For interpretation of the references to colour in this figure, the reader is referred to the web version of this article.)*

magnetic susceptibility (AMS) has revealed a pore shape anisotropy in sandstones: the pore major axis in a wide variety of porous sandstones was found to be sub-parallel to bedding (Louis et al., 2003; Benson et al., 2005; Robion et al., 2014). Recent advances in μCT have also provided a detailed description of the shape of pores within sandstone. For example, Schmitt et al. (2016) showed that pore shapes in reservoir sandstones are typically plate- and cube-like.

Mechanical data from uniaxial and triaxial experiments on sandstone show that they are strongest when deformed perpendicular to bedding (Baud et al., 2005 and references therein; Louis et al., 2009). For example, the peak stress of Rothbach sandstone deformed at an effective pressure of 5 MPa was ~60 MPa when the sample was deformed perpendicular to bedding, and ~50 MPa when the sample was deformed parallel to bedding (Louis et al., 2009). These porous sandstones are therefore weaker when the loading direction is parallel to the pore major axis, an observation in conflict with the modelling results (Figure 5a) and the experimental data for porous basalt (Bubeck et al., 2017). We complement existing data on strength anisotropy in porous sandstones by performing constant strain rate (10^{-5} s^{-1}) uniaxial compressive strength (UCS) tests on dry sandstone cores (20 mm in diameter and nominally 40 mm in length) prepared so that their axes were either parallel or perpendicular to bedding (Table 3). The four sandstones chosen—Adamswiller (e.g., Baud et al., 2006), Rothbach (e.g., Louis et al., 2009), Bleurswiller (e.g., Heap et al., 2015b), and Bentheim (e.g., Klein et al., 2001)—contain similar connected porosities (0.225 to 0.245; Table 3) and have similar average grain diameters (~200 μm). The results of our uniaxial deformation experiments are in agreement with the data presented in Baud et al. (2005) and Louis et al. (2009): the sandstones are systematically weaker when they are deformed parallel to bedding (ratios of perpendicular to parallel strength are between 1.12 and 1.54; Table 3). Based on these and the published data, we conclude that pore shape anisotropy in sandstone may not play a first-order role in dictating their strength anisotropy. The alignment of grains or platy minerals such as clays may therefore control strength anisotropy in the porous sandstones studied here. Indeed, Louis et al. (2003; 2009) concluded that the mechanical anisotropy observed in Rothbach sandstone was the result of the preferential alignment of grains. A result of this preferential alignment is that the total grain-to-grain contact surface is highest when the sample is loaded perpendicular to bedding. In this scenario, the stress on the individual contacts is at its lowest and the macroscopic strength of the sample is high as a result. By contrast, the total grain-to-grain contact area is lowest when the sample is loaded parallel to bedding. In this scenario, the stress on the individual contacts is at its highest, allowing microcracks to form at a lower given applied stress, and the macroscopic strength of the sample is low as a result (Louis et al., 2003; 2009). We further note that, although the pores shapes within sandstones can be approximated as plate- or cube-like (Schmitt et al., 2016), they are typically much less defined than the pores found within extrusive volcanic rocks, especially basalts (Bubeck et al., 2017).

Table 3: *Unconfined compressive strength (UCS) of sandstone samples deformed either parallel or perpendicular to bedding (data unique to this study)*

Sample	Connected porosity	Orientation of sample axis with respect to bedding	Uniaxial compressive strength (MPa)	Ratio of perpendicular ($\sigma_{p(90°)}$) to parallel ($\sigma_{p(0°)}$) strength
Adamswiller	0.245	Perpendicular	49.4	1.21
Adamswiller	0.245	Parallel	40.8	
Rothbach	0.225	Perpendicular	26.7	1.54
Rothbach	0.225	Parallel	17.3	
Bleurswiller	0.240	Perpendicular	41.4	1.21
Bleurswiller	0.240	Parallel	34.3	
Bentheim	0.230	Perpendicular	47.8	1.12
Bentheim	0.230	Parallel	41.3	

Several studies have observed a pore shape anisotropy in limestones (e.g., Ji et al., 2012; Robion et al., 2014; Ji et al., 2015). Ji et al. (2012; 2015) showed that the sphericity of macropores within Indiana and Majella

limestone (limestones that contain a dual porosity of micro- and macropores) decreases as their equivalent diameter increases. For example, while the majority of micropores in Indiana limestone (pores with a diameter < 33 μm) have a sphericity > 0.78, macropores with an equivalent diameter of $>$ ~200 μm are characterised by a sphericity of ≤ 0.59 (Ji et al., 2012). Data for Majella limestone were similar: the majority of micropores are close to a sphericity of unity, while macropores $>$ ~100 μm are characterised by a sphericity of ≤ 0.59 (Ji et al., 2015). A combination of AMS and P-wave velocity data for Jurassic limestones from the Western part of the Paris Basin revealed prolate pores with their major axis typically orientated parallel to bedding (Robion et al., 2014). However, comparison between our modelled results and data for carbonate rocks is difficult not only due to the paucity of laboratory strength anisotropy data, but also the lack of studies that combine pore geometry analysis and mechanical testing. UCS tests on microporous Oxfordian limestones from the Eastern part of the Paris Basin showed no evidence of mechanical anisotropy (Baud et al., 2016), whilst limestones from Central Anatolia were found to be strongest when deformed perpendicular to bedding and weakest when the bedding was at an angle of 30° to the loading direction (Karakul et al., 2010). Studies on limestones combining detailed pore geometry and orientation analysis with mechanical strength testing are now required to test the modelled predictions presented herein (Figures 5, 6, and 7).

4.3 Strength anisotropy in crustal rocks

Strength anisotropy in crustal rocks is typically attributed to planar fabrics in rock, such as bedding in sedimentary rocks (e.g., Millien, 1993; Baud et al., 2005; Louis et al., 2003; 2009) or foliation in metamorphic rocks (e.g., Donath, 1972; Shea and Kronenberg, 1993; Baud et al., 2005). Here we have shown that significant strength anisotropy can also arise as a result of the preferential alignment of elliptical pores (Figures 5, 6, and 7; see also Bubeck et al., 2017). Interestingly, the evolution of strength as a function of the angle between the applied stress and each of these three fabrics—bedding, foliation, and pore major axis—is markedly different (Figure 11). As this angle is increased from 0 to 90°, the strength of sandstone increases, the strength of basalt decreases, and the strength of phyllite first decreases (with a minimum at about 45°) and then increases (Figure 11). Figure 11 highlights that the strength anisotropy as a result of the preferential alignment of elliptical pores is of a similar magnitude to that for bedding and foliation. The numerous sources of mechanical anisotropy in the crust, and their varied contribution to such anisotropy (Figure 11), highlight the importance of orienting rocks either collected or catalogued in the field and providing a complete description of their textural heterogeneity.

4.4 Implications

The results from our numerical simulations highlight that the aspect ratio of elliptical pores (the ratio of the minor to major axis) and the angle of their major axis with respect to the loading direction play important roles in controlling rock strength (Figures 5a, 6a, and 7a) and stiffness (Figures 5b, 6b, and 7b). Therefore, porous rock containing preferentially oriented elliptical pores can exhibit a considerable strength and stiffness anisotropy. Further, elliptical pores with their major axis oriented perpendicular to the direction of loading may control the strength of rock containing randomly oriented non-spherical pores. These results explain in part the variability that is typically observed in plots of UCS as a function of porosity for porous rock (e.g., Chang et al., 2006; Baud et al., 2014; Schaefer et al., 2015; Heap et al., 2016; Zhu et al., 2016; Bubeck et al., 2017).

In this study we considered the influence of pore geometry and orientation and porosity on the strength and stiffness of porous rock. We did not consider changes in pore size, a variable exposed to influence both strength and stiffness in two-dimensional micromechanical (Sammis and Ashby, 1986) and numerical (Heap et al., 2014) modelling of materials containing circular pores. Recent data on basalts from Mt. Etna (Italy) showed that porosity and pore size are not necessarily independent: higher porosity samples had larger pores, and vice-versa (Zhu et al., 2016). Future modelling efforts on the mechanical influence of pore geometry and orientation should therefore consider variations in pore size.

Through comparison of our modelling results with new and previously published experimental data, we can

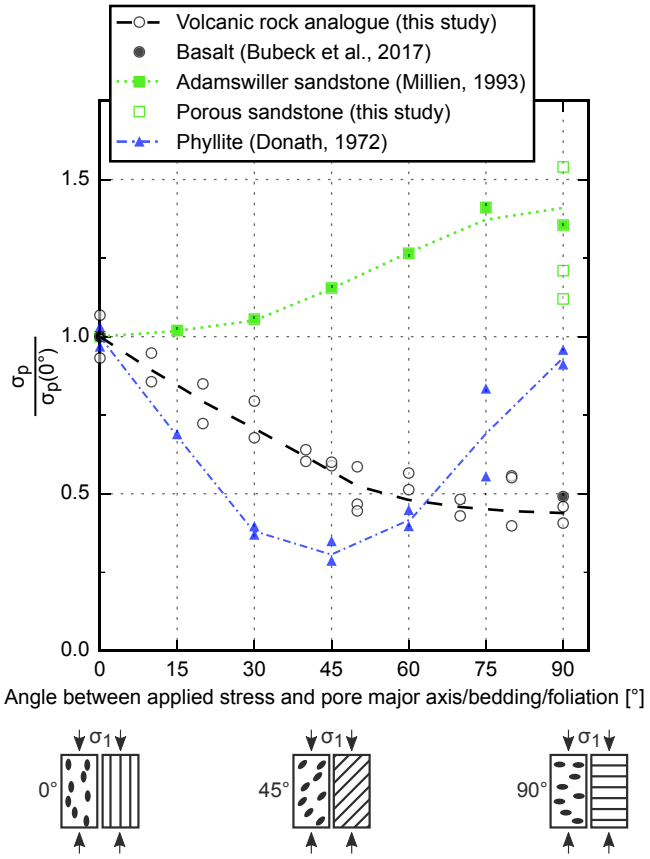

Figure 11: *The ratio between the peak stress (σ_p) and the peak stress when the angle between the applied stress and the pore major axis/bedding/foliation is 0° ($\sigma_{p(0)}$) as a function of the angle between the applied stress and the pore major axis/bedding/foliation. For the sandstone data (uniaxial compressive strength tests on Adamswiller sandstone, taken from Millien, 1993; and uniaxial compressive strength tests from this study, Table 3), the angle corresponds to the angle between the applied stress and the bedding. For the volcanic rock analogue (the simulations of this study; porosity = 0.1 and pore aspect ratio = 0.5) and basalt data (uniaxial compressive strength tests on basalt from Kīlauea (Hawaii, USA), taken from Bubeck et al., 2017), the angle corresponds to the angle between the applied stress and the pore major axis. For the phyllite data (triaxial compressive strength tests on Moretown phyllite performed at a confining pressure of 50 MPa, taken from Donath, 1972), the angle corresponds to the angle between the applied stress and the foliation. We also provide cartoons to illustrate the direction of the applied stress (σ_1) with regard to the pore major axis (cartoon on the left) and the bedding/foliation (cartoon on the right).*

conclude that the modelling presented herein is particularly relevant for extrusive volcanic rocks, but does not capture the complexity of sandstones, for which grain orientation may play an important role in dictating their strength anisotropy (e.g., Louis et al., 2009). Discrete element methods (DEM), in which grains can be represented as circular disks or spheres, may better capture the behaviour of clastic materials such as sandstones (e.g., Wang et al., 2008). There are unfortunately too few data to make firm conclusions as to whether our modelled results are relevant for porous limestones.

As demonstrated by our modelling, and the experimental data of Bubeck et al. (2017), the preserved pore shape and orientation in volcanic rock can greatly impact their strength and stiffness (Figures 5, 6, and 7). Therefore, if the pore major axis is typically oriented parallel to bedding in lavas, as was the case for the basalts collected from the south flank of Kīlauea, Hawaii (Bubeck et al., 2017), then the rocks will be weaker and less stiff in the vertical direction, and stronger and stiffer in the horizontal direction. These rocks may therefore be more prone to porosity and permeability reduction driven by vertical lithostatic stresses than similarly porous rock with spherical pores. By contrast, and as discussed in Bubeck et al. (2017), such rocks may be better equipped to withstand horizontal stresses (such as tectonic stresses, or stresses transferred from the magma-filled conduit to the adjacent volcanic rock during volcanic unrest) that could help to safeguard against reductions to porosity and permeability at depths where the rocks will compact in response to an applied stress (Heap et al., 2015c; 2017), or prevent faulting at shallow depths. A pronounced strength anisotropy could therefore create permeability heterogeneity within a reservoir or volcanic edifice.

Large differences in the strength and Young's modulus of superimposed layers of volcanic rock, such as the difference between a stiff and strong lava layer and a compliant and weak tuff layer, can promote dyke arrest and therefore impede dyke-fed eruptions (Gudmundsson, 2006), and influence fault zone architecture and fluid flow (Walker et al., 2013). Our modelling has demonstrated that differences in pore shape and orientation between superimposed layers of the same lithology (i.e., rocks that appear similar in the field) may also provide the mechanical contrast required to influence dyke propagation and fault zone architecture. We further note that the pore geometry within lava is also likely to vary within an individual flow unit (e.g., Planke, 1994; Self et al., 1998). Therefore, for example, a difference in Young's modulus between the top of a lava unit that contains spherical pores and the base that contains flattened pores (i.e., pores with their pore major axis parallel to the macroscopic bedding) may be sufficient to hamper dyke propagation.

To conclude, the mechanical anisotropy within individual units and sequences of volcanic rock can be large due to pore geometry alone. Therefore, the orientation of volcanic blocks collected or catalogued in the field, and an accurate description of their pore geometry, should form an important part of volcanic rock reservoir characterisation (e.g., Millett et al., 2015; Chen et al., 2016) and studies that assess the propagation and arrest of dykes (e.g., Gudmundsson, 2006), and the structural stability of (e.g., Voight, 2000; Apuani et al., 2005; Heap et al., 2015c) and permeability anisotropy in (e.g., Lavallée et al., 2013; Gaunt et al., 2014; Heap and Kennedy, 2016; Farquharson et al., 2016a; 2016b) volcanic edifices.

5 Conclusions

Our numerical modelling highlights that pore geometry and orientation (with respect to the loading direction) can greatly influence the compressive strength and Young's modulus of porous rock. Our modelled results align with experimental data for porous basalt (Bubeck et al., 2017), but not with data for porous sandstone (Baud et al., 2005; Louis et al., 2009; and new data). We conclude that the modelling presented herein is particularly relevant for extrusive volcanic rocks, but that the alignment of grains (or platy minerals such as clays) may play a more important role in dictating strength anisotropy in porous sandstones than pore geometry and orientation (as suggested in Louis et al., 2009). There are unfortunately too few data to make firm conclusions as to whether our results are relevant for porous limestones. Through comparison with published data, we show that the strength anisotropy that arises as a result of preferentially aligned elliptical pores is of a similar magnitude to that generated by bedding in porous sandstones and foliation in low-porosity metamorphic rocks. Pore geometry and orientation therefore emerges as an important metric for a variety of geophysical and geotechnical applications, and as an important consideration in the development of new micromechanical models designed to explore the mechanical behaviour of porous materials.

Acknowledgements

The authors of this study gratefully acknowledge a Cai Yuanpei Partenariats Hubert Curien (PHC) grant (project number 36605ZB), implemented and funded by the Ministry of Foreign Affairs (MAEDI) and the Ministry of Higher Education and Research (MENESR) in France, and the Ministry of Education and the China Scholarship Council (CSC) in China. L. Griffiths, M. Heap, and P. Baud also acknowledge LABEX grant ANR-11-LABX-0050 G-EAU- THERMIE-PROFONDE; this study therefore benefits from state funding managed by the Agence National de la Recherche (ANR) as part of the "Investissements d'avenir" program. We gratefully acknowledge Thierry Reuschlé and Marie Lenoir for experimental support. T. Xu acknowledges the National Natural Science Foundation of China (grant number 51474051, 41672301), the National Basic Research Program of China (grant number 2013CB227900 and 2014CB047100), and Fundamental Research Funds for the Central Universities of China (grant number N150102002). We are grateful for the constructive comments of Alodie Bubeck, Hasan Karakul, and Toru Takeshita, which helped improve this manuscript. The paper also benefitted from a conversation with Alan George Heap.

References

Al-Harthi, A.A., Al-Amri, R.M., Shehata, W.M., 1999. The porosity and engineering properties of vesicular basalt in Saudi Arabia. Eng. Geol. 54, 313–320. doi:10.1016/S0013-7952(99)00050-2

Andrews, G.D., Branney, M.J., 2011. Emplacement and rheomorphic deformation of a large, lava-like rhyolitic ignimbrite: Grey's Landing, southern Idaho. Geol. Soc. Am. Bull. 123, 725–743.

Apuani, T., Corazzato, C., Cancelli, A. and Tibaldi, A., 2005. Physical and mechanical properties of rock masses at Stromboli: a dataset for volcano instability evaluation. Bulletin of Engineering Geology and the Environment 64(4), 419-431.

Arbaret, L., Bystricky, M., Champallier, R., 2007. Microstructures and rheology of hydrous synthetic magmatic suspensions deformed in torsion at high pressure. J. Geophys. Res. Solid Earth 112.

Ashby, M.F., Sammis, C.G., 1990. The damage mechanics of brittle solids in compression. Pure Appl. Geophys. 133, 489–521.

Baud, P., Louis, L., David, C., Rawling, G.C., Wong, T.-f., 2005. Effects of bedding and foliation on mechanical anisotropy, damage evolution and failure mode. Geological Society of London Special Publications 245, 223-249.

Baud, P., Vajdova, V. and Wong, T.F., 2006. Shear-enhanced compaction and strain localization: Inelastic deformation and constitutive modeling of four porous sandstones. Journal of Geophysical Research: Solid Earth, 111(B12).

Baud, P., Wong, T., Zhu, W., 2014. Effects of porosity and crack density on the compressive strength of rocks. Int. J. Rock Mech. Min. Sci. 67, 202–211. doi:10.1016/j.ijrmms.2013.08.031.

Baud, P., Rolland, A., Heap, M. J., Xu, T., Nicolé, M., Ferrand, T., Reuschlé, T., Toussaint, R., Conil, N., 2016. Impact of Stylolites on the mechanical strength of limestones, Tectonophysics 690, 4-20.

Benson, P.M., Meredith, P.G., Platzman, E.S. and White, R.E., 2005. Pore fabric shape anisotropy in porous sandstones and its relation to elastic wave velocity and permeability anisotropy under hydrostatic pressure. International Journal of Rock Mechanics and Mining Sciences 42(7), 890-899.

Bourbié, T., Zinszner, B., 1985. Hydraulic and acoustic properties as a function of porosity in Fontainebleau Sandstone. J. Geophys. Res. Solid Earth 90, 11524–11532. doi:10.1029/JB090iB13p11524.

Bubeck, A., Walker, R.J., Healy, D., Dobbs, M., and Holwell, D.A., 2017. Pore geometry as a control on rock strength. Earth and Planetary Science Letters, DOI: 10.1016/j.epsl.2016.09.050.

Chang, C., Zoback, M.D., Khaksar, A., 2006. Empirical relations between rock strength and physical properties in sedimentary rocks. J. Pet. Sci. Eng. 51, 223–237. doi:10.1016/j.petrol.2006.01.003.

Chen, Z., Liu, W., Zhang, Y., Yan, D., Yang, D., Zha, M., Li, L., 2016. Characterization of the paleocrusts of weathered Carboniferous volcanics from the Junggar Basin, western China: Significance as gas reservoirs, Marine and Petroleum Geology, 77, 216-234.

Dingwell, D.B., Lavallée, Y., Hess, K.-U., Flaws, A., Marti, J., Nichols, A.R., Gilg, H.A., Schillinger, B., 2016. Eruptive shearing of tube pumice: pure and simple. Solid Earth 7, 1383.

Donath, F.A., 1972. Effects of cohesion and granularity on deformational behaviour of anisotropic rock. In: Doe, B.R. and Smith, D.K. (eds) Studies in Mineralogy and Precambrian Geology, Geological Society of America Memoir, 135, 95-128.

Farquharson, J., Heap, M.J., Varley, N.R., Baud, P., Reuschlé, T., 2015. Permeability and porosity relationships of edifice-forming andesites: A combined field and laboratory study. J. Volcanol. Geotherm. Res. 297, 52–68. doi:10.1016/j.jvolgeores.2015.03.016.

Farquharson, J.I., Heap, M.J., Lavallée, Y., Varley, N.R. and Baud, P., 2016a. Evidence for the development of permeability anisotropy in lava domes and volcanic conduits. Journal of Volcanology and Geothermal Research 323, 163-185.

Farquharson, J.I., Heap, M.J. and Baud, P., 2016b. Strain-induced permeability increase in volcanic rock. Geophysical Research Letters 43, DOI: 10.1002/2016GL071540.

Gaunt, H.E., Sammonds, P.R., Meredith, P.G., Smith, R. and Pallister, J.S., 2014. Pathways for degassing during the lava dome eruption of Mount St. Helens 2004–2008. Geology 42(11), 947-950.

Gudmundsson, A., 2006. How local stresses control magma-chamber ruptures, dyke injections, and eruptions in composite volcanoes. Earth-Sci. Rev. 79, 1–31. doi:10.1016/j.earscirev.2006.06.006

Heap, M.J., Xu, T., Chen, C., 2014. The influence of porosity and vesicle size on the brittle strength of volcanic rocks and magma. Bull. Volcanol. 76, 1–15.

Heap, M.J., Xu, T., Kushnir, A.R.L., Kennedy, B.M., Chen, C., 2015a. Fracture of magma containing overpressurised pores. J. Volcanol. Geotherm. Res. 301, 180–190. doi:10.1016/j.jvolgeores.2015.05.016.

Heap, M.J., Brantut, N., Baud, P. and Meredith, P.G., 2015b. Time-dependent compaction band formation in sandstone. Journal of Geophysical Research: Solid Earth, 120(7), 4808-4830.

Heap, M.J., Farquharson, J.I., Baud, P., Lavallée, Y. and Reuschlé, T., 2015c. Fracture and compaction of andesite in a volcanic edifice. Bulletin of Volcanology 77(6), 1-19.

Heap, M.J., Wadsworth, F.B., Xu, T., Chen, C., Tang, C., 2016. The strength of heterogeneous volcanic rocks: A 2D approximation. J. Volcanol. Geotherm. Res. 319, 1–11. DOI:10.1016/j.jvolgeores.2016.03.013.

Heap, M.J. and Kennedy, B.M., 2016. Exploring the scale-dependent permeability of fractured andesite. Earth and Planetary Science Letters 447, 139-150.

Heap, M.J., Violay, M., Wadsworth, F.B., and Vasseur, J., 2017. From rock to magma and back again: The evolution of temperature and deformation mechanism in conduit margin zones, Earth and Planetary Science Letters, DOI: 10.1016/j.epsl.2017.01.021.

Jaeger, J.C., Cook, N.G., Zimmerman, R., 2009. Fundamentals of rock mechanics. John Wiley & Sons.

Ji, Y., Baud, P., Vajdova, V., Wong, T.-f., 2012. Characterization of pore geometry of Indiana limestone in relation to mechanical compaction. Oil Gas Sci. Technol. D'IFP Energ. Nouv. 67, 753–775.

Ji, Y., Hall, S.A., Baud, P., Wong, T.-f., 2015. Characterization of pore structure and strain localization in Majella limestone by X-ray computed tomography and digital image correlation. Geophys. J. Int. 200, 701–719.

Kachanov, M., Tsukrov, I. and Shafiro, B., 1994. Effective moduli of solids with cavities of various shapes. Applied Mechanics Reviews 47(1S), 151-174.

Karakul, H., Ulusay, R., and Isik, N.S., 2010. Empirical models and numerical analysis for assessing strength anisotropy based on block punch index and uniaxial compression tests, International Journal of Rock Mechanics and Mining Sciences, 47, 657-665.

Klein, E., Baud, P., Reuschlé, T. and Wong, T.F., 2001. Mechanical behaviour and failure mode of Bentheim sandstone under triaxial compression. Physics and Chemistry of the Earth, Part A: Solid Earth and Geodesy, 26(1-2), 21-25.

Kushnir, A.R., Martel, C., Champallier, R. and Arbaret, L., 2016. In situ confirmation of permeability development in shearing bubble-bearing melts and implications for volcanic outgassing. Earth and Planetary Science Letters, 458, 315-326. DOI: 10.1016/j.epsl.2016.10.053.

Lavallée, Y., Benson, P.M., Heap, M.J., Hess, K.U., Flaws, A., Schillinger, B., Meredith, P.G. and Dingwell, D.B., 2013. Reconstructing magma failure and the degassing network of dome-building eruptions. Geology 41(4), 515-518.

Lemaitre, J., Chaboche, J.-L., 1994. Mechanics of solid materials. Cambridge university press.

Louis, L., David, C. and Robion, P., 2003. Comparison of the anisotropic behaviour of undeformed sandstones under dry and saturated conditions. Tectonophysics 370(1), 193-212.

Louis, L., Baud, P., and Wong, T.-f., 2009. Microstructural inhomogeneity and mechanical anisotropy associated with bedding in Rothbach sandstone. Pure Appl. Geophys. 166, 1063-1087.

Luquot, L., Hebert, V., Rodriguez, O., 2016. Calculating structural and geometrical parameters by laboratory measurements and X-ray microtomography: a comparative study applied to a limestone sample before and after a dissolution experiment. Solid Earth, 7, 441-456.

Marti, J., Soriano, C., Dingwell, D.B., 1999. Tube pumices as strain markers of the ductile–brittle transition during magma fragmentation. Nature 402, 650–653.

Millett, J., Hole, M., Jolley, D., Schofield, N., and Campbell, E., 2015. Frontier exploration and the North Atlantic Igneous Province: New insights from a 2.6 km offshore volcanic sequence in the NE Faroe–Shetland Basin, Journal of the Geological Society, 173, DOI: 10.1144/0016-76492015-069.

Millien, A., 1993. Comportement anisotrope du grès des Vosges : élasto-plasticité, localisation, rupture. Thèse de Doctorat en Sciences, Université Joseph Fourier, Grenoble.

Okumura, S., Nakamura, M., Nakano, T., Uesugi, K., Tsuchiyama, A., 2010. Shear deformation experiments on vesicular rhyolite: Implications for brittle fracturing, degassing, and compaction of magmas in volcanic conduits. J. Geophys. Res. Solid Earth 115.

Quane, S.L., Russell, J.K. and Friedlander, E.A., 2009. Time scales of compaction in volcanic systems. Geology, 37(5), 471-474.

Rice, R.W., 1997. Limitations of pore-stress concentrations on the mechanical properties of porous materials. Journal of Materials Science 32, 4731–4736. DOI:10.1023/A:1018674713006.

Robion, P., David, C., Dautriat, J., Colombier, J.C., Zinsmeister, L. and Collin, P.Y., 2014. Pore fabric geometry inferred from magnetic and acoustic anisotropies in rocks with various mineralogy, permeability and porosity. Tectonophysics, 629, 109-122.

Rozenbaum, O., Rolland du Roscat, S., 2014. Representative elementary volume assessment of three-dimensional x-ray microtomography images of heterogeneous materials: Application to limestones. Physical Review E 89:53304, DOI: 10.1103/PhysRevE.89.053304.

Sammis, C.G., Ashby, M.F., 1986. The failure of brittle porous solids under compressive stress states. Acta Metall. 34, 511–526. doi:10.1016/0001-6160(86)90087-8

Schaefer, L.N., Kendrick, J.E., Oommen, T., Lavallée, Y., Chigna, G., 2015. Geomechanical rock properties of a basaltic volcano. Volcanology 3, 29. doi:10.3389/feart.2015.00029

Schmitt, M., Halisch, M., Müller, C., Fernandes, C.P., 2016. Classification and quantification of pore shapes in sandstone reservoir rocks with 3-D X-ray micro-computed tomography. Solid Earth 7, 285–300.

Shea, T., Houghton, B.F., Gurioli, L., Cashman, K.V., Hammer, J.E., Hobden, B.J., 2010. Textural studies of vesicles in volcanic rocks: An integrated methodology. J. Volcanol. Geotherm. Res. 190, 271–289. doi:10.1016/j.jvolgeores.2009.12.003

Shea, W.T. and Kronenberg, A.K., 1993. Strength and anisotropy of foliated rocks with varied mica contents. Journal of Structural Geology, 15(9-10), 1097-1121.

Shields, J.K., Mader, H.M., Pistone, M., Caricchi, L., Floess, D., Putlitz, B., 2014. Strain-induced outgassing of three-phase magmas during simple shear. J. Geophys. Res. Solid Earth 119, 6936–6957.

Simmons, G., Richter, D., 1976. Microcracks in rocks. Phys. Chem. Miner. Rocks 105–137.

Tang, C., 1997. Numerical simulation of progressive rock failure and associated seismicity. Int. J. Rock Mech. Min. Sci. 34, 249–261.

Tsukrov, I., Kachanov, M., 1997. Stress concentrations and microfracturing patterns in a brittle-elastic solid with interacting pores of diverse shapes. International Journal of Solids and Structures 34, 2887–2904. DOI:10.1016/S0020-7683(96)00202-8.

Vasseur, J., Wadsworth, F.B., Lavallée, Y., Hess, K.U. and Dingwell, D.B., 2013. Volcanic sintering: timescales of viscous densification and strength recovery. Geophysical Research Letters, 40(21), 5658-5664.

Voight, B., 2000. Structural stability of andesite volcanoes and lava domes. Philosophical Transactions of the Royal Society of London A: Mathematical, Physical and Engineering Sciences 358(1770), 1663-1703.

Walker, R.J., Holdsworth, R.E., Imber, J., Faulkner, D.R. and Armitage, P.J., 2013. Fault zone architecture and fluid flow in interlayered basaltic volcaniclastic-crystalline sequences. Journal of Structural Geology, 51, 92-104.

Weibull, W., 1951. Wide applicability. J. Appl. Mech. 103, 293–297.

Wong, T., Wong, R.H.C., Chau, K.T., Tang, C.A., 2006. Microcrack statistics, Weibull distribution and micromechanical modeling of compressive failure in rock. Mech. Mater. 38, 664–681. doi:10.1016/j.mechmat.2005.12.002

Wright, H.M.N., Roberts, J.J., Cashman, K.V., 2006. Permeability of anisotropic tube pumice: Model calculations and measurements. Geophys. Res. Lett. 33, L17316. doi:10.1029/2006GL027224.

Xu, T., Tang, C., Zhao, J., Li, L., Heap, M.J., 2012. Modelling the time-dependent rheological behaviour of heterogeneous brittle rocks. Geophys. J. Int. 189, 1781–1796.

Wang, B., Chen, Y., Wong, T.-f., 2008. A discrete element model for the development of compaction localization in granular rock. J. Geophys. Res. 113, DOI: 10.1029/2006JB004501.

Zhu, W., Baud, P., Vinciguerra, S., Wong, T.-f., 2011. Micromechanics of brittle faulting and cataclastic flow in Alban Hills Tuff. J. Geophys. Res. Solid Earth, 106, DOI: 10.1029/2010JB008046.

Zhu, W., Baud, P., Vinciguerra, S., Wong, T.-f., 2016. Micromechanics of brittle faulting and cataclastic flow in Mt Etna basalt. J. Geophys. Res. Solid Earth, 121, DOI: 10.1002/2016JB012826.

D

RÉSUMÉ EN FRANÇAIS

D.1 CHAPITRE 1 : INTRODUCTION

Les roches contiennent souvent des fissures microscopiques (Kranz, 1983; Simmons and Richter, 1976). Ces microfissures ont typiquement une longueur inférieure ou égale à 0,1 mm (Simmons and Richter, 1976) et un faible facteur de forme, le rapport entre leur ouverture et leur longueur, inférieur à 0,01. Les microfissures peuvent être induites mécaniquement, chimiquement ou thermiquement (Kranz, 1983). Cette thèse se concentre sur la microfissuration thermique. Les microfissures thermiques se forment à cause de variations de température dans le temps et dans l'espace qui peuvent se produire dans de nombreux contextes géophysiques de la croûte terrestre.

Les microfissures thermiques peuvent affecter de manière significative les propriétés physiques des roches. Par exemple, David et al. (1999) ont mesuré une diminution de la vitesse des ondes acoustiques de plus de 30 % dans un granite à grain fin chauffé jusqu'à 450 °C. David et al. (1999) ont mesuré aussi une augmentation de la perméabilité (sa capacité de transmettre des fluides) de la roche de 3 ordres de grandeur. Kant et al. (2017) ont mesuré une diminution de 75 % de la conductivité thermique d'un granite après l'avoir chauffé à 500 °C, et Homand-Etienne and Houpert (1989) ont mesuré une diminution de 30–40 % de la résistance uniaxiale de deux granites une fois chauffés à 600 °C.

Des changements de température ont lieu de façon naturelle dans la croûte terrestre. Au niveau des zones tectoniques actives, de la chaleur peut être générée par le frottement sur le plan de faille lors des séismes (voir par exemple, Cardwell et al. (1978)). Dans les volcans, la remontée du magma provoque des changements cycliques de température de la roche environnante (Heap et al., 2017). A la surface de la Terre, les variations de température liées au soleil peuvent entraîner la décomposition des roches et la formation des sols (Eppes et al., 2016).

Les variations de température peuvent également être significatives dans de nombreux contextes de géo-ingénierie, comme les réservoirs géothermiques (Grant, 2013; Huenges et al., 2013; Kolditz et al., 2013) et les sites de stockage géologique des déchets nucléaires (Faletti and Ethridge, 1988; Hodgkinson et al., 1983; Ougier-Simonin et al., 2011; Paterson and Wong, 2005). Dans de tels environnements, il est fonda-

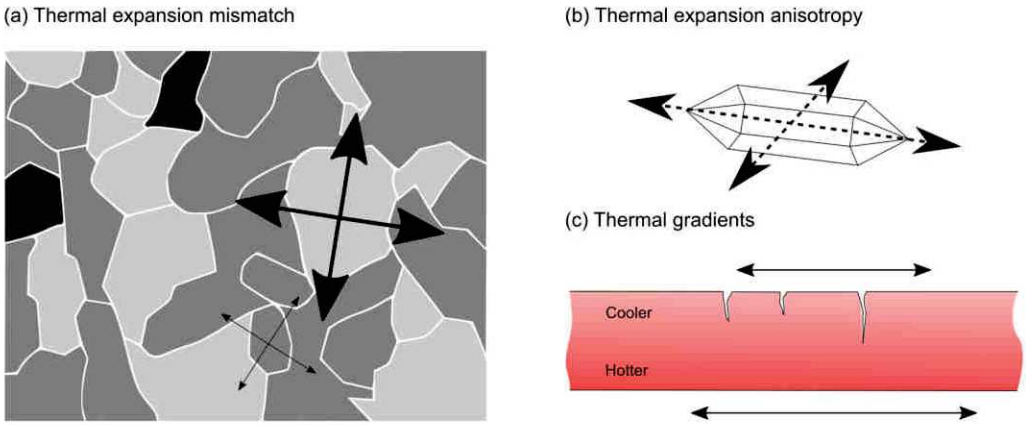

Figure D.1: Des variations spatiales de la dilatation thermique dans la roche peuvent être dues à : une différence entre les modules thermoélastiques de grains voisins ; (b) une anisotropie des modules thermoélastiques entre grains voisins ; et (c) un gradient thermique.

mental de quantifier l'influence des microfissures thermiques sur les propriétés des roches.

La fissuration thermique est liée à l'expansion thermique des minéraux (Kranz, 1983; Meredith et al., 2001), et peut-être due à :

(a) une différence entre les modules thermoélastiques de grains voisins;

(b) une anisotropie des modules thermoélastiques entre grains voisins;

(c) un gradient thermique à travers des grains ou un même grain.

La Figure D.1 illustre les trois causes principales de développement de contraintes d'origine thermique dans une roche.

Pour étudier et suivre l'endommagement des matériaux en laboratoire, une méthode classique consiste à enregistrer les émissions acoustiques (des ondes élastiques transitoires émises lors de l'extension des fissures). Si l'enregistrement d'émissions acoustiques (Acoustic Emission, AE) a été utilisé pour étudier la microfissuration thermique (e.g., Glover et al. (1995), Todd (1973), and Wang et al. (1989)) lors du chauffage, cela a été rarement le cas pendant le refroidissement (e.g., Browning et al. (2016)) et pendant plusieurs cycles de chauffage et de refroidissement. Les vitesses des ondes élastiques sont aussi très sensibles à la présence de microfissures. Généralement, les mesures des vitesses des ondes élastiques sont faites avant et après le chauffage/refroidissement pour quantifier post mortem l'endommagement accumulé pendant l'expérience, et les mesures des vitesses des ondes élastiques in situ sont plus rares (e.g., Ide (1937) and Wang et al. (1989)).

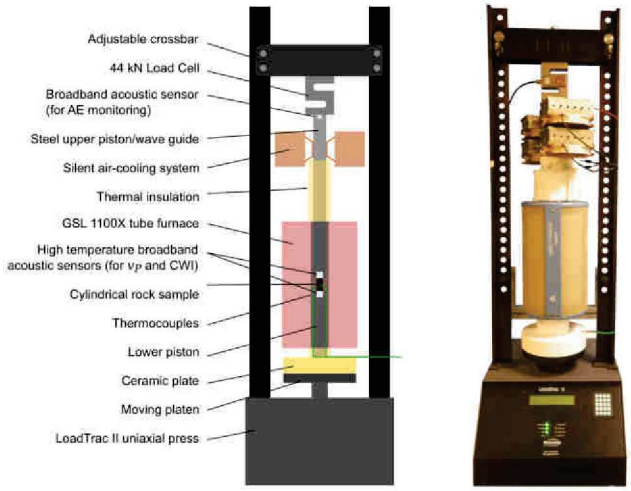

Figure D.2: Schéma de principe et photo du dispositif expérimental pour la surveillance des émissions acoustiques et les mesures de vitesse à des températures élevées. L'appareil est équipé d'une presse uniaxiale LoadTrac II et d'un four tubulaire GSL 1100X. Pour l'enregistrement des AE, un capteur acoustique est intégré dans le haut du piston supérieur. Pour les mesures du temps de parcours des ondes P et l'interférométrie des ondes codas (Coda Wave Inteferometry ; CWI), deux capteurs acoustiques à haute température sont en contact direct avec les extrémités opposées de l'échantillon.

Ici, l'enregistrement des AE et des mesures de vitesse des ondes élastiques a été effectué lors de plusieurs cycles de chauffage et de refroidissement d'échantillons de roche.

D.2 CHAPITRE 2 : MÉTHODES

D.2.1 *Dispositifs expérimentaux*

Le dispositif expérimental principal, conçu spécifiquement pour cette thèse, est une presse uniaxiale associée à un four tubulaire (Figure D.2). Un échantillon cylindrique de roche (40 mm de longueur et 20 mm de diamètre) est placé dans le four, entre les deux pistons de la presse. La contrainte uniaxiale peut atteindre 110 MPa et le four permet de chauffer l'échantillon jusqu'à 1000 °C. La température et le chargement sont asservis pendant toutes les expériences.

L'enregistrement des émissions acoustiques se fait à l'aide un capteur acoustique placé à l'extrémité du piston supérieur, à 450 mm de l'échantillon. Ce capteur reste à température ambiante grâce à un système de ventilation. Pour optimiser le transfert d'énergie entre l'échantillon et le capteur, ce dernier se trouve à l'intérieur du piston, face à l'échantillon. L'acquisition des émissions acoustiques fournit leurs amplitudes et leurs énergies. L'analyse de ces données

permet de distinguer les caractéristiques des émissions acoustiques enregistrées pour différentes roches, ainsi que leur évolution lors de multiples cycles de chauffage/refroidissement.

Pour les mesures de vitesse, deux capteurs acoustiques à haute température (pouvant supporter 500 °C) sont chacun en contact direct avec une face opposée de l'échantillon cylindrique. Leur couplage est assuré par les pistons, qui appliquent une contrainte faible asservie pendant toute la durée des expériences. Cet asservissement de la contrainte axiale est un point fondamental du dispositif expérimental car il permet de compenser les effets de l'expansion thermique des pistons, susceptible notamment de faire osciller le chargement. On utilise deux méthodes pour quantifier les changements de vitesse : (1) une mesure directe de la vitesse des ondes P (v_P) à l'aide du temps d'arrivée ; (2) une mesure par Interférométrie des Ondes de Coda (Coda Wave Interferometry (Snieder (2002); CWI). Si la première méthode est très classique en géophysique, elle a rarement été utilisée à des températures élevées. La deuxième méthode, plus répandue en sismologie mais encore peu utilisée en laboratoire, permet de suivre précisément des changements d'un milieu à travers les délais en temps d'arrivée des ondes diffusées dans l'échantillon. A partir des décalages en temps des ondes de coda, on peut en déduire une variation apparente de vitesse. Cette variation apparente est surtout sensible aux changements de vitesse des ondes S (v_S) ; la mesure de v_S dans la gamme de températures étudiée est un des aspects originaux de cette thèse.

D.2.2 *Caractérisation pétrophysiques des roches thermiquement fissurées.*

Ce chapitre détaille aussi les dispositifs et méthodes de mesure des propriétés physiques, thermiques, et mécaniques sur des échantillons de roche. Ces mesures sont faites à température ambiante, sur des échantillons qui ont été chauffés à des températures différentes, pour caractériser l'influence de la température sur la microfissuration dans la roche, et l'influence des microfissures sur leurs propriétés.

D.3 CHAPITRE 3 : QUANTIFICATION DE L'ENDOMMAGEMENT DANS UN GRANITE FISSURÉ THERMIQUEMENT

Pour modéliser le comportement mécanique de roches fracturées à l'aide d'une approche micromécanique, il faut quantifier la densité de fissures et leurs géométries. Dans ce but, un certain nombre des lames minces ont été préparées à partir d'échantillons de granite traités thermiquement (Garibaldi Grey Granite de British Columbia, Canada) et des images de leur microstructure ont été prises à l'aide d'une caméra haute résolution associée à un microscope optique. Un nouvel algorithme a été créé (en Python) qui permet d'extraire de ces images,

une image binaire ne contenant que les fissures (Figure D.3). A partir de cette image, on peut calculer le nombre de fissures par unité de surface et leurs longueurs. La procédure utilise plusieurs techniques de traitement d'image comme le filtrage et la segmentation pour isoler les éléments fins dans l'image, et révéler le réseau de fissures. L'algorithme est appliqué à des échantillons de granites ayant subi un traitement thermique à des températures comprises entre 100 et 900 °C. Les résultats montrent une augmentation de la densité de fissures avec la température, surtout autour de 573 °C, où a lieu la transition α/β du quartz qui s'accompagne d'une large expansion volumique (Glover et al., 1995). Les valeurs de longueur de fissures et les densités surfaciques sont en accord avec les résultats publiés par des études antérieures, dans lesquelles les fractures avaient été comptées manuellement. La mise en place d'une méthode automatique a permis d'analyser rapidement des centaines d'images et de quantifier l'endommagement de façon systématique et reproductible. Les valeurs d'endommagement sont compatibles avec le modèle de rupture d'Ashby and Sammis (1990) qui permet de prédire la résistance mécanique en compression d'un milieu fracturé. De plus, grâce au modèle de David et al. (2012) (une extension du modèle deWalsh (1965)) pour la raideur de matériaux fissurés, on a pu déduire des densités de fissures à partir de données de compression uniaxiale sur différents échantillons. Les prédictions de ces deux modèles sont généralement en accord avec les mesures expérimentales des propriétés mécaniques, et des densités de fissures mesurées dans les échantillons chauffés.

Ce chapitre de la thèse a été publié dans International Journal of Rock Mechanics and Mining Sciences (IJRMMS ; 17/10/2017). Les méthodes présentées dans ce chapitre sont également utilisées dans les Chapitres 4 et 5 consacrés à la microfissuration thermique dans le granite et les roches volcaniques, afin de quantifier l'endommagement dû aux variations de température.

D.4 CHAPITRE 4 : LA MICROFISSURATION THERMIQUE DANS LE GRANITE

Le granite Westerly (Rhode Island, USA) a été choisi pour cette partie de la thèse car il a fait l'objet de nombreuses études antérieures, certaines consacrées à l'influence de la microfissuration thermique sur ses propriétés physiques. Ce chapitre a pour but de quantifier l'influence de la température sur les vitesses des ondes dans le granite, et en particulier de distinguer l'impact des processus réversibles (l'expansion thermique élastique des grains) et irréversibles (la fissuration). On s'intéresse aussi à la phase de refroidissement et à l'influence de plusieurs cycles de chauffage.

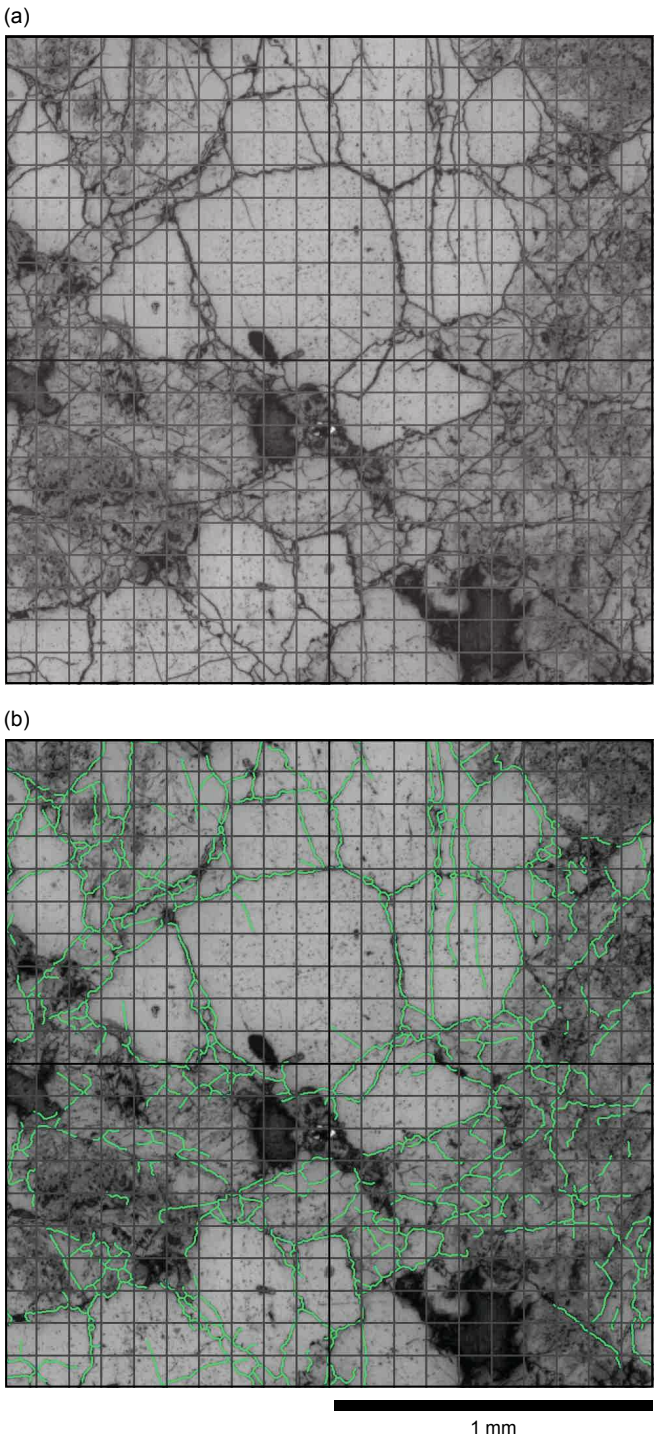

Figure D.3: (a) Une image prise au microscope optique d'une lame mince d'un échantillon de granite Garibaldi Grey chauffé à 600 °C. (b) La même image avec les résultats du traitement d'images superposées.

Grâce au nouveau dispositif décrit au Chapitre 2, un échantillon de granite de Westerly a été soumis à trois cycles de chauffage et de refroidissement, jusqu'à une température maximale de 450 °C (Figure D.4). On a simultanément enregistré les AE et effectué des mesures de vitesse des ondes élastiques (ondes P et CWI). Pendant la première phase de chauffage, on a observé des AE et une forte diminution de v_P (de 50 % entre 25 °C et 450 °C) à partir de 70 °C: 70 °C est la température seuil de la fissuration thermique. Des AE ont été observées pendant le refroidissement, mais l'augmentation de vitesse mesurée suggère que ces AE sont en grande partie dues aux frottements entre les grains, et non à la création ou propagation de microfissures. Ces mesures indiquent une forte microfissuration thermique pendant le premier cycle, surtout pendant la phase de chauffage. Pendant le deuxième cycle, nous observons significativement moins d'AE, et moins encore pendant le troisième cycle, où les variations de v_P sont quasiment réversibles. Il est à noter que pendant chaque cycle, les écarts entre les mesures de vitesse à 25 °C et à 450 °C sont significatifs, et confirment l'importance de mesures aux conditions in situ de température. Ces mesures sont donc fondamentales dans le contexte de la géothermie profonde, comme dans la région du Rhine Graben, où le réservoir est dans un socle granitique. Dans ce genre d'environnement, on interprète souvent les variations des vitesses des ondes P et S comme des changements de saturation de fluide. Ces résultats montrent qu'au moins une partie de ces variations pourraient être liée aux variations de température, avec des conséquences importantes sur les modèles de vitesse dans la zone étudiée. Un article contenant l'ensemble de ces résultats a été publié à Journal of Geophysical Research: Solid Earth (1/3/2018).

Les méthodes utilisées sur le granite de Westerly ont ensuite été appliquées aux granites Garibaldi Grey (British Columbia, Canada) et Lanhélin (Brittany, France), pour étudier l'influence de la taille des grains (la taille moyenne des grains est 0.75 mm dans le granite Westerly, 1 mm dans le granite Garibaldi Grey, et 1.5 mm dans le granite Lanhélin). Pendant les trois cycles de chauffage jusqu'à 450 °C et de refroidissement des granites, la vitesse des ondes P des granites a diminué avec la température pendant chaque cycle, et en particulier pendant le premier cycle (de 30 % dans le granite Garibaldi, et d'environ 50 % dans les granites Lanhélin et Westerly). Grace aux mesures de vitesse et au monitoring des AE, on a pu montrer que la microfissuration thermique a eu lieu pendant le chauffage lors du premier cycle. Comme pour le Westerly Granite, il est suggéré que les émissions acoustiques détectées pendant la phase de refroidissement du premier cycle sont dues aux frottements entre les grains plutôt qu'à la formation de nouvelles fissures.

Ce chapitre se termine par une étude de l'influence de la fissuration thermique sur les propriétés pétrophysiques des granites Garibaldi

Grey et Lanhélin, à travers des mesures sur des échantillons chauffées à des températures allant jusqu'à 1000 °C. Les mesures pétrophysiques comprennent des mesures de la porosité, de la vitesse des ondes acoustiques, de la perméabilité, du module de Young, et de la résistance mécanique. Comme dans le Chapitre 3, une étude approfondie de la microstructure à partir de lames minces a été effectuée, pour décrire les microfissures et quantifier leurs distributions dans chaque roche. Dans les granites, une forte baisse de la vitesse des ondes acoustiques a été observée avec la température à cause de la microfissuration thermique, qui est accentuée entre 500 et 600 °C, à cause de la transition α/β du quartz. Les variations relatives de la porosité, la vitesse acoustique, la perméabilité et de la résistance mécanique avec la température sont plus importantes dans le granite Lanhélin que dans le granite Garibaldi Grey. Ceci s'explique en partie par le fait que le Garibaldi Grey est au départ plus fissuré que le Lanhélin, et peut donc mieux accommoder l'expansion thermique des grains, et aussi par la taille moyenne des grains, qui est plus grande pour le granite Lanhélin et qui par conséquent favorise des fissures plus larges. L'influence de la vitesse de refroidissement a aussi été étudiée : des échantillons des deux granites ont été chauffés à 300 °C et 700 °C et refroidis rapidement par immersion dans de l'eau à environ 15 °C. Le refroidissement rapide, qui est susceptible d'avoir lieu dans des réservoirs géothermales, accentue l'influence de la température sur la microfissuration thermique.

D.5 CHAPITRE 5 : LA MICROFISSURATION THERMIQUE DANS LES ROCHES VOLCANIQUES

Trois roches volcaniques de microstructures différentes ont été sélectionnées : un basalte provenant de Mt. Etna, Italie (porosité d'environ 4 %) ; un basalte "Rubble Creek" de Canada (porosité 1 %) ; et une andésite ("La Lumbre") de Volcàn de Colima, Mexique de porosité plus élevée (23 %). Comme pour les granites, des échantillons de chaque roche ont été chauffés jusqu'à 450 °C et refroidis à 1 °C/min sur trois cycles, et les émissions acoustiques ont été enregistrées et les vitesses des ondes élastiques mesurées (v_P et CWI).

L'influence de la température sur les vitesses au cours du premier cycle varie beaucoup d'une roche à l'autre (Figure D.5). La vitesse v_P a augmenté dans le basalte d'Etna de façon réversible avec la température, du fait de la fermeture des microfissures thermiques lors du chauffage : v_P a augmenté de 3.3 km/s à 3.7 km/s à 450 °C, et ces résultats seront très utiles pour l'interprétation des modèles sismiques de la région de l'Etna. La v_P du basalte Rubble Creek a diminué pendant le chauffage, et nos nouvelles données mettent en évidence une importante microfissuration thermique et une forte diminution de v_P lors le refroidissement. Des AE avaient déjà été enregistrées en re-

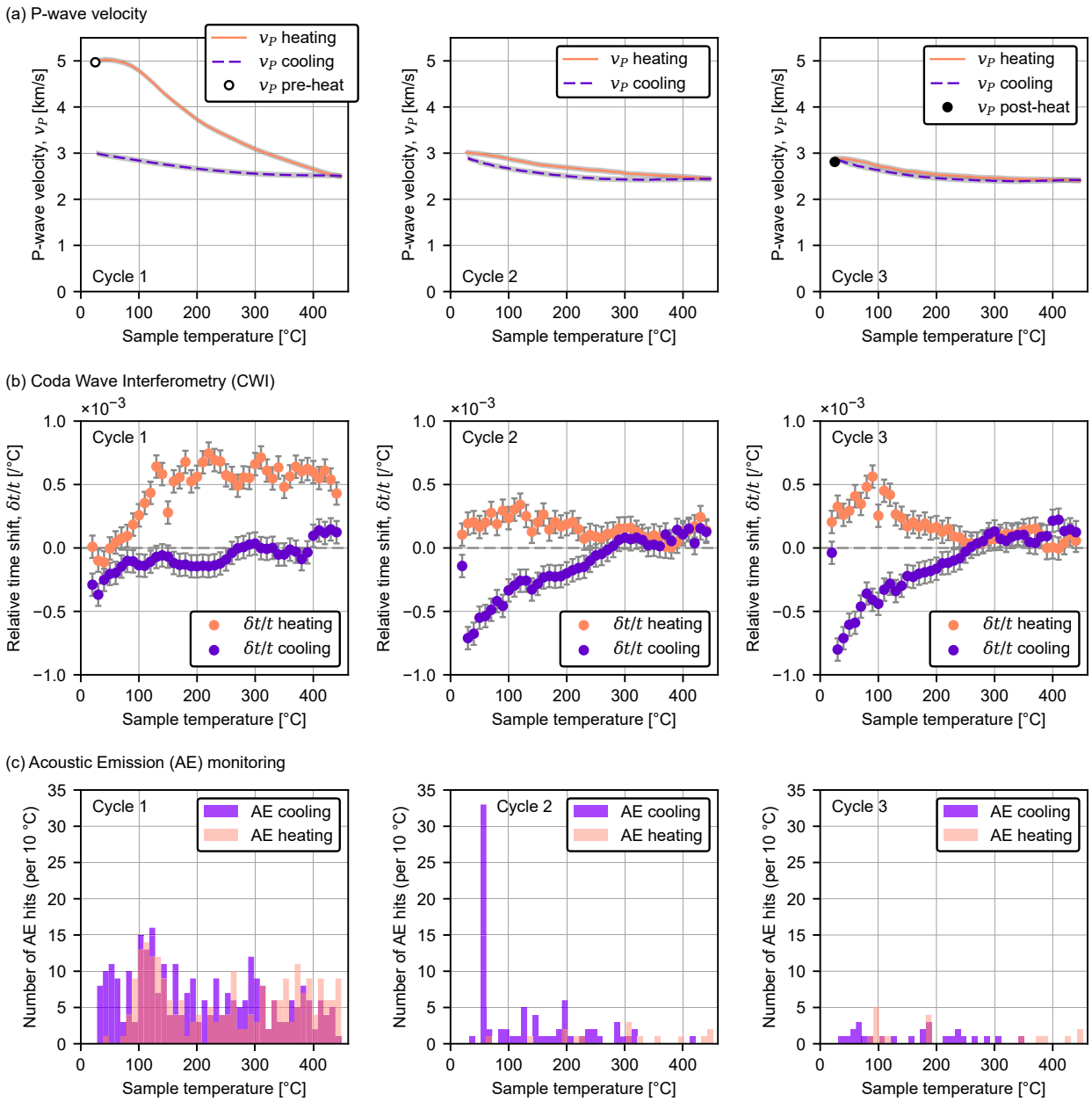

Figure D.4: Mesures effectués pendant trois cycles de chauffage/refroidissement sur un échantillon de granite de Westerly jusqu'à une température maximale de 450 °C. (a) la vitesse des ondes P (v_P) : les cercles représentent les mesures de v_P effectuées à température ambiante avant et après les trois cycles. Les lignes représentent v_P mesurée pendant le chauffage (lignes pleines) et refroidissement (lignes pointillées), calculée à partir du décalage cumulé du temps d'arrivée des ondes P et de la valeur initiale de v_P mesurée avant le chauffage. L'erreur (en gris) est égale à la précision de la mesure de v_P initiale. (b) Interférométrie des ondes coda (CWI) : le décalage relatif en temps des ondes par °C (moyennée sur des intervalles de 10 °C) par rapport à l'échantillon non chauffé. Les barres d'erreur représentent la variabilité potentielle, égale à deux écarts-type de la moyenne des mesures CWI sur un échantillon de verre de quartz (c) émissions acoustiques: le nombre d'AE détecté par intervalle de 10 °C.

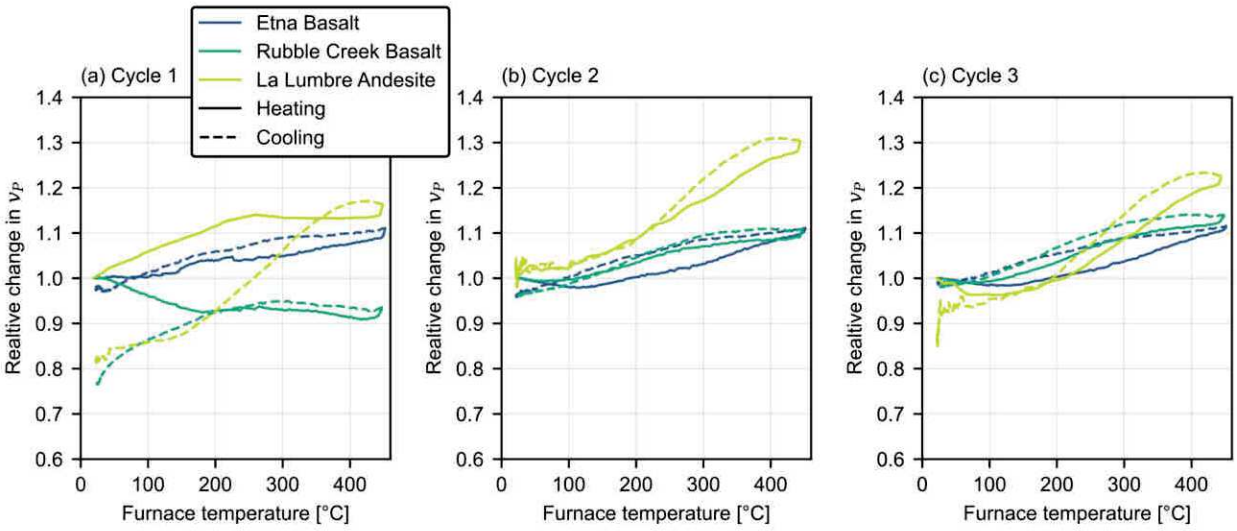

Figure D.5: Les variations relatives de la vitesse des ondes P (v_P) (normalisées aux valeurs initiales de v_P au début de chaque cycle) en fonction de la température de l'échantillon lors de trois cycles de chauffage (lignes pleines) et de refroidissement (lignes pointillées) jusqu'à une température maximale de 450 °C (a-c) des échantillons de basalte de Mt. Etna, Italie (~4 % de porosité), de basalte de Rubble Creek, Canada (~1 % de porosité) et d'andésite de Volcàn de Colima, Mexique (~23 % de porosité).

froidissant (après chauffage) un autre basalte (Browning et al., 2016). Grâce aux mesures de vitesse, nous confirmons qu'il s'agit bien de fissuration. La vitesse v_P dans l'andésite « La Lumbre » augmente pendant le chauffage à cause à la fermeture des fissures préexistantes, jusqu'à ce que l'augmentation de vitesse soit stoppée par la microfissuration à environ 250 °C. Pendant le refroidissement la vitesse de l'andésite diminue, à cause de l'ouverture des fissures.

Comme pour les granites Garibaldi Grey et Lanhélin, des mesures pétrophysiques ont été mises en œuvre sur des échantillons chauffées du basalte Rubble Creek. Avec une augmentation de la température maximale de traitement thermique, il y a eu une baisse de v_P et une augmentation de la perméabilité. La porosité et la résistance mécanique à la rupture ont été quasi-constantes avec le chauffage, ce qui suggère que les nouvelles fissures thermiques sont plus fines que celles dans les granites et n'influencent pas la rupture de la roche. Contrairement aux granites, le refroidissement rapide par immersion dans l'eau n'a pas eu d'influence notable sur l'état de microfissuration du basalte Rubble Creek.

Pour les roches volcaniques, il a été conclu que la microfissuration thermique se produit : pendant le refroidissement dans les roches volcaniques à faible densité de fissures (v_P élevée ; le cas pour le basalte de Rubble Creek) ; pendant le chauffage dans la roche à forte

porosité (andésite La Lumbre) ; et ni pendant le chauffage, ni le refroidissement dans les roches à forte densité de fissures préexistantes (faible v_P ; basalte de Mt Etna).

D.6 CHAPITRE 6 : FISSURATION THERMIQUE SOUS CHARGEMENT UNIAXIAL

Ce dernier chapitre présente une étude pilote de l'influence d'un chargement uniaxial sur la fissuration thermique. Le granite de Westerly et le basalte de Rubble Creek ont été sélectionnées pour cette étude. Des échantillons de ces deux roches ont été chauffés à des températures comprises entre 400 et 700 °C, sous chargement uniaxial à des contraintes comprises entre 0.3 MPa à 30 MPa. La porosité et la vitesse des ondes P ont été mesurées avant et après chaque expérience et les résultats montrent que le chargement uniaxial n'a pas d'influence significative sur l'état de fissuration. Ceci suggère que l'amplitude des contraintes thermiques dans l'échantillon sont plus importantes que les contraintes mécaniques liées au chargement, dans la gamme étudiée.

Une étude plus approfondie comprendra des expériences au cours desquelles des échantillons sont chauffés sous des charges uniaxiales plus importantes et à des températures moins élevées. Une étude quantitative de la microstructure (comme dans le Chapitre 3) permettra une meilleure interprétation des mesures des propriétés physiques et de transport des roches fissurées thermiquement sous chargement.

D.7 CHAPITRE 7 : CONCLUSIONS ET PERSPECTIVES

D.7.1 *Conclusions*

A travers une approche heuristique combinant des techniques classiques et nouvelles d'expérimentation, d'analyse de données, et de modélisation, cette thèse étudie la microfissuration thermique dans la roche de son initiation à ses conséquences sur les propriétés à l'échelle de la roche. A une plus grande échelle, nos résultats s'appliquent à tout environnement sujet à des fluctuations de température, comme les volcans ou les réservoirs géothermiques.

Une partie significative de ce travail de thèse a été consacrée à la conception, le montage et la calibration d'un nouveau dispositif expérimental pour l'enregistrement des AE et des mesures de vitesse des ondes dans des échantillons de roche à haute température. L'interférométrie des ondes coda a été appliquée pour la première fois en laboratoire sur des échantillons de roches à des températures allant jusqu'à 450 °C. La combinaison de ces techniques, lors de plusieurs cycles de chauffage des échantillons a permis de mieux comprendre les niveaux de températures nécessaires à la microfissur-

ation thermique dans les granites et dans les roches volcaniques, et d'identifier différents mécanismes dans les différentes roches.

D.7.2 *Perspectives*

Dans cette thèse, l'influence de la température sur la microstructure des roches a été étudiée à pression ambiante. Une prochaine étape serait d'analyser la formation des microfissures thermiques sous une pression de confinement plus représentative des conditions in situ dans des volcans et des réservoirs géothermiques. A la surface de la Terre les contraintes thermiques induites par le soleil sont suffisantes pour provoquer la microfissuration (Eppes et al., 2016). Il serait intéressant de reproduire les conditions de température et d'humidité présentes à la surface pour mieux comprendre les mécanismes d'altération et de formation des sols. Au cours de ce travail, l'interférométrie des ondes coda a été utilisée pour identifier des changements de microstructure de roches pendant le chauffage et le refroidissement. Ces changements ont été interprétés comme des changements de vitesse (qui est considéré comme le facteur principal), mais ils sont en partis dues à la déformation. Des simulations numériques (par exemple les recherches actuelles de J. Azzola à l'Université de Strasbourg) de la diffusion des ondes dans la roche pourraient amener à une meilleure compréhension de l'influence de ces différents facteurs sur les ondes coda à l'échelle du laboratoire.

BIBLIOGRAPHY

Ackermann, R. J. and C. A. Sorrell (1974). 'Thermal expansion and the high–low transformation in quartz. I. High-temperature X-ray studies.' en. In: *Journal of Applied Crystallography* 7.5, pp. 461–467. ISSN: 0021-8898. DOI: 10.1107/S0021889874010211.

Aggelis, D. G. (2011). 'Classification of cracking mode in concrete by acoustic emission parameters.' en. In: *Mechanics Research Communications* 38.3, pp. 153–157. ISSN: 00936413. DOI: 10.1016/j.mechrescom.2011.03.007.

Aki, K. (1965). 'Maximum likelihood estimate of b in the formula log N= a-bM and its confidence limits.' In: *Bull. Earthq. Res. Inst., Tokyo Univ.* 43, pp. 237–239.

Arena, A., C. Delle Piane, and J. Sarout (2014). 'A new computational approach to cracks quantification from 2D image analysis: Application to micro-cracks description in rocks.' In: *Computers & Geosciences* 66, pp. 106–120. ISSN: 0098-3004. DOI: 10.1016/j.cageo.2014.01.007.

Ashby, M. F. and C. G. Sammis (1990). 'The damage mechanics of brittle solids in compression.' In: *Pure and Applied Geophysics* 133.3, pp. 489–521.

Atkinson, B. K., D. MacDonald, and P. G. Meredith (1984). 'Acoustic Response and Fracture Mechanics of Granite Subjected to Thermal and Stress Cycling Experiments.' English. In: *Ser. Rock Soil Mech.; (United States)* 8.

Atkinson, B. K. (1984). 'Subcritical crack growth in geological materials.' In: *Journal of Geophysical Research: Solid Earth* 89.B6, pp. 4077–4114.

Ayling, M. R., P. G. Meredith, and S. A. F. Murrell (1995). 'Microcracking during triaxial deformation of porous rocks monitored by changes in rock physical properties, I. Elastic-wave propagation measurements on dry rocks.' In: *Tectonophysics*. Influence of Fluids on Deformation Processes in Rocks 245.3–4, pp. 205–221. ISSN: 0040-1951. DOI: 10.1016/0040-1951(94)00235-2.

Battistelli, A., A. Yiheyis, C. Calore, C. Ferragina, and W. Abatneh (2002). 'Reservoir engineering assessment of Dubti geothermal field, Northern Tendaho Rift, Ethiopia.' In: *Geothermics* 31.3, pp. 381–406. ISSN: 0375-6505. DOI: 10.1016/S0375-6505(01)00039-6.

Batzle, M. L. and G. Simmons (1976). 'Microfractures in rocks from two geothermal areas.' In: *Earth and Planetary Science Letters* 30.1, pp. 71–93. ISSN: 0012-821X. DOI: 10.1016/0012-821X(76)90010-8.

Baud, P., T. Reuschlé, and P. Charlez (1996). 'An improved wing crack model for the deformation and failure of rock in compression.'

In: *International journal of rock mechanics and mining sciences & geomechanics abstracts*. Vol. 33. Pergamon, pp. 539–542.

Baud, P., T.-f. Wong, and W. Zhu (2014). 'Effects of porosity and crack density on the compressive strength of rocks.' In: *International Journal of Rock Mechanics and Mining Sciences* 67, pp. 202–211. ISSN: 1365-1609. DOI: 10.1016/j.ijrmms.2013.08.031.

Baud, P. (1995). 'Etude Théorique et Expérimentale de la Fracturation des Roches de la Croûte.' PhD thesis.

Baud, P., A. Schubnel, and T.-f. Wong (2000). 'Dilatancy, compaction, and failure mode in Solnhofen limestone.' en. In: *Journal of Geophysical Research: Solid Earth* 105.B8, pp. 19289–19303. ISSN: 2156-2202. DOI: 10.1029/2000JB900133.

Bauer, S. J., B. Johnson, and others (1979). 'Effects of slow uniform heating on the physical properties of the Westerly and Charcoal granites.' In: *20th US Symposium on Rock Mechanics (USRMS)*. American Rock Mechanics Association.

Bauer, S. J. and J. Handin (1983). 'Thermal expansion and cracking of three confined water-saturated igneous rocks to 800° C.' In: *Rock Mechanics and Rock Engineering* 16.3, pp. 181–198.

Baujard, C., A. Genter, E. Dalmais, V. Maurer, R. Hehn, R. Rosillette, J. Vidal, and J. Schmittbuhl (2017). 'Hydrothermal characterization of wells GRT-1 and GRT-2 in Rittershoffen, France: Implications on the understanding of natural flow systems in the rhine graben.' In: *Geothermics* 65, pp. 255–268.

Björnsson, A., K. Saemundsson, P. Einarsson, E. Tryggvason, and K. Grönvold (1977). 'Current rifting episode in north Iceland.' In: *Nature* 266.5600, p. 318.

Bonnet, E., O. Bour, N. E. Odling, P. Davy, I. Main, P. Cowie, and B. Berkowitz (2001). 'Scaling of fracture systems in geological media.' en. In: *Reviews of Geophysics* 39.3, pp. 347–383. ISSN: 1944-9208. DOI: 10.1029/1999RG000074.

Brace, W. F. and A. H. Jones (1971). 'Comparison of uniaxial deformation in shock and static loading of three rocks.' In: *Journal of Geophysical Research* 76.20, pp. 4913–4921.

Brace, W. F., B. W. Paulding, and C. Scholz (1966). 'Dilatancy in the fracture of crystalline rocks.' en. In: *Journal of Geophysical Research* 71.16, pp. 3939–3953. ISSN: 2156-2202. DOI: 10.1029/JZ071i016p03939.

Brace, W. F., J. B. Walsh, and W. T. Frangos (1968). 'Permeability of granite under high pressure.' en. In: *Journal of Geophysical Research* 73.6, pp. 2225–2236. ISSN: 2156-2202. DOI: 10.1029/JB073i006p02225.

Brace, W. F., E. Silver, K. Hadley, and C. Goetze (1972). 'Cracks and pores: A closer look.' In: *Science* 178.4057, pp. 162–164.

Bérard, T. and F. Cornet (2003). 'Evidence of thermally induced borehole elongation: a case study at Soultz, France.' In: *International Journal of Rock Mechanics and Mining Sciences* 40.7-8, pp. 1121–1140. ISSN: 13651609. DOI: 10.1016/S1365-1609(03)00118-7.

Brownell, D. H., S. K. Garg, and J. W. Pritchett (1977). 'Governing equations for geothermal reservoirs.' en. In: *Water Resources Research* 13.6, pp. 929–934. ISSN: 1944-7973. DOI: 10.1029/WR013i006p00929.

Browning, J., P. Meredith, and A. Gudmundsson (2016). 'Cooling-dominated cracking in thermally stressed volcanic rocks.' en. In: *Geophysical Research Letters* 43.16, 2016GL070532. ISSN: 1944-8007. DOI: 10.1002/2016GL070532.

Bésuelle, P., J. Desrues, and S. Raynaud (2000). 'Experimental characterisation of the localisation phenomenon inside a Vosges sandstone in a triaxial cell.' In: *International Journal of Rock Mechanics and Mining Sciences* 37.8, pp. 1223–1237.

Budiansky, B. and R. J. O'Connell (1976). 'Elastic moduli of a cracked solid.' In: *International Journal of Solids and Structures* 12.2, pp. 81–97. ISSN: 0020-7683. DOI: 10.1016/0020-7683(76)90044-5.

Calò, M., C. Dorbath, F. Cornet, and N. Cuenot (2011). 'Large-scale aseismic motion identified through 4-D P-wave tomography: Temporal subsetting of the stimulation period.' en. In: *Geophysical Journal International* 186.3, pp. 1295–1314. ISSN: 0956540X. DOI: 10.1111/j.1365-246X.2011.05108.x.

Cardwell, R. K., D. S. Chinn, G. F. Moore, and D. L. Turcotte (1978). 'Frictional heating on a fault zone with finite thickness.' In: *Geophysical Journal International* 52.3, pp. 525–530. ISSN: 0956-540X. DOI: 10.1111/j.1365-246X.1978.tb04247.x.

Case, E. D. (1984). 'The effect of microcracking upon the Poisson's ratio for brittle materials.' In: *Journal of materials science* 19.11, pp. 3702–3712.

Chaki, S., M. Takarli, and W. Agbodjan (2008). 'Influence of thermal damage on physical properties of a granite rock: Porosity, permeability and ultrasonic wave evolutions.' In: *Construction and Building Materials* 22.7, pp. 1456–1461. ISSN: 0950-0618. DOI: 10.1016/j.conbuildmat.2007.04.002.

Chayes, F (1952). 'The Finer-Grained Calcalkaline Granites of New England.' In: *Journal of Geology - J GEOL* 60, pp. 207–254. DOI: 10.1086/625960.

Chen, S., C. Yang, and G. Wang (2017). 'Evolution of thermal damage and permeability of Beishan granite.' In: *Applied Thermal Engineering* 110, pp. 1533–1542. ISSN: 1359-4311. DOI: 10.1016/j.applthermaleng.2016.09.075.

Choi, N.-S., T.-W. Kim, and K. Y. Rhee (2005). 'Kaiser effects in acoustic emission from composites during thermal cyclic-loading.' In: *NDT & E International* 38.4, pp. 268–274. ISSN: 0963-8695. DOI: 10.1016/j.ndteint.2004.09.005.

Clarke, D. R. (1980). 'Microfracture in brittle solids resulting from anisotropic shape changes.' In: *Acta Metallurgica* 28.7, pp. 913–924.

Clauser, C and E Huenges (1995). 'Thermal conductivity of rocks and minerals.' In: *A Handbook of Physical Constants: Global Earth Physics* 3, pp. 105–126. ISSN: 0-87590-851-9. DOI: 10.1029/RF003p0105.

Coelho, L. P. (2013). 'Mahotas: Open source software for scriptable computer vision.' en. In: *Journal of Open Research Software* 1.1. ISSN: 2049-9647. DOI: 10.5334/jors.ac.

Cornet, F. H. and T. Bérard (2003). 'A case example of integrated stress profile evaluation.' In: *3rd International Symposium on Rock Stress, edited by K. Sugawara, Y. Obara, and A. Sato*, pp. 23–24.

Crampin, S. (1981). 'A review of wave motion in anisotropic and cracked elastic-media.' In: *Wave motion* 3.4, pp. 343–391.

Darot, M., Y. Gueguen, and M.-L. Baratin (1992). 'Permeability of thermally cracked granite.' In: *Geophysical Research Letters* 19.9, pp. 869–872. ISSN: 0094-8276. DOI: 10.1029/92GL00579.

David, C., B. Menendez, and M. Darot (1999). 'Influence of stress-induced and thermal cracking on physical properties and microstructure of La Peyratte granite.' In: *International Journal of Rock Mechanics and Mining Sciences* 36.4, pp. 433–448.

David, E. C., N. Brantut, A. Schubnel, and R. W. Zimmerman (2012). 'Sliding crack model for nonlinearity and hysteresis in the uniaxial stress-strain curve of rock.' In: *International Journal of Rock Mechanics and Mining Sciences* 52, pp. 9–17. DOI: 10.1016/j.ijrmms.2012.02.001.

Davidge, R. W. (1981). 'Cracking at grain boundaries in polycrystalline brittle materials.' In: *Acta Metallurgica* 29.10, pp. 1695–1702.

De Luca, G., L. Filippi, G. Patanè, R. Scarpa, and S. Vinciguerra (1997). 'Three-dimensional velocity structure and seismicity of Mt. Etna Volcano, Italy.' In: *Journal of Volcanology and Geothermal Research* 79.1, pp. 123–138. ISSN: 0377-0273. DOI: 10.1016/S0377-0273(97)00026-7.

De Simone, S., V. Vilarrasa, J. Carrera, A. Alcolea, and P. Meier (2013). 'Thermal coupling may control mechanical stability of geothermal reservoirs during cold water injection.' en. In: *Physics and Chemistry of the Earth, Parts A/B/C* 64, pp. 117–126. ISSN: 14747065. DOI: 10.1016/j.pce.2013.01.001.

Delle Piane, C., A. Arena, J. Sarout, L. Esteban, and E. Cazes (2015). 'Micro-crack enhanced permeability in tight rocks: An experimental and microstructural study.' In: *Tectonophysics*, pp. 1–8. DOI: 10.1016/j.tecto.2015.10.001.

Dempsey, D., S. Kelkar, N. Davatzes, S. Hickman, and D. Moos (2015). 'Numerical modeling of injection, stress and permeability enhancement during shear stimulation at the Desert Peak Enhanced Geothermal System.' In: *International Journal of Rock Mechanics and Mining Sciences* 78, pp. 190–206. ISSN: 1365-1609. DOI: 10.1016/j.ijrmms.2015.06.003.

Dezayes, C., A. Genter, and B. Valley (2010). 'Structure of the low permeable naturally fractured geothermal reservoir at Soultz.' In: *Comptes Rendus Geoscience* 342.7-8, pp. 517–530. ISSN: 1631-0713. DOI: 10.1016/j.crte.2009.10.002.

Dong, G. and Y. Zou (2017). 'A Novel Study of Waveguide Propagation Rules of Coal Rock AE Signal: Effects of Waveguide Size and Installation Method on the Propagation Rules of Coal Rock AE Signal.' en. In: *Sustainability* 9.7, p. 1209. DOI: 10.3390/su9071209.

Duclos, R. and J. Paquet (1991). 'High-temperature behaviour of basalts—role of temperature and strain rate on compressive strength and Kic toughness of partially glassy basalts at atmospheric pressure.' In: *International Journal of Rock Mechanics and Mining Sciences & Geomechanics Abstracts*. Vol. 28. Elsevier, pp. 71–76.

Edwards, R. H. (1951). 'Stress concentrations around spheroidal inclusions and cavities.' In: *JOURNAL OF APPLIED MECHANICS-TRANSACTIONS OF THE ASME* 18.1, pp. 19–30.

Eichelberger, J. C., C. R. Carrigan, H. R. Westrich, and R. H. Price (1986). 'Non-explosive silicic volcanism.' In: *Nature* 323.6089, pp. 598–602.

Elders, W. A., J. R. Hoagland, S. D. McDowell, and J. M. Cobo (1979). 'Hydrothermal mineral zones in the geothermal reservoir of Cerro Prieto.' In: *Geothermics* 8.3, pp. 201–209. ISSN: 0375-6505. DOI: 10.1016/0375-6505(79)90042-7.

Engelder, T. (1987). 'Joints and shear fractures in rock.' In: *Fracture mechanics of rock*, pp. 27–69.

Eppes, M. C., B. Magi, B. Hallet, E. Delmelle, P. Mackenzie-Helnwein, K. Warren, and S. Swami (2016). 'Deciphering the role of solar-induced thermal stresses in rock weathering.' en. In: *Geological Society of America Bulletin*, B31422.1. ISSN: 0016-7606, 1943-2674. DOI: 10.1130/B31422.1.

Evans, A. G. (1978a). *Acoustic emission sources in brittle solids*. Tech. rep. California Univ., Berkeley (USA). Lawrence Berkeley Lab.

— (1978b). 'Microfracture from thermal expansion anisotropy—I. Single phase systems.' In: *Acta Metallurgica* 26.12, pp. 1845–1853. ISSN: 0001-6160. DOI: 10.1016/0001-6160(78)90097-4.

Faletti, D. W. and L. J. Ethridge (1988). 'A method for predicting cracking in waste glass canisters.' In: *Nuclear and chemical waste management* 8.2, pp. 123–133.

Farquharson, J. I., M. J. Heap, Y. Lavallée, N. R. Varley, and P. Baud (2016). 'Evidence for the development of permeability anisotropy in lava domes and volcanic conduits.' en. In: *Journal of Volcanology and Geothermal Research* 323, pp. 163–185. ISSN: 03770273. DOI: 10.1016/j.jvolgeores.2016.05.007.

Farquharson, J. I., P. Baud, and M. J. Heap (2017). 'Inelastic compaction and permeability evolution in volcanic rock.' en. In: *Solid*

Earth 8.2, pp. 561–581. ISSN: 1869-9529. DOI: 10.5194/se-8-561-2017.

Farquharson, J., M. J. Heap, N. R. Varley, P. Baud, and T. Reuschlé (2015). 'Permeability and porosity relationships of edifice-forming andesites: A combined field and laboratory study.' In: *Journal of Volcanology and Geothermal Research* 297, pp. 52–68. ISSN: 0377-0273. DOI: 10.1016/j.jvolgeores.2015.03.016.

Fortin, J., S. Stanchits, S. Vinciguerra, and Y. Guéguen (2011). 'Influence of thermal and mechanical cracks on permeability and elastic wave velocities in a basalt from Mt. Etna volcano subjected to elevated pressure.' In: *Tectonophysics*. Thermo-Hydro-Chemo-Mechanical Couplings in Rock Physics and Rock Mechanics 503.1, pp. 60–74. ISSN: 0040-1951. DOI: 10.1016/j.tecto.2010.09.028.

Fredrich, J. T. and T.-f. Wong (1986). 'Micromechanics of thermally induced cracking in three crustal rocks.' In: *Journal of Geophysical Research* 91.B12, pp. 12743–12743. ISSN: 0148-0227. DOI: 10.1029/JB091iB12p12743.

Fredrich, J. T., B. Evans, and T.-f. Wong (1989). 'Micromechanics of the brittle to plastic transition in Carrara marble.' en. In: *Journal of Geophysical Research: Solid Earth* 94.B4, pp. 4129–4145. ISSN: 2156-2202. DOI: 10.1029/JB094iB04p04129.

Fukuhara, M. and A. Sanpei (1994). 'High temperature-elastic moduli and internal dilational and shear frictions of fused quartz.' In: *Japanese journal of applied physics* 33.5S, p. 2890.

Gaunt, H. E., P. R. Sammonds, P. G. Meredith, and A. Chadderton (2016). 'Effect of temperature on the permeability of lava dome rocks from the 2004–2008 eruption of Mount St. Helens.' en. In: *Bulletin of Volcanology* 78.4, p. 30. ISSN: 0258-8900, 1432-0819. DOI: 10.1007/s00445-016-1024-5.

Genter, A., K. Evans, N. Cuenot, D. Fritsch, and B. Sanjuan (2010). 'Contribution of the exploration of deep crystalline fractured reservoir of Soultz to the knowledge of enhanced geothermal systems (EGS).' In: *Comptes Rendus Geoscience*. Vers l'exploitation des ressources géothermiques profondes des systèmes hydrothermaux convectifs en milieux naturellement fracturésOn the way to the exploitation of deep geothermal resources in naturally fractured environments 342.7–8, pp. 502–516. ISSN: 1631-0713. DOI: 10.1016/j.crte.2010.01.006.

Germanovich, L. N., R. L. Salganik, A. V. Dyskin, and K. K. Lee (1994). 'Mechanisms of brittle fracture of rock with pre-existing cracks in compression.' In: *Pure and Applied Geophysics* 143.1, pp. 117–149.

Ghahremani, F. (1980). 'Effect of grain boundary sliding on anelasticity of polycrystals.' In: *International Journal of Solids and Structures* 16.9, pp. 825–845.

Glover, P. W. J., P. Baud, M. Darot, P. G. Meredith, S. A. Boon, M. LeRavalec, S. Zoussi, and T. Reuschlé (1995). 'Alpha/Beta Phase

Transitions in Quartz Monitored using Acoustic Emissions.' In: *Geophysical Journal International* 120, pp. 775–782.

Grant, M. (2013). *Geothermal Reservoir Engineering*. en. Elsevier. ISBN: 978-0-323-15291-4.

Grant, M., J. Clearwater, J. Quinao, P. Bixley, and M. Le Brun (2013). 'Thermal Stimulation of Geothermal Wells: A Review of Field Data.' In: *Thirty-Eighth Workshop on Geothermal Reservoir Engineering*.

Gérard, A. and O. Kappelmeyer (1987). 'The Soultz-sous-Forêts project.' In: *Geothermics* 16.4, pp. 393–399.

Gérard, A., A. Genter, T. Kohl, P. Lutz, P. Rose, and F. Rummel (2006). 'The deep EGS (Enhanced Geothermal System) project at Soultz-sous-Forêts (Alsace, France).' en. In: *Geothermics* 35.5-6, pp. 473–483. ISSN: 03756505. DOI: 10.1016/j.geothermics.2006.12.001.

Géraud, Y. (1994). 'Variations of connected porosity and inferred permeability in a thermally cracked granite.' en. In: *Geophysical Research Letters* 21.11, pp. 979–982. ISSN: 1944-8007. DOI: 10.1029/94GL00642.

Griffith, A. A. (1921). 'The phenomena of rupture and flow in solids.' In: *Philosophical transactions of the royal society of london. Series A, containing papers of a mathematical or physical character* 221, pp. 163–198.

Griffiths, L., M. J. Heap, F. Wang, D. Daval, H. A. Gilg, P. Baud, J. Schmittbuhl, and A. Genter (2016). 'Geothermal implications for fracture-filling hydrothermal precipitation.' In: *Geothermics* 64, pp. 235–245. ISSN: 0375-6505. DOI: 10.1016/j.geothermics.2016.06.006.

Griffiths, L., M. J. Heap, P. Baud, and J. Schmittbuhl (2017a). 'Quantification of microcrack characteristics and implications for stiffness and strength of granite.' In: *International Journal of Rock Mechanics and Mining Sciences* 100, pp. 138–150. ISSN: 13651609. DOI: 10.1016/j.ijrmms.2017.10.013.

Griffiths, L., M. J. Heap, T. Xu, C.-f. Chen, and P. Baud (2017b). 'The influence of pore geometry and orientation on the strength and stiffness of porous rock.' In: *Journal of Structural Geology* 96, pp. 149–160. ISSN: 01918141. DOI: 10.1016/j.jsg.2017.02.006.

Griffiths, L., O. Lengliné, M. J. Heap, P. Baud, and J. Schmittbuhl (2018). 'Thermal Cracking in Westerly Granite Monitored Using Direct Wave Velocity, Coda Wave Interferometry, and Acoustic Emissions.' In: *Journal of Geophysical Research: Solid Earth* 0.0. ISSN: 2169-9313. DOI: 10.1002/2017JB015191.

Grêt, A. (2005). 'Monitoring rapid temporal change in a volcano with coda wave interferometry.' en. In: *Geophysical Research Letters* 32.6. ISSN: 0094-8276. DOI: 10.1029/2004GL021143.

Grêt, A. A. (2004). 'Time-lapse monitoring with coda wave interferometry.' PhD thesis. Colorado School of Mines.

Grêt, A., R. Snieder, and J. Scales (2006). 'Time-lapse monitoring of rock properties with coda wave interferometry.' In: *Journal of Geophysical Research: Solid Earth* 111.3, pp. 1–11. ISSN: 0148-0227. DOI: 10.1029/2004JB003354.

Guéguen, Y. and J. Dienes (1989). 'Transport properties of rocks from statistics and percolation.' In: *Mathematical geology* 21.1, pp. 1–13.

Guéguen, Y. and A. Schubnel (2003). 'Elastic wave velocities and permeability of cracked rocks.' In: *Tectonophysics*. Physical Properties of Rocks and other Geomaterials, a Special Volume to honour Professor H. Kern 370.1, pp. 163–176. ISSN: 0040-1951. DOI: 10.1016/S0040-1951(03)00184-7.

Hadley, K. (1976). 'Comparison of calculated and observed crack densities and seismic velocities in westerly granite.' en. In: *Journal of Geophysical Research* 81.20, pp. 3484–3494. ISSN: 2156-2202. DOI: 10.1029/JB081i020p03484.

Hall, D. L. and R. J. Bodnar (1989). 'Comparison of fluid inclusion decrepitation and acoustic emission profiles of Westerly granite and Sioux quartzite.' In: *Tectonophysics* 168.4, pp. 283–296. ISSN: 0040-1951. DOI: 10.1016/0040-1951(89)90223-0.

Hansen, A. and J. Schmittbuhl (2003). 'Origin of the universal roughness exponent of brittle fracture surfaces: stress-weighted percolation in the damage zone.' In: *Physical review letters* 90.4, p. 045504.

Hashin, Z. (1988). 'The differential scheme and its application to cracked materials.' In: *Journal of the Mechanics and Physics of Solids* 36.6, pp. 719–734. ISSN: 0022-5096. DOI: 10.1016/0022-5096(88)90005-1.

Hasselman, D. P. H. (1969). 'Unified theory of thermal shock fracture initiation and crack propagation in brittle ceramics.' In: *Journal of the American Ceramic society* 52.11, pp. 600–604.

Healy, D., R. E. Rizzo, D. G. Cornwell, N. J. C. Farrell, H. Watkins, N. E. Timms, E. Gomez-Rivas, and M. Smith (2017). 'FracPaQ: A MATLAB™ toolbox for the quantification of fracture patterns.' In: *Journal of Structural Geology* 95, pp. 1–16. ISSN: 0191-8141. DOI: 10.1016/j.jsg.2016.12.003.

Heap, M. J., S. Vinciguerra, and P. G. Meredith (2009a). 'The evolution of elastic moduli with increasing crack damage during cyclic stressing of a basalt from Mt. Etna volcano.' In: *Tectonophysics* 471.1-2, pp. 153–160. ISSN: 00401951. DOI: 10.1016/j.tecto.2008.10.004.

Heap, M. J., P. Baud, P. G. Meredith, A. F. Bell, and I. G. Main (2009b). 'Time-dependent brittle creep in Darley Dale sandstone.' In: *Journal of Geophysical Research: Solid Earth* 114.B7.

Heap, M. J., Y. Lavallée, a. Laumann, K. U. Hess, P. G. Meredith, D. B. Dingwell, S. Huismann, and F. Weise (2013a). 'The influence of thermal-stressing (up to 1000 °c) on the physical, mechanical, and chemical properties of siliceous-aggregate, high-strength con-

crete.' In: *Construction and Building Materials* 42, pp. 248–265. DOI: 10.1016/j.conbuildmat.2013.01.020.

Heap, M. J., S. Mollo, S. Vinciguerra, Y. Lavallée, K. U. Hess, D. B. Dingwell, P. Baud, and G. Iezzi (2013b). 'Thermal weakening of the carbonate basement under Mt. Etna volcano (Italy): Implications for volcano instability.' In: *Journal of Volcanology and Geothermal Research* 250, pp. 42–60. DOI: 10.1016/j.jvolgeores.2012.10.004.

Heap, M. J., Y. Lavallée, L. Petrakova, P. Baud, T. Reuschlé, N. R. Varley, and D. B. Dingwell (2014a). 'Microstructural controls on the physical and mechanical properties of edifice-forming andesites at Volcán de Colima, Mexico.' en. In: *Journal of Geophysical Research: Solid Earth* 119.4, 2013JB010521. ISSN: 2169-9356. DOI: 10.1002/2013JB010521.

Heap, M. J., M. Violay, F. B. Wadsworth, and J. Vasseur (2017). 'From rock to magma and back again: The evolution of temperature and deformation mechanism in conduit margin zones.' en. In: *Earth and Planetary Science Letters* 463, pp. 92–100. ISSN: 0012821X. DOI: 10.1016/j.epsl.2017.01.021.

Heap, M. J., T. Xu, and C.-f. Chen (2014b). 'The influence of porosity and vesicle size on the brittle strength of volcanic rocks and magma.' In: *Bulletin of Volcanology* 76.9, pp. 1–15.

Heap, M. J., F. B. Wadsworth, T. Xu, C.-f. Chen, and C. Tang (2016). 'The strength of heterogeneous volcanic rocks: A 2D approximation.' en. In: *Journal of Volcanology and Geothermal Research* 319, pp. 1–11. ISSN: 03770273. DOI: 10.1016/j.jvolgeores.2016.03.013.

Heard, H. C. and L. Page (1982). 'Elastic moduli, thermal expansion, and inferred permeability of two granites to 350°C and 55 megapascals.' In: *Journal of Geophysical Research* 87.2, pp. 9340–9340. DOI: 10.1029/JB087iB11p09340.

Heimisson, E. R., P. Einarsson, F. Sigmundsson, and B. Brandsdóttir (2015). 'Kilometer-scale Kaiser effect identified in Krafla volcano, Iceland: Large-Scale Kaiser Effect.' en. In: *Geophysical Research Letters* 42.19, pp. 7958–7965. ISSN: 00948276. DOI: 10.1002/2015GL065680.

Heuze, F. E. (1983). 'High-temperature mechanical, physical and Thermal properties of granitic rocks— A review.' In: *International Journal of Rock Mechanics and Mining Sciences & Geomechanics Abstracts* 20.1, pp. 3–10. ISSN: 0148-9062. DOI: 10.1016/0148-9062(83)91609-1.

Hill, R. (1952). 'The elastic behaviour of a crystalline aggregate.' In: *Proceedings of the Physical Society. Section A* 65.5, p. 349.

Hodgkinson, D. P., D. A. Lever, and J. Rae (1983). 'Thermal aspects of radioactive waste burial in hard rock.' In: *Progress in Nuclear Energy* 11.2, pp. 183–218.

Homand-Etienne, F. and R. Houpert (1989). 'Thermally induced microcracking in granites: characterization and analysis.' In: *International Journal of Rock Mechanics and Mining Sciences & Geomechanics Abstracts* 26.2, pp. 125–134. ISSN: 0148-9062. DOI: 10.1016/0148-9062(89)90001-6.

Homand-Etienne, F. and J.-P. Troalen (1984). 'Behaviour of granites and limestones subjected to slow and homogeneous temperature changes.' In: *Engineering Geology* 20, pp. 219–233. ISSN: 0013-7952. DOI: 10.1016/0013-7952(84)90002-4.

Horii, H. and S. Nemat-Nasser (1986). 'Brittle Failure in Compression: Splitting, Faulting and Brittle-Ductile Transition.' In: *Philosophical Transactions of the Royal Society A: Mathematical, Physical and Engineering Sciences* 319.1549, pp. 337–374. DOI: 10.1098/rsta.1986.0101.

Huenges, E., T. Kohl, O. Kolditz, J. Bremer, M. Scheck-Wenderoth, and T. Vienken (2013). 'Geothermal energy systems: research perspective for domestic energy provision.' In: *Environmental Earth Sciences* 70.8, pp. 3927–3933.

Hughes, D. S. and C. Maurette (1957). 'Variation of elastic wave velocities in basic igneous rocks with pressure and temperature.' In: *Geophysics* 22.1, pp. 23–31.

Ide, J. M. (1937). 'The Velocity of Sound in Rocks and Glasses as a Function of Temperature.' en. In: *The Journal of Geology* 45.7, pp. 689–716. ISSN: 0022-1376, 1537-5269. DOI: 10.1086/624595.

Jaeger, J. C., N. G. Cook, and R. Zimmerman (2009). *Fundamentals of rock mechanics*. John Wiley & Sons.

Jeanne, P., J. Rutqvist, and P. F. Dobson (2017). 'Influence of injection-induced cooling on deviatoric stress and shear reactivation of pre-existing fractures in Enhanced Geothermal Systems.' In: *Geothermics* 70, pp. 367–375. ISSN: 0375-6505. DOI: 10.1016/j.geothermics.2017.08.003.

Johnson, B., A. F. Gangi, J. Handin, and others (1978). 'Thermal cracking of rock subjected to slow, uniform temperature changes.' In: *19th US Symposium on Rock Mechanics (USRMS)*. American Rock Mechanics Association.

Jones, C, G Keaney, P. Meredith, and S. Murrell (1997). 'Acoustic emission and fluid permeability measurements on thermally cracked rocks.' In: *Physics and Chemistry of the Earth* 22.1, pp. 13–17. DOI: 10.1016/S0079-1946(97)00071-2.

Kaiser, J. (1953). 'Erkenntnisse und Folgerungen aus der Messung von Geräuschen bei Zugbeanspruchung von metallischen Werkstoffen.' de. In: *Archiv für das Eisenhüttenwesen* 24.1-2, pp. 43–45. ISSN: 1869-344X. DOI: 10.1002/srin.195301381.

Kant, M. A., J. Ammann, E. Rossi, C. Madonna, D. Höser, and P. R. von Rohr (2017). 'Thermal properties of Central Aare granite for temperatures up to 500°C: irreversible changes due to thermal

crack formation.' en. In: *Geophysical Research Letters*, 2016GL070990. ISSN: 1944-8007. DOI: 10.1002/2016GL070990.

Karner, S. L., C. Marone, and B. Evans (1997). 'Laboratory study of fault healing and lithification in simulated fault gouge under hydrothermal conditions.' In: *Tectonophysics*. Earthquake Generation Processes: Environmental Aspects and Physical Modelling 277.1, pp. 41–55. ISSN: 0040-1951. DOI: 10.1016/S0040-1951(97)00077-2.

Kemeny, J. M. and N. G. Cook (1991). 'Micromechanics of deformation in rocks.' In: *Toughening mechanisms in quasi-brittle materials*. Springer, pp. 155–188.

Kendrick, J. E., R. Smith, P. Sammonds, P. G. Meredith, M. Dainty, and J. S. Pallister (2013). 'The influence of thermal and cyclic stressing on the strength of rocks from Mount St. Helens, Washington.' en. In: *Bulletin of Volcanology* 75.7, p. 728. ISSN: 0258-8900, 1432-0819. DOI: 10.1007/s00445-013-0728-z.

Kern, H. (1978). 'The effect of high temperature and high confining pressure on compressional wave velocities in quartz-bearing and quartz-free igneous and metamorphic rocks.' In: *Tectonophysics* 44.1, pp. 185–203.

— (1979). 'Effect of high-low quartz transition on compressional and shear wave velocities in rocks under high pressure.' In: *Physics and Chemistry of Minerals* 4.2, pp. 161–171. DOI: 10.1007/BF00307560.

— (1982). 'Elastic-wave velocity in crustal and mantle rocks at high pressure and temperature: the role of the high-low quartz transition and of dehydration reactions.' In: *Physics of the Earth and Planetary Interiors* 29.1, pp. 12–23.

Kitao, K., K. Ariki, H. Watanabe, and K. Wakita (1995). 'Cold-water well stimulation experiments in the Sumikawa geothermal field, Japan.' In: *Bulletin of the Geothermal Resources Council* 24.2, pp. 53–61.

Klein, E. and T. Reuschlé (2004). 'A pore crack model for the mechanical behaviour of porous granular rocks in the brittle deformation regime.' In: *International journal of rock mechanics and mining sciences* 41.6, pp. 975–986.

Klinkenberg, L. J. (1941). 'The permeability of porous media to liquids and gases.' In: *Drilling and production practice*. American Petroleum Institute.

Kohl, T., K. F. Evansi, R. J. Hopkirk, and L. Rybach (1995). 'Coupled hydraulic, thermal and mechanical considerations for the simulation of hot dry rock reservoirs.' In: *Geothermics*. Hot Dry Rock (HDR) Reservoir Modelling Activities within Europe 24.3, pp. 345–359. ISSN: 0375-6505. DOI: 10.1016/0375-6505(95)00013-G.

Kolditz, O., L. A. Jakobs, E. Huenges, and T. Kohl (2013). *Geothermal Energy: a glimpse at the state of the field and an introduction to the journal*. Springer.

Kranz, R. L. (1983). 'Microcracks in rocks: a review.' In: *Tectonophysics* 100.1-3, pp. 449–480.

Kushnir, A. R., C. Martel, J.-L. Bourdier, M. J. Heap, T. Reuschlé, S. Erdmann, J.-C. Komorowski, and N. Cholik (2016). 'Probing permeability and microstructure: Unravelling the role of a low-permeability dome on the explosivity of Merapi (Indonesia).' In: *Journal of Volcanology and Geothermal Research* 316, pp. 56–71.

Kushnir, A. R., C. Martel, R. Champallier, and L. Arbaret (2017a). 'In situ confirmation of permeability development in shearing bubble-bearing melts and implications for volcanic outgassing.' In: *Earth and Planetary Science Letters* 458, pp. 315–326.

Kushnir, A. R. L., C. Martel, R. Champallier, and F. B. Wadsworth (2017b). 'Permeability evolution in variably glassy basaltic andesites measured under magmatic conditions.' In: *Geophysical Research Letters* 44.20.

Kuszyk, J. A. and R. C. Bradt (1973). 'Influence of grain size on effects of thermal expansion anisotropy in MgTi2O5.' In: *Journal of the American Ceramic Society* 56.8, pp. 420–423.

Laigle, M., A. Hirn, M. Sapin, J.-C. Lépine, J. Diaz, J. Gallart, and R. Nicolich (2000). 'Mount Etna dense array local earthquake P and S tomography and implications for volcanic plumbing.' en. In: *Journal of Geophysical Research: Solid Earth* 105.B9, pp. 21633–21646. ISSN: 2156-2202. DOI: 10.1029/2000JB900190.

Lamb, O. D., S. De Angelis, R. J. Wall, A. Lamur, N. R. Varley, G. Reyes-Dávila, R. Arámbula-Mendoza, A. J. Hornby, J. E. Kendrick, and Y. Lavallée (2017). 'Seismic and experimental insights into eruption precursors at Volcán de Colima.' en. In: *Geophysical Research Letters* 44.12, 2017GL073350. ISSN: 1944-8007. DOI: 10.1002/2017GL073350.

Larose, E. and S. Hall (2009). 'Monitoring stress related velocity variation in concrete with a 2$\times$ 10- 5 relative resolution using diffuse ultrasound.' In: *The Journal of the Acoustical Society of America* 125.4, pp. 1853–1856.

Le Ravalec, M., M. Darot, T. Reuschle, and Y. Gueguen (1996). 'Transport properties and microstructural characteristics of a thermally cracked mylonite.' In: *pure and applied geophysics* 146.2, pp. 207–227.

Legarth, B., E. Huenges, and G. Zimmermann (2005). 'Hydraulic fracturing in a sedimentary geothermal reservoir: Results and implications.' en. In: *International Journal of Rock Mechanics and Mining Sciences* 42.7-8, pp. 1028–1041. ISSN: 13651609. DOI: 10.1016/j.ijrmms.2005.05.014.

Lehujeur, M., J. Vergne, A. Maggi, and J. Schmittbuhl (2017). 'Ambient noise tomography with non-uniform noise sources and low aperture networks: case study of deep geothermal reservoirs in northern Alsace, France.' en. In: *Geophysical Journal International* 208.1, pp. 193–210. ISSN: 0956-540X, 1365-246X. DOI: 10.1093/gji/ggw373.

Lockner, D. A. (1998). 'A generalized law for brittle deformation of Westerly granite.' en. In: *Journal of Geophysical Research: Solid Earth* 103.B3, pp. 5107–5123. ISSN: 2156-2202. DOI: 10.1029/97JB03211.

Magnenet, V., C. Fond, A. Genter, and J. Schmittbuhl (2014). 'Two-dimensional THM modelling of the large scale natural hydrothermal circulation at Soultz-sous-Forêts.' en. In: *Geothermal Energy* 2.1. ISSN: 2195-9706. DOI: 10.1186/s40517-014-0017-x.

Mavko, G., T. Mukerji, and J. Dvorkin (2009). *The rock physics handbook: Tools for seismic analysis of porous media*. Cambridge university press.

McClintock, F. A. and J. B. Walsh (1962). 'Friction on Griffith cracks in rocks under pressure.' In: *Proc. 4th US Nat. Congr. Appl. Mech.* Vol. 2, pp. 1015–1022.

McNamara, D. D., A. Lister, and D. J. Prior (2016a). 'Calcite sealing in a fractured geothermal reservoir: Insights from combined EBSD and chemistry mapping.' In: *Journal of Volcanology and Geothermal Research* 323, pp. 38–52. ISSN: 0377-0273. DOI: 10.1016/j.jvolgeores.2016.04.042.

McNamara, D. D., S. Sewell, E. Buscarlet, and I. C. Wallis (2016b). 'A review of the Rotokawa Geothermal Field, New Zealand.' In: *Geothermics*. Taupo Volcanic Zone Geothermal Systems, New Zealand : Exploration, Science and Development 59, Part B, pp. 281–293. ISSN: 0375-6505. DOI: 10.1016/j.geothermics.2015.07.007.

Melnik, O, A. A. Barmin, and R. S. J. Sparks (2005). 'Dynamics of magma flow inside volcanic conduits with bubble overpressure buildup and gas loss through permeable magma.' In: *Journal of Volcanology and Geothermal Research* 143.1-3, pp. 53–68. DOI: 10.1016/j.jvolgeores.2004.09.010.

Menéndez, B., C. David, and M. Darot (1999). 'A study of the crack network in thermally and mechanically cracked granite samples using confocal scanning laser microscopy.' In: *Physics and Chemistry of the Earth, Part A: Solid Earth and Geodesy* 24.7, pp. 627–632. ISSN: 1464-1895. DOI: 10.1016/S1464-1895(99)00091-5.

Meredith, P. G. and B. K. Atkinson (1985). 'Fracture toughness and subcritical crack growth during high-temperature tensile deformation of Westerly granite and Black gabbro.' In: *Physics of the Earth and Planetary Interiors* 39.1, pp. 33–51. ISSN: 0031-9201. DOI: 10.1016/0031-9201(85)90113-X.

Meredith, P. G., I. G. Main, O. C. Clint, and L. Li (2012). 'On the threshold of flow in a tight natural rock.' en. In: *Geophysical Research Letters* 39.4, p. L04307. ISSN: 1944-8007. DOI: 10.1029/2011GL050649.

Meredith, P. G., K. S. Knight, S. A. Boon, and I. G. Wood (2001). 'The microscopic origin of thermal cracking in rocks: An investigation by simultaneous time-of-flight neutron diffraction and acoustic emission monitoring.' en. In: *Geophysical Research Letters* 28.10, pp. 2105–2108. ISSN: 1944-8007. DOI: 10.1029/2000GL012470.

Mitchell, T. M. and D. R. Faulkner (2008). 'Experimental measurements of permeability evolution during triaxial compression of initially intact crystalline rocks and implications for fluid flow in fault zones.' en. In: *Journal of Geophysical Research: Solid Earth* 113.B11, B11412. ISSN: 2156-2202. DOI: 10.1029/2008JB005588.

— (2009). 'The nature and origin of off-fault damage surrounding strike-slip fault zones with a wide range of displacements: a field study from the Atacama fault system, northern Chile.' In: *Journal of Structural Geology* 31.8, pp. 802–816.

Molen, I Van der (1981). 'The shift of the α-β transition temperature of quartz associated with the thermal expansion of granite at high pressure.' In: *Tectonophysics* 73.4, pp. 323–342. ISSN: 0040-1951. DOI: 10.1016/0040-1951(81)90221-3.

Murphy, H. D. (1978). *Thermal stress cracking and the enhancement of heat extraction from fractured geothermal reservoirs*. Tech. rep. Los Alamos Scientific Lab., N. Mex.(USA).

Murrell, S. A. F. and P. J. Digby (1970). 'The theory of brittle fracture initiation under triaxial stress conditions—II.' In: *Geophysical Journal International* 19.5, pp. 499–512.

Nara, Y., P. G. Meredith, T. Yoneda, and K. Kaneko (2011). 'Influence of macro-fractures and micro-fractures on permeability and elastic wave velocities in basalt at elevated pressure.' In: *Tectonophysics* 503.1-2, pp. 52–59. ISSN: 0040-1951. DOI: 10.1016/j.tecto.2010.09.027.

Nasseri, M. H. B., A. Schubnel, P. M. Benson, and R. P. Young (2009a). 'Common evolution of mechanical and transport properties in thermally cracked westerly granite at elevated hydrostatic pressure.' In: *Pure and Applied Geophysics* 166.5-7, pp. 927–948. ISSN: 0033-4553. DOI: 10.1007/s00024-009-0485-2.

Nasseri, M. H. B., B. S. A. Tatone, G. Grasselli, and R. P. Young (2009b). 'Fracture Toughness and Fracture Roughness Interrelationship in Thermally treated Westerly Granite.' en. In: *Rock Physics and Natural Hazards*. Pageoph Topical Volumes. Birkhäuser Basel, pp. 801–822. ISBN: 978-3-0346-0121-4 978-3-0346-0122-1. DOI: 10.1007/978-3-0346-0122-1_4.

Nasseri, M., A. Schubnel, and R. Young (2007). 'Coupled evolutions of fracture toughness and elastic wave velocities at high crack density in thermally treated Westerly granite.' In: *International Journal*

of Rock Mechanics and Mining Sciences 44.4, pp. 601–616. ISSN: 1365-1609. DOI: 10.1016/j.ijrmms.2006.09.008.

O'Connell, R. J. and B. Budiansky (1974). 'Seismic velocities in dry and saturated cracked solids.' en. In: *Journal of Geophysical Research* 79.35, pp. 5412–5426. ISSN: 2156-2202. DOI: 10.1029/JB079i035p05412.

Obermann, A., T. Kraft, E. Larose, and S. Wiemer (2015). 'Potential of ambient seismic noise techniques to monitor the St. Gallen geothermal site (Switzerland): Monitoring the St. Gallen Geothermal Site.' en. In: *Journal of Geophysical Research: Solid Earth* 120.6, pp. 4301–4316. ISSN: 21699313. DOI: 10.1002/2014JB011817.

Oda, M., T. Takemura, and T. Aoki (2002). 'Damage growth and permeability change in triaxial compression tests of Inada granite.' In: *Mechanics of Materials* 34.6, pp. 313–331. ISSN: 0167-6636. DOI: 10.1016/S0167-6636(02)00115-1.

Odling, N. W., S. C. Elphick, P. Meredith, I. Main, and B. T. Ngwenya (2007). 'Laboratory measurement of hydrodynamic saline dispersion within a micro-fracture network induced in granite.' en. In: *Earth and Planetary Science Letters* 260.3-4, pp. 407–418. ISSN: 0012821X. DOI: 10.1016/j.epsl.2007.05.034.

Ohno, K. and M. Ohtsu (2010). 'Crack classification in concrete based on acoustic emission.' In: *Construction and Building Materials*. Special Issue on Fracture, Acoustic Emission and NDE in Concrete (KIFA-5) 24.12, pp. 2339–2346. ISSN: 0950-0618. DOI: 10.1016/j.conbuildmat.2010.05.004.

Ohtsu, M., T. Isoda, and Y. Tomoda (2007). 'Acoustic emission techniques standardized for concrete structures.' In: *Journal of Acoustic Emission* 25, pp. 21–32.

Ortiz, M. (1988). 'Microcrack coalescence and macroscopic crack growth initiation in brittle solids.' In: *International Journal of Solids and Structures* 24.3, pp. 231–250.

Ougier-Simonin, A., J. Fortin, Y. Guéguen, A. Schubnel, and F. Bouyer (2011). 'Cracks in glass under triaxial conditions.' In: *International Journal of Engineering Science*. Recent Advances in Micromechanics of Materials 49.1, pp. 105–121. ISSN: 0020-7225. DOI: 10.1016/j.ijengsci.2010.06.026.

Patane, D., C. Chiarabba, O. Cocina, P. De Gori, M. Moretti, and E. Boschi (2002). 'Tomographic images and 3D earthquake locations of the seismic swarm preceding the 2001 Mt. Etna eruption: Evidence for a dyke intrusion.' en. In: *Geophysical Research Letters* 29.10, pp. 135–1. ISSN: 1944-8007. DOI: 10.1029/2001GL014391.

Paterson, M. S. and T.-f. Wong (2005). *Experimental rock deformation-the brittle field*. Springer Science & Business Media.

Poupinet, G., W. L. Ellsworth, and J. Frechet (1984). 'Monitoring velocity variations in the crust using earthquake doublets: An application to the Calaveras Fault, California.' en. In: *Journal of Geo-*

physical Research: Solid Earth 89.B7, pp. 5719–5731. ISSN: 2156-2202. DOI: 10.1029/JB089iB07p05719.

Ramez, M. R. H. and S. A. F. Murrell (1964). 'A petrofabric analysis of Carrara marble.' In: *International Journal of Rock Mechanics and Mining Sciences & Geomechanics Abstracts*. Vol. 1. Elsevier, pp. 217–229.

Rawling, G. C., P. Baud, and T.-f. Wong (2002). 'Dilatancy, brittle strength, and anisotropy of foliated rocks: Experimental deformation and micromechanical modeling.' en. In: *Journal of Geophysical Research: Solid Earth* 107.B10, p. 2234. ISSN: 2156-2202. DOI: 10.1029/2001JB000472.

Reuschlé, T., S. Gbaguidi Haore, and M. Darot (2003). 'Microstructural control on the elastic properties of thermally cracked granite.' In: *Tectonophysics* 370.1-4, pp. 95–104. ISSN: 0040-1951. DOI: 10.1016/S0040-1951(03)00179-3.

Reuschlé, T., S. Gbaguidi Haore, and M. Darot (2006). 'The effect of heating on the microstructural evolution of La Peyratte granite deduced from acoustic velocity measurements.' In: *Earth and Planetary Science Letters* 243.3-4, pp. 692–700. DOI: 10.1016/j.epsl.2006.01.038.

Saltykov, S. A. (1958). 'Stereometric metallography.' In: *Metallurgizdat, Moscow* 267.

Sammis, C. and M. Ashby (1986). 'The failure of brittle porous solids under compressive stress states.' en. In: *Acta Metallurgica* 34.3, pp. 511–526. ISSN: 00016160. DOI: 10.1016/0001-6160(86)90087-8.

Sanders, C. O., S. C. Ponko, L. D. Nixon, and E. A. Schwartz (1995). 'Seismological evidence for magmatic and hydrothermal structure in Long Valley caldera from local earthquake attenuation and velocity tomography.' In: *Journal of Geophysical Research: Solid Earth* 100.B5, pp. 8311–8326.

Schaefer, L. N., J. E. Kendrick, T. Oommen, Y. Lavallée, and G. Chigna (2015). 'Geomechanical rock properties of a basaltic volcano.' In: *Volcanology* 3, p. 29. DOI: 10.3389/feart.2015.00029.

Scheu, B., H. Kern, O. Spieler, and D. B. Dingwell (2006). 'Temperature dependence of elastic P- and S-wave velocities in porous Mt. Unzen dacite.' In: *Journal of Volcanology and Geothermal Research*. MULTIMO: Multi-Parameter Monitoring, Modelling and Forecasting of Volcanic Hazard 153.1, pp. 136–147. ISSN: 0377-0273. DOI: 10.1016/j.jvolgeores.2005.08.007.

Sens-Schönfelder, C. and U. Wegler (2006). 'Passive image interferemetry and seasonal variations of seismic velocities at Merapi Volcano, Indonesia.' In: *Geophysical Research Letters* 33.21, pp. 1–5. ISSN: 2006101029. DOI: 10.1029/2006GL027797.

Siddiqi, G. and B. Evans (2015). 'Permeability and thermal cracking at pressure in Sioux Quartzite.' In: *Geological Society, London, Special Publications* 409.1, pp. 49–66.

Signorelli, S., S. Bassetti, D. Pahud, and T. Kohl (2007). 'Numerical evaluation of thermal response tests.' In: *Geothermics* 36.2, pp. 141–166. ISSN: 0375-6505. DOI: 10.1016/j.geothermics.2006.10.006.

Simmons, G. and D. Richter (1976). 'Microcracks in rocks.' In: *The physics and chemistry of minerals and rocks*, pp. 105–137.

Simmons, G., T. Todd, and W. S. Baldridge (1975). 'Toward a quantitative relationship between elastic properties and cracks in low porosity rocks.' In: *American Journal of Science* 275.3, pp. 318–345.

Siratovich, P. A., I. Sass, S. Homuth, and A. Bjornsson (2011). 'Thermal stimulation of geothermal reservoirs and laboratory investigation of thermally-induced fractures.' In: *Proc., Geothermal Resources Council Annual Meeting*, pp. 1529–1535.

Siratovich, P. A., M. J. Heap, M. C. Villenueve, J. W. Cole, and T. Reuschlé (2014). 'Physical property relationships of the Rotokawa Andesite, a significant geothermal reservoir rock in the Taupo Volcanic Zone, New Zealand.' en. In: *Geothermal Energy* 2.1, p. 10. ISSN: 2195-9706. DOI: 10.1186/s40517-014-0010-4.

Siratovich, P. A., M. C. Villeneuve, J. W. Cole, B. M. Kennedy, and F. Bégué (2015). 'Saturated heating and quenching of three crustal rocks and implications for thermal stimulation of permeability in geothermal reservoirs.' In: *International Journal of Rock Mechanics and Mining Sciences* 80, pp. 265–280. ISSN: 1365-1609. DOI: 10.1016/j.ijrmms.2015.09.023.

Snieder, R. (2002). 'Coda wave interferometry and the equilibration of energy in elastic media.' en. In: *Physical Review E* 66.4. ISSN: 1063-651X, 1095-3787. DOI: 10.1103/PhysRevE.66.046615.

— (2006). 'The Theory of Coda Wave Interferometry.' en. In: *Pure and Applied Geophysics* 163.2-3, pp. 455–473. ISSN: 0033-4553, 1420-9136. DOI: 10.1007/s00024-005-0026-6.

Souley, M., F. Homand, S. Pepa, and D. Hoxha (2001). 'Damage-induced permeability changes in granite: a case example at the URL in Canada.' In: *International Journal of Rock Mechanics and Mining Sciences* 38.2, pp. 297–310.

Sparks, R. S. J., M. I. Bursik, S. N. Carey, J. Gilbert, L. S. Glaze, H. Sigurdsson, and A. W. Woods (1997). *Volcanic plumes*. Wiley.

Stanchits, S., S. Vinciguerra, and G. Dresen (2006). 'Ultrasonic velocities, acoustic emission characteristics and crack damage of basalt and granite.' In: *Pure and Applied Geophysics* 163, pp. 974–993. DOI: 10.1007/s00024-006-0059-5.

Stimac, J., G. Nordquist, A. Suminar, and L. Sirad-Azwar (2008). 'An overview of the Awibengkok geothermal system, Indonesia.' In: *Geothermics*. Indonesian geothermal prospects and developments

37.3, pp. 300–331. ISSN: 0375-6505. DOI: 10.1016/j.geothermics.2008.04.004.

Tapponnier, P. and W. F Brace (1976). 'Development of stress-induced microcracks in Westerly Granite.' In: *International Journal of Rock Mechanics and Mining Sciences & Geomechanics Abstracts* 13.4, pp. 103–112. ISSN: 0148-9062. DOI: 10.1016/0148-9062(76)91937-9.

Teklemariam, M., K. Beyene, Y. AmdeBerhan, and Z. Gebregziabher (2000). 'Geothermal development in Ethiopia.' In: *Proceedings, World Geothermal Congress 2000*, pp. 475–480.

Thirumalai, K. and S. G. Demou (1974). 'Thermal Expansion Behavior of Intact and Thermally Fractured Mine Rocks.' en. In: ASCE, pp. 60–71. ISBN: 978-0-88318-116-4. DOI: 10.1063/1.2945937.

Thór Gudmundsson, B. and S. Arnórsson (2002). 'Geochemical monitoring of the Krafla and Námafjall geothermal areas, N-Iceland.' In: *Geothermics* 31.2, pp. 195–243. ISSN: 0375-6505. DOI: 10.1016/S0375-6505(01)00022-0.

Todd, T. P. (1973). 'Effect of cracks on elastic properties of low porosity rocks.' PhD thesis. Massachusetts Institute of Technology.

Trégourès, N. P. and B. A. van Tiggelen (2002). 'Quasi-two-dimensional transfer of elastic waves.' en. In: *Physical Review E* 66.3. ISSN: 1063-651X, 1095-3787. DOI: 10.1103/PhysRevE.66.036601.

Underwood, E. E. (1967). 'Quantitative Evaluation of Sectioned Material.' en. In: *Stereology*. Ed. by H. Elias. Springer Berlin Heidelberg, pp. 49–60. ISBN: 978-3-540-03987-7 978-3-642-88260-9. DOI: 10.1007/978-3-642-88260-9_5.

Unnþórsson, R. (2013). 'Hit Detection and Determination in AE Bursts.' In: *Acoustic Emission - Research and Applications*, pp. 1–20. DOI: 10.5772/54754.

Valley, B. and K. F. Evans (2007). 'Stress state at Soultz-sous-Forêts to 5 km depth from wellbore failure and hydraulic observations.' In: *Proceedings, 32nd workshop on geothermal reservoir engineering*, pp. 17481–17469.

Villaseñor, A., H. M. Benz, L. Filippi, G. De Luca, R. Scarpa, G. Patanè, and S. Vinciguerra (1998). 'Three-dimensional P-wave velocity structure of Mt. Etna, Italy.' en. In: *Geophysical Research Letters* 25.11, pp. 1975–1978. ISSN: 1944-8007. DOI: 10.1029/98GL01240.

Vinciguerra, S., C. Trovato, P. G. Meredith, and P. M. Benson (2005). 'Relating seismic velocities, thermal cracking and permeability in Mt. Etna and Iceland basalts.' In: *International Journal of Rock Mechanics and Mining Sciences* 42, pp. 900–910. ISSN: 1365-1609. DOI: 10.1016/j.ijrmms.2005.05.022.

Violay, M., M. J. Heap, M. Acosta, and C. Madonna (2017). 'Porosity evolution at the brittle-ductile transition in the continental crust: Implications for deep hydro-geothermal circulation.' In: *Scientific Reports* 7. ISSN: 2045-2322. DOI: 10.1038/s41598-017-08108-5.

Vosteen, H. and R. Schellschmidt (2003). 'Influence of temperature on thermal conductivity, thermal capacity and thermal diffusivity for different types of rock.' In: *Physics and Chemistry of the Earth* 28, pp. 499–509. DOI: 10.1016/S1474-7065(03)00069-X.

Walsh, J. B. (1965). 'The effect of cracks on the compressibility of rock.' In: *Journal of Geophysical Research* 70.2, pp. 381–381. ISSN: 0148-0227. DOI: 10.1029/JZ070i002p00381.

Walt, S. Van der, J. L. Schönberger, J. Nunez-Iglesias, F. Boulogne, J. D. Warner, N. Yager, E. Gouillart, and T. Yu (2014). 'scikit-image: image processing in Python.' In: *PeerJ* 2, e453.

Wang, H. F., B. P. Bonner, S. R. Carlson, B. J. Kowallis, and H. C. Heard (1989). 'Thermal stress cracking in granite.' en. In: *Journal of Geophysical Research* 94.B2, p. 1745. ISSN: 0148-0227. DOI: 10.1029/JB094iB02p01745.

Wang, X.-Q., A. Schubnel, J. Fortin, E. C. David, Y. Guéguen, and H.-K. Ge (2012). 'High Vp/Vs ratio: Saturated cracks or anisotropy effects?' en. In: *Geophysical Research Letters* 39.11, p. L11307. ISSN: 1944-8007. DOI: 10.1029/2012GL051742.

Wang, X.-Q., A. Schubnel, J. Fortin, Y. Guéguen, and H.-K. Ge (2013). 'Physical properties and brittle strength of thermally cracked granite under confinement.' In: *Journal of Geophysical Research: Solid Earth* 118, pp. 6099–6112. ISSN: 2169-9356. DOI: 10.1002/2013JB010340.

Wedepohl, K. H. (1995). 'The composition of the continental crust.' In: *Geochimica et cosmochimica Acta* 59.7, pp. 1217–1232.

Wong, R. H. C., K. T. Chau, C. A. Tang, and P. Lin (2001). 'Analysis of crack coalescence in rock-like materials containing three flaws—part I: experimental approach.' In: *International Journal of Rock Mechanics and Mining Sciences* 38.7, pp. 909–924.

Wong, T.-f. (1982). 'Micromechanics of faulting in westerly granite.' In: *International Journal of Rock Mechanics and Mining Sciences & Geomechanics Abstracts* 19.2, pp. 49–64. ISSN: 0148-9062. DOI: 10.1016/0148-9062(82)91631-X.

Wong, T.-f. and W. F. Brace (1979). 'Thermal expansion of rocks: some measurements at high pressure.' In: *Tectonophysics* 57.2, pp. 95–117. ISSN: 0040-1951. DOI: 10.1016/0040-1951(79)90143-4.

Wong, T.-f. (1985). 'Geometric probability approach to the characterization and analysis of microcracking in rocks.' In: *Mechanics of Materials* 4.3, pp. 261–276. ISSN: 0167-6636. DOI: 10.1016/0167-6636(85)90023-7.

Wu, X. Y., P Baud, and T.-f. Wong (2000). 'Micromechanics of compressive failure and spatial evolution of anisotropic damage in Darley Dale sandstone.' In: *International Journal of Rock Mechanics and Mining Sciences* 37.1–2, pp. 143–160. ISSN: 1365-1609. DOI: 10.1016/S1365-1609(99)00093-3.

Wyering, L., M. Villeneuve, I. Wallis, P. Siratovich, B. Kennedy, D. Gravley, and J. Cant (2014). 'Mechanical and physical proper-

ties of hydrothermally altered rocks, Taupo Volcanic Zone, New Zealand.' en. In: *Journal of Volcanology and Geothermal Research* 288, pp. 76–93. ISSN: 03770273. DOI: 10.1016/j.jvolgeores.2014.10.008.

Xu, T., C.-a. Tang, J. Zhao, L. Li, and M. J. Heap (2012). 'Modelling the time-dependent rheological behaviour of heterogeneous brittle rocks.' In: *Geophysical Journal International* 189.3, pp. 1781–1796.

Yong, C. and C.-y. Wang (1980). 'Thermally induced acoustic emission in Westerly granite.' In: *Geophysical Research Letters* 7.12, pp. 1089–1092.

Yukutake, H. (1989). 'Fracturing process of granite inferred from measurements of spatial and temporal variations in velocity during triaxial deformations.' In: *Journal of Geophysical Research: Solid Earth* 94.B11, pp. 15639–15651.

Zappone, A. S. and P. M. Benson (2013). 'Effect of phase transitions on seismic properties of metapelites: A new high-temperature laboratory calibration.' en. In: *Geology* 41.4, pp. 463–466. ISSN: 0091-7613. DOI: 10.1130/G33713.1.

Zhang, Y., O. Abraham, V. Tournat, A. Le Duff, B. Lascoup, A. Loukili, F. Grondin, and O. Durand (2013). 'Validation of a thermal bias control technique for Coda Wave Interferometry (CWI).' en. In: *Ultrasonics* 53.3, pp. 658–664. ISSN: 0041624X. DOI: 10.1016/j.ultras.2012.08.003.

Zhou, C., Z. Wan, Y. Zhang, and B. Gu (2018). 'Experimental study on hydraulic fracturing of granite under thermal shock.' In: *Geothermics* 71.Supplement C, pp. 146–155. ISSN: 0375-6505. DOI: 10.1016/j.geothermics.2017.09.006.

Zhu, W., P. Baud, S. Vinciguerra, and T.-f. Wong (2016). 'Micromechanics of brittle faulting and cataclastic flow in Mount Etna basalt: Micromechanics of deformation in basalt.' en. In: *Journal of Geophysical Research: Solid Earth* 121.6, pp. 4268–4289. ISSN: 21699313. DOI: 10.1002/2016JB012826.

Zimmerman, R. W. (1985). 'The effect of microcracks on the elastic moduli of brittle materials.' In: *Journal of Materials Science Letters* 4.12, pp. 1457–1460. DOI: 10.1007/BF00721363.

— (1989). 'Thermal conductivity of fluid-saturated rocks.' In: *Journal of Petroleum Science and Engineering* 3.3, pp. 219–227.

Zoback, M. D. (2010). *Reservoir geomechanics*. Cambridge University Press.

Zoback, M. D. and J. D. Byerlee (1975). 'The effect of microcrack dilatancy on the permeability of westerly granite.' en. In: *Journal of Geophysical Research* 80.5, pp. 752–755. ISSN: 2156-2202. DOI: 10.1029/JB080i005p00752.

Zuberek, W., B. Zogała, R. Dubiel, and J. Pierwoła (1998). 'Maximum temperature memory in sandstone and mudstone observed with acoustic emission and ultrasonic measurements.' en. In: *Interna-*

tional Journal of Rock Mechanics and Mining Sciences 35.4-5, pp. 416–417. ISSN: 13651609. DOI: 10.1016/S0148-9062(98)00115-6.

COLOPHON

This document was typeset using the typographical look-and-feel `classicthesis` developed by André Miede and Ivo Pletikosić. The style was inspired by Robert Bringhurst's seminal book on typography "*The Elements of Typographic Style*". `classicthesis` is available for both LaTeX and LyX:

https://bitbucket.org/amiede/classicthesis/

Luke Griffiths

La fissuration thermique dans les roches

Résumé

Lorsqu'elle est chauffée, la roche peut subir une microfissuration thermique, qui influence ses propriétés physiques, mécaniques, thermiques, et de transport. La surveillance de la microfissuration thermique en laboratoire a été principalement réalisée pendant le chauffage, et rarement lors du refroidissement ou du chauffage cyclique que la roche subit dans les volcans et les réservoirs géothermiques. Un nouvel appareil a été élaboré pour surveiller les émissions acoustiques et mesurer les vitesses des ondes élastiques à haute température. L'état de fissuration a été évalué grâce à un nouvel algorithme d'analyse microstructurale, et l'influence des microfissures sur les propriétés des roches a été mesurée et modélisée. Selon la microstructure, la microfissuration peut avoir lieu pendant le chauffage ou le refroidissement, et les microfissures existantes peuvent s'ouvrir et se fermer de façon réversible avec des changements de température, et influencer les propriétés de la roche.

Mots clés : Température, fissuration thermique, granite, roches volcaniques, émissions acoustiques, vitesse des ondes acoustiques, interférométrie des ondes coda, déformation, permeabilité, géothermie.

Résumé en anglais

Rock may undergo thermal microcracking when heated, affecting its physical, mechanical, thermal, and transport properties. Thermal microcrack monitoring in the laboratory has mainly been performed during heating, and rarely during the cyclic heating and cooling relevant for volcanoes and geothermal reservoirs. For this, a new dedicated apparatus for the acoustic emission monitoring and wave velocity measurement at high temperatures was elaborated, building on previous designs. Microcrack damage was assessed with a new algorithm for quantitative microstructural analysis, and the influence of thermal microcracks on rock properties was measured and modelled. Depending on the rock type and initial microcrack content, microcracking occurred during either heating, cooling, or neither, and existing microcracks reversibly opened or closed with increasing temperature. In Earth's crust, the evolution of rock properties with temperature may be significant and is determined by the microstructure.

Keywords : Temperature, thermal microcracking, granite, volcanic rock, acoustic emissions, acoustic wave velocity, coda wave interferometry, deformation, permeability, geothermal energy.